DISSERTATION

# THE RIGHT VENTRICLE—THE FORGOTTEN CHAMBER THAT DESERVES MORE LOVE

Submitted by

Michael Nguyen-Truong

School of Biomedical Engineering

In partial fulfillment of the requirements

For the Degree of Doctor of Philosophy

Colorado State University

Fort Collins, Colorado

Spring 2022

Doctoral Committee:

Advisor: Zhijie Wang

Adam Chicco
Yan Vivian Li
Kirk McGilvray
Ketul Popat

# ABSTRACT

# THE RIGHT VENTRICLE—THE FORGOTTEN CHAMBER THAT DESERVES MORE LOVE

Right ventricle failure (RVF) is associated with serious cardiac and pulmonary diseases that contribute significantly to the morbidity and mortality of patients. The prevalence of RVF is significantly increased in the later stages of pulmonary hypertension, congenital heart disease, and left heart failure with preserved ejection fraction. Moreover, the mortality rate of these patients has not improved with currently limited treatment options. The persistent clinical challenge is mainly due to an incomplete understanding of the structure-function relationships of the RV, partly attributed to the lack of large animal models, as well as the lack of RV-specific therapies.

Therefore, **the overall goal of the study** is to fill knowledge gaps in the biomechanics of right ventricle failure secondary to pressure overload and in the regenerative potential of mesenchymal stromal cells (MSCs) regulated by RV mechanics. The specific aims are:

1. Assess the unique *ex vivo* biomechanics of the RV free wall in contrast to the LV free wall.
2. Assess the *ex vivo* biomechanics of the "significant other" of the RV chamber – the septum wall.
3. Establish a novel ovine model of RV failure and investigate RV biomechanical changes during RV failure progression.
4. Investigate the pro-angiogenic paracrine effect in the context of mesenchymal stromal cell mechanobiology to ultimately improve RV therapy.

From ovine models, there was distinct anisotropic mechanical behavior of the RV compared to the left side in healthy adults, and the low-strain mechanical behavior was correlated to collagen III. Multiscale computational model indicated softer collagen fibers in the RV. The investigation on the septal wall originally revealed transmural biomechanical changes and a significantly more compliant wall than the ventricular free walls. A new ovine model of adult RV failure was established, and there was stiffening of the RV in the outflow tract direction and altered tissue anisotropy with RV failure progression. Finally, from prior and our own RV mechanical data, biomimetic scaffolds that represent healthy and diseased RV mechanics were fabricated for the first time. The pro-angiogenic potentials of MSCs on these scaffolds were assessed by cytokine production and neovessel formation. There were synergistic effects of matrix stiffness and anisotropy on MSC pro-angiogenic functionality.

# ACKNOWLEDGEMENTS

I would like to acknowledge the outstanding and wonderful mentorship by my advisor, Dr. Zhijie Wang. I have learned so much, become a better scientist, and have gone to new heights thanks to your mentorship.

I also would like to thank my committee members: Dr. Adam Chicco, Dr. Yan Vivian Li, Dr. Kirk McGilvray, and Dr. Ketul Popat for their resources, guidance, support, and insights in my project.

My success also would not be without the support of my lab-mates, particularly Wenqiang Liu, Brian Funfgeld, Kristen LeBar, Elisabeth Gray, Courtney Doherty, and Megan Frederes. Thank you for making my PhD study a wonderful experience.

Lastly, to my parents who have been supporting me throughout my academic journey, I am forever grateful for your encouragement, love, and care.

# TABLE OF CONTENTS

ABSTRACT ii
ACKNOWLEDGEMENTS iv
LIST OF TABLES vii
LIST OF FIGURES viii
1. Introduction: Pressure Overload Induced Right Ventricle Failure 1
  1.1 Overall Function and Structure of the Heart 1
  1.2 Right Ventricle Failure (RVF) Investigation 4
References 8
2. Specific Aims 10
3. Multiscale Contrasts between the Right and Left Ventricle Biomechanics in Healthy Adult Sheep and Translational Implications 11
  3.1 Introduction 11
  3.2 Methods 14
  3.3 Results 22
  3.4 Discussion 28
References 36
4. The Interventricular Septum Is Biomechanically Distinct from the Ventricular Free Walls 40
  4.1 Introduction 40
  4.2 Methods 43
  4.3 Results 48
  4.4 Discussion 54
References 62
5. *In Vivo* Ovine Model of RV Failure Progression 65
  5.1 Establishment of Adult Right Ventricle Failure in Ovine Using a Graded, Animal-Specific Pulmonary Artery Constriction Model 65
    5.1.1 Introduction 65
    5.1.2 Methods 70
    5.1.3 Results 73
    5.1.4 Discussion 81
  5.2. Failing RV Free Wall Biomechanics 88
    5.2.1 Introduction 88
    5.2.2 Methods 89
    5.2.3 Results 92
    5.2.4 Discussion 93
References 95
6. Mechanical Regulation of Pro-angiogenic Paracrine Effect of Mesenchymal Stromal Cells 101
  6.1 Mechanical Considerations of Electrospun Scaffolds for Myocardial Tissue and Regenerative Engineering 101
    6.1.1 Clinical Significance 101
    6.1.2 Types of Scaffolds in Cardiac Tissue Engineering and Regenerative Medicine 103
    6.1.3 Electrospinning of Microfibrous Scaffolds 104
    6.1.4 *In Vivo* Studies: Electrospun Scaffolds in Cardiac Therapies 107

- 6.1.5 Mechanical Measurement of Scaffolds ..... 111
- 6.1.6 Discrepant Elastic Moduli Reported from Native Myocardial Tissues in the Literature ..... 117
- 6.1.7 *In Vitro* Studies: Matrix Mechanics Dependent Cellular Functions in Regenerative Research ..... 120
- 6.1.8 Are Current Scaffolds Mechanically Biomimetic Enough? ..... 123
- 6.1.9 Conclusion and Other Future Perspectives ..... 124

6.2 Current Status of Myocardial Restoration via the Paracrine Function of Mesenchymal Stromal Cells (MSCs) ..... 125
- 6.2.1 Emerging Non-differentiating Roles of MSCs in Tissue Regeneration ..... 125
- 6.2.2 Unique Characteristics of MSCs ..... 127
- 6.2.3 Acellular Components Derived from MSCs Emerging as a New Therapy ..... 128
- 6.2.4 MSC Paracrine Effect: Mechanisms of Action and Potential Enhancement Strategies ..... 143
- 6.2.5 Remaining Challenges of MSC Mediated Paracrine Effects for Cardiac Restoration ..... 152
- 6.2.6 Conclusions ..... 153

6.3 Pro-angiogenic Potential of Mesenchymal Stromal Cells Regulated by Matrix Stiffness and Anisotropy Mimicking Right Ventricles ..... 154
- 6.3.1 Introduction ..... 154
- 6.3.2 Methods ..... 156
- 6.3.3 Results ..... 161
- 6.3.4 Discussion ..... 168

References ..... 175

7. Conclusions and Future Work ..... 194

Appendix ..... 197

# LIST OF TABLES

Table 1.1 – Differences between LV and RV chambers ....6
Table 3.1 – Equibiaxial maximum in-plane and shear stretches ....17
Table 3.2 – Fung model fitting results of LVs and RVs ....24
Table 3.3 – Structurally informed model fitting results of LVs and RVs ....26
Table 4.1 – Maximum normal strains and corresponding shear strains of septum ....45
Table 4.2 – Myofiber angle of LV-side, midwall, and RV-side of septum ....48
Table 4.3 – Fung model fitting results of LV and RV sides of the septum ....52
Table 5.1 – Review of PA banding/constriction in small and large animals ....67
Table 5.2 – Volume of saline injections for PAC animals over 11 weeks ....71
Table 5.3 – Overall structural changes in ovine hearts with PAC ....77
Table 5.4 – Hemodynamics, structure, and function measurements of ovine RV in CTL and PAC ....77
Table 6.1 – Various ranges of Young's moduli of electrospun scaffolds in cardiac tissue engineering ....110
Table 6.2 – Mechanical testing methods to derive elastic modulus of materials ....116
Table 6.3 – Different Young's moduli reported for LV and RV tissues ....118
Table 6.4 – Preclinical regenerative therapy studies for infarcted heart using cell products ....132
Table 6.5 – Clinical trials of MSC EVs for safety or efficacy to treat non-cardiac diseases ....135
Table 6.6 – Clinical trials of MSC conditioned medium for safety or efficacy to treat non-cardiac diseases ....139
Table 6.7 – Key altered parameters for electrospinning of different scaffolds ....157
Table 6.8 – Representative SEM images and other structural factors of PEUU scaffolds ....162
Table 6.9 – Average values of 18 pro-angiogenic cytokines from conditioned media at 48 h ....166

# LIST OF FIGURES

Fig. 1.1 – Graphic representation of myocardium ....................2
Fig. 1.2 – Graphic representation of ventricular compliance differences between LV and RV......5
Fig. 1.3 – Workflow for RV failure research....................7
Fig. 3.1 – Representative photo of fresh ovine heart and outflow tract label....................15
Fig. 3.2 – Comparison of LV and RV average stress-strain curves in longitudinal and circumferential directions ....................22
Fig. 3.3 – Different elastic moduli of LVs and RVs ....................23
Fig. 3.4 – Equibiaixal stress-strain curves from four-parameter Fung Model ....................25
Fig. 3.5 – Zero-load elastic moduli and anisotropic parameter *K* of LVs and RVs ....................26
Fig. 3.6 – Representative fitting results using structurally informed model ....................27
Fig. 3.7 – Histological measurement and correlation analysis for collagen of LVs and RVs.......28
Fig. 4.1 – Schematic of septum split into two even sides ....................40
Fig. 4.2 – Schematic of orientations for each side of septum ....................44
Fig. 4.3 – Average stress-strain curves of LV and RV sides of the septum ....................49
Fig. 4.4 – Comparison of elastic moduli of septum and ventricles ....................50
Fig. 4.5 – Comparison of elastic moduli between left and right sides of septum ....................51
Fig. 4.6 – Zero-load elastic modulus of LV and RV sides of the septum ....................53
Fig. 4.7 – Comparisons of collagen area fraction between septum and ventricles ....................54
Fig. 5.1 – Workflow of PAC sheep model and timeline....................71
Fig. 5.2 – Decline in RV hemodynamics and function with PAC....................74
Fig. 5.3 – Temporal changes of RV diastolic geometry with PAC ....................75
animals ....................76
Fig. 5.4 – Correlations between RV structure and function of CTL and PAC groups....................79
Fig. 5.5 – Correlations between echocardiography and Swan-Ganz catheterization measurements ....................80
Fig. 5.6 – More correlations between echocardiography and Swan-Ganz catheterization measurements.. ....................81
Fig. 5.7 – Comparison of RV average stress-strain curves from different testing conditions ......91
Fig. 5.8 – Different RV elasticities derived from stress-strain curves of CTL and PH groups ....93
Fig. 6.1 – Schematic of electrospinning methods to create and random and aligned scaffolds .107
Fig. 6.2 – Mechanisms of action for MSC paracrine effect from conditioned medium or MSC EVs....................144
Fig. 6.3 – Mechanical regulation of MSC paracrine effect probed by *in vitro* experiments.......152
Fig. 6.4 – Mechanical properties of PEUU scaffolds ....................162
Fig. 6.5 – Effect of stiffness and anisotropy on total VEGF, MSC count, and VEGF/MSC at 48 h ....................164
Fig. 6.6 – Pro-angiogenic factors in conditioned media at 48 h ....................165
Fig. 6.7 – Tube formation results from conditioned media at 22 h ....................167

# 1. Introduction: Pressure Overload Induced Right Ventricle Failure[1]

## 1.1 Overall Function and Structure of the Heart

### *1.1.1 Overview*

Central to human life, the heart serves to maintain the systemic and pulmonary blood circulations which provide nutrients and oxygen while removing wastes from all organs in the body. The heart, often analogous to a 'pump', is made up of four chambers (i.e., left and right atriums, left and right ventricles) and four valves (i.e., mitral valve, aortic valve, tricuspid valve and pulmonary valve). In this unique architecture of the organ, the blood is 'pumped' out of the heart into systemic or pulmonary circulation via the contraction of the left ventricle (LV) or right ventricle (RV), respectively. The LV and RV chambers are divided by the shared interventricular septum wall (**Fig. 1.1**). The open and close of the valves during systole (contractile) and diastole (relaxing or dilated) phases are also important steps to ensure the sequential, unidirectional blood flow between the chambers.

---

[1] Adapted by permission from Springer Nature Customer Service Centre GmbH: Springer. *Cardiac Extracellular Matrix.* "Biomechanical Properties and Mechanobiology of Cardiac ECM". Nguyen-Truong M and Wang Z, 2018. https://doi.org/10.1007/978-3-319-97421-7_1

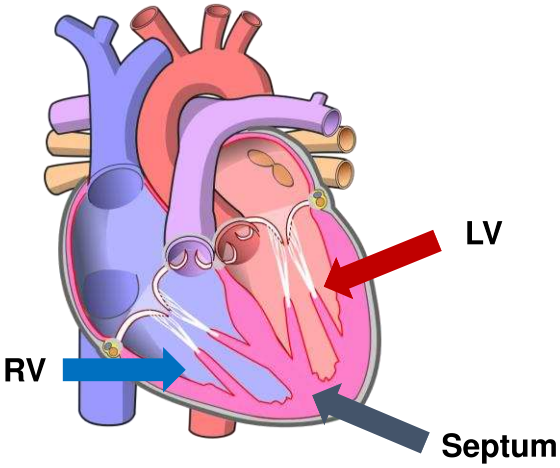

**Figure 1.1.** Graphic representation of the myocardium. RV: right ventricle. LV: left ventricle. Adapted from Stenemo - derivative work Diagram of the human heart (cropped).svg, CC BY-SA 4.0, https://commons.wikimedia.org/w/index.php?curid=63920599.

### *1.1.2 Different Cardiac Cell Types*

The composition of cardiac tissues varies depending on the location of the tissue. In the myocardium (i.e., the muscular layer of the ventricular wall), the typical cell types include cardiomyocytes (cardiac muscle cells), cardiac fibroblasts (CFs), endothelial cells (ECs) and smooth muscle cells (SMCs). The cardiomyocytes occupy around 70% of the volumes of the ventricular wall under normal circumstances[1]. However, the CF is the most abundant cell type in the myocardium and the main role of fibroblasts lies in the synthesis and maintenance of the extracellular matrix (ECM) in the myocardium[2]. The number of CFs (or the ratio of fibroblasts to myocytes) varies depending on tissue regions, species and age[3].

In the heart valves, the main cells include the interstitial cells and endothelial cells. The interstitial cells are specialized cells that mostly exhibit the characteristics of smooth muscle cells and myofibroblast cells. They are responsible for the synthesis and maintenance of ECM in the heart valves[4]. Valvular ECs play essential roles in establishing the valve structures during embryonic development and are important for maintaining lifelong valve integrity and function[5].

### *1.1.3 Extracellular Matrix (ECM) Composition in Cardiac Tissues*

The cells in the heart are supported by the architecture maintained by the ECM components (**Table A1**). The conventional wisdom considers the ECM as a passive component that mainly affects the mechanical properties of cardiac tissue. However, more and more evidence suggest that cardiac ECM can play an active role in the tissue remodeling process in response to altered mechanical loadings.

In the myocardium, the ECM consists of proteins such as collagen, elastin, fibronectin, proteoglycan and laminin. Collagen is the most abundant ECM protein in the heart, with at least 5 different types of collagen (I, III, IV, V and VI) that have been identified in the myocardium[1]. Whereas types IV and V collagen are mostly found in the basement membrane of the myocytes, types I and III collagen are the main constituents in the ECM: type I collagen represents 75~80% of total collagen content and type III collagen represents approximately 15~20% of the total collagen[6]. A small percentage of collagen is composed of type V collagen (less than 5%)[1, 7]. The collagen content in the heart depends on species: the larger the mammal, the greater the collagen content of the heart[3]. Cardiac collagen metabolism, i.e., the balance of synthesis and degradation, is profoundly affected by various cardiac cells and secreted cytokines, growth factors, hormones, enzymes and other reagents[1]. Lastly, because of the branching of cardiomyocytes and the spiral orientation of these cells called the ‘myocardial band’, the investigation on the structure and arrangement of ECM surrounding the myocytes as well as its interaction with the cells has been challenging and remains a matter of debate.

The heart valves are leaflets that can be divided into three layers (the fibrosa, spongiosa and ventricularis layers) when viewed from the cross-sectional structure. Each layer has a distinct ECM composition that aids in normal mechanical behavior of the valve. The mechanical function of valves is achieved by a highly organized and hydrated network of ECM proteins including collagen (rich in fibrosa layer), elastin (rich in ventricularis layer), glycosaminoglycans (GAGs) and proteoglycans (PGs) (rich in spongiosa layer)[8, 9]. Water comprises about 60-70% of the valves by weight, which is similar to other soft tissues such as arteries, skin, cartilages, etc. The hydrated nature may be especially important for heart valves because it enables the diffusion of nutrients and oxygen through the valvular tissue, which is largely avascular in adults[10].

### 1.2 Right Ventricle Failure (RVF) Investigation

In both the U.S. and worldwide, heart failure is the leading cause of death[11]. Among the various types of heart failure, RV failure is gaining more attention in the clinical and scientific communities. RV failure (RVF) is associated with serious cardiac and pulmonary diseases that contribute significantly to the morbidity and mortality of patients[12]. The prevalence of RVF is significantly increased with the advanced stage of diseases such as pulmonary hypertension, congenital heart disease, and left heart failure with preserved ejection fraction[13-15]. Despite the increasing clinical relevance, the management and treatment of RVF remains severely limited and thus the mortality rate of these patients has not improved despite the advancement in therapeutic interventions over the past few decades[14-18]. During the current COVID-19 pandemic, reports have shown a strong correlation between hospitalization/mortality and RV abnormality[19-21]. The persistent clinical challenge is mainly due to an incomplete understanding of the fundamental structure-function relationships of the organ[22, 23] and that current surgical and pharmacological treatments are only palliative remedies.

Despite the ample research output on the LV, the findings from the LV with regards to its performance, treatment, etc. cannot be applied to the RV. For example, therapies that have been developed for LV failure are not always effective against RV failure. The RV is a unique chamber—it differs from the LV in embryologic origin, anatomy and function, and pathology[24-27]. In physiological conditions, the left ventricle (LV) and RV experience dramatically different hemodynamic environments: while the LV experiences a high pressure, high resistance and low compliance circulatory system, the RV experiences a low pressure, low resistance and high compliance circulatory system[24, 28, 29]. The RV has been long considered as a 'compliant' chamber compared to the LV because of its larger chamber compliance, an extrinsic mechanical property calculated by ΔVolume/ΔPressure (ΔV/ΔP) over a cardiac cycle. However, the higher compliance is mostly due to the lower physiological pressure range (0-25 mmHg) compared to that of the LV (0-120 mmHg) (**Fig. 1.2, Table 1.1, Table A2**).

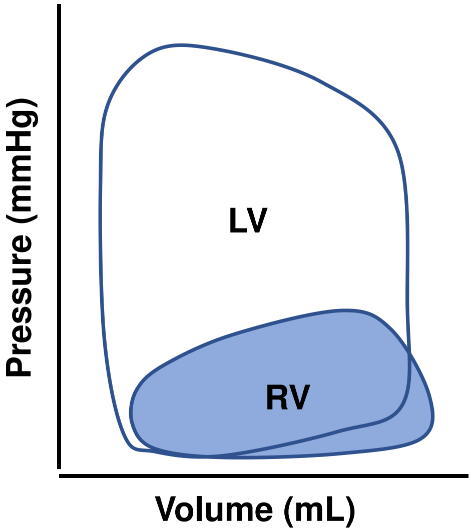

**Figure 1.2**. A sample graphic representation of ventricular compliance differences between the two chambers.

**Table 1.1.** Differences between the RV and LV chambers[28]. $\Delta V/\Delta P = \Delta\text{Volume}/\Delta\text{Pressure}$

| | **LV** | **RV** |
|---|---|---|
| **Pressure (mmHg)** | 0-140 | 0-40 |
| **Resistance** | High | Low |
| **Compliance ($\Delta V/\Delta P$)** | Low | High |
| **Wall thickness (mm)** | 7-11 | 2-5 |

Thus, these differences suggest that the unique understanding of the RV must be independently investigated and that the chamber itself is distinct from the more extensively studied LV. The incomplete understanding of the mechanisms of RVF and relevant treatments can be attributed to some key factors: 1) the knowledge gap of how exactly the RV free wall differs from the LV free wall in terms of the RV's intrinsic mechanical properties, which is crucial for RV-specific therapies; 2) the dearth of information on the intrinsic mechanical properties of the interventricular septum, an important component of the RV chamber that is neglected in *ex vivo* biomechanical studies; 3) the establishment of an *adult* RV failure in a large animal model and the accompanying RV biomechanical changes with disease progression are not documented but are critical to the study of this disease's pathogenesis[30-32]; 4) the response of mesenchymal stromal cells (MSC) to a mechanical environment that mimics healthy and diseased RV tissue mechanics is unknown, which potentially limits the optimal therapeutic outcomes of MSC delivery to treat a failing RV.

In order to fill in the aforementioned knowledge gaps in RV failure mechanisms, I assessed the *ex vivo* ventricular free wall and interventricular septum tissue biomechanics and established an *in vivo* large animal model of RV failure which was used to study the changes of RV biomechanics with disease progression. Lastly, I investigated MSC behavior on a novel, *in vitro* platform mimicking right ventricle mechanics that furthers our understanding of MSC mechanobiology and can potentially improve MSC regenerative treatment (**Fig. 1.3**).

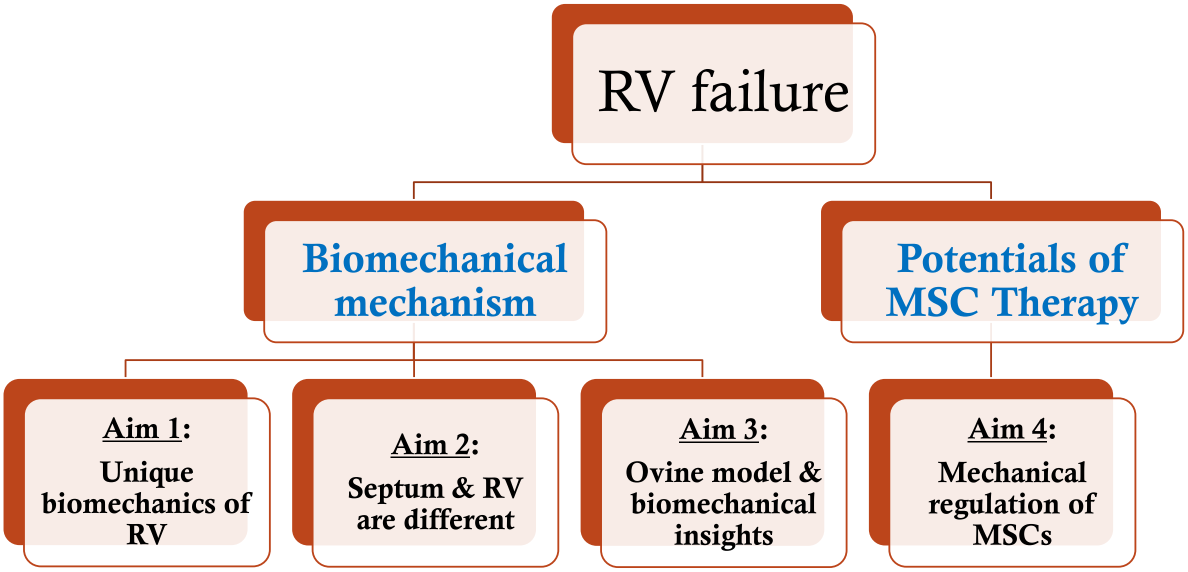

**Figure 1.3.** Overall diagram of workflow to understand RV failure in terms of biomechanical mechanisms and regenerative treatment.

# References

1. Villarreal FJe. *Interstitial fibrosis in heart failure*. Boston: Springer Science + Business Media, Inc.; 2005.
2. MacKenna D, Summerour SR, Villarreal FJ. Role of mechanical factors in modulating cardiac fibroblast function and extracellular matrix synthesis. *Cardiovasc Res*. 2000;46:257-263
3. Banerjee I, Fuseler JW, Price RL, Borg TK, Baudino TA. Determination of cell types and numbers during cardiac development in the neonatal and adult rat and mouse. *Am J Physiol Heart Circ Physiol*. 2007;293:H1883-1891
4. Taylor PM, Batten P, Brand NJ, Thomas PS, Yacoub MH. The cardiac valve interstitial cell. *Int J Biochem Cell Biol*. 2003;35:113-118
5. Tao G, Kotick JD, Lincoln J. Heart valve development, maintenance, and disease: The role of endothelial cells. *Current topics in developmental biology*. 2012;100:203-232
6. Leonard BL, Smaill BH, LeGrice IJ. Structural remodeling and mechanical function in heart failure. *Microscopy and microanalysis : the official journal of Microscopy Society of America, Microbeam Analysis Society, Microscopical Society of Canada*. 2012;18:50-67
7. Bashey RI, Donnelly M, Insinga F, Jimenez SA. Growth properties and biochemical characterization of collagens synthesized by adult rat heart fibroblasts in culture. *J Mol Cell Cardiol*. 1992;24:691-700
8. Hasan A, Ragaert K, Swieszkowski W, Selimovic S, Paul A, Camci-Unal G, et al. Biomechanical properties of native and tissue engineered heart valve constructs. *J Biomech*. 2014;47:1949-1963
9. Wiltz D, Arevalos CA, Balaoing LR, Blancas AA, Sapp MC, Zhang X, et al. Extracellular matrix organization, structure, and function. In: Aikawa E, ed. *Calcific aortic valve disease*. InTech; 2013.
10. Sacks MS, Merryman WD, Schmidt DE. On the biomechanics of heart valve function. *J Biomech*. 2009;42:1804-1824
11. Inamdar AA, Inamdar AC. Heart failure: Diagnosis, management and utilization. *Journal of Clinical Medicine*. 2016;5:62
12. Haddad F, Hunt SA, Rosenthal DN, Murphy DJ. Right ventricular function in cardiovascular disease, part i: Anatomy, physiology, aging, and functional assessment of the right ventricle. *Circulation*. 2008;117:1436-1448
13. Kohler D, Arnold R, Loukanov T, Gorenflo M. Right ventricular failure and pathobiology in patients with congenital heart disease - implications for long-term follow-up. *Front Pediatr*. 2013;1:37
14. Konstam MA, Kiernan MS, Bernstein D, Bozkurt B, Jacob M, Kapur NK, et al. Evaluation and management of right-sided heart failure a scientific statement from the american heart association. *Circulation*. 2018;137:E578-E622
15. Lahm T, Douglas IS, Archer SL, Bogaard HJ, Chesler NC, Haddad F, et al. Assessment of right ventricular function in the research setting: Knowledge gaps and pathways forward. An official american thoracic society research statement. *Am J Respir Crit Care Med*. 2018;198:e15-e43

16. Gorter TM, van Veldhuisen DJ, Bauersachs J, Borlaug BA, Celutkiene J, Coats AJS, et al. Right heart dysfunction and failure in heart failure with preserved ejection fraction: Mechanisms and management. Position statement on behalf of the heart failure association of the european society of cardiology. *Eur J Heart Fail*. 2018;20:16-37
17. Raina A, Meeran T. Right ventricular dysfunction and its contribution to morbidity and mortality in left ventricular heart failure. *Curr Heart Fail Rep*. 2018;15:94-105
18. Besinque GM, Lickert CA, Pruett JA. The myth of the stable pulmonary arterial hypertension patient. *Am J Manag Care*. 2019;25:S47-S52
19. Fayssoil A, Mustafic H, Mansencal N. The right ventricle in covid-19 patients. *Am J Cardiol*. 2020;130:166-167
20. Li Y, Li H, Zhu S, Xie Y, Wang B, He L, et al. Prognostic value of right ventricular longitudinal strain in patients with covid-19. *JACC Cardiovasc Imaging*. 2020;13:2287-2299
21. Argulian E, Sud K, Vogel B, Bohra C, Garg VP, Talebi S, et al. Right ventricular dilation in hospitalized patients with covid-19 infection. *JACC Cardiovasc Imaging*. 2020;13:2459-2461
22. Jang S, Vanderpool RR, Avazmohammadi R, Lapshin E, Bachman TN, Sacks M, et al. Biomechanical and hemodynamic measures of right ventricular diastolic function: Translating tissue biomechanics to clinical relevance. *Journal of the American Heart Association*. 2017;6
23. Liu W, Wang Z. Current understanding of the biomechanics of ventricular tissues in heart failure. *Bioengineering (Basel)*. 2019;7
24. Friedberg MK, Redington AN. Right versus left ventricular failure. *Circulation*. 2014;129:1033-1044
25. Zaffran S, Kelly RG, Meilhac SM, Buckingham ME, Brown NA. Right ventricular myocardium derives from the anterior heart field. *Circ Res*. 2004;95:261-268
26. Rouleau JL, Paradis P, Shenasa H, Juneau C. Faster time to peak tension and velocity of shortening in right versus left ventricular trabeculae and papillary muscles of dogs. *Circ Res*. 1986;59:556-561
27. Pham T, Zgierski-Johnston CM, Tran K, Taberner AJ, Loiselle DS, Han J-C. Energy expenditure for isometric contractions of right and left ventricular trabeculae over a wide range of frequencies at body temperature. *Scientific Reports*. 2019;9:8841
28. Nguyen-Truong M, Wang Z. Biomechanical properties and mechanobiology of cardiac ecm. In: al ESe, ed. *Cardiac extracellular matrix*. Springer Nature 2018.
29. Klingensmith M, Chen L, Glasgow S, Goers T, Melby S. Lippincott manual series. *The washington manual of surgery*. Philadelphia, PA: Lippincott Willians & Wilkins; 2008:509-528.
30. Borgdorff MAJ, Dickinson MG, Berger RMF, Bartelds B. Right ventricular failure due to chronic pressure load: What have we learned in animal models since the nih working group statement? *Heart Failure Reviews*. 2015;20:475-491
31. Voelkel NF, Bogaard HJ, Gomez-Arroyo J. The need to recognize the pulmonary circulation and the right ventricle as an integrated functional unit: Facts and hypotheses (2013 grover conference series). *Pulm Circ*. 2015;5:81-89
32. Vonk Noordegraaf A, Galie N. The role of the right ventricle in pulmonary arterial hypertension. *Eur Respir Rev*. 2011;20:243-253

# 2. Specific Aims

1. Assess the unique *ex vivo* biomechanics of the RV free wall in contrast to the LV free wall.

    *Hypothesis 1: The adult healthy LV and RV free walls have distinct passive anisotropic biomechanical properties.*

2. Assess the *ex vivo* biomechanics of the "significant other" of the RV chamber – the septum wall.

    *Hypothesis 2: There are transmural differences between the LV-side and RV-side of the adult septum, and these two sides are distinct from that of the LV and RV free walls, respectively.*

3. Establish a novel ovine model of RV failure and investigate RV biomechanical changes during RV failure progression.

    *Hypothesis 3: Animal-specific, graded pulmonary artery constriction (PAC) will lead to chronic RVF in adult ovine, and the RV will stiffen in the longitudinal direction.*

4. Investigate the pro-angiogenic paracrine effect in the context of mesenchymal stromal cell mechanobiology to ultimately improve RV therapy.

    *Hypothesis 4: The pro-angiogenic potential of individual MSCs is highest on the substrate with isotropic, diseased RV-like stiffness.*

# 3. Multiscale Contrasts between the Right and Left Ventricle Biomechanics in Healthy Adult Sheep and Translational Implications

## 3.1 Introduction

In both the U.S. and worldwide, structural heart diseases (SHDs) are the leading cause of death. The progression of SHDs is associated with unique ventricular biomechanical alterations that affect either single or double sides of the ventricles. Diastolic dysfunction is common in many SHDs and confers poor outcome in both the left and right ventricular diseases including heart failure with preserved ejection fraction and pulmonary hypertension. Despite the development of modern therapies, effective treatments for diastolic dysfunction in heart failure patients remain limited. As diastolic dysfunction is directly influenced by the passive biomechanical behavior of the myocardium, a detailed knowledge of this behavior could facilitate developing new therapeutic targets and personalized treatment approaches for diastolic dysfunction. Although several studies have characterized the passive biomechanics of the myocardium[1], these studies often focus on either the left or right ventricle and the key question of how different the passive behavior of the two ventricles remains unanswered. This question becomes very important as often therapies that work for left ventricle (LV) failure patients (e.g., valsartan and pirfenidone) do not achieve similar effectiveness in right ventricle (RV) failure patients[2-4], which indicates that different failing mechanisms, stemming from differences in baseline biomechanical behavior, exist between the ventricles and calls for the development of chamber-specific treatment.

Under physiological conditions, the LV and RV experience dramatically different hemodynamic environments: while the LV experiences a high pressure, high resistance and low compliance circulatory system, the RV experiences a low pressure, low resistance and high compliance circulatory system. The RV has been long considered as a 'compliant' chamber (i.e., the ratio of volume change to pressure change from end-diastole to end-systole). However, whether their intrinsic mechanical properties such as elastic modulus differ from each other remains a knowledge gap[5, 6]. Moreover, in hypertensive remodeling, the RV can face as high as ~5-fold increase of afterload under pulmonary hypertension, but the LV only faces a ~1.5-fold increase of afterload in systemic hypertension[5, 7, 8]. Different baseline mechanics and mechanical afterloads may be responsible for the poor adaptation of the RV to pressure overload compared to the LV[9, 10]. The RV also has been shown to have higher collagen content (key contributor to ventricular biomechanics) than the LV[11], which suggests that the extracellular matrix remodeling may be different for each chamber. Therefore, it is crucial to investigate the baseline biomechanical differences between the ventricles to further delineate the different mechanisms of and subsequent treatment for LV- versus RV-associated SHDs.

To date, there are only a few studies directly comparing the mechanical properties of the LV and RV. Among earlier studies, Humphrey et al. reported the equibiaxial mechanical behavior of the canine epicardium tissues[12]. The stress-stretch curves were similar between the LV and RV: the tissues were isotropic at low strains and became stiffer and anisotropic at high strains. But there was no further analysis of the elastic properties. Later, the canine RV biaxial properties were measured and compared with the literature LV data by Sacks et al.[13]. Their data, as well as the human myocardium data from Fatemifar et al.[14], both suggested a stiffer RV compared to the LV in the main fiber direction. Javani et al.[15] and Kakaletsis et al.[16] measured adult ovine hearts by equibiaxial and multi-modal uniaxial tensile/compression and simple shear mechanical tests, respectively. These studies reported a stiffer material property of the LV than the RV in the main fiber direction. This finding is contradictory to the former studies. Recently, human ventricles were examined by Sommer et al.[17] and the results suggested a stiffer RV than LV, although the sample size was small (n=3 for RV). Since both human studies included samples from patients with and without cardiovascular diseases, the baseline information of healthy ventricles still remains unclear. Finally, healthy neonatal porcine hearts were examined by Ahmad et al.[18] and the RV was shown to be stiffer than the LV in the main fiber direction in the developing myocardium. However, the ventricular wall is different in functionality and structure between the neonate and adult[19, 20]. Therefore, the mechanical difference between the RV and LV in healthy adults remains inconclusive.

The lack of baseline biomechanics data for LV and RV and particularly in large animal species has limited the expenditure of cardiac research in two main fields. Firstly, ventricular passive biomechanical properties can serve as a benchmark for image-based inverse modeling technologies to non-invasively estimate myocardial properties in the RV and LV[21-24]. The image-based inverse model technology offers a promising platform to measure tissue-level stiffness and decouple fiber-level contributors to this stiffness. The information derived from this approach can significantly improve the diagnosis and prognosis that are solely based on global functional metrices (e.g., end-diastolic pressure-volume relation). Second, the design of biomaterials for cardiac tissue engineering and regenerative medicine encompasses a wide range of substrate elasticity from 20 kPa to 92 MPa, which represents the elasticity either at a small deformation of ~20% or that is non-physiological as we recently reviewed[25]. There are two layers of problems here. The biomaterial stiffnesses are oftentimes outside of the physiological range of myocardium stiffness, and most studies used the benchmark of LV stiffness, which leads to the lack of RV-specific therapy development[25] in this rapidly expanding research field.

With the persistent need to establish computational tools for the estimation of large animal (including human) cardiac biomechanics and to guide cellular and tissue bioengineering research, the goal of this study is to compare the biomechanical properties of the LV and RV in healthy adults. We hypothesize that the adult healthy LV and RV free walls have distinct passive anisotropic biomechanical properties. Sheep were chosen for their closer similarities to adult human anatomy, function, and physiology[26] than small animals, and thus the findings are more translatable to human cardiac biomechanics. We measured the passive biaxial properties of ovine LV and RV and quantified collagen distribution in the tissues. Moreover, there is increasing agreement that a constitutive model that incorporates the microstructural information has greater potential to characterize the heterogenous mechanical behavior of myocardium[27, 28]. Equibiaxial data were then fitted to a four-parameter Fung type model[15, 29] and a structurally informed model[27] with additional measurements from serial histology sections on the myo-/collagen fibers, separately. Our results indicated significant discrepancies between anisotropic behaviors of the LV and RV (relative to OT coordinates) that were concisely described by the anisotropic parameter $K$ derived from the Fung type model. The structurally informed model indicated stiffer collagen fibers in the LV than the RV, which awaits further investigation. Furthermore, the elasticity at low strains was correlated with type III collagen content in both ventricles. These findings advance the fundamental understanding of the differences between LV and RV biomechanics, which can be used to guide cardiac tissue engineering and regenerative studies with chamber-specific mechanical environments and to develop image-based inverse modeling technologies to non-invasively estimate myocardial properties in the ventricles.

## 3.2 Methods

### *3.2.1 Tissue sample preparation*

Fresh hearts (n=11) were obtained from 4+ year-old female sheep with no known cardiovascular disease or defects after the animals were euthanized for unrelated studies. Within four hours of sacrifice, the tissues were immersed in physiological saline solution (PBS) at room temperature until mechanical testing[30]. The outflow tract (OT) direction was used as the longitudinal direction as in previous studies[31-34]. A cruciform section (total dimensions: 30x30 mm; center square dimensions: 20x20 mm) was cut from each ventricle in a similar anatomic region (anterior free wall, with similar distance to the apex and base) and free of fibrotic deposition (**Fig. 3.1**). For both ventricles, we used the middle layer for mechanical tests after cleaning of the endocardial and epicardial surfaces, including the removal of papillary muscles and trabeculae. The tissue thickness was ~3 to 4 mm in all testing samples to achieve negligible shear deformation requirement for the biaxial test[35].

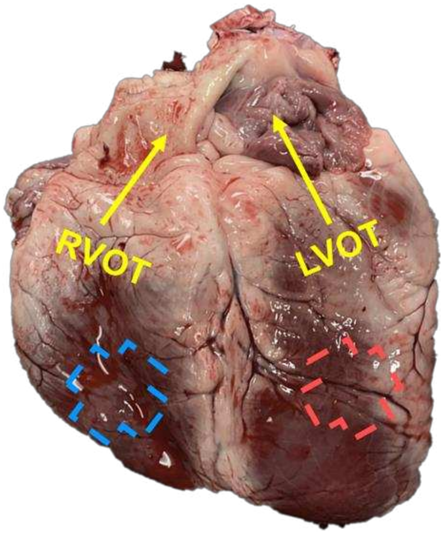

**Figure 3.1.** A representative image of the ovine heart with the labeling of the outflow (OT, longitudinal) direction for each ventricle.

*3.2.2 Biaxial testing*

The sample was then mounted onto an in-house biaxial tester and then *ex vivo* mechanical tests were performed at room temperature, with a regular spray of PBS solution to keep the tissue moist. Prior to testing, graphite powder (AGS, MI) was dusted onto the sample for strain characterization. Before testing, approximately 0.1 N of force was applied to pre-load the tissue in both directions. Next, biaxial testing was performed at two different displacement ratios (longitudinal:circumferential) in random order (2:1 and 1:2) and then at an equibiaxial test (2:2). The first ratio test was completed with 15 cycles including preconditioning cycles. The following ratios' tests were completed with 8 cycles per ratio. Finally, the first ratio test was repeated to confirm that no tissue damage occurred. Data acquisition was performed with an in-house LabVIEW program[35].

Each sample underwent a maximum of 25% strain following the reported physiological strains[36] and the maximum strain rate was 1% $s^{-1}$. Sample images were taken with a CCD camera (Nikon) at 1 fps and tissue deformations were obtained by digital image correlation[35]. The digital image correlation was applied to the region of interest (ROI), which was the central, square-shaped region far enough from the boundaries, and we have verified that the deformation in the ROI was nearly homogeneous. The Cauchy ($\boldsymbol{\sigma}$) and the second Piola-Kirchhoff (P-K) (**S**) stresses, and Green strain (**E**) were calculated for each direction ($\sigma = \lambda_i P$, $S = P/\lambda_i$, and $P = F/A_0$, $E = \frac{1}{2}(\lambda_i^2 - 1)$, where F is the measured force, P is the engineering stress, $A_0$ is the initial cross-section area, and $\lambda_i$ is the stretch in the $i = \mathrm{L}, \mathrm{C}$ direction with L and C subscripts denoting the longitudinal and circumferential directions, respectively), where the width and thickness were the original dimensions at no load. The elastic moduli (*M*) were derived as the slopes of the stress-strain curves at the low and high strain ranges (i.e., the first and last 20% of the loading stress-strain curve) [32], and the ratio $M/\varepsilon$ in the low or high strain range was used to assess the modulus ($M$) normalized by the maximal Green strain ($\varepsilon$) in the corresponding strain range and the respective direction [34].

### *3.2.3 Constitutive modeling*

Next, we fitted our equibiaxial data to a phenomenological constitutive model (Fung type model) and a structurally informed model. We used the phenomenological Fung type model to assess the overall *tissue-level* stiffness and anisotropic behavior in the LV and RV in a comparative manner; and the structurally informed model was used to provide insights into the differences between *fiber-level* mechanical and architectural properties of the LV and RV myocardium. An affine deformation was assumed within the samples under equibiaxial loading as commonly adopted in biaxial soft tissue testing.

#### *3.2.3.1 Fung type model*

We calculated the shear deformations $k_{LC}$ and $k_{CL}$ from our experimental data. (**Table 3.1**). The shear deformation was minimal compared to the in-plane stretches along longitudinal (OT) and circumferential (cross-OT) directions. Accordingly, shear stresses were assumed to be negligible in our modeling work.

**Table 3.1.** Maximum stretches in the in-plane and shear directions during equibiaxial tests. Data are presented as mean ± SEM.

| **Ventricle** | $\lambda_L$ | $\lambda_C$ | $k_{LC}$ **(shear)** | $k_{CL}$ **(shear)** |
|---|---|---|---|---|
| **LV (n=7)** | 1.14±0.02 | 1.19 ±0.02 | 1.04 ±0.01 *,† | 1.02±0.02 *,† |
| **RV (n=7)** | 1.20±0.02 | 1.14±0.01 | 1.02±0.01 *,† | 1.03±0.01 *,† |

$\lambda_L$: stretch in the longitudinal direction, $\lambda_C$: stretch in the circumferential direction, $k_{LC}$ and $k_{CL}$: stretches in the shear directions. *: $p<0.001$ vs. $\lambda_L$, †: $p<0.001$ vs. $\lambda_C$.

Furthermore, the relevant Green strain tensor (**E**) components were calculated as:

$$E_L = \frac{1}{2}(\lambda_L^2 - 1), E_C = \frac{1}{2}(\lambda_C^2 - 1) \tag{1}$$

where $\lambda_L$ and $\lambda_C$ are the stretch in longitudinal and circumferential directions, respectively.

Next, a four-parameter Fung type constitutive model[15, 29] with the following energy function ($\Psi$) was fit to the biaxial stress-strain data:

$$\Psi = \frac{B}{2}(e^Q - 1), Q = b_L {E_L}^2 + 2b_{LC}E_LE_C + b_C {E_C}^2 \tag{2}$$

The 2nd P-K and Cauchy stresses for an incompressible tissue were calculated as:

$$\mathbf{S} = 2\,\frac{\partial\Psi}{\partial\mathbf{C}} - p\mathbf{C}^{-1},\ \boldsymbol{\sigma} = \mathbf{F}\mathbf{S}\mathbf{F}^T \tag{3}$$

where **F** is the deformation gradient tensor, **C** is the right Cauchy-Green tensor, *p* is an unknown hydrostatic pressure to enforce det(**C**) =1, and $b_L$, $b_{LC}$, $b_C$ and *B* are the material constants. The stress-strain relationships in the L and C directions were derived as:

$$\sigma_L = (2E_L + 1)(b_LE_L + b_{LC}E_C)Be^{(b_L {E^2}_L + 2b_{LC}E_LE_C + b_C {E^2}_C)}$$

$$\sigma_C = (2E_C + 1)(b_{LC}E_L + b_CE_C)Be^{(b_L {E^2}_L + 2b_{LC}E_LE_C + b_C {E^2}_C)} \tag{4}$$

The Fung strain energy function was fitted to the equibiaxial experimental data for each specimen. The fitting was performed with a Levenberg-Marquardt least squares algorithm with the tolerance of $10^{-8}$ in MATLAB. The sensitivity to initial guesses was checked for every fit and a minimal dependency to initial guess was found for all the fits. The root mean square (RMS) was calculated to assess the fitting results. Finally, the anisotropic parameter *K* and elasticity at zero load in two directions ($M_{0,L}$ and $M_{0,C}$) were calculated as described in previous studies[15, 29, 37].

### *3.2.3.2 Structurally informed model*

Next, we used a structurally informed model that incorporates the transmural changes of myo-/collagen fibers to reveal the contributions of each fiber type to the tissue-level myocardial biomechanical behavior[27, 38]. Briefly, the total energy function (Ψ) was written as the sum of the mechanical contributions of the ground matrix and myo- and collagen fibers as,

$$\Psi(\mathbf{C}) = \phi^g \Psi^g(\mathbf{C}) + \phi^m \Psi^m(\mathbf{C}) + \phi^c \Psi^c(\mathbf{C}) \tag{5}$$

where $\Phi^g, \Phi^m$ and $\Phi^c$ are volume fractions for the ground matrix (including non-structural extracellular matrix proteins, fibroblasts, interstitial fluid, etc.), myo- and collagen fibers, respectively, and $\Psi^g, \Psi^m,$ and $\Psi^c$ are strain energy functions associated with each phase. The volume fraction measurement is described in the next section (see §2.4.2).

At the tissue level, the 2nd P-K stress tensor (**S**) was described in terms of the energy function $\Psi(\mathbf{C})$:

$$\mathbf{S} = 2\frac{\partial \Psi}{\partial \mathbf{C}} - p\mathbf{C}^{-1} = \mathbf{S}^g + \mathbf{S}^m + \mathbf{S}^c \tag{6}$$

The stress-strain relationships for ground matrix, myo- and collagen fibers were derived as:

$$\mathbf{S}^g = \phi^g k^g \mathbf{I} - p\mathbf{C}^{-1} \tag{7}$$

$$\mathbf{S}^m = \frac{\phi^m k_1^m}{H} \int_0^H \int_{-\pi/2}^{\pi/2} \Gamma^m(\theta^m, z) \frac{(\sqrt{I^m}-1)}{\sqrt{I^m}} \times \exp\,[k_2^m\left(\sqrt{I^m} - 1\right)^2](\mathbf{n}^m \otimes \mathbf{n}^m)\, d\theta^m dz$$

(8)

$$\mathbf{S}^C =$$

$$\begin{cases} \dfrac{\phi^c k_1^c}{H} \int_0^H \int_{-\pi/2}^{\pi/2} \Gamma^c(\theta^c, z) \times (e^{k_2^c E^c} - 1)(\mathbf{n}^c \otimes \mathbf{n}^c)\, d\theta^m dz\,, \ for\ E^c \leq E_{ub} \\ \dfrac{\phi^c {k^c}_1}{H} \int_0^H \int_{-\pi/2}^{\pi/2} \Gamma^c(\theta^c, z)\left[\left(e^{k_2^c E^c} - 1\right) + k_2^c\, e^{k_2^c E^c}\, (E^c - E_{ub})\right](\mathbf{n}^c \otimes \mathbf{n}^c)\, d\theta^m dz\,, \ for\ E^c > E_{ub} \end{cases}$$

(9)

where **I** is the identity tensor, $I^m = 2(\mathbf{n}^m \cdot \mathbf{E}\mathbf{n}^m) + 1$ , $E^c = \mathbf{n}^c \cdot \mathbf{E}\mathbf{n}^c$ are the pertinent kinematic measures, $k$'s are model parameters, and **n**'s are the defined unit vectors that describe the planar orientations of the myo-and collagen fibers, respectively. We adapted the previous model and derived the fiber orientation parameters $\theta^m$ *and* $\theta^c$ (ranged from 0 to $\pi/2$) from serial histology measurements (see §3.2.4.2). The parameters describing the transmural orientation distribution ($\Gamma$) were derived for myo- and collagen fibers using a modified Beta distribution function[27]. In the transmural direction, the normalized tissue thickness was denoted as H and a value of 100 represents the entire tissue thickness. $E_{ub}$ is the upper bound of the transition region derived from the average stress-strain curve calculated from each direction.

The myofiber model parameter $k_1^m$ was estimated from the fit to experimental data in the low strain region as described previously[31], and the parameter for amorphous ground matrix $k^g$ was fixed at a value of 10 kPa due to its much lower contribution to the mechanical behavior of myocardium compared to that of myo-/collagen fibers[39]. The same fitting method was used as described in the above Fung type model section.

### *3.2.4 Microstructural measurements*

After biaxial testing, the samples were fixed in 10% buffered formalin and embedded in paraffin for collagen content measurement. In some samples (n=3 for LV and n=4 for RV), the tissue blocks were further sectioned into 4-8 serial sections (~125 μm apart) from the epicardial to endocardial side and stained for fiber orientation measurement.

#### *3.2.4.1 Collagen content measurement*

The tissue slices were stained with Picrosirius Red (PSR) and imaged and analyzed via a transmission microscope (Nikon Eclipse E800) and Image Pro Premier software (Media Cybernetics, Rockville, MD) for collagen content quantification. For each sample, three regions were randomly selected under polarized light microscopy. An image thresholding method in which yellow, green, brown and dark blue colors were chosen to represent type I collagen, type III collagen, ground matrix and muscle, respectively. The amounts of type I and III collagen were quantified as the area percentage to total tissue area, and the amount of collagen content was quantified as the total area percentage of type I and III collagen[40, 41].

We further performed immunohistochemistry (IHC) to LV (n=4) and RV (n=4) specimens to confirm the area fraction measurement of type III collagen in PSR staining slides. Tissue samples were stained with rabbit polyclonal anti-human collagen III antibody (1:500 dilution, ab7778, Abcam, Cambridge, United Kingdom). Image thresholding via ImageJ (U.S. NIH, Bethesda, Maryland) was used to determine the area fraction of collagen III.

#### *3.2.4.2 Myo- and collagen fibers orientation measurement*

From the serial histology sections with PSR staining, the transmural change of fiber orientation was measured using in-house MATLAB codes adapted from a previous study[27]. Briefly, each serial tissue slice was imaged under bright field light microscopy and separated by the color of tissue component using ColorDeconvolution2, a plug-in in ImageJ. Fiber angle was calculated for collagen and myofiber, respectively. The transmural fiber orientation distribution was then represented by a Beta distribution function to fit a surface to the 3D data. The mean transmural fiber orientations for both myo- and collagen fibers were calculated from the Hermitian fit parameters[27]. These data were used to derive the transmural orientation distribution ($\Gamma$) for the structurally informed modeling.

### *3.2.5 Statistical analysis*

Comparisons between directions (longitudinal versus circumferential) were performed with the Wilcoxon signed-rank test for the paired equibiaxial data. For all other statistical comparisons, the Mann-Whitney U test was used for the unpaired data. Pearson correlation analysis was performed to investigate the correlations between the modeling parameters or collagen content and mechanical properties. All analyses were performed in GraphPad Prism (v8.0.2). Data are presented as mean ± SEM and $p<0.05$ was considered statistically significant.

## 3.3 Results

### *3.3.1 Differences in elastic behaviors along each direction*

The average stress-strain curves from equibiaxial tests are shown in **Fig. 3.2**. The curves for the LV were leftward of the curves for the RV in the longitudinal direction (**Fig. 3.2A**), indicating a stiffer mechanical property of the LV in this direction. The opposite behavior was observed in the circumferential direction (**Fig. 3.2B**), indicating a stiffer mechanical property of the RV in this direction. Similar behavior was observed from the stress-strain data from non-equibiaxial tests (data not shown).

We further investigated the elastic moduli at low and high strain ranges, which typically represent the mechanical behavior of myofibers and collagen fibers, respectively[32]. At the low strains, the ventricles presented similar properties except that the LV showed a higher circumferential $M$ than the RV for the non-equibiaxial tests (**Fig. 3.3B**, $p=0.052$). At the high strains, the LV had a higher $M$ or $M/\varepsilon$ than the RV in the longitudinal direction, whereas the RV had a higher $M$ or $M/\varepsilon$ than the LV in the circumferential direction (**Fig. 3.3**).

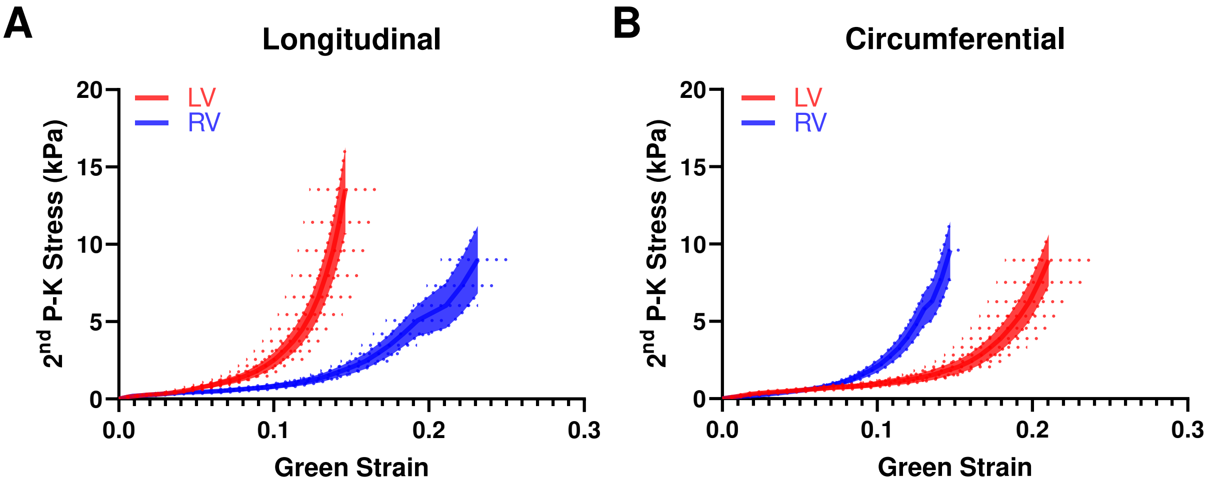

**Figure 3.2.** Average equibiaxial stress-strain curves in the longitudinal (A) and circumferential (B)

directions in the LV and RV (n=7 per group). The shaded area is the variance of the stress data, and the dash line is the variance for the strain data.

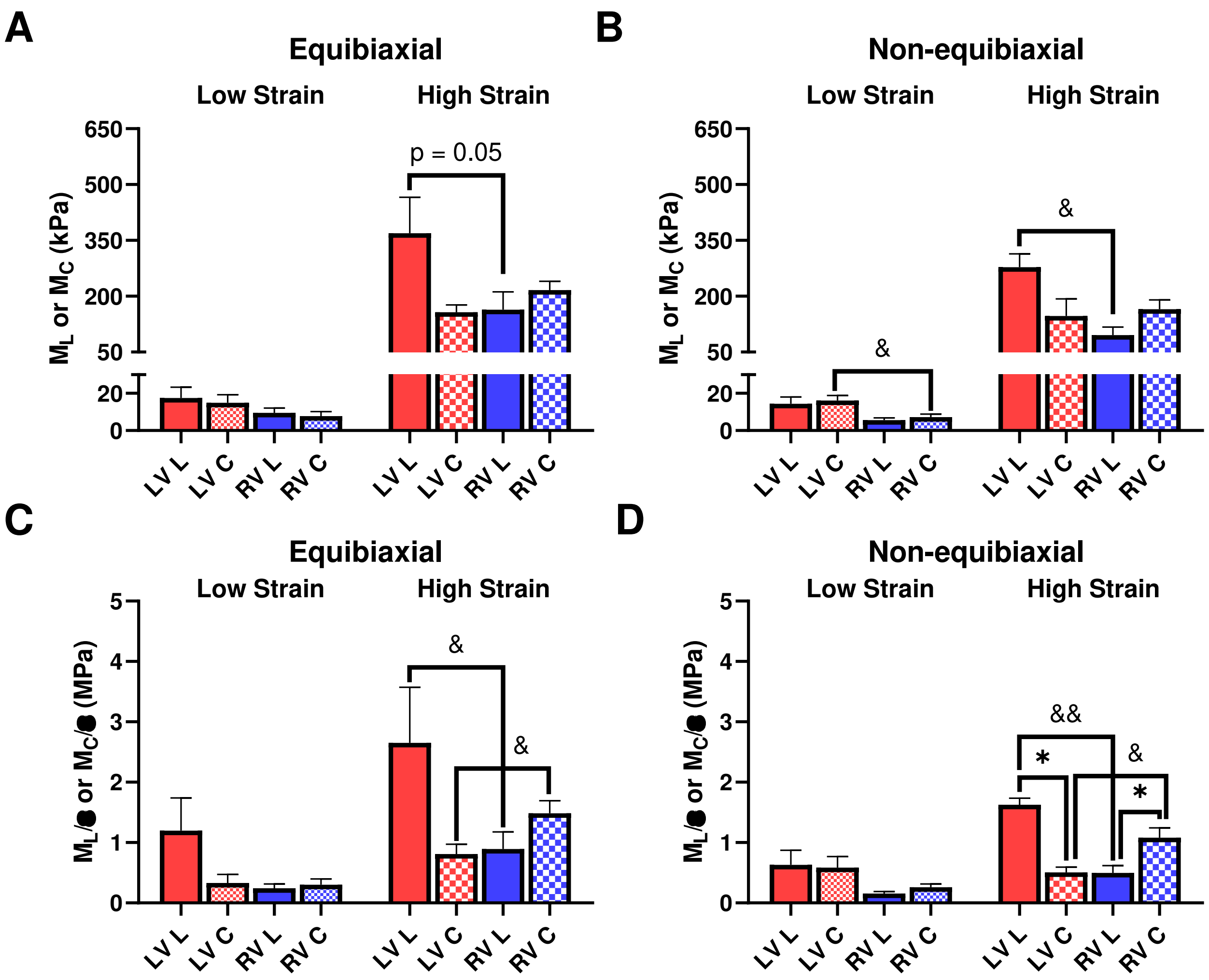

**Figure 3.3.** (A-B) Elastic moduli ($M$) of LVs and RVs from the equibiaxial (A) and non-equibiaxial tests (B). (C-D) Strain-weighted elastic moduli ($M/\varepsilon$) of LVs and RVs from the equibiaxial (C) and non-equibiaxial tests (D). For the equibiaxial tests, n=7 per group; for the non-equibiaxial tests, LV, L: n=4; LV, C: n=5; RV, L: n=7; RV, C: n=6. *: $p < 0.05$ comparison between the directions and &: $p < 0.05$ and &&: $p < 0.01$ for comparison between the ventricles.

### *3.3.2 Differences in anisotropic behaviors*

We compared the $M$ and $M/\varepsilon$ between the two axes to examine the anisotropic behavior of the tissue. For the LV, the $M$ and $M/\varepsilon$ in the circumferential direction were significantly smaller than those in the longitudinal direction (**Fig. 3.3D**), indicating that the LV was stiffer in the longitudinal direction. In contrast for the RV, the $M$ and $M/\varepsilon$ in the circumferential direction were higher compared to the longitudinal direction (**Fig. 3.3D**), suggesting that the RV was stiffer in the circumferential direction. Therefore, the LV and RV had different anisotropic behaviors.

### *3.3.3 Experimental data fitting with Fung type model*

We performed fitting of the equibiaxial stress-strain curves using the four-parameter Fung type model. A good fit to the experimental data was observed for both ventricles and at both directions (low RMS values), and the fitting results are summarized in **Table 3.2**. The simulated equibiaxial stress-strain curves using the mean values of the estimated constants showed similar behaviors as our experimental data: the LV and RV had different anisotropic behaviors (**Fig. 3.4**) and the LV was stiffer than the RV in the longitudinal direction (**Fig. 3.4**).

**Table 3.2.** Fung model fitting results. Average data are presented as mean ± SEM.

| Ventricle | $b_L$ | $b_C$ | $b_{LC}$ | $B$ (kPa) | RMS (kPa) |
|---|---|---|---|---|---|
| **LV #1** | 145.67 | 25.16 | $4.40 \times 10^{-11}$ | 0.15 | 0.63 |
| **LV #2** | 41.63 | 17.91 | 0.01 | 0.09 | 0.09 |
| **LV #3** | 103.43 | 13.94 | 0.01 | 0.18 | 0.58 |
| **LV #4** | 96.74 | 53.68 | 0.01 | 0.17 | 0.14 |
| **LV #5** | 42.00 | 83.08 | $1.33 \times 10^{-10}$ | 0.10 | 0.28 |
| **LV #6** | 38.36 | 37.54 | 0.01 | 0.03 | 0.60 |
| **LV #7** | 33.51 | 27.33 | 0.01 | 0.88 | 0.25 |
| **LV (n=7)** | 71.62±16.52 | 36.95±9.17 | 0.007±0.002 | 0.23±0.11 | 0.37±0.09 |
| **RV #1** | 17.44 | 35.07 | $8.48 \times 10^{-14}$ | 0.23 | 0.25 |
| **RV #2** | 45.49 | 20.05 | 0.01 | 0.38 | 0.24 |
| **RV #3** | 20.96 | 46.14 | 0.01 | 0.25 | 0.22 |
| **RV #4** | 57.19 | 79.55 | $1.55 \times 10^{-10}$ | 0.13 | 0.19 |
| **RV #5** | 51.30 | 99.99 | 0.01 | 0.07 | 0.42 |
| **RV #6** | 28.42 | 43.74 | $8.29 \times 10^{-11}$ | 0.15 | 0.10 |

| | | | | | |
|---|---|---|---|---|---|
| **RV #7** | 20.95 | 48.57 | 0.01 | 0.07 | 0.17 |
| **RV (n=7)** | 34.54±6.20 | 53.30±10.32 | 0.006±0.002 | 0.18±0.04 | 0.23±0.04 |

$b_L$, $b_C$, $b_{LC}$ and $B$ are the material constants, and RMS is root mean square.

We further compared the zero-load modulus $M_0$ in each ventricle and in each direction, using the model fitting parameters. The $M_{0,C}$ was significantly larger than the $M_{0,L}$ in the RV ($p<0.05$), and there was a strong trend of larger $M_{0,L}$ compared to the $M_{0,C}$ in the LV, indicating different anisotropic behaviors between the ventricles (**Fig. 3.5A**). Expectedly, the anisotropic parameter $K$ was significantly different between the LV and RV (**Fig. 3.5B**, $p<0.01$). Finally, we performed correlation analyses and found that $K$ was significantly correlated with the ratios of longitudinal to circumferential elastic moduli ($M$ and $M/\varepsilon$) in both strain ranges ($p < 0.05$, $r = 0.75\text{-}0.85$, data not shown).

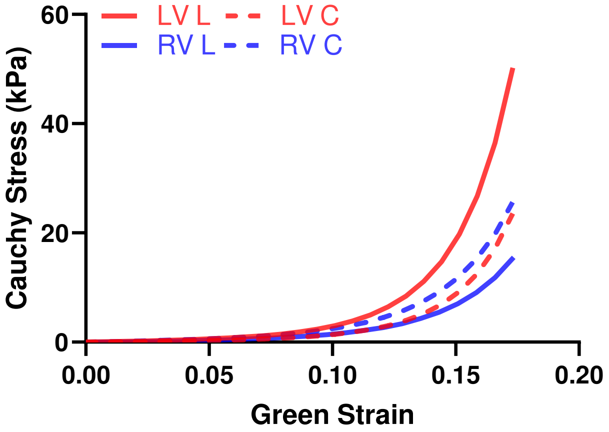

**Figure 3.4.** Simulated equibiaxial stress-strain curves generated by the four-parameter Fung model, using the average values of the fitting parameters for both ventricles in two directions.

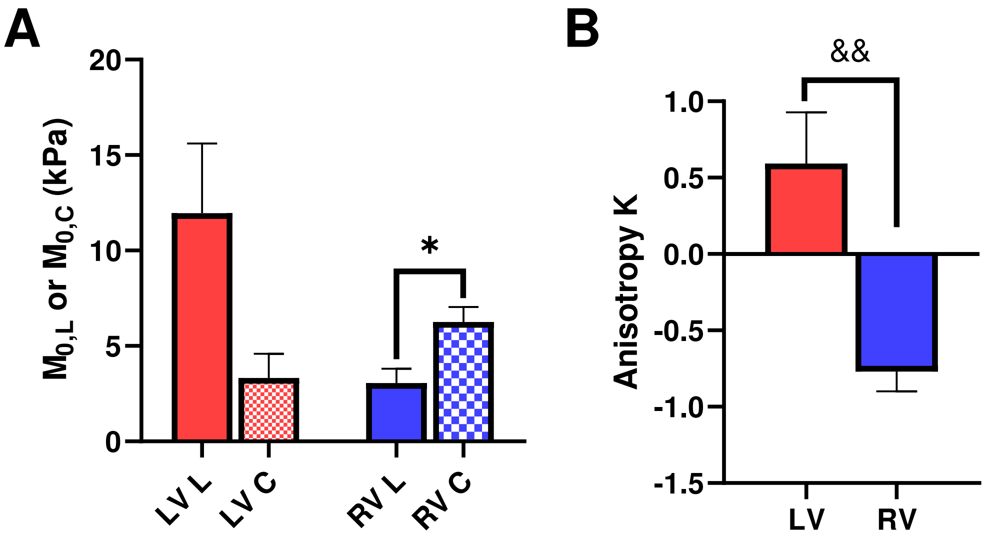

**Figure 3.5.** (A) Longitudinal and circumferential zero-load elastic modulus $M_0$ for each ventricle type, and (B) Anisotropic parameter $K$ for each ventricle type. *: $p < 0.05$ comparison between the directions and &&: $p < 0.01$ comparison between the ventricles, respectively.

### *3.3.4 Experimental fitting with structurally informed model*

We fit the equibiaxial stress-strain curves with the structurally informed model to investigate the different contributions of myocardial components (myo- and collagen fibers) to tissue mechanics in these chambers. The fitting results are summarized in **Table 3.3**, and a representative fitting result is shown in **Fig. 3.6**. The model fit our experimental data well, which is evident by the small values of RMS. Compared to the RV, the LV tended to have larger stiffness for myo- and collagen fibers (see $k_1^m$ and $k_1^c$). Furthermore, the LV tended to have a larger transition strain ($E_{ub}$) than that of the RV.

**Table 3.3.** Structurally informed model fitting results. Average data are presented as mean ± SEM.

| | **Myofiber** | | **Collagen** | | | **RMS** |
|---|---|---|---|---|---|---|
| | $k_1^m$(kPa) | $k_2^m$ | $k_1^c$(MPa) | $k_2^c$ | $E_{ub}$ | **(kPa)** |
| **LV #1** | 5.04 | 384.38 | 21.61 | 56.70 | 0.14 | 0.25 |
| **LV #2** | 15.77 | 301.81 | 69.41 | 38.15 | 0.2 | 0.65 |

|  |  |  |  |  |  |  |
|---|---|---|---|---|---|---|
| **LV #3** | 54.65 | 304.28 | 12.52 | 26.35 | 0.10 | 0.27 |
| **LV (n=3)** | 25.15±15.07 | 330.16±27.12 | 34.51±17.64 | 40.40±8.83 | 0.15±0.03 | 0.39±0.13 |
| **RV #1** | 25.10 | 10.07 | 9.73 | 34.54 | 0.14 | 0.87 |
| **RV #2** | 9.87 | $1.54 \times 10^{-9}$ | 10.08 | 68.37 | 0.09 | 0.37 |
| **RV #3** | 26.55 | 573.59 | 12.68 | 59.94 | 0.13 | 1.28 |
| **RV #4** | 18.05 | 263.93 | 28.63 | 25.34 | 0.14 | 0.68 |
| **RV (n=4)** | 19.89±3.82 | 211.89±135.14 | 15.28±4.50 | 47.05±10.20 | 0.12±0.01 | 0.80±0.19 |

*k*'s are model parameters, $E_{ub}$ is the upper bond of the transition region.

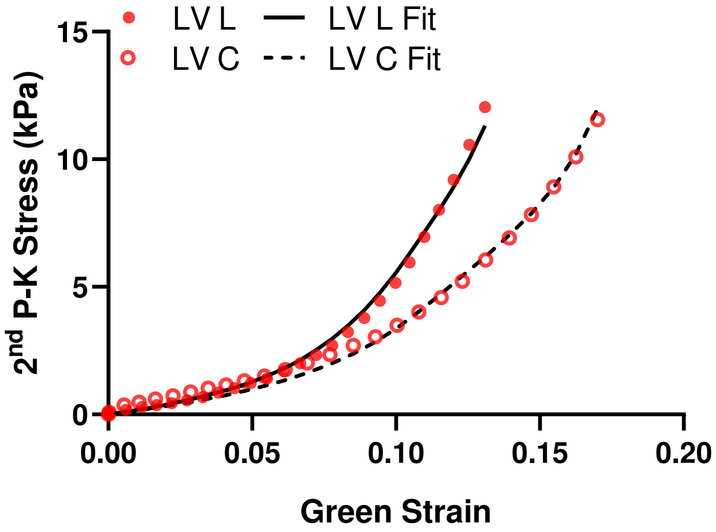

**Figure 3.6.** Representative fitting results using the structurally informed model.

### *3.3.5 Collagen content correlated with low-strain or high-strain elasticity in all ventricles*

Next, we examined the difference in collagen content between the LV and RV. There were trends of higher total collagen and type I collagen contents in the RV compared to the LV (**Fig. 3.7A**, $p<0.1$). Our immunohistochemistry measurement of collagen III isoform agreed with the polarized light PSR measurement in collagen III (data not shown). Furthermore, we observed a significant correlation between type III collagen percentage and the longitudinal $M$ ($M_L$) at the low-strain range in all samples (**Fig. 3.7B**, $p<0.05$). In addition, we observed a significant correlation between the total collagen and circumferential $M/\varepsilon$ at the high-strain range (**Fig. 3.7C**, $p<0.05$).

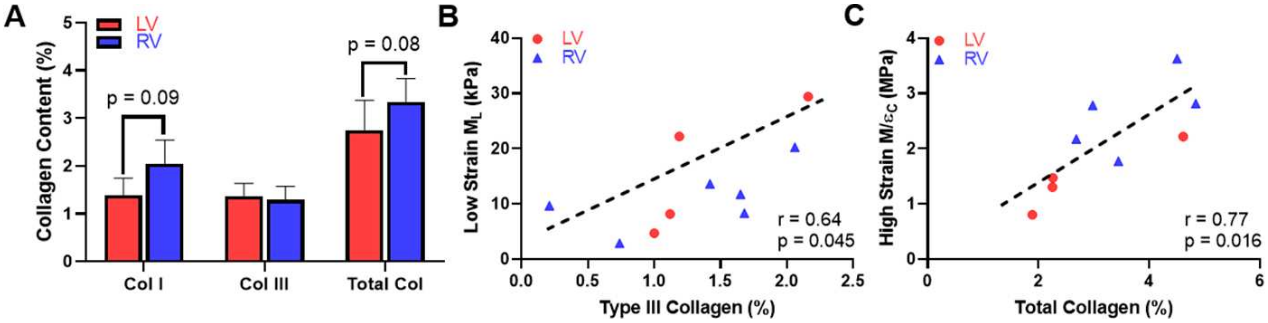

**Figure 3.7.** Histological measurement and correlation analysis for the collagen. (A) Variations in the content of collagen isoforms and the total collagen between the LV and RV, and (B) Significant correlation between the type III collagen content and longitudinal $M$ ($M_L$) at the low-strain range. (C) Significant correlation between the total collagen content and circumferential $M/\varepsilon$ at the high-strain range.

### *3.4 Discussion*

In this study, we aimed to compare the passive biaxial mechanical properties of the LV and RV in healthy adult ovine. We found that (1) the LV and RV had different anisotropic behaviors, with the LV being stiffer in the longitudinal (OT) than circumferential (cross-OT) direction and the RV showing the opposite result; (2) the RV was more compliant than the LV in the longitudinal direction, and was stiffer than the LV in the circumferential direction; (3) the anisotropic parameter *K* derived from the Fung type model provided consistent finding in the opposite anisotropy of LV and RV as observed experimentally; (4) using the structurally informed model, the LV was predicted to have stiffer collagen fibers than the RV; (5) the type III collagen played an important role in the longitudinal elasticity in all ventricles, especially at the low strain range. These findings provide fundamental information on the biomechanics of the LV and RV, which is valuable for the design of tissue and regenerative engineering studies and the development of image-based inverse modeling technologies to non-invasively estimate myocardial properties.

### *3.4.1 Different anisotropic behaviors between the LV and RV*

Both the LV and RV are reported to present anisotropic behaviors in prior studies, but the anisotropic behavior is inconsistent even within the same animal species. For instance, studies have found the healthy rat RV is stiffer in the longitudinal compared to circumferential direction[31, 33]. These findings are supported by longitudinal stress-strain curves being shifted leftward relative to the circumferential stress-strain curves in rodent RV[42]. However, another study reporting the low and high strain *M's* suggests that the rat RV was stiffer in the circumferential compared to longitudinal direction, and the difference reversed and became larger in pulmonary hypertensive animals[32]. These studies used the same (anatomical) coordinate system as in the present study, yet the anisotropic behavior of the RV still remains inconclusive. Moreover, it is unclear if the small and large animal species share similar anisotropic behaviors in the myocardium, and thus it is imperative to investigate the biaxial properties in large animal species independently.

In this study, we found that the ovine LV and RV had different anisotropic behaviors: the LV had larger M in the longitudinal direction compared to the circumferential direction, whereas the RV had the opposite trend of difference between these directions. The anisotropy parameter $K$ derived from constitutive modeling was significantly correlated with the experimental data, confirming the different anisotropic behaviors. We speculate that the reason for this difference is the different need to facilitate blood filling and ejection in each ventricle. The LV is more conically shaped and is comprised of helical fibers that allows it to deform more circumferentially during cardiac cycles (majority of LV contractility occurs due to circumferential shortening); in contrast, the RV is crescent shaped and is comprised of wrap-around transverse fibers that deforms more longitudinally (majority of RV contractility occurs due to longitudinal shortening)[43, 44]. Thus, our findings show a more compliant passive mechanical property of the wall in the main axis of cyclic deformation for both ventricles, which suggests that passive elasticity is maintained at a low level to reduce the elastic ‘resistance’ and facilitate blood filling (as well as ‘pumping’ potentially). The understanding of the differences in baseline anisotropy between the two ventricles will help to develop chamber-specific therapies aimed at reducing wall stress along the main axis of deformation.

### *3.4.2 Different elasticity at each axis between the LV and RV*

To date, discrepant findings are reported on the comparison of elasticity of the LV and RV. Please note that the intrinsic mechanical property measurements should be distinguished from the general ‘consensus’ that the RV is a more compliant chamber (an extrinsic mechanical measurement). In human myocardium, the RV tissue tended to achieve higher wall stresses in both biaxial axes compared to the LV tissue, but whether the difference reached statistical significance is unknown[17]. In contrast, various mechanical tests (biaxial test, triaxial shear test, uniaxial tensile/compression tests) on healthy ovine hearts showed that the LV was ‘overall’ stiffer compared to the RV[15, 16]. Another recent study characterized neonatal porcine ventricles and found no difference between LV and RV stress-strain curves nor peak engineering stress[18]. Hence, although all these studies used a different definition of biaxial axes (the main fiber and cross-fiber coordinate system), it remains unclear if the LV and RV have distinct intrinsic elastic property and how different they are.

The present study is the first investigation on the biaxial behavior of the ventricles in large animal species using an anatomical coordinate system (more adopted in the RV research area). Our results showed that the RV was stiffer than the LV in the circumferential direction, and the opposite trend of difference (i.e., LV was stiffer than the RV) was shown in the longitudinal direction (**Figs. 3.2&3.3**). Because of the different trends of comparison at different directions, it is not appropriate to simply conclude that the ‘LV is stiffer than the RV’ or vice versa at the tissue level. Moreover, the heterogenous organization of myofiber layers and the nonlinear, anisotropic nature determine that one cannot refer to a single value of mechanical parameter (e.g., elastic modulus) to describe the myocardium. Unfortunately, such knowledge has not been well recognized by emerging fields like cell and tissue engineering for cardiac research. There are also mixed citations of ‘tensile’ and ‘compressive’ elastic modulus to represent the stiffness of myocardium. As a result, a variety of elastic moduli (from ones of kPa to tens of MPa) has been adopted for the matrix or bioscaffold to simulate ventricles in the tissue engineering or mechanobiology studies[25, 45]. Lastly, there is no distinction between the LV and RV tissue mechanics due to the lack of knowledge of baseline contrasts of their biomechanical properties. Our data provides fundamental information on the LV versus RV passive, anisotropic mechanical behaviors. The data collected on large animal species further offers valuable data for translational applications in exploring mechanically regulated disease mechanism and/or regenerative therapy. We highly recommend future studies to incorporate the anisotropic, nonlinear elastic behavior of myocardium into considerations to better mimic *in vivo* conditions.

### *3.4.3 Insight from the structurally informed model*

The phenomenological computational models typically provide good capture of the macroscopic mechanical behavior; however, they lack detailed information on the structural and material properties of the myocardium constituents[1]. Instead, the structural constitutive model, such as the one used in this study, is formulated to capture the underlying microstructural mechanisms for the macroscopic behavior of the tissue. From our results, the LV tended to have a larger transition strain than the RV, which suggests that the LV recruit collagen later than the RV. Furthermore, the LV tended to have a larger $k_1^m$ value (myofiber stiffness) and a larger $k_1^c$ value (collagen stiffness) than those of the RV, suggesting a stiffer fiber material property. This finding is similar to the recent report of Kakaletsis et. al[16]. The cause for stiffer collagen fibers in the LV than the RV awaits further investigation. The ventricular differences in the diastolic function and the adaptation to mechanical loading conditions depend on microstructural characteristics like myofiber and collagen stiffness. The structurally informed model here can help to highlight the myofiber and collagen contributions to that of organ-level remodeling, which will in turn help to develop targeted therapies that prevent or reverse maladaptive remodeling[22].

### *3.4.4 Correlation between collagen content and ventricle elasticity*

In this study, we also found novel correlations between collagen and ventricular biomechanics. Firstly, we observed a trend of higher collagen content including type I collagen in the RV compared to the LV. This is consistent with the prior report of collagen content in human LV and RV determined from hydroxyproline assays[46]. Second, although type I collagen is the most abundant type of collagen in ventricles[47], the type III collagen content was significantly correlated with the $M_L$ in all ventricles and at low strains (**Fig. 3.7B**, $p<0.05$). This indicates that the longitudinal elasticity partly stemmed from type III collagen recruitment. It is known that type III collagen is mesh-like in structure and more compliant than fibrillar type I collagen[48], but how these fibers are recruited during the nonlinear deformation is unclear. Our data suggest that the type III collagen may play an equally important role as myofiber in low-strain tissue mechanics, which is key to ventricular diastolic function[32]. It is also possible that type III collagen is recruited earlier than type I collagen and presents a similar role as elastin in vascular tissues. Lastly, the total collagen content was significantly correlated with the circumferential $M/\varepsilon$ in both ventricles and at high strains (**Fig. 3.7C**, $p<0.05$). The strong influence of collagen fibers in high-strain elasticity is likely the outcome of more fully recruited collagen at larger deformation.

### *3.4.5 Limitations*

Several limitations were present in the study. Our samples were from female ovine. Sex differences have been found in ventricular function in both physiological and pathological conditions[49], but its effect on the myocardium mechanical property has not been reported. Next, the middle portion of the ventricles were tested to fulfill the plane stress requirement in biaxial test. This was viewed as standard for biaxial tests of myocardium[30]. But it resulted in an incomplete characterization of tissue mechanics and transmural fiber orientation, especially in the LV wall. Such limitation is not rare for *ex vivo* mechanical measurement of myocardium from large animals or human patients due to a large tissue size. Prior studies typically sectioned the LV into two or three layers[14, 15, 17] or at different anatomical regions[15, 18], and then performed the biaxial tests. However, the entire ventricle's mechanical behavior is 'interrupted' by sectioning. Therefore, the full description of mechanical properties of the LV (or hypertrophied RV) would require the development of *in vivo* computational modeling using intact, complete structural information of the patient. Third, the samples were sectioned in cruciform shape and mounted by clamps in our biaxial tests, similar to a prior rat RV study[30]. We chose this method based on a prior examination of our in-house biaxial system on brain tissues[35]. The impact of sample shape and mounting method on biaxial tests has been explored by Sun et al.[50]. We acknowledge that our methodology is different than other studies with square samples and sutures mounting, but an examination of the strain data indicates relatively homogenous deformation in the center region of the tissue. Thus, we expect that the discrepancy induced by this methodology should be minimal. Furthermore, we tested the samples at room temperature with a regular spray of PBS rather than immerse the tissue in a relaxant solution at body temperature. We investigated the effects of these testing conditions on the passive mechanical properties by using extra ventricles. We compared the stress-strain curves and observed no significant changes of the mechanical behavior between these two conditions.

Lastly, myocardium is a nonlinear, orthotropic, and viscoelastic material. In order to fully characterize the mechanical property, the combination of shear and biaxial tests and the inclusion of viscoelasticity measurement are recommended[17, 51]. Nevertheless, the ex vivo planar biaxial test is still widely performed in cardiac mechanical testing[52], and it provides an initial examination of passive mechanical properties that are independent of physiological conditions such as in vivo pressure and volume, heart rate, sympathetic nervous stimulation, etc. The study of biaxial planar mechanics is critical to understand RV diastolic function as the deformation replicates the physiological motion[53-55]. The relatively simple testing protocol minimizes the testing time to ensure tissue viability[28, 33]. Therefore, this method remains common to characterize myocardium passive properties[14, 15, 18, 31, 42, 56-58].

### *3.4.6 Conclusions*

In this study, we examined the biomechanical differences between healthy LVs and RVs in adult ovine. We observed differences in the anisotropic behavior between the LV and RV, with the LV being stiffer in the longitudinal (OT) direction and the RV being stiffer in the circumferential (cross-OT) direction. Interventricular comparison showed that the RV was more compliant than the LV in the longitudinal direction and was stiffer than the LV in the circumferential direction, which suggests different impacts of passive mechanics of these ventricles on the blood filling during diastole. These anisotropic properties were captured by the zero-load elastic moduli as well as the anisotropic parameter $K$ derived from the four-parameter Fung type model. Results from the structurally informed model imply stiffer collagen fibers in the LV than the RV, which awaits further investigation. Moreover, type III collagen content was correlated with the low-strain elastic moduli in the longitudinal direction in both ventricles. Our findings provide significant insights for guiding cardiac tissue engineering and regenerative studies and call for the development of RV-specific therapy based on its unique biomechanics. In addition, our results can serve as a benchmark for image-based inverse modeling technologies to non-invasively estimate myocardial properties in various types of heart failure patients.

# References

1. Avazmohammadi R, Soares JS, Li DS, Raut SS, Gorman RC, Sacks MS. A contemporary look at biomechanical models of myocardium. *Annual review of biomedical engineering*. 2019;21:417-442
2. Sharifi Kia D, Benza E, Bachman TN, Tushak C, Kim K, Simon MA. Angiotensin receptor-neprilysin inhibition attenuates right ventricular remodeling in pulmonary hypertension. *J Am Heart Assoc*. 2020;9:e015708
3. Andersen S, Birkmose Axelsen J, Ringgaard S, Randel Nyengaard J, Holm Nielsen S, Genovese F, et al. Pressure overload induced right ventricular remodeling is not attenuated by the anti-fibrotic agent pirfenidone. *Pulm Circ*. 2019;9:2045894019848659
4. Pfau D, Thorn SL, Zhang J, Mikush N, Renaud JM, Klein R, et al. Angiotensin receptor neprilysin inhibitor attenuates myocardial remodeling and improves infarct perfusion in experimental heart failure. *Sci Rep*. 2019;9:5791
5. Andersen S, Nielsen-Kudsk JE, Vonk Noordegraaf A, de Man FS. Right ventricular fibrosis. *Circulation*. 2019;139:269-285
6. Vonk Noordegraaf A, Westerhof BE, Westerhof N. The relationship between the right ventricle and its load in pulmonary hypertension. *J Am Coll Cardiol*. 2017;69:236-243
7. Abel FL. Effects of alterations in peripheral resistance on left ventricular function. *Proc Soc Exp Biol Med*. 1965;120:52-56
8. Pahuja M, Burkhoff D. Right ventricular afterload sensitivity has been on my mind. *Circulation: Heart Failure*. 2019;12:e006345
9. Guyton AC, Lindsey AW, Gilluly JJ. The limits of right ventricular compensation following acute increase in pulmonary circulatory resistance. *Circ Res*. 1954;2:326-332
10. Laver MB, Strauss HW, Pohost GM. Herbert shubin memorial lecture. Right and left ventricular geometry: Adjustments during acute respiratory failure. *Crit Care Med*. 1979;7:509-519
11. Oken DE, Boucek RJ. Quantitation of collagen in human myocardium. *Circ Res*. 1957;5:357-361
12. Humphrey JD, Strumpf RK, Yin FCP. Biaxial mechanical-behavior of excised ventricular epicardium. *American Journal of Physiology*. 1990;259:H101-H108
13. Sacks MS, Chuong CJ. Biaxial mechanical properties of passive right ventricular free wall myocardium. *Journal of Biomechanical Engineering*. 1993;115:202-205
14. Fatemifar F, Feldman M, Oglesby M, Han HC. Comparison of biomechanical properties and microstructure of trabeculae carneae, papillary muscles, and myocardium in human heart. *J Biomech Eng*. 2018
15. Javani S, Gordon M, Azadani AN. Biomechanical properties and microstructure of heart chambers: A paired comparison study in an ovine model. *Annals of Biomedical Engineering*. 2016;44:3266-3283
16. Kakaletsis S, Meador WD, Mathur M, Sugerman GP, Jazwiec T, Malinowski M, et al. Right ventricular myocardial mechanics: Multi-modal deformation, microstructure, modeling, and comparison to the left ventricle. *Acta Biomater*. 2021;123:154-166

17. Sommer G, Schriefl AJ, Andrä M, Sacherer M, Viertler C, Wolinski H, et al. Biomechanical properties and microstructure of human ventricular myocardium. *Acta Biomaterialia*. 2015;24:172-192
18. Ahmad F, Prabhu Rj, Liao J, Soe S, Jones MD, Miller J, et al. Biomechanical properties and microstructure of neonatal porcine ventricles. *Journal of the Mechanical Behavior of Biomedical Materials*. 2018;88:18-28
19. Lindsey ML, Goshorn DK, Squires CE, Escobar GP, Hendrick JW, Mingoia JT, et al. Age-dependent changes in myocardial matrix metalloproteinase/tissue inhibitor of metalloproteinase profiles and fibroblast function. *Cardiovasc Res*. 2005;66:410-419
20. Wang B, Wang G, To F, Butler JR, Claude A, McLaughlin RM, et al. Myocardial scaffold-based cardiac tissue engineering: Application of coordinated mechanical and electrical stimulations. *Langmuir : the ACS journal of surfaces and colloids*. 2013;29:11109-11117
21. Avazmohammadi R, Mendiola EA, Soares JS, Li DS, Chen Z, Merchant S, et al. A computational cardiac model for the adaptation to pulmonary arterial hypertension in the rat. *Ann Biomed Eng*. 2019;47:138-153
22. Avazmohammadi R, Mendiola EA, Li DS, Vanderslice P, Dixon RAF, Sacks MS. Interactions between structural remodeling and hypertrophy in the right ventricle in response to pulmonary arterial hypertension. *Journal of Biomechanical Engineering*. 2019;141
23. Yap CH, Park DW, Dutta D, Simon M, Kim K. Methods for using 3-d ultrasound speckle tracking in biaxial mechanical testing of biological tissue samples. *Ultrasound Med Biol*. 2015;41:1029-1042
24. Mojsejenko D, McGarvey JR, Dorsey SM, Gorman JH, 3rd, Burdick JA, Pilla JJ, et al. Estimating passive mechanical properties in a myocardial infarction using mri and finite element simulations. *Biomech Model Mechanobiol*. 2015;14:633-647
25. Nguyen-Truong M, Li YV, Wang Z. Mechanical considerations of electrospun scaffolds for myocardial tissue and regenerative engineering. *Bioengineering (Basel)*. 2020;7
26. Camacho P, Fan H, Liu Z, He J-Q. Large mammalian animal models of heart disease. *Journal of cardiovascular development and disease*. 2016;3:30
27. Avazmohammadi R, Hill MR, Simon MA, Zhang W, Sacks MS. A novel constitutive model for passive right ventricular myocardium: Evidence for myofiber-collagen fiber mechanical coupling. *Biomech Model Mechanobiol*. 2017;16:561-581
28. Avazmohammadi R, Li DS, Leahy T, Shih E, Soares JS, Gorman JH, et al. An integrated inverse model-experimental approach to determine soft tissue three-dimensional constitutive parameters: Application to post-infarcted myocardium. *Biomech Model Mechanobiol*. 2018;17:31-53
29. Matsumoto T, Fukui T, Tanaka T, Ikuta N, Ohashi T, Kumagai K, et al. Biaxial tensile properties of thoracic aortic aneurysm tissues. *Journal of Biomechanical Science and Engineering*. 2009;4:518-529
30. Witzenburg C, Raghupathy R, Kren SM, Taylor DA, Barocas VH. Mechanical changes in the rat right ventricle with decellularization. *J Biomech*. 2012;45:842-849
31. Hill MR, Simon MA, Valdez-Jasso D, Zhang W, Champion HC, Sacks MS. Structural and mechanical adaptations of right ventricular free wall myocardium to pulmonary-hypertension induced pressure overload. *Annals of biomedical engineering*. 2014;42:2451-2465

32. Jang S, Vanderpool RR, Avazmohammadi R, Lapshin E, Bachman TN, Sacks M, et al. Biomechanical and hemodynamic measures of right ventricular diastolic function: Translating tissue biomechanics to clinical relevance. *Journal of the American Heart Association*. 2017;6
33. Valdez-Jasso D, Simon MA, Champion HC, Sacks MS. A murine experimental model for the mechanical behaviour of viable right-ventricular myocardium. *The Journal of Physiology*. 2012;590:4571-4584
34. Liu W, Nguyen-Truong M, Ahern M, Labus KM, Puttlitz CM, Wang Z. Different passive viscoelastic properties between the left and right ventricles in healthy adult ovine. *J Biomech Eng*. 2021;143
35. Labus KM, Puttlitz CM. An anisotropic hyperelastic constitutive model of brain white matter in biaxial tension and structural–mechanical relationships. *Journal of the Mechanical Behavior of Biomedical Materials*. 2016;62:195-208
36. Rappaport D, Adam D, Lysyansky P, Riesner S. Assessment of myocardial regional strain and strain rate by tissue tracking in b-mode echocardiograms. *Ultrasound in Medicine & Biology*. 2006;32:1181-1192
37. Nguyen-Truong M, Liu W, Doherty C, LeBar K, Labus KM, Puttlitz CM, et al. The interventricular septum is biomechanically distinct from the ventricular free walls. *Bioengineering (Basel)*. 2021;8
38. Fan R, Sacks MS. Simulation of planar soft tissues using a structural constitutive model: Finite element implementation and validation. *J Biomech*. 2014;47:2043-2054
39. Humphrey JD. *Cardiovascular solid mechanics: Cells, tissues, and organs*. 2002.
40. Namba T, Tsutsui H, Tagawa H, Takahashi M, Saito K, Kozai T, et al. Regulation of fibrillar collagen gene expression and protein accumulation in volume-overloaded cardiac hypertrophy. *Circulation*. 1997;95:2448-2454
41. Nguyen-Truong M, Liu W, Boon J, Nelson B, Easley J, Monnet E, et al. Establishment of adult right ventricle failure in ovine using a graded, animal-specific pulmonary artery constriction model. *Animal Model Exp Med*. 2020;3:182-192
42. Park DW, Sebastiani A, Yap CH, Simon MA, Kim K. Quantification of coupled stiffness and fiber orientation remodeling in hypertensive rat right-ventricular myocardium using 3d ultrasound speckle tracking with biaxial testing. *PLOS ONE*. 2016;11:e0165320
43. Friedberg MK, Redington AN. Right versus left ventricular failure: Differences, similarities, and interactions. *Circulation*. 2014;129:1033-1044
44. Prisco SZ, Thenappan T, Prins KW. Treatment targets for right ventricular dysfunction in pulmonary arterial hypertension. *JACC Basic Transl Sci*. 2020;5:1244-1260
45. Reis LA, Chiu LLY, Feric N, Fu L, Radisic M. Biomaterials in myocardial tissue engineering. *Journal of Tissue Engineering and Regenerative Medicine*. 2016;10:11-28
46. Miles C, Westaby J, Ster IC, Asimaki A, Boardman P, Joshi A, et al. Morphometric characterization of collagen and fat in normal ventricular myocardium. *Cardiovascular pathology : the official journal of the Society for Cardiovascular Pathology*. 2020;48:107224
47. LeBar K, Wang Z. Extracellular matrix in cardiac tissue mechanics and physiology: Role of collagen accumulation. 2021.
48. Silver FH, Horvath I, Foran DJ. Mechanical implications of the domain structure of fiber-forming collagens: Comparison of the molecular and fibrillar flexibilities of the alpha1-chains found in types i-iii collagen. *Journal of theoretical biology*. 2002;216:243-254

49. Lahm T, Douglas IS, Archer SL, Bogaard HJ, Chesler NC, Haddad F, et al. Assessment of right ventricular function in the research setting: Knowledge gaps and pathways forward. An official american thoracic society research statement. *Am J Respir Crit Care Med*. 2018;198:e15-e43

50. Sun W, Sacks MS, Scott MJ. Effects of boundary conditions on the estimation of the planar biaxial mechanical properties of soft tissues. *J Biomech Eng*. 2005;127:709-715

51. Holzapfel GA, Ogden RW. Constitutive modelling of passive myocardium: A structurally based framework for material characterization. *Philosophical Transactions of the Royal Society A*. 2009;367:3445-3475

52. Voorhees AP, Han HC. Biomechanics of cardiac function. *Compr Physiol*. 2015;5:1623-1644

53. Taverne Y, Sadeghi A, Bartelds B, Bogers A, Merkus D. Right ventricular phenotype, function, and failure: A journey from evolution to clinics. *Heart Fail Rev*. 2021;26:1447-1466

54. Haddad F, Hunt SA, Rosenthal DN, Murphy DJ. Right ventricular function in cardiovascular disease, part i: Anatomy, physiology, aging, and functional assessment of the right ventricle. *Circulation*. 2008;117:1436-1448

55. Pettersen E, Helle-Valle T, Edvardsen T, Lindberg H, Smith HJ, Smevik B, et al. Contraction pattern of the systemic right ventricle shift from longitudinal to circumferential shortening and absent global ventricular torsion. *J Am Coll Cardiol*. 2007;49:2450-2456

56. Avazmohammadi R, Hill M, Simon M, Sacks M. Transmural remodeling of right ventricular myocardium in response to pulmonary arterial hypertension. *APL Bioeng*. 2017;1

57. Ghaemi H, Behdinan K, Spence AD. In vitro technique in estimation of passive mechanical properties of bovine heart: Part i. Experimental techniques and data. *Medical Engineering & Physics*. 2009;31:76-82

58. Velez-Rendon D, Pursell E, Shieh J, Valdez-Jasso D. Contribution of matrix remodeling to biaxial mechanics of right-ventricular myocardium in pulmonary arterial hypertension. *J Biomech Eng*. 2019

# 4. The Interventricular Septum Is Biomechanically Distinct from the Ventricular Free Walls[2]

## 4.1 Introduction

Heart failure is the leading cause of death worldwide[1]. Among the many types of heart failure, left and right ventricular (LV/RV) failure are the most common causes. The investigation of ventricular dysfunction has mostly focused on the adaptation and remodeling of the ventricular free wall, whereas the interventricular septum (**Fig. 4.1**), the dividing wall between the left and right ventricles, has received much less attention. Therefore, an improved understanding of the septum, including its biomechanical behavior, is needed.

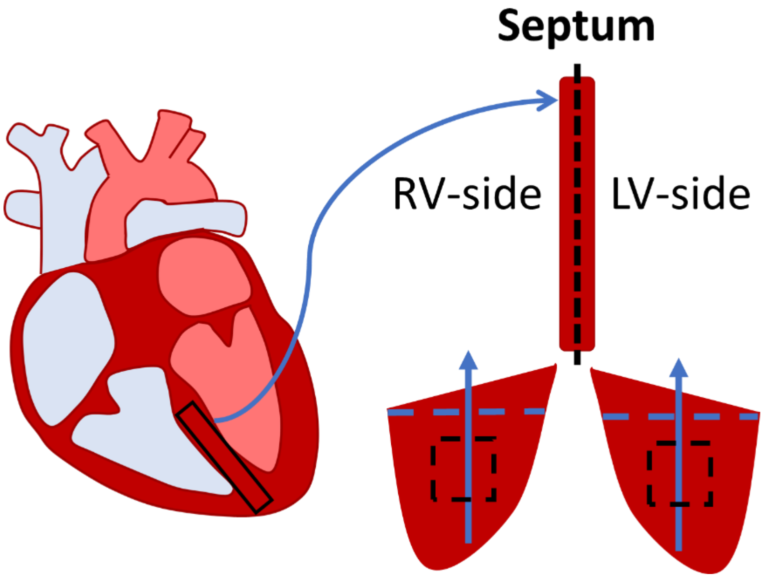

**Figure 4.1**. Schematic of septum split into two even sides.

---

[2] Adapted from Nguyen-Truong M, Liu W, Doherty C, LeBar K, Labus KM, Puttlitz CM, Easley J, Monnet E, Chicco A, Wang Z. The Interventricular Septum Is Biomechanically Distinct from the Ventricular Free Walls. *Bioengineering (Basel)*. 2021 Dec 15;8(12):216. doi: 10.3390/bioengineering8120216.

The septum has been traditionally viewed as a single entity and a part of the LV chamber (e.g., the septal thickness is used as an indicator of LV mass), having similar contribution to LV function as the LV free wall[2]. However, the septum has also been shown to play an important role in RV function. Evidence exists that RV function was maintained despite elimination or alteration of the RV free wall[3-5], and the induction of septum dysfunction resulted in reduced RV function[6, 7]. An excellent review of the septum's contribution to RV function was provided by Buckberg et al. in 2014[8]. Moreover, it has been widely observed that in RV failure secondary to pulmonary hypertension, the septal wall position is shifted towards the left side of the heart with intact LV function[9, 10]. Therefore, the septum does not belong to any single chamber; instead, it participates in the physiological function of both ventricles.

Furthermore, *in vivo* evidence suggests that the septum wall is a layered structure with transmural variations. For instance, Boettler et al. reported from echocardiography an abrupt change in echogenicity (acoustic reflectance) down the middle of septum, suggesting a shift in tissue density dividing the left and right sides. In the left side of the septum, the longitudinal strain and strain rate were larger than those of the radial direction, and the opposite was observed in the right side of the septum[11]. Their findings suggest that the septum wall may be structurally and mechanically different between the LV- and RV-side. Moreover, Holland et al. observed different ultrasonic properties that are sensitive to tissue structure and function between the two septal sides[12]. In another study, Lindqvist et al. virtually 'divided' the septum into three layers with equal thickness and then observed from Doppler echocardiography that the two endocardial layers and the middle layer showed different strain, strain rate, as well as tissue anisotropy[13]. Although these imaging studies arbitrarily 'separated' the septum into two or three layers without known anatomic boundaries, their results indeed imply a transmural variation of the mechanical behavior within the septum.

Nevertheless, the full *ex vivo* characterization of the transmural biomechanical variation of the septum is lacking. To date, only two studies reported the *ex vivo* mechanical properties of the septum from canine or human samples. These studies tested either the mid-layer[14] or non-specified layer[15] of the septal wall. They found similar elasticity (by constitutive modeling) or maximal stress values between the septum wall and the LV free wall[14, 15], with an underlying assumption that there is no transmural difference in the septum. Therefore, the biaxial and transmural variation of the passive mechanics of septum remains a knowledge gap.

The aims of this study are to characterize the biaxial and transmural variation of the passive mechanical properties of the septum and compare them to their respective ventricle free walls in healthy adult ovine. Sheep were chosen because of the similarities between human and ovine cardiovascular anatomy, physiology and function[16, 17]. Because the septum is formed by 'fusion' of the bilateral tubes from two embryonic ventricles that have distinct embryological origins[18-20], we chose to investigate the transmural variation by dividing the wall into two sides. We hypothesize that in healthy adults, there are transmural differences between the LV-side and RV-side of the septum, and that these two sides are distinct from that of the LV and RV free walls, respectively. Using biaxial tensile mechanical tests and constitutive modeling, we found that both sides of the septum were significantly softer than their respective ventricular free wall counterparts. Additionally, we found that the collagen content in the septum was significantly less than the ventricles. At low strains, the septum presented anisotropy in both sides, with a stiffer material property in the longitudinal direction. At high strains, both sides of septum were isotropic.

These biomechanical findings will fill a fundamental knowledge gap in cardiac biomechanics and facilitate a more complete understanding of heart physiology.

## 4.2 Methods

### *4.2.1 Sample preparation*

Fresh hearts were obtained from adult female sheep (36+ months old: n=12) with no known cardiovascular diseases from unrelated studies at the Colorado State University Veterinary Teaching Hospital. Within 30 hours after harvest, the hearts were placed in cardioplegic solution (CPS) on ice or at 4°C to maintain tissue viability. The epicardial layer was extracted from the LV and RV free walls. Next, the septal wall was cleaned with removal of trabeculae and papillary muscles, and then sliced down approximately the middle into two halves to elucidate transmural differences between the LV and RV sides of the septum. The ventricle and septal sections were then cut into square sections (septum: 900 $mm^2$, ventricle: 625 $mm^2$) with thickness of ~3 mm and kept in CPS and 30 mM of 2,3-butanedione 2-monoxime (BDM) at body temperature (37°C) for at least 10 minutes to prepare for the passive mechanical tests in physiological conditions. The long axis (apex-to-base) was defined as the longitudinal direction (90°) and the perpendicular axis was defined as the circumferential direction (0° for LV-side or 180° for RV-side) in the septum. The outflow tracts were defined as the longitudinal direction in the ventricular free wall samples[21, 22]. A protractor was used to measure the dominant myofiber angle in the septum samples (n=9) (**Fig. 4.2**).

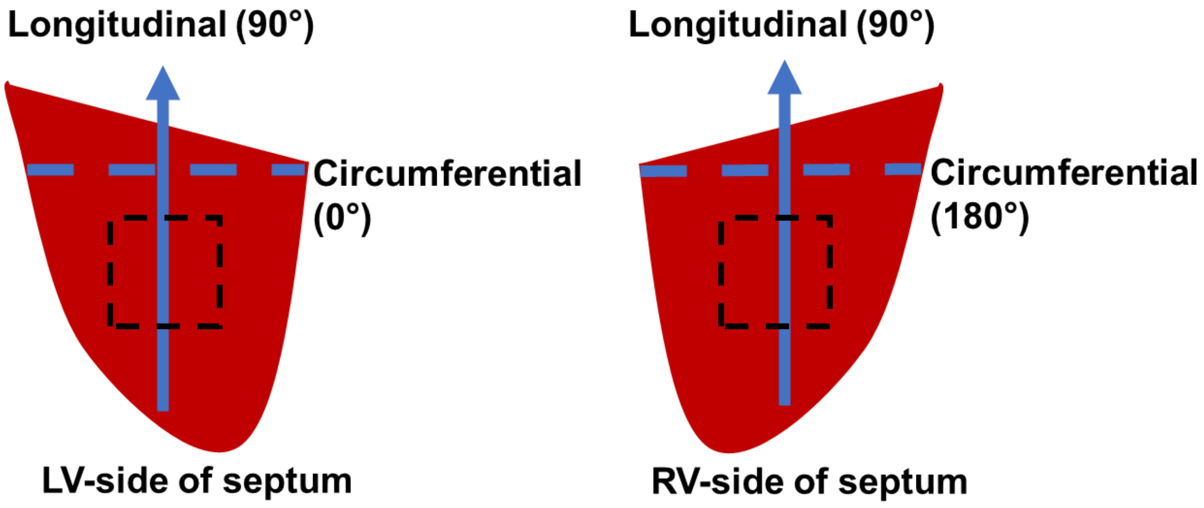

**Figure 4.2**. Schematic of orientations for each side of the septum. The arrowhead (longitudinal direction) represents the apex-to-base direction. The black, dashed line square represents the region at which samples were taken for fiber angle measurements and mechanical testing.

### *4.2.2 Biaxial testing*

After mounting on an in-house biaxial tester, the samples were preloaded with approximately 0.1 N and underwent 10-15 cycles of equibiaxial stretch for preconditioning. An additional 5 cycles of equibiaxial stretch at quasi-static testing frequency (ventricle: 0.01 Hz and septum: 0.02 Hz) were performed and the data from the last cycle were used for mechanical analysis. All preconditioning and tests were performed in a tissue bath of CPS and 30 mM of BDM at 26-37°C to ensure that the cardiomyocytes were relaxed, and passive biomechanical behavior was obtained[23, 24]. All samples underwent a maximum displacement of 20% of the reference configuration to cover the physiological septal strain range[25, 26]. Deformations of graphite powder-speckled samples were tracked with a camera (Nikon, Tokyo, Japan). Biaxial stretch forces were obtained by 50-lb load cells (Honeywell Sensotec, Columbus, OH).

### 4.2.3 Constitutive modeling

Second Piola-Kirchhoff (P-K) stress - Green strain curves were then derived from the loading curve of the last testing cycle. The formulas were as follows: Second P-K stress (**S**) ($S = P/\lambda$, and $P = F/A_0$, where $F$ is the measured force, $P$ is the engineering stress, $A_0$ is the initial cross-section area, and $\lambda$ is stretch) and Green strain ($E = \frac{1}{2}(\lambda^2 - 1)$). The elastic moduli ($M$) were derived as the slope of the stress-strain curve in the low and high strain ranges (i.e., using the first and last 20% of data points of the curve, respectively)[22, 27].

From our experimental data, we calculated the shear deformation and presented the average normal strains and shear strains in **Table 4.1**. Because a majority of the samples had much smaller shear strains than the corresponding normal strains, we neglected shear strain in the constitutive modeling below. The Fung type model uses individual fitting results to predict an average equibiaxial behavior as well as overall elastic and anisotropic properties of the tissues from the same group. Thus, we adopted this constitutive model in our study.

**Table 4.1**. Maximum normal strains and the corresponding shear strains of the septum samples. $\varepsilon_L$ and $\varepsilon_C$ are normal strains in the longitudinal and circumferential directions, and $\varepsilon_{LC}$ and $\varepsilon_{CL}$ are shear strains in the shear directions. Data presented as mean ± SEM.

| **Group** | $\varepsilon_L$ | $\varepsilon_C$ | $\varepsilon_{LC}$ | $\varepsilon_{CL}$ |
|---|---|---|---|---|
| **LV-side (n=12)** | 0.11±0.01 | 0.18±0.02 | 0.03±0.02 | 0.05±0.02 |
| **RV-side (n=12)** | 0.15±0.02 | 0.21±0.03 | 0.01±0.02 | 0.01±0.02 |

Green strain tensor (**E**) components were calculated by using the following equations:

$$E_L = \frac{1}{2}({\lambda_L}^2 - 1), E_C = \frac{1}{2}({\lambda_C}^2 - 1), \quad (1)$$

where $E_{\mathrm{L}}$ and $E_{\mathrm{C}}$ are the Green strains in longitudinal and circumferential directions, respectively, and $\lambda_{\mathrm{L}}$ and $\lambda_{\mathrm{C}}$ are the stretches in longitudinal and circumferential directions, respectively.

As in previous studies[28, 29], a four-parameter Fung exponential strain energy function ($\Psi$) was applied:

$$\Psi = \frac{B}{2}(e^{Q} - 1),\, Q = b_{\mathrm{L}}{E_{\mathrm{L}}}^{2} + 2b_{\mathrm{LC}}E_{\mathrm{L}}E_{\mathrm{C}} + b_{\mathrm{C}}{E_{\mathrm{C}}}^{2}, \tag{2}$$

where $b_{\mathrm{L}}$, $b_{\mathrm{LC}}$, $b_{\mathrm{C}}$ and $B$ are the material constants.

The Second P-K stress and Cauchy stress ($\boldsymbol{\sigma}$) for an incompressible tissue were calculated using the following equation:

$$\mathbf{S} = 2\,\frac{\partial\Psi}{\partial\mathbf{C}} - p\mathbf{C}^{-1}, \boldsymbol{\sigma} = \mathbf{FSF}^{T}, \tag{3}$$

where **F** is the gradient tensor, **C** is the right Cauchy-Green tensor, and *p* is an unknown hydrostatic pressure to enforce det(**C**) =1.

Then, the stress-strain relationships in the longitudinal and circumferential directions were derived as:

$$\sigma_{L} = (2E_{\mathrm{L}} + 1)(b_{\mathrm{L}}E_{\mathrm{L}} + b_{\mathrm{LC}}E_{\mathrm{C}})Be^{(b_{\mathrm{L}}E^{2}{}_{\mathrm{L}} + 2b_{\mathrm{LC}}E_{\mathrm{L}}E_{\mathrm{C}} + b_{\mathrm{C}}E^{2}{}_{\mathrm{C}})}$$

$$\sigma_{C} = (2E_{\mathrm{C}} + 1)(b_{\mathrm{LC}}E_{\mathrm{L}} + b_{\mathrm{C}}E_{\mathrm{C}})Be^{(b_{\mathrm{L}}E^{2}{}_{\mathrm{L}} + 2b_{\mathrm{LC}}E_{\mathrm{L}}E_{\mathrm{C}} + b_{\mathrm{C}}E^{2}{}_{\mathrm{C}})}. \tag{4}$$

The Fung strain energy function was fitted to the experimental data for each specimen. The fitting was performed with a Levenberg-Marquardt least squares algorithm with the tolerance of $10^{-8}$ in MATLAB. Every fit was checked with at least twenty different initial guesses and all optimizations converged to the consistent values which indicated the optimization algorithm was independent of the initial guesses. The root mean square (RMS) was calculated to assess the fitting results.

In order to further quantify tissue anisotropy, the stress-strain curves were numerically converted to the equibiaxial stretch condition, where $E_{\mathrm{L}} = E_{\mathrm{C}} = E$, and then the material difference between the two directions was assessed by an anisotropic parameter *K*:

$$K = \frac{2(b_{\mathrm{L}} - b_{\mathrm{C}})}{(b_{\mathrm{L}} + b_{\mathrm{C}} + 2b_{\mathrm{LC}})}. \tag{5}$$

Therefore, a positive *K* value ($b_{\mathrm{L}} > b_{\mathrm{C}}$) indicated that the material is stiffer in the longitudinal direction, whereas a negative *K* value ($b_{\mathrm{L}} < b_{\mathrm{C}}$) indicated that the material is stiffer in the circumferential direction.

By using the converted equibiaxial stress-strain curves, the elasticity at zero load in the longitudinal and circumferential directions were:

$$M_{0,\mathrm{L}} = \frac{d\sigma_{\mathrm{L}}{}^{equi}}{dE}\Big|_{E=0}$$

$$M_{0,\mathrm{C}} = \frac{d\sigma_{\mathrm{C}}{}^{equi}}{dE}\Big|_{E=0}, \tag{6}$$

where the $M_{0,\mathrm{L}}$ and $M_{0,\mathrm{C}}$ are the zero-load elastic moduli derived from the four-parameter Fung type model under the equibiaxial condition in longitudinal and circumferential directions, respectively.

### *4.2.4 Histology*

Tissue samples were fixed in 10% formalin, dehydrated, embedded in paraffin, sectioned, and stained with Picrosirius Red. Histology images were acquired by an inverted microscope (Motic AE31E, Motic, San Antonio, TX). Three regions of interest to represent the overall tissue were randomly selected. To quantify collagen content, the areas positive for collagen (dark red) were identified using a color thresholding function in ImageJ (NIH, Bethesda, Maryland, USA), and collagen area fraction (%) was calculated as the ratio of collagen area to total tissue area. All images were analyzed by the same observer blinded to the group information. Because the ventricle and septum tissues were stained in different batches, the non-specific staining in the background was different and thus different thresholding values were set for these batches. But this did not affect the identification of the positive staining of collagen fibers, and the images from the same batch were acquired at the same setting.

### *4.2.5 Statistical analysis*

Data are presented as mean ± SEM. The Mann-Whitney U-test was used for myofiber angle and mechanical comparisons in septum. One-way ANOVA and Tukey post-hoc tests were performed between directions and between the septal and ventricular *M* and collagen data. $p<0.05$ was considered statistically significant.

## 4.3 Results

### *4.3.1 Transmural change in septum myofiber orientation*

From the myofiber angle measurements, we observed a change in the fiber angle from the LV-side to the RV-side of the septum. As shown in **Table 4.2**, the myofiber angle shifted from a longitudinal orientation on the LV-side to a circumferential orientation in the midwall, and then back to a longitudinal orientation on the RV-side of the septum. Therefore, the transmural distribution of myofibers was to some degree symmetric (‘mirrored’) between the two sides of the septum.

**Table 4.2**. Dominant myofiber angle of the LV-side, midwall, and RV-side of the septum. Longitudinal direction was defined as $90^{\circ}$. Data presented as mean ± SEM. $^{*}p<0.05$ vs. LV-side and $^{\#}p<0.05$ vs. RV-side.

| | **LV-side (n=4)** | **Midwall (n=9)** | **RV-side (n=4)** |
|---|---|---|---|
| **Myofiber angle** (°) | 78±3 | $9\pm2^{*,\#}$ | 108±8 |

### *4.3.2 Softer septal side compared to the corresponding side of ventricular free wall*

The average stress-strain curves of the ventricular free walls and both sides of the septum are presented in **Fig. 4.3**. In both sides of the heart chamber, the ventricular free wall showed stiffer behavior compared to the corresponding side of the septum, which is demonstrated by the leftward shifted stress-strain curves. This difference was clearly seen in both longitudinal and circumferential directions of the respective septum side with its corresponding free wall.

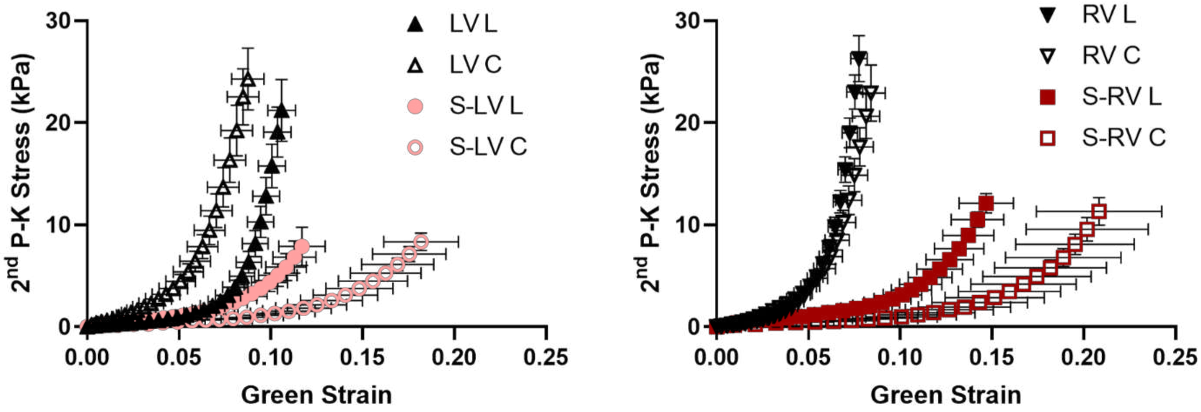

**Figure 4.3.** Average stress-strain curves of the ventricular free walls (LV, RV) and the LV-side and RV-side of the septum. n=12 for septum; n=8 for ventricles. S-LV: LV-side of septum; S-RV: RV-side of septum; L: longitudinal direction; C: circumferential direction.

Next, we compared the elastic moduli (*M*) between groups and between directions at low and high strains (**Fig. 4.4**). In the low strains, the free walls had larger *M* than the corresponding side of the septum in the circumferential direction only, indicating a stiffer ventricle free wall than septum wall. In the high strains, the *M* was larger in the free walls than the corresponding septum side in both directions, indicating stiffer ventricle free wall than septum wall at larger deformations.

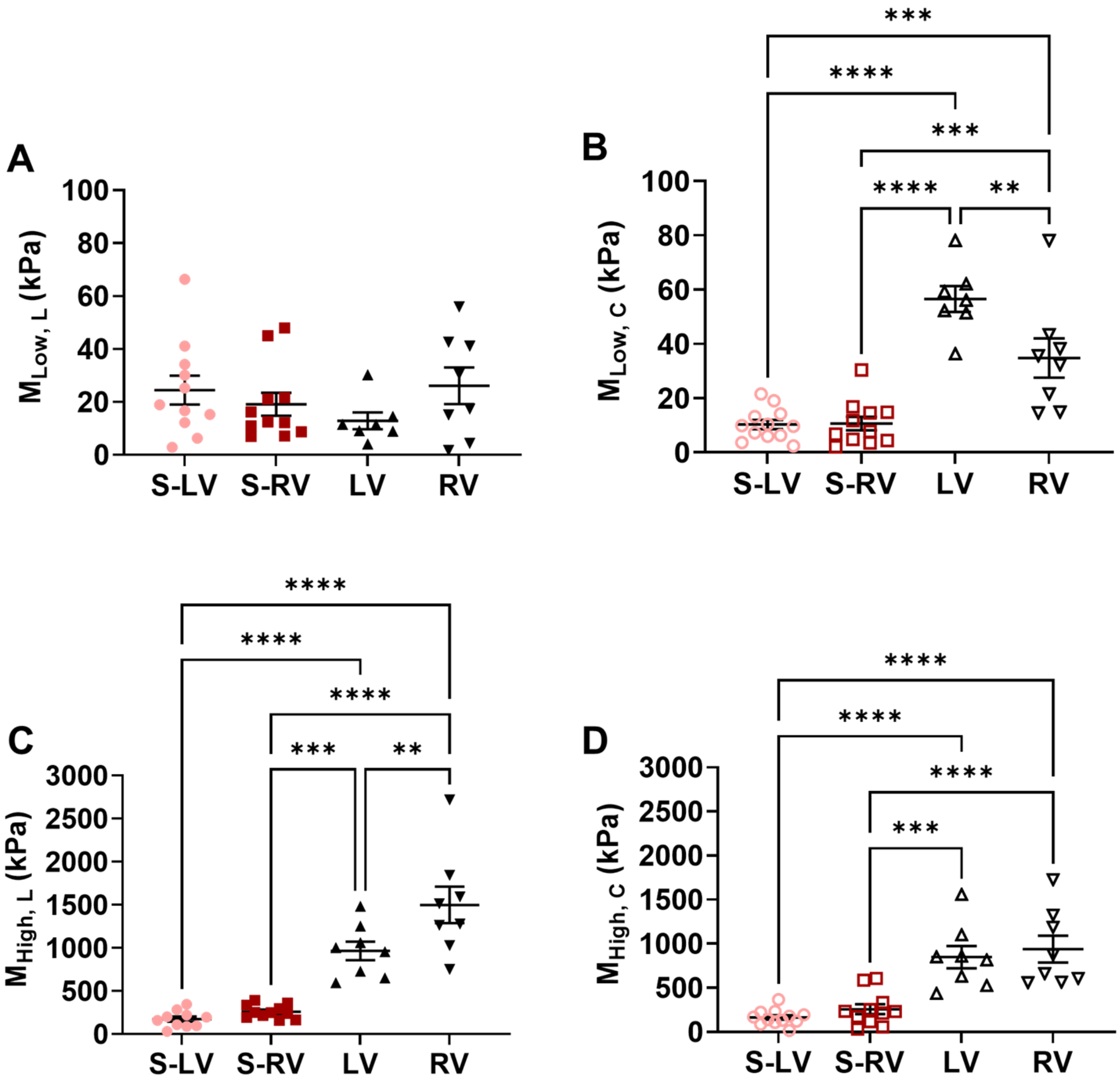

**Figure 4.4.** Comparisons of elastic moduli (*M*) at low (**A-B**) and high (**C-D**) strains from the septal sides and ventricles. Left columns show the *M* obtained in the longitudinal direction and right columns show the *M* obtained in the circumferential direction. n=10-12 per group for septum; n=7-8 per group for ventricles. S-LV: LV-side of septum; S-RV: RV-side of septum.

*4.3.3 Transmural differences in the septum obtained from experimental data*

Similar anisotropies are shown from the low-strain elastic modulus (*M*) between the two sides of septum (**Figs. 4.5A&B**). Compared to the *M* in the circumferential direction, the *M* in the longitudinal direction was higher. There was stronger (p=0.002) anisotropy in the LV-side of the septum compared to the RV-side (p=0.049). At high strains, however, both sides of the septum presented isotropic behavior. Next, we compared the elastic moduli (*M*) of the two sides from the same direction. There was no difference in the *M* between the two sides of the septum in all strain ranges or in both directions, although there was a trend of a stiffer RV-side septum compared to LV-side in the high strain range in the circumferential direction (p=0.06).

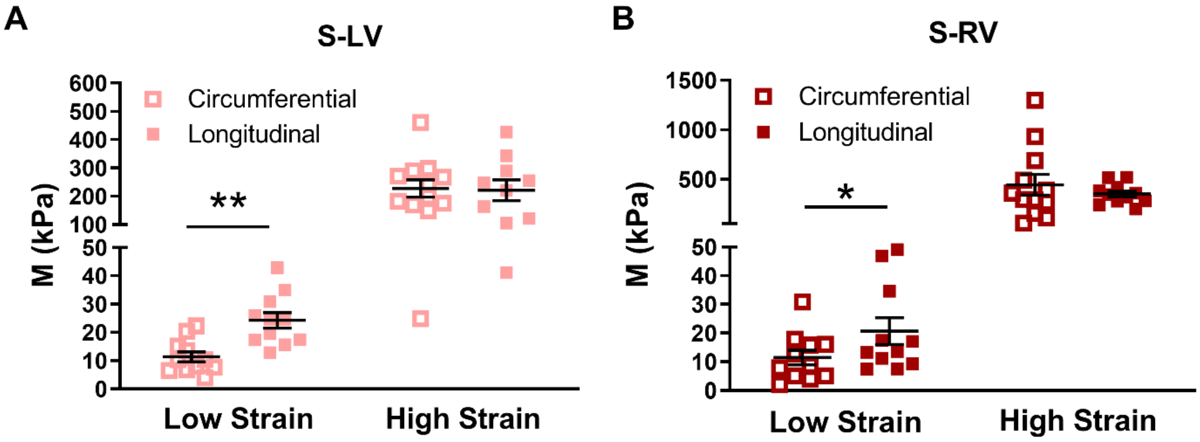

**Figure 4.5.** (**A&B**) Comparison of elastic moduli (*M*) between biaxial directions in the left and right sides of the septum. Significant anisotropy in both S-LV and S-RV at low strains, and the degree of anisotropy was much stronger in the S-LV. *p<0.05 vs. circumferential in the same strain range. **p<0.01 vs. circumferential in the same strain range. n=10-12 per group for septum; n=10-12 per group. S-LV: LV-side of septum; S-RV: RV-side of septum.

### *4.3.4 Transmural differences in the septum obtained from computational modeling*

We fit the septum equibiaxial stress-strain curves using a four-parameter Fung type model described previously in myocardium studies[28, 29]. A good fitting with the experimental data was observed for all tissues and in both directions (i.e., with low RMS values), and the fitting results are summarized in **Table 4.3**. We did not observe any statistical significance in the model parameters (**Table 4.3**) between the LV-side and RV-side of the septum, indicating similar material property (overall elasticity) of the tissue. The simulated stress-strain curves that were numerically converted to the equibiaxial condition showed similar shapes as our experimental data.

**Table 4.3.** Model fitting results. Data presented as mean ± SEM.

| Septum | $b_L$ | $b_C$ | $b_{LC}$ | $B$ (kPa) | RMS (kPa) |
|---|---|---|---|---|---|
| **LV-side** | 62.54±12.62 | 40.84±7.74 | 0.004±0.002 | 0.21±0.04 | 0.21±0.04 |
| **RV-side** | 46.50±7.21 | 32.66±7.63 | 0.005±0.001 | 0.19±0.04 | 0.30±0.04 |

$b_L$, $b_C$, $b_{LC}$, and $B$ are the material constants, and RMS is root mean square. L and C represent longitudinal and circumferential directions, respectively.

We further compared the zero-load elastic modulus ($M_0$) derived from the model fitting in each ventricle type and in different directions. This parameter serves as an indicator of myofiber stiffness. As shown in Fig. 4.6, there was a trend of larger $M_{0,L}$ compared to the $M_{0,C}$ in the LV-side septum (p=0.08), indicating the LV-side was more anisotropic and stiffer in the longitudinal direction than the circumferential direction (**Fig. 4.6**). There was no difference in the $M_0$ between directions for the RV-side septum. Moreover, the anisotropic parameter $K$ was positive for both sides (0.40±0.17 in LV-side and 0.25±0.28 in RV-side), which indicated a stiffer behavior in the longitudinal direction. These results agreed with our experimental data, especially at the low strain range (**Figs. 4.5A&B**).

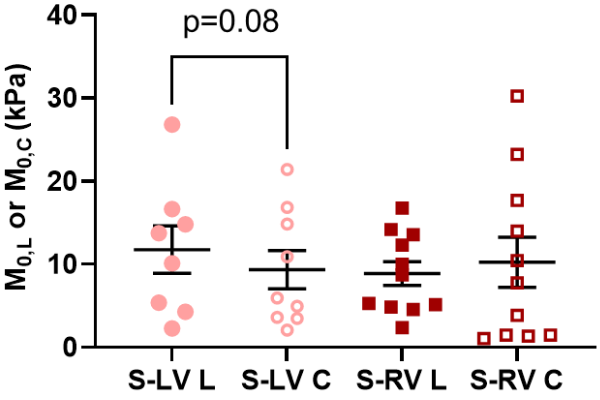

**Figure 4.6.** Longitudinal (L) and circumferential (C) zero-load elastic modulus ($M_0$) at zero load derived from the fitting parameters for each side of septum. n=9-11 per group. S-LV: LV-side of septum; S-RV: RV-side of septum.

### *4.3.5 Difference in collagen content between septum and ventricular tissues*

When comparing the overall collagen content between both sides of the septum, we found a trend of higher collagen content in the LV-side compared to the RV-side, but the difference was not significant. Furthermore, the collagen content in the LV or RV was significantly higher than that of the corresponding side of septum ($p<0.05$), indicating a marked reduced collagen in the septal wall compared to the ventricular free walls (**Fig. 4.7**). This may explain the difference in elastic moduli between the ventricle and its respective septum side.

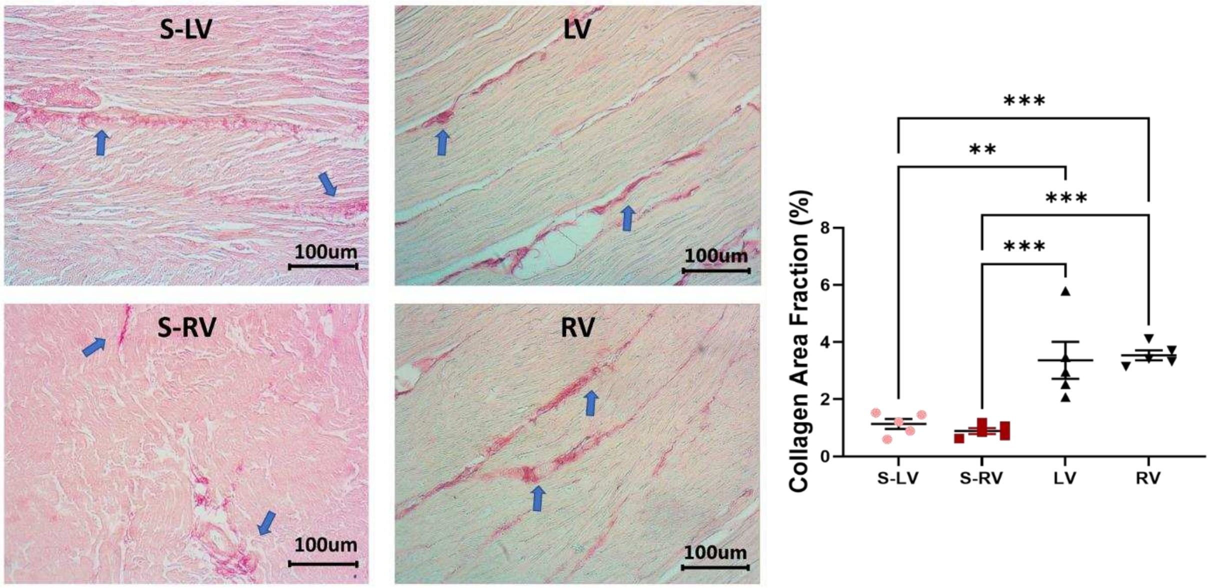

**Figure 4.7.** Representative histology images (left) and the comparisons of collagen area fraction (right) between the S-LV, S-RV, LV, and RV groups. Arrows show the positive staining of collagen fibers. $^{**}p<0.01$, $^{***}p<0.001$. n=5 per group. S-LV: LV-side of septum; S-RV: RV-side of septum.

## 4.4 Discussion

This is the first study to characterize the *ex vivo* passive mechanical properties of the LV-side and RV-side of the septum and compare them to their respective ventricles in healthy, adult ovine. We found that the ventricular free walls were stiffer than their respective septal counterparts. Histology examination showed that the collagen amount was higher in the ventricles compared to their respective septal counterparts. This suggests that the septum has unique structure-function relationships compared to both ventricles. Transmurally, the two sides of septum showed symmetric distribution of fibers that shifted from longitudinal direction at the endocardial layer to the circumferential direction at the mid-layer. Thus, similar anisotropic behavior existed in both sides (i.e., stiffer longitudinal behavior than circumferential behavior), but the degree of the anisotropy was stronger in the LV-side. The intrinsic elasticity was similar between the two sides of septum and in both directions. Our results suggest that the septum should not be treated as a part of LV or RV, and the unique transmural distribution of biomechanical properties of the septum will assist in the understanding of left and right ventricular function.

### *4.4.1 Different mechanical behavior between ventricle free walls and septum*

The two ventricles have different embryological origins. The early heart ventricles, which are formed from bilateral tubes, fuse to form the septum during cardiac development[18-20]. Therefore, it is reasonable to speculate that the transmural differences in mechanical behavior are likely attributable to the different cell lineages[20] and the growth patterns and demands between the two ventricles[9]. To our knowledge, only two studies have performed *ex vivo* mechanical tests on the septum, and both neglected the transmural variations in the septum. Novak et al. was the first to compare the biaxial mechanical properties of the inner, middle and outer layers of the LV and the middle portion of the septum in canine[14]. They did not find significant differences in the stored strain energy – inferring similar elasticity of the tissues. But a trend of stiffer inner and outer LV free wall than the middle layer of LV and septum was noted. More recently, Sommer et al. obtained peak Cauchy stress in the human LV and RV free walls and septum[15]. They found a higher stress in the RV compared to the LV and septum, which had similar stresses. But the finding may be compromised by two factors: first, the samples were from patients with cardiac related diseases; second, the measurements of septum and RV tissues at high stretches were missing due to tissue failure close to the hook, and there were only three RV samples. Therefore, a complete mechanical comparison between the septum and the LV and RV free walls is not available from this study.

Our study is the first to examine the biaxial mechanical behavior of the septum wall in two halves and compare each side of the septum to its respective ventricular free wall. We found significantly stiffer ventricular free walls than the corresponding side of the septum, and the stiffer behavior was more pronounced in the higher stretch (strain) regions. It is known that collagen is a load bearing protein and that more collagen is correlated with stiffer elastic behavior[30]. The larger collagen content in the ventricles than the septum may thus explain the observation. Other structural differences such as myofibers may contribute to the tissue mechanics as well. Unfortunately, there is a lack in understanding of whether the cardiomyocytes in the septum are identical to those in the ventricle free walls.

Our data partly agreed with the previous reports noted above. For example, it is found that the outer and inner layers of the LV free wall tended to be stiffer than the midwall of the septum[14], and the RV free wall showed higher peak stresses compared to the septum for the same strain[15]. Akin to the former findings, we observed similar mechanical behavior between the LV and septum at the low strain range in the longitudinal direction, and stiffer RV free wall compared to the septum. We did not intend to make in-depth comparisons between our study and previous studies because of the different layers of myocardium used and different biaxial orientations (outflow tract or apex-to-base direction as the longitudinal direction in our study versus the main fiber direction as the longitudinal direction in previous studies). The relatively new biaxial axes system has been adopted by other studies, and it provides more information about the relation of tissue mechanics to ventricle function (see our discussion in 4.4.3). Overall, our finding that the septum is intrinsically more compliant than the ventricles should be further studied in different species and with the use of multi-scale approaches (from organ to cell biomechanics).

The stark differences in the elasticity between the free walls and septum can explain *in vivo* findings of different contributions of the septum and free walls to overall ventricular function. Assuming similar mechanical property and contractility of the septum and LV free wall, we would expect 16-35% of cardiac work contributed by the septum (versus 65-84% contribution by the LV free wall) based on its volume fraction from sheep and human data[31, 32]. However, Ostenfeld et al.

reported that, in healthy subjects, the septum contraction contributed only ~8% of the stroke volume, while the LV free wall contributed ~96% of the stroke volume[33]. Similar findings were shown by Stephensen et al. where ~7% of septal motion contributed to LV stroke volume[34]. Similarly, if we treat the septum as part of the RV chamber, it contributes somewhat similarly as the RV free wall in pumping, where 36%-54% of cardiac work is attributed to the septum (versus 45%-64% contribution by the RV free wall)[31, 32]. Thus, the mechanical differences between the septum and ventricles found in our study suggest that the septal wall is not 'similar' to the ventricle free walls, and the mechanical difference may be linked to altered muscle shortening velocity, leading to a 'weaker' contribution to the overall cardiac function than that of the ventricle free walls.

### *4.4.2 Fiber orientation in the septum*

It has been reported that the ventricle free walls exhibit a transmural fiber orientation shift[21, 35]. In the LV free wall, studies have reported that the myofibers shift from a longitudinal (endocardium) to circumferential (midwall) to longitudinal (epicardium) orientation[35, 36]. Other measurements of LV myofiber transmural changes using myocardial diffusion imaging[37] or a protractor[38] documented a total angle change of 120°-180°. In the RV free wall, the myofiber angle changed from a circumferential to longitudinal orientation in the epicardium to endocardium, respectively[21]. Therefore, it is not surprising that the septum wall presents a transmural change in myofiber orientation as well.

In the present study, we had a preliminary examination of the transmural change of fiber orientation in the septum, and we originally found that the average fiber orientation shifted from 78±3° (LV-side) to 9±2° (midwall) and finally to 108±8° (RV-side). Our data showed a ~150° of main myofiber angle transmural shift through the entire septum. The transmural change may be related to the individual support of the pumping demand for each ventricle. For instance, the longitudinal myofiber orientation on each endocardial side potentially better aids in blood ejection along the outflow tracts of each ventricle.

### *4.4.3 Anisotropy behavior of the septum*

As we mentioned above, the *ex vivo* mechanical properties of the septum reported in prior studies used the main fiber and cross-fiber directions as the testing axes. It is not surprising that these studies reported similar anisotropy, i.e., a stiffer behavior in the fiber direction than cross-fiber direction, probably due to the aligned myosin-actin cross-bridge and titin in the 'fiber direction' (direction of myofiber shortening). However, such measurement cannot provide the anatomic relations between the tissue anisotropy and ventricular deformation in systole and diastole, thus preventing an investigation of the relation between the biaxial mechanical behavior and the physiological function of myocardium. Furthermore, using the main fiber and cross-fiber coordinate system for biaxial tests can be problematic for tissues that have a significant transmural change in the fiber orientation. The myocardium tissue (LV/RV free wall) is composed of helical and heterogenous myofibers that vary in orientations transmurally[8, 39]; similarly, we observed marked transmural changes in myofiber orientation in the septum (**Table 4.2**). Thus, it is difficult to accurately determine the 'main fiber' direction of a myocardial wall in a single section plane.

In all septum tissues, we observed stiffer behavior in the longitudinal direction in the low strain range (**Figs. 4.5A&B,** $p<0.05$), indicating a similar pattern of anisotropic behavior of the LV-side and RV-side of septum. Because it is shown that the low strain mechanical behavior of myocardium is primarily due to myofibers[22, 40], the appearance of tissue anisotropy only in the low strain range indicates that myofibers are the main cause of septum anisotropy. Furthermore, although the anisotropy is quite 'mirrored' between the two sides, the anisotropy in the LV-side of septum was highly significant ($p<0.01$), whereas that in the RV-side of septum was marginal ($p=0.049$). The different degrees of anisotropy between the two sides have been evident by the different *in vivo* strains (a surrogate of elasticity) between the longitudinal and radial axes of each septum side. Boettler et al. found the global longitudinal and radial strain difference was larger in the septal LV-side than the RV-side (LV-side: Δ strain ~ 13%; RV-side: Δ strain ~ 5%), indicating a more anisotropic behavior of the left-side of the septum than the right-side[11]. In the current study, we did not obtain the mechanical property of septum in the radial (i.e., transmural) direction, but we found a similarly stronger tissue anisotropy in the septal LV-side than the RV-side. This was further confirmed by our modeling results of LV-side zero-load elastic modulus ($M_0$), which tended to be larger than that of the RV-side. Given that two septal sides have different strains and different degrees of anisotropy, it is reasonable to anticipate different elastic resistances in different axes or septum sides, which results in varied impacts on the LV and RV diastolic functions. Therefore, a further investigation of the relations of septum mechanics and ventricular function is needed.

### *4.4.4 Transmural differences between LV-side and RV-side of the septum*

We also compared the strain-dependent elastic moduli and modeling parameters of elasticity between the two sides of the septum. We did not observe any difference in the intrinsic mechanical property. We further examined the potential differences in myofibers and collagen fibers in the septum sides. There was no difference in the zero-load elastic modulus ($M_0$) predicted from the constitutive model, which suggests that the myofiber stiffness is comparable between the two sides. The examination of the collagen fraction also showed no significant difference between the two sides. Therefore, the main transmural change in the septum is related to the orientation of the myofibers (anisotropy), not the material properties or tissue composition.

### *4.4.5 Limitations*

In this study, we sliced the septum into approximately two equal halves after cleaning the endocardial surfaces. To our knowledge, there is no anatomic mark to distinguish the LV- and RV-side of septum, although the two sides share distinct embryologic origins[19, 20]. The only data about these thicknesses is provided by Boettler et al.[11], which showed ~1 mm of thickness difference at diastole (with the LV-side to be thicker). But this difference is about the typical required resolution for medical ultrasound. Thus, due to a lack of clear data to guide the slicing, we tested the two layers with similar thickness. Such methodology may lead to under or overestimation of transmural differences of the septum. Another limitation is that the same long axis (apex-to-base) was defined as the longitudinal direction of the septum on both sides. But it is possible that the two sides may have different 'shortening' directions as we defined for the ventricular free wall (outflow tract direction). Future studies should investigate the *in vivo* shortening axis for each side of the septum. Finally, we assumed negligible shear deformation, but a certain level of shear deformation occurred (as shown in **Table 4.1**). Since it is impossible to completely rule out the shear deformation for anisotropic tissues in biaxial tests, a better characterization of the septum biomechanics should also involve the shear or triaxial test to fully measure the 3D mechanical behavior of the anisotropic tissue.

### *4.4.6 Conclusions*

In summary, this original study investigates the transmural variation of the *ex vivo* passive mechanical properties of the septum in healthy adult ovine. The septum sides were significantly softer than their corresponding ventricular free walls, and the collagen content was less than that of the ventricular walls. At low strains, there was similar anisotropic behavior between the two sides, but the degree of the anisotropy was stronger in the LV-side than the RV-side. At high strains, both sides were isotropic. Our results suggest that the septum should not be treated as a part of the LV or RV, and that the tissue presents distinct structure-function relationships from the ventricle free wall. The investigation of septum biomechanics will further disclose the biomechanical mechanism of ventricular function and dysfunction in heart failure progression.

# References

1. Inamdar AA, Inamdar AC. Heart failure: Diagnosis, management and utilization. *Journal of Clinical Medicine*. 2016;5:62
2. Flachskampf FA, Voigt JU. The interventricular septum is functionally bilayered: A fresh look at a well known structure. *Heart*. 2005;91:1260-1261
3. Damiano RJ, Jr., La Follette P, Jr., Cox JL, Lowe JE, Santamore WP. Significant left ventricular contribution to right ventricular systolic function. *Am J Physiol*. 1991;261:H1514-1524
4. Hoffman D, Sisto D, Frater RW, Nikolic SD. Left-to-right ventricular interaction with a noncontracting right ventricle. *J Thorac Cardiovasc Surg*. 1994;107:1496-1502
5. Sawatani S, Mandell G, Kusaba E, Schraut W, Cascade P, Wajszczuk WJ, et al. Ventricular performance following ablation and prosthetic replacement of right ventricular myocardium. *Transactions - American Society for Artificial Internal Organs*. 1974;20 B:629-636
6. Agarwal JB, Yamazaki H, Bodenheimer MM, Banka VS, Helfant RH. Effects of isolated interventricular septal ischemia on global and segmental function of the canine right and left ventricle. *Am Heart J*. 1981;102:654-658
7. Li KS, Santamore WP. Contribution of each wall to biventricular function. *Cardiovascular Research*. 1993;27:792-800
8. Buckberg G, Hoffman JI. Right ventricular architecture responsible for mechanical performance: Unifying role of ventricular septum. *J Thorac Cardiovasc Surg*. 2014;148:3166-3171 e3161-3164
9. Friedberg MK, Redington AN. Right versus left ventricular failure: Differences, similarities, and interactions. *Circulation*. 2014;129:1033-1044
10. Dwivedi A, Axel L. Abnormal motion patterns of the interventricular septum. *JACC Cardiovasc Imaging*. 2017;10:1281-1284
11. Boettler P, Claus P, Herbots L, McLaughlin M, D'Hooge J, Bijnens B, et al. New aspects of the ventricular septum and its function: An echocardiographic study. *Heart*. 2005;91:1343-1348
12. Holland MR, Gibson AA, Bauer AQ, Peterson LR, Schaffer JE, Bach RG, et al. Echocardiographic tissue characterization demonstrates differences in the left and right sides of the ventricular septum. *Ultrasound Med Biol*. 2010;36:1653-1661
13. Lindqvist P, Morner S, Karp K, Waldenstrom A. New aspects of septal function by using 1-dimensional strain and strain rate imaging. *J Am Soc Echocardiogr*. 2006;19:1345-1349
14. Novak VP, Yin FCP, Humphrey JD. Regional mechanical properties of passive myocardium. *J Biomech*. 1994;27:403-412
15. Sommer G, Schriefl AJ, Andrä M, Sacherer M, Viertler C, Wolinski H, et al. Biomechanical properties and microstructure of human ventricular myocardium. *Acta Biomaterialia*. 2015;24:172-192
16. Camacho P, Fan H, Liu Z, He J-Q. Large mammalian animal models of heart disease. *Journal of cardiovascular development and disease*. 2016;3:30

17. Silva KAS, Emter CA. Large animal models of heart failure: A translational bridge to clinical success. *JACC Basic Transl Sci*. 2020;5:840-856
18. Annabi MR, Kerndt CC, Makaryus AN. Embryology, atrioventricular septum. *Statpearls*. Treasure Island (FL); 2021.
19. Meilhac SM, Esner M, Kelly RG, Nicolas JF, Buckingham ME. The clonal origin of myocardial cells in different regions of the embryonic mouse heart. *Dev Cell*. 2004;6:685-698
20. Tan CMJ, Lewandowski AJ. The transitional heart: From early embryonic and fetal development to neonatal life. *Fetal Diagn Ther*. 2020;47:373-386
21. Hill MR, Simon MA, Valdez-Jasso D, Zhang W, Champion HC, Sacks MS. Structural and mechanical adaptations of right ventricle free wall myocardium to pressure overload. *Ann Biomed Eng*. 2014;42:2451-2465
22. Jang S, Vanderpool RR, Avazmohammadi R, Lapshin E, Bachman TN, Sacks M, et al. Biomechanical and hemodynamic measures of right ventricular diastolic function: Translating tissue biomechanics to clinical relevance. *Journal of the American Heart Association*. 2017;6
23. Lin DH, Yin FC. A multiaxial constitutive law for mammalian left ventricular myocardium in steady-state barium contracture or tetanus. *J Biomech Eng*. 1998;120:504-517
24. Kirton RS, Taberner AJ, Nielsen PM, Young AA, Loiselle DS. Effects of bdm, [ca2+]o, and temperature on the dynamic stiffness of quiescent cardiac trabeculae from rat. *Am J Physiol Heart Circ Physiol*. 2005;288:H1662-1667
25. Park JH, Choi JO, Park SW, Cho GY, Oh JK, Lee JH, et al. Normal references of right ventricular strain values by two-dimensional strain echocardiography according to the age and gender. *Int J Cardiovasc Imaging*. 2018;34:177-183
26. Lee J-H, Park J-H. Strain analysis of the right ventricle using two-dimensional echocardiography. *J Cardiovasc Imaging*. 2018;26:111-124
27. Liu W, Nguyen-Truong M, Ahern M, Labus KM, Puttlitz CM, Wang Z. Different passive viscoelastic properties between the left and right ventricles in healthy adult ovine. *J Biomech Eng*. 2021;143
28. Javani S, Gordon M, Azadani AN. Biomechanical properties and microstructure of heart chambers: A paired comparison study in an ovine model. *Annals of Biomedical Engineering*. 2016;44:3266-3283
29. Matsumoto T, Fukui T, Tanaka T, Ikuta N, Ohashi T, Kumagai K, et al. Biaxial tensile properties of thoracic aortic aneurysm tissues. *Journal of Biomechanical Science and Engineering*. 2009;4:518-529
30. Fratzl P. *Collagen : Structure and mechanics*. New York: Springer; 2008.
31. Nguyen-Truong M, Liu W, Boon J, Nelson B, Easley J, Monnet E, et al. Establishment of adult right ventricle failure in ovine using a graded, animal-specific pulmonary artery constriction model. *Animal Model Exp Med*. 2020;3:182-192
32. Lorenz CH, Walker ES, Graham TP, Powers TA. Right ventricular performance and mass by use of cine mri late after atrial repair of transposition of the great arteries. *Circulation*. 1995;92:233-239
33. Ostenfeld E, Stephensen SS, Steding-Ehrenborg K, Heiberg E, Arheden H, Rådegran G, et al. Regional contribution to ventricular stroke volume is affected on the left side, but not on the right in patients with pulmonary hypertension. *Int J Cardiovasc Imaging*. 2016;32:1243-1253

34. Stephensen S, Steding-Ehrenborg K, Munkhammar P, Heiberg E, Arheden H, Carlsson M. The relationship between longitudinal, lateral, and septal contribution to stroke volume in patients with pulmonary regurgitation and healthy volunteers. *American Journal of Physiology-Heart and Circulatory Physiology*. 2014;306:H895-H903
35. Holzapfel GA, Ogden RW. Constitutive modelling of passive myocardium: A structurally based framework for material characterization. *Philosophical Transactions of the Royal Society A*. 2009;367:3445-3475
36. Streeter Daniel D, Spotnitz Henry M, Patel Dali P, Ross J, Sonnenblick Edmund H. Fiber orientation in the canine left ventricle during diastole and systole. *Circulation Research*. 1969;24:339-347
37. Reese TG, Weisskoff RM, Smith RN, Rosen BR, Dinsmore RE, Wedeen VJ. Imaging myocardial fiber architecture in vivo with magnetic resonance. *Magn Reson Med*. 1995;34:786-791
38. Streeter Jr DD, Bassett DL. An engineering analysis of myocardial fiber orientation in pig's left ventricle in systole. *The Anatomical Record*. 1966;155:503-511
39. Shi X, Liu Y, Copeland KM, McMahan SR, Zhang S, Butler JR, et al. Epicardial prestrained confinement and residual stresses: A newly observed heart ventricle confinement interface. *J R Soc Interface*. 2019;16:20190028
40. Avazmohammadi R, Hill MR, Simon MA, Zhang W, Sacks MS. A novel constitutive model for passive right ventricular myocardium: Evidence for myofiber-collagen fiber mechanical coupling. *Biomech Model Mechanobiol*. 2017;16:561-581

# 5. *In Vivo* Ovine Model of RV Failure Progression[3]

## 5.1 Establishment of Adult Right Ventricle Failure in Ovine Using a Graded, Animal-Specific Pulmonary Artery Constriction Model

### 5.1.1 Introduction

Right ventricle failure (RVF) is associated with serious cardiac and pulmonary diseases that contribute significantly to the morbidity and mortality of patients.[1] The prevalence of RVF is significantly increased in the later stages of pulmonary hypertension (PH), congenital heart disease (CHD), and left heart failure with preserved ejection fraction (HFpEF).[2-4] Moreover, the mortality rate of these patients has not improved despite proposed therapeutic interventions.[3-6] The lack of effective treatment can be attributed to the incomplete understanding of the mechanisms of RVF and the lack of robust large animal models in adult RVF.[7-9]

Preclinical (animal) models are powerful tools to investigate various human diseases including RVF.[7] Compared to small animal models, large animal models better mimic human physiology and pathophysiology[10-13] and thus are advantageous in studying both the pathogenesis and potential therapeutics that are more translatable to human patients[14]. To date, various methods have been used to establish RV pressure overload, the most common etiology of RVF. These methodologies include pulmonary artery (PA) (**Table 5.1**) or pulmonary vein banding[13, 15], thromboembolic induction[11, 16, 17], chronic hypoxia[18], monocrotaline[19, 20], and the combination of sugen and chronic hypoxia[21-23]. However, some of these models are essentially the models of

---

[3] Adapted from Nguyen-Truong M, Liu W, Boon J, Nelson B, Easley J, Monnet E, Wang Z. Establishment of adult right ventricle failure in ovine using a graded, animal-specific pulmonary artery constriction model. *Animal Model Exp Med*. 2020 Jun 14;3(2):182-192. doi: 10.1002/ame2.12124.
Adapted from Liu W, Nguyen-Truong M, Labus K, Boon J, Easley J, et al. (2020) Correlations Between the Right Ventricular Passive Elasticity and Organ Function in Adult Ovine. *J Integr Cardiol*. 6. doi: 10.15761/JIC.1000294

pulmonary hypertension (PH), which mainly focus on the pulmonary vascular disease and do not necessarily involve the establishment of RVF. (Reviews of the PH models are cited here[24-27].)

Compared to other RV pressure overload models, the PA banding/constriction (PAB or PAC) model is a model of RV adaptation or dysfunction alone with no pulmonary vascular diseases. While this model has been critiqued less realistic than the other PH models, it is unique and advantageous since the changes in the RV are the sole effect of the hemodynamic insult, i.e., the pressure overload. Such a model provides us an opportunity to investigate the biomechanical mechanism of RV failure without other confounding factors such as altered systemic inflammation from pulmonary vascular diseases[28]. PAB/PAC has been used in different animal species and with a mix of ages (from newborn to young adult) for RV adaptation or RVF studies (**Table 5.1**). To our knowledge, the only large animal study of chronic, adult RVF was performed in canine in the early 1990s, while the clinical standard of RVF was absent at the time[29]. Moreover, both adult and non-adult large animals have been used in the literature, with mixed goals of studying pediatric or adult RV diseases, as well as using PAC as a treatment option or means to induce RV dysfunction. For instance, lambs were commonly used and the response of the RV was associated with congenital heart diseases (CHD)[30-34]. In adult ovine studies, it was the acute changes of the RV that were examined and the chronic remodeling and outcomes were not studied[10, 35]. Therefore, despite the 'apparently' widely used PAC model in large animals, to date, no chronic RVF has been established in adult ovine.

The goal of the present study is to adopt an animal-specific, graded pressure overload method to establish chronic RVF in adult ovine and to investigate the structural and functional changes with RVF development. Our hypothesis is that animal-specific, graded pulmonary artery constriction (PAC) will lead to chronic RVF in adult ovine. Sheep were chosen due to the widely reported similarities between human and ovine cardiovascular anatomy, function, and physiology[14, 16, 25]. Our data suggest that the revised PAC method led to RVF development in sheep and can serve as a large animal model of chronic, adult RVF.

**Table 5.1.** Review of prior small and large animal models of pulmonary arterial (PA) banding/constriction. All studies adopted the same degree of constriction (i.e., with a fixed diameter, area reduction, or pressure level) except for Leeuwenburgh et al.[30-32, 34], Ramos et al.[36], Gold et al.[37], Gaynor et al.[38], and Verbelen et al.[35], which used the same criteria as our study to elevate the RV pressure to the individual's systemic pressure.

| Study | Animal | Weight/Age | Method | Application | Mortality Rate (%) | Model Duration |
|---|---|---|---|---|---|---|
| **Heitmeier et al., 2019[39]** | Mice | 20-25 kg/12 weeks (adult) | Titanium clip around PA; reduce cross sectional area to about 66% of original area | Assess ubiquitin proteasome system in right heart hypertrophy; No RVF reported | N/A | 3 weeks |
| **Kuroha et al., 1991[40]** | Rat | 2-month, 7-month, and 18-month old (non-adult and adult) | Silk thread around PA; increase of RV pressure by 15 mmHg in each animal | Effect of age on RV hypertrophy due to RV pressure overload; No RVF reported | N/A | 3 weeks |
| **Schou et al., 2007[41]** | Rat | 150-200 g (adult) | Pulmonary trunk clip; compressed to outer diameter of 0.9 mm | Establish rat model of right sided heart failure and characterize systemic and cardiac changes | N/A | 17 weeks |
| **Bogaard et al., 2009[42]** | Rat | 200 g (adult) | PA silk thread constriction; tightened to outer diameter 18G needle | Investigate if pressure overload alone can explain RVF associated with pulmonary hypertension; No RVF reported with PA constriction | N/A | 6 weeks |
| **Hill et al., 2014[43]** | Rat | 8 weeks (adult) | PA surgical clip; uniform RV pressure of 45-50 mmHg | Structural and mechanical adaptations of RV free wall; No RVF reported | N/A | 3 weeks |
| **Hirata et al., 2015[44]** | Rat | 240-260 g (adult) | PA clip or suture ligation; tightened to the outer diameter of an 18G needle | Comparison of methods to constrict PA; signs of RVF indicated by fibrosis and reduced TAPSE but not CO | 22 | 8 weeks |
| **Jang et al., 2017[45]** | Rat | 8 weeks (adult) | PA surgical clip; RV maximum systolic pressure > 50 mmHg | RV biomechanical and hemodynamic changes under pressure overload; No RVF reported | N/A | 3 weeks |

| | | | | | | |
|---|---|---|---|---|---|---|
| **Wang et al., 2017[46]** | Rat | Neonatal | PA constriction with nylon; tightened to outer diameter of 30G needle | Study of pathophysiological remodeling of RV due to congenital heart disease with RV afterload | 25 | 7 days |
| **Chery et al., 2019[47]** | Rat | 200-225 g (adult) | PA suture over 18 G tube; PA band peak gradient of 25-60 mmHg | Human neonatal thymus stem cell therapy for RV; No RVF reported | 33 | 100 days |
| **Axelsen et al., 2019[48]** | Rat | 112±12 kg (non-adult) | Titanium clip; set to inner diameter of 0.7 mm | Assess treatment of pulmonary hypertension with 6-mercaptopurine | 5 | 7 weeks |
| **McKellar et al., 2015[49]** | Rabbit | 2.0-2.5 kg (non-adult) | Weekly PA banding with cuff; RV end systolic pressure > 25 mmHg | To establish chronic, reversible RVF model to study RVF progression and recovery; RVF indicated by RV pressure and morphology, septum position, and histology only | Exact rate unknown; several out of 15 died | 43±1.6 days banding or 16.6±3.3 days recovery post RVF |
| **Ramos et al., 2018[36]** | Rabbit | 3.00±0.23 kg (non-adult) | Adjustable PA banding with C-shaped ring; weekly inflations to achieve systemic pressures | Early and late cardiac remodeling due to RV pressure loading and therapy with endothelin-1 receptor blockers; No RVF reported | N/A | 3-6 weeks |
| **Gold et al., 2019[37]** | Rabbit | 3.00±0.23 kg (non-adult) | Adjustable PA banding device (C-shaped ring); weekly PAB inflations to achieve systemic RV pressures by day 21 | Relationship between RV wall stress, fibrosis, and function under RV pressure loading; No RVF reported | N/A | 3-6 weeks |
| **Hsieh et al., 1992[29]** | Dog | 18-23 kg (adult) | PA banding; increase of RVSP to 50 mmHg at the end of first month and then by 20 mmHg monthly increase, if necessary | RVF confirmed by fraction shortening decrease and RV dilation. Study the reversibility of right heart failure | 14 | 3 months PAB and additional 4 months recovery |
| **Gaynor et al., 2005[38]** | Dog | 20-25 kg (adult) | PA banding; Weekly 0.3 to 0.5 mL of saline injection (ΔRVP ~10-20 mmHg) to achieve near-systemic pressures | RA and RV hemodynamic adaptations to RV pressure overload; No RVF established | N/A | 3 months |
| **Barbera et al., 2000[33]** | Ovine | 121±1 day gestation | Inflation of vascular occluder around PA to increase RVSP by ~10-30 mmHg over first 3 days of pressure loading | Assessment of myocyte maturation due to pressure load in fetal ovine | N/A | 10 days |
| **Hon et al., 2001[50]** | Ovine | 3 months (non-adult) | PA ligation with band; PA systolic | Acute effects of overload on RV | N/A | 30 minutes |

|  |  |  |  |  |  |  |
|---|---|---|---|---|---|---|
|  |  |  | pressure > 60 mmHg | contractile function; No RVF reported |  |  |
| **Leeuwenburgh et al., 2001[32]** | Lamb | 2-3 weeks (non-adult) | PA constriction with an adjustable occluder for up to 12-week period; RVSP matched to systolic pressure | Evaluation of biventricular systolic function; No RVF reported | 23 | 64±8 days |
| **Leeuwenburgh et al., 2002[31]** | Lamb | 2-3 weeks (non-adult) | PA constriction with an adjustable occluder for up to 12-week period; RVSP matched to systolic pressure | Evaluation of biventricular diastolic function; No RVF reported | 23 | 64±8 days |
| **Leeuwenburgh et al., 2003[30]** | Lamb | 2-3 weeks (non-adult) | PA constriction with an adjustable occluder for up to 12-week period; RVSP elevated to systemic level | Test feasibility of a device for PA constriction as a treatment in children with congenital heart disease; No signs of heart failure | 23 | 64±8 days |
| **Leeuwenburgh et al., 2008[34]** | Lamb | 2-3 weeks (non-adult) | PA constriction with an adjustable occluder up to 12-week period; RVSP matched to systolic pressure | Evaluation of cellular and biochemical myocardial response; No RVF reported | 23 | 64±8 days |
| **Yerebakan et al., 2009[51]** | Ovine | 4 months (non-adult) | 3 mm Dacron band on pulmonary trunk; Elevation of RVSP to 50-60% above baseline | Acute and chronic response of RV to pressure and volume overload; No RVF reported | N/A | Immediately after PAB or 3 months |
| **Verbelen et al., 2015[35]** | Ovine | 10.5±0.8 months (adult) | PA constriction as much as was hemodynamically tolerated | Test ventricular assist device for pressure overloaded RV | N/A | 10 minutes |
| **Malinowski et al., 2018[10]** | Ovine | 50-60 kg (adult) | PA occluder; increase RV peak pressure to >150% of pre-occlusion value | To establish acute RVF model with functional tricuspid regurgitation; No RVF with PA banding alone | N/A | 15 minutes |
| **Gufler et al., 2019[52]** | Ovine | 25 weeks (adult) | PA banding; target maximal RVSP set to 50-60% above baseline | Adaptive response of RV to chronic pressure overload; No RVF reported | N/A | 3 months |
| **Corno et al., 2003[53]** | Porcine (mini-pig) | 18.2±0.1 weeks; 8.6± weeks (non-adult) | Adjustable PA band; perimeter range = 23-30 mm | Evaluation of FloWatch (implantable device for PA banding) as a treatment for congenital heart disease; No RVF reported | N/A | 24 weeks; 10 weeks |

### 5.1.2 Methods

#### *5.1.2.1 Animal-specific and graded pulmonary artery constriction (PAC) in ovine*

All procedures were approved by Colorado State University Institutional Animal Care and Use Committee. Prior to surgery, 8-month old male sheep (n=3) were placed under general anesthesia with 3.3-5 mg/kg ketamine and 0.1 mg/kg midazolam. During the surgical procedure, animals received 15 mcg/kg/min of ketamine and 35 mcg/kg/min of lidocaine. To induce RV pressure overload, an adjustable hydraulic occluder (AUS-PORT 12x14 mm, Norfolk Vet Products, IL) was placed around the main pulmonary artery and secured with two 2-0 polybutester sutures. Next, under pressure monitoring, saline was injected to the occluder acutely until the RV systolic pressure (RVSP) reached an equivalent number of its left ventricle (LV) systolic pressure as described previously[30-32, 34]. The amount of saline was recorded and the saline was withdrawn from the occluder to allow the animal to recover from the surgical procedure for two days. This minimized the 'surgical insult' to the RV and thus the response was mainly a result of hemodynamic overload induced via saline injections starting two days post-surgery. Besides the baseline measurements in the PAC sheep, age-matched, healthy intact sheep (n = 3) were used as additional controls (CTL).

Animal-specific, graded filling of the occluder with saline was induced in awake animals at weeks 0, 1 and 4 post surgery (**Fig. 5.1**). The amount of saline injections was determined by the procedure described above as well as the RV morphology and function from bi-weekly echocardiography. If we observed signs of heart failure (e.g., difficulty in breathing, anorexia, grinding teeth, etc.), continuous RV dilation and RV hypertrophy (e.g., increased RV area or RV wall thickness), or function decline (e.g., decreased flow velocity across the PA valve and decreased TAPSE), we reduced the injection volume or did not inject any saline further (**Table**

**5.2**). In a separate study, the chronic pressure overload was maintained for 20 weeks and thus different phases of RV failure were included in these PH ovine (n=3).

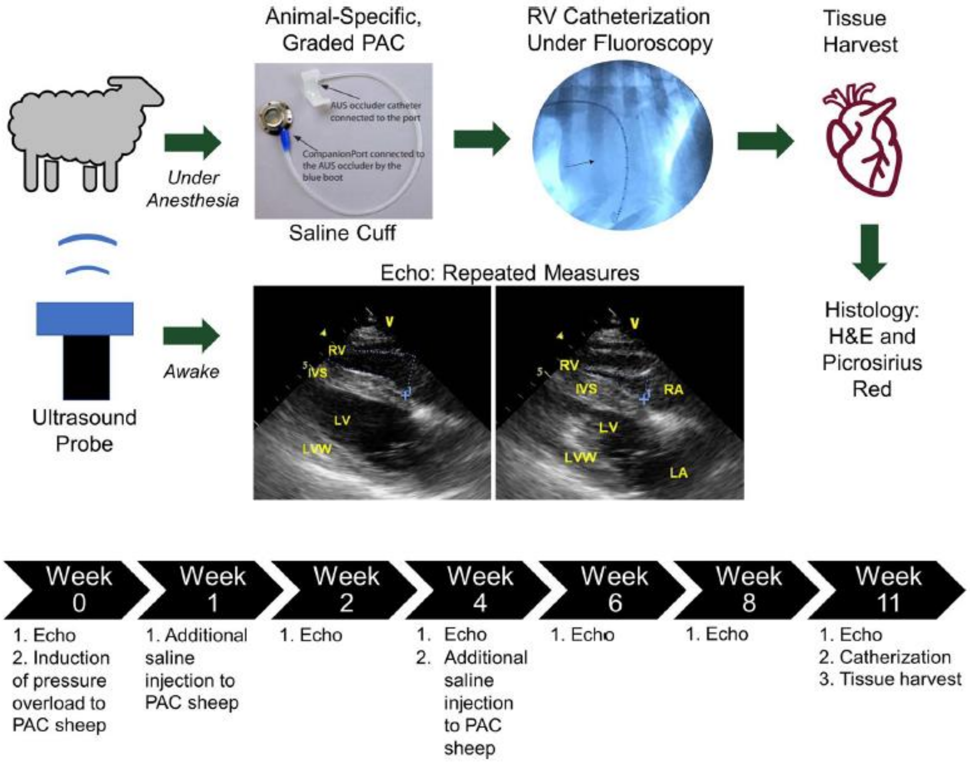

**Figure 5.1.** Visualized workflow of PAC sheep model and timeline of study. Saline cuff figure reproduced with permission from Norfolk Vet Prodcuts (https://norfolkvetproducts.com/wp-content/uploads/2019/03/NVP_Catalog_2019-01_email.pdf). Representative 4-chamber view images obtained by echocardiography (echo) are from a PAC sheep at week 2 (left: diastole; right: systole).

**Table 5.2**. Volumes of saline injections for the PAC animals at three time points over the 11-week study.

| | Week 0 | Week 1 | Week 4 | Total |
|---|---|---|---|---|
| **Sheep 1 Injection (mL)** | 0.4 | 0.4 | 0.1 | 0.9 |
| **Sheep 2 Injection (mL)** | 0.6 | 0.6 | 0 | 1.2 |
| **Sheep 3 Injection (mL)** | 0.2 | 0.4 | 0.1 | 0.7 |

#### *5.1.2.2 Echocardiography*

Transthoracic two-dimensional echocardiography was performed bi-weekly (weeks 0, 2, 4, 6, 8, 11) using a 2.5 MHz transducer on a GE Vivid 7 (GE Healthcare, Chicago, IL) ultrasound machine. Briefly, parasternal images were obtained in the awake sheep in lateral recumbency, using American Society of Echocardiography guidelines with minor imaging plane modifications in the sheep[54]. Ventricular dimensions (such as RV area, septum diameter, and RV or LV inner diameter; RVID/LVID), tricuspid annular plane systolic excursion (TAPSE) and flow dynamics were measured.

#### *5.1.2.3 Hemodynamic measurements and terminal procedure*

Prior to euthanasia, the CTL and PAC animals were anesthetized and RV catheterization was performed to obtain hemodynamic measurements. A 7 Fr Swan Ganz catheter (Edwards Lifesciences Corporation, Irvine, CA) was floated to the RV through the jugular vein and cranial vena cava under pressure monitoring and fluoroscopic guidance. Cardiac output (CO) and stroke volume (SV) were measured using the thermodilution method[11, 13]. Finally, the RV systolic pressure was obtained by a pressure-volume catheter (Millar, Houston, TX). Immediately following the hemodynamic measurements, the animals were euthanized with pentobarbital (IV) at 88 mg/kg and the hearts were harvested. RV tissue hypertrophy was measured by the wet weight, Fulton index (RV/(LV+Septum)), and wall thickness using a digital caliper.

#### *5.1.2.4 Structural measurements*

RV samples from the center of the anterior RV free wall were fixed in 10% formalin. Specimens were then dehydrated, embedded in paraffin, sectioned and stained with H&E for cardiomyocyte morphology and Picro Sirius Red for collagen fibers. Cardiomyocyte morphology was imaged by an inverted microscope (Motic AE31E) and quantified with AmScope software

(AmScope, Irvine, CA); collagen content and fiber orientation were imaged under polarized light by a transmission microscope (Nikon Eclipse E800) and quantified with Image Pro Premier software (Media Cybernetics, Rockville, MD). Color thresholding method was used to measure type I collagen, type III collagen and non-collagen areas, respectively[18, 55].

#### *5.1.2.5 Statistical and correlation analysis*

One-way ANOVA with repeated measures and Dunnett's post-hoc tests were performed by Prism (GraphPad Software, San Diego, CA) to examine the functional changes of the RV during the PAC. Unpaired Student's t-test was performed between the CTL and PAC groups in Excel (Microsoft). Pearson correlation analysis was used to investigate the correlations between the structural and functional properties. Data are presented as mean ± SD. $P<0.05$ was considered statistically significant and $0.05 \leq p < 0.1$ was considered a trend[56-58]. $r > 0.8$ was considered as a strong correlation.

### 5.1.3 Results

#### *5.1.3.1 Hemodynamic and functional changes in the RV with PAC*

Eleven weeks post PAC, there was a significant increase in RVSP compared to the CTL group and a gradual decrease of the ratio of pulmonary artery acceleration time/ejection time (PA AT/ET) over time, with a significant reduction at the endpoint (**Figs. 5.2A&B**, $p<0.05$). These results indicate the successful induction of pressure overload and establishment of RVF in the sheep. Moreover, there was a significant decrease in SV in the PAC group compared to the CTL group at 11 weeks (**Fig. 5.2C**, $p<0.05$). Lastly, we found that TAPSE was significantly decreased at week 11 compared to the baseline (**Fig. 5.2D**, $p<0.05$). These results indicate that pressure elevation was successful, and RVF was evident in these animals.

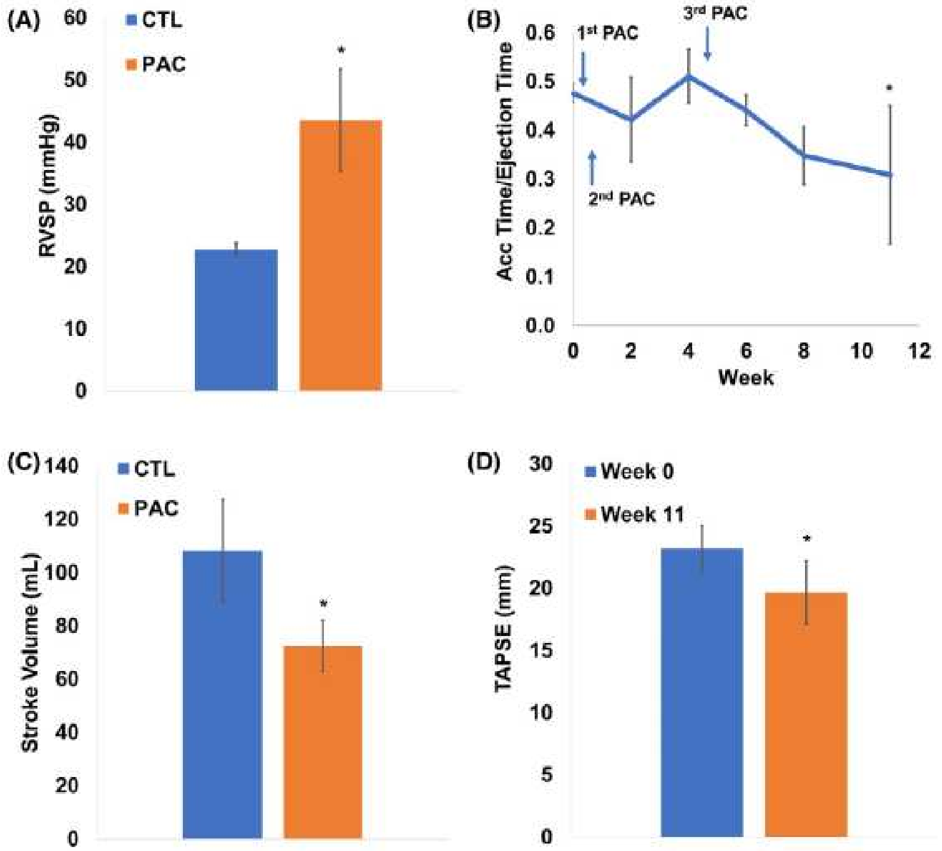

**Figure 5.2.** Decline in RV hemodynamics and function with 11-week PAC. A) Increase in RV systolic pressure. B) Decrease in pulmonary artery acceleration time/ejection time. C-D) Decrease in stroke volume and TAPSE in PAC sheep. $^{*}$ $\boldsymbol{P} < 0.05$ vs. CTL group or Week 0.

### *5.1.3.2 Morphological changes in the RV with PAC*

With the chronic pressure overload, there were significant increases in diastolic RV area and RVID as measured by echocardiography (**Fig. 5.3**), suggesting a progressive dilatation of the chamber. Some global changes of the hearts were examined after tissue harvest (**Table 5.3**). Both the RV weight/body weight (p<0.05) and wall thickness (p<0.05) were larger in the PAC group, and the Fulton index as a routine RV hypertrophy index was significantly increased as well (p<0.05).

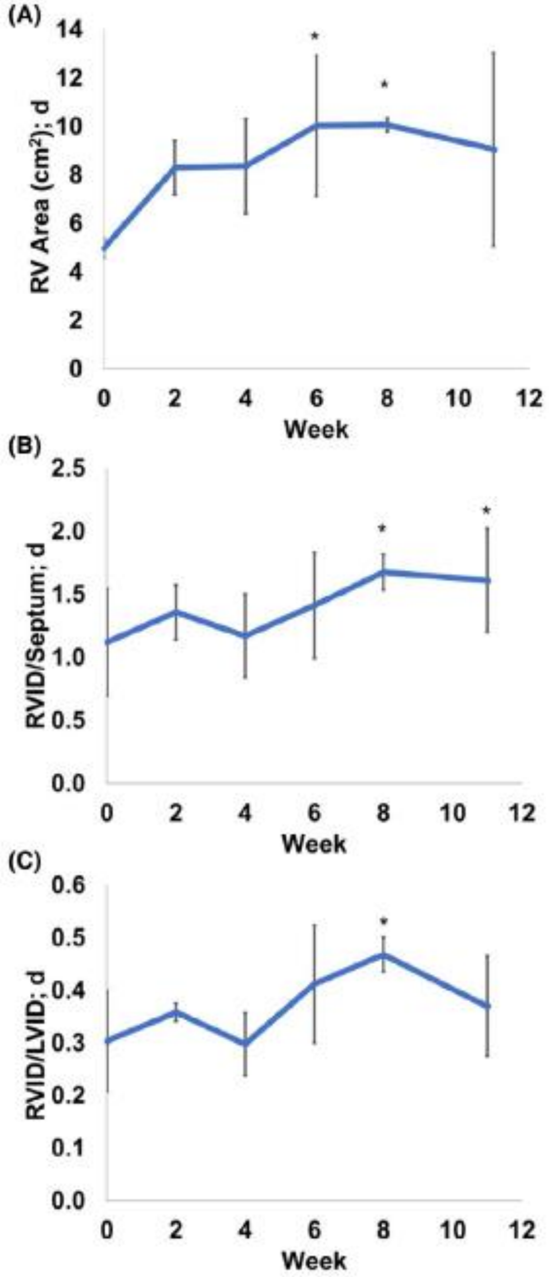

**Figure 5.3.** Temporal changes in diastolic geometry of the RVs over 11 weeks of pressure overload (PAC). PAC led to gradual increases in A) RV diastolic area, B) RV Inner Diameter/Septum diameter at diastole, and C) RV Inner Diameter/LV Inner Diameter at diastole. $^{*}P < 0.05$ vs. Week 0.

#### *5.1.3.3 Structural changes in the RV with PAC*

From the H&E staining, we quantified RV cardiomyocyte width and found that there was a significant increase in the cell width with PAC (**Table 5.3**, $p<0.05$). From the Picro Sirius Red staining, we examined RV collagen content and fiber orientation in the CTL and PAC groups using polarized microscope images. PAC tended to lead to more collagen accumulation ($p=0.065$), especially type III collagen accumulation in the RV (**Table 5.3**, $p=0.05$) (**Table 5.3**). There was no difference in collagen fiber orientation between the CTL and PAC groups (**Table 5.3**).

#### *5.1.3.4 Changes in RV geometry and hemodynamic function with PH development (11-20 weeks PAC)*

The results of the individual RV geometry and hemodynamic function of 11-20 weeks PAC were summarized in Table 5.4. There was a significant increase in RVSP and significant decreases in SV and CO in the PH group compared to the CTL group ($p<0.05$). PH also led to a trend of decrease in the AT ($p = 0.07$) and significant increases in the DT, ET, as well as the AT/ET ratio compared to the CTL group ($p<0.05$). Lastly, the RV became significantly hypertrophic with the PH development ($p<0.05$). These results indicate the successful induction of pressure overload of the RV and the establishment of RV failure in the PH animals.

**Table 5.3.** Overall structural changes in ovine hearts with PAC after 11 weeks. Data are presented as mean ± SD. *p<0.05; ξp = 0.05.

| | **CTL** | **PAC** |
|---|---|---|
| **Body Weight (kg)** | 81.6 ± 12.2 | 84.8 ± 4.5 |
| **RV Weight (g)** | 61.7 ± 10.9 | 84.1 ± 13.1 |
| **RV Weight/Body Weight (g/kg)** | 0.8 ± 0.0 | 1.0 ± 0.1* |
| **Fulton Index (%)** | 28.4 ± 1.3 | 43.0 ± 3.5* |
| **RV Wall Thickness (mm)** | 5.9 ± 0.2 | 7.4 ± 0.6* |
| **Myocyte Width (μm)** | 13.5 ± 1.2 | 17.1 ± 0.7* |
| **Collagen Fiber Angle (degrees)** | 54.0 ± 8.0 | 57.0 ± 12.0 |
| **Type I Collagen Content (%)** | 2.9 ± 1.0 | 4.3 ± 1.3 |
| **Type III Collagen Content (%)** | 0.7 ± 0.1 | 1.8 ± 0.7$^{\xi}$ |
| **Total Collagen Content (%)** | 3.6 ± 1.0 | 6.1 ± 1.4 |

**Table 5.4.** Individual hemodynamics, structure and function measurements of the ovine RV in CTL and PAC animals (weeks 11-20). CTL: control group, PH: pulmonary hypertension group. RVSP: right ventricle systolic pressure, SV: stroke volume, CO: cardiac output; TAPSE: tricuspid annular plane systolic excursion, FS: fraction shortening, AT: accelerate time and ET: ejection time. /: unable to obtain the data. *: p<0.05 vs CTL group.

| **Sample** | **RVSP (mmHg)** | **SV (mL)** | **CO (mL)** | **TAPSE (mm)** | **FS (%)** | **AT (msec)** | **ET (msec)** | **DT (msec)** | **AT/ET** | **Fulton Index (%)** |
|---|---|---|---|---|---|---|---|---|---|---|
| CTL1 | 22.7 | 96 | 9.2 | 19 | / | 94 | 231 | 137 | 0.41 | 28.8 |
| CTL2 | 23.8 | 99 | 13.3 | 21 | / | 73 | 160 | 87 | 0.46 | 29.5 |
| CTL3 | 21.7 | 130 | 11.6 | 28 | / | 68 | 198 | 130 | 0.34 | 27.0 |
| *Mean ± SEM* | *23± 1* | *108 ± 11* | *11 ± 1* | *23 ± 3* | */* | *78 ± 8* | *196 ± 21* | *118 ± 16* | *0.40 ± 0.03* | *28 ± 1* |
| PH1 | 35 | 69 | 6.5 | 17 | 32.7 | / | 321 | / | / | 43.9 |
| PH2 | 51 | 65 | 5.9 | 20 | 11.1 | 69 | 335 | 266 | 0.21 | 46.0 |
| PH3 | 45 | 83 | 9.4 | 22 | / | 59 | 237 | 178 | 0.25 | 39.2 |
| PH4 | 42 | 39 | 3.8 | 25 | 35.9 | 62 | 271 | 209 | 0.23 | 58.8 |
| PH5 | 28 | 56 | 5.6 | 22 | 11.9 | 67 | 360 | 293 | 0.19 | 58.2 |
| PH6 | 51 | 47 | 3.9 | 20 | 27.0 | 44 | 278 | 234 | 0.16 | 64.1 |
| *Mean ± SEM* | *42 ± 4*$^{*}$ | *60 ± 7*$^{*}$ | *6 ± 1*$^{*}$ | *21 ± 1* | *24 ± 5* | *60 ± 4* | *300 ± 19*$^{*}$ | *236 ± 20*$^{*}$ | *0.21 ± 0.02*$^{*}$ | *52 ± 4*$^{*}$ |

#### *5.1.3.5 Correlation analyses of the structure and function in the RV*

We first examined the relations of RV pressure (RVSP) and the structures. As shown in Figures 5.4A&B, we found a significant correlation between RVSP and the Fulton index ($p < 0.05$), which has been used to indicate RV hypertrophy at the tissue level[23]; there was also a trend of correlation between the RVSP and the width of cardiomyocytes. These correlations indicated that the degree of RV pressure overload was associated with RV hypertrophy at both cellular and tissue levels.

As we found that both Fulton index and width of the cardiomyocyte were correlated with the RVSP, we further investigated the relations between these two hypertrophy indices. It was not surprising to see that there was a significant correlation between the cardiomyocyte width and Fulton index in the RVs of the experimental groups, suggesting that the enlarged cardiomyocytes would contribute to increased RV mass ($p < 0.05$, **Fig. 5.4C**). Interestingly, we also found a strong correlation between type III collagen and Fulton index ($p = 0.05$, $r = 0.80$, **Fig. 5.4D**), and this relation was absent between the type I collagen and Fulton index (data not shown). These results indicated that RV fibrosis, especially the accumulation in type III collagen, was correlated with the RV hypertrophy. Next, we examined the relations between the RV hypertrophy or fibrosis and its function indices. As shown in Figures 5.4E&F, we found a significant correlation between the Fulton index (hypertrophy) and RV ejection time (ET) and a significant correlation between the Fulton index and the stroke volume, respectively ($p < 0.05$). Furthermore, we found a significant correlation between type III collagen content and ejection time and a trend of moderate correlation between type III collagen content and stroke volume (**Figs. 5.4G&H**). However, there were no correlations between type I collagen content and the RV function (data not shown).

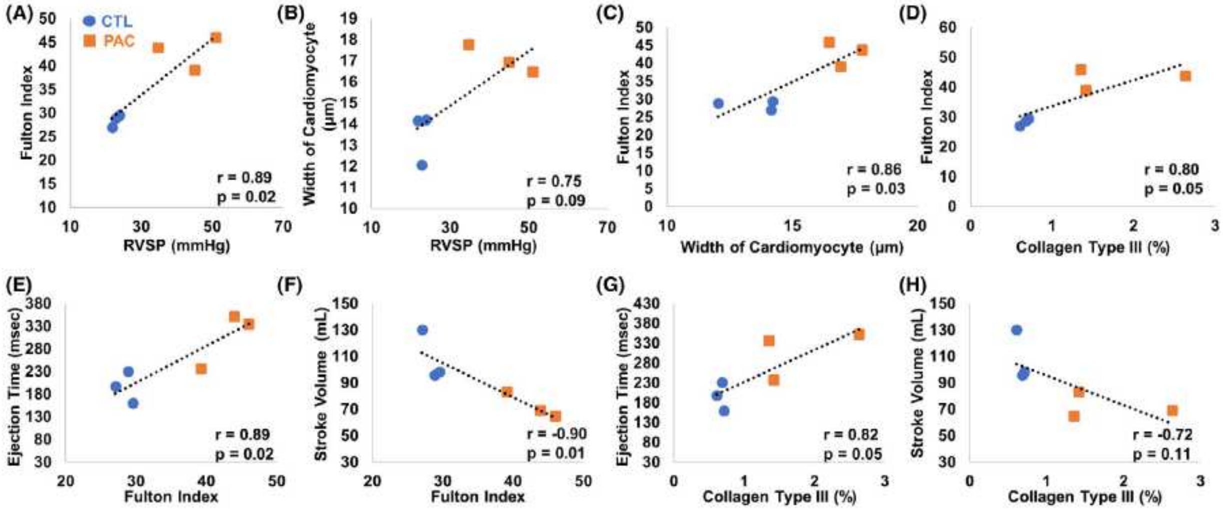

**Figure 5.4.** Correlations between the structure and function in the RVs of CTL and PAC groups. A - B) correlations between the RVSP and Fulton index or width of the cardiomyocyte, respectively. C - D) correlations between the width of the cardiomyocyte or the type III collagen content and Fulton index, respectively. E - F) Correlations between the Fulton index and ejection time or stroke volume, respectively. G - H) Correlations between the collagen type III content and ejection time or stroke volume, respectively.

### *5.1.3.5 Correlation analyses of between echocardiography and Swan-Ganz catheter*

As any clinical diagnosis is preferred to be noninvasive, we sought to find correlations between the non-invasive and invasive measures. The idea would be to use these non-invasive measures to help be predictive of preclinical or clinical trends and outcomes that could traditionally only be measured invasively.

We have observed several interesting correlations between non-invasive echocardiography and invasive Swan-Ganz catheterization. RVSP and AT/ET showed significant correlation (**Fig. 5.5A**, $p<0.05$), suggesting that AT/ET was impaired due to the significant pressure overload. Cardiac output and stroke volume were positively correlated with PV velocity, suggesting that larger cardiac output/stroke volume is associated with higher velocity across the pulmonary valve (**Figs. 5.5B-D**, $p<0.05$). Cardiac output was also significantly positively correlated with PV flow pressure gradient (**Figs. 5.5E-F**, $p<0.05$), suggesting the pressure gradient is larger when cardiac output is larger.

Other trends of correlations included a correlation between echocardiography and Swan-Ganz catheterization for cardiac output (**Fig. 5.6A**, $p=0.069$), as well as AT/ET and fraction shortening with PV peak velocity (**Figs. 5.6B&C**, $p=0.64$ and $p=0.05$ respectively).

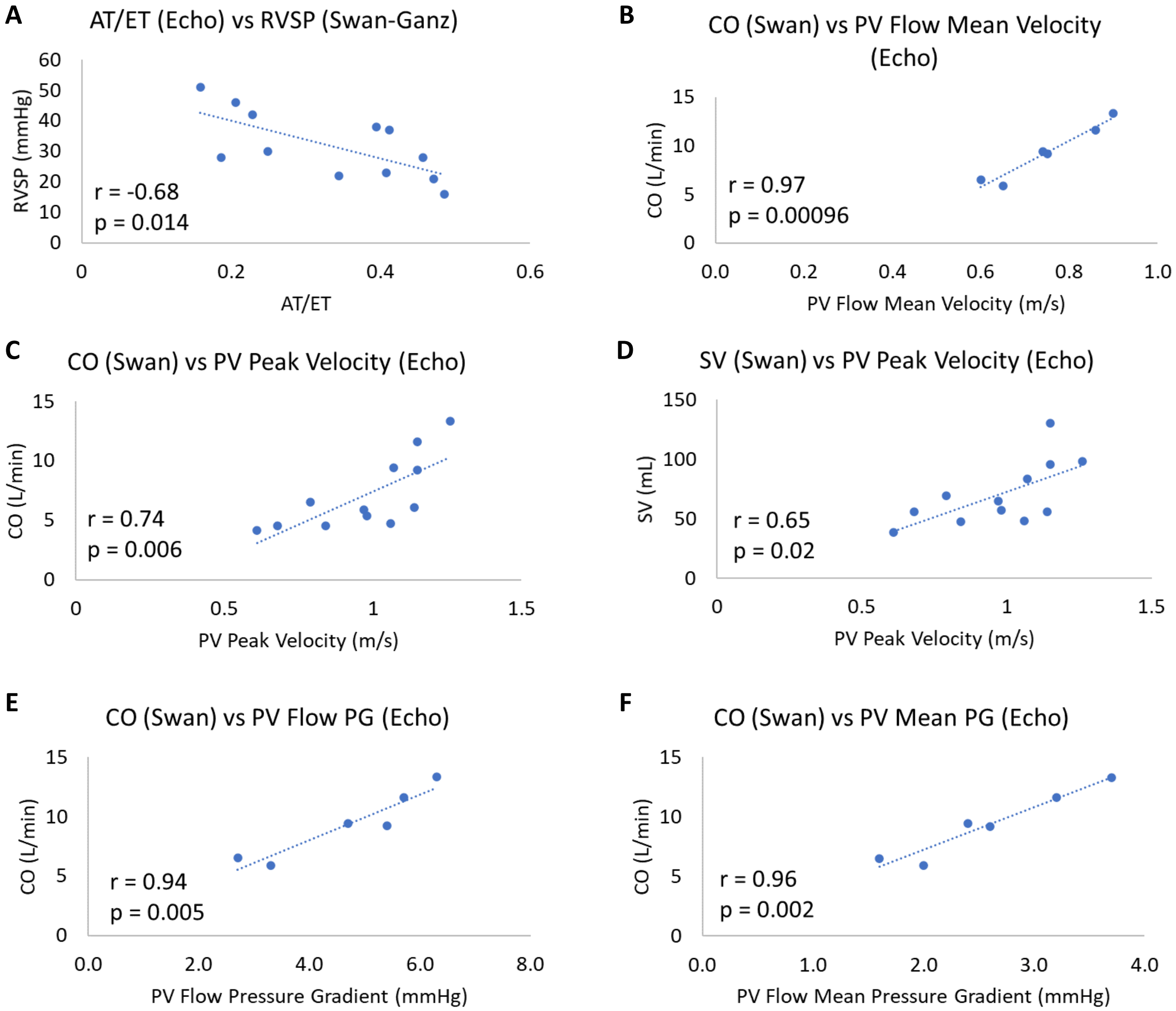

**Figure 5.5**. Correlations between echocardiography and Swan-Ganz catheterization measurements: A) acceleration time/ejection time and RV systolic pressure; B) cardiac output and pulmonary valve flow mean velocity; C) cardiac output and pulmonary peak velocity; D) stroke volume and pulmonary valve peak velocity; E) cardiac output and pulmonary valve flow pressure gradient; F) cardiac output and pulmonary valve mean pulmonary gradient.

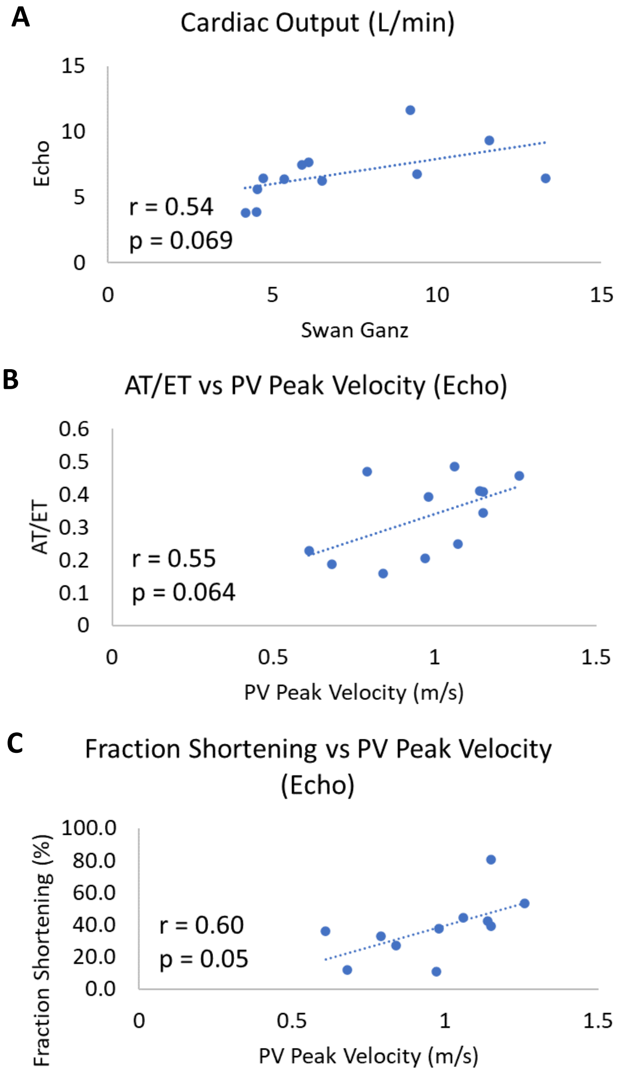

**Figure 5.6**. Correlations of A) cardiac output between echocardiography and Swan-Ganz catheterization measurements; B) acceleration time/ejection and pulmonary valve peak velocity from echocardiography; C) fraction shortening and pulmonary valve peak velocity from echocardiography.

### 5.1.4 Discussion

In this study, we described a revised PAC ovine model of adult RVF secondary to pressure overload. This model allowed for a customizable constriction between individual animals and at multiple time points. RV hypertrophy and fibrosis were evident in the pressure overloaded sheep. Surprisingly, the increase in type III collagen was more pronounced than the increase in type I collagen. Functionally, RV pressure elevation resulted in declines in RV SV and TAPSE, and progression of chamber dilation and ejection dysfunction, indicating RVF development. The degree of RV hypertrophy and the amount of type III collagen were correlated with the function of the RV.

#### *5.1.4.1 The revised PAC ovine model of adult RV failure*

To date, this study is the first report of an ovine model of adult, chronic RVF. Historically, lambs have been used in the study of RV dysfunction or therapeutics in pediatric patients (**Table 5.1**). Since ovine reach sexual maturity at 6-8 months old[59], we explored the potential of RVF establishment in young adults. From the prior literature, it can be found that not all PAC surgeries induced RVF (**Table 5.1**). If the PAC induction is too mild, RV adaptation rather than RVF will occur; on the other hand, if the PAC induction is too severe, animal deaths often occur prior to data collection. In the present study, we adopted the same criteria as used previously[30-32, 34] to induce a similar degree of hemodynamic insult in these sheep and then examined the remodeling of the RVs. As a result, different (customized) degrees of PAC were induced (**Table 5.2**) to ensure that the proper degree of pressure overload was achieved for RVF establishment in different individuals. Therefore, even with a small number of animals (n = 3 per group), we were able to confirm significant structural changes (i.e., RV hypertrophy and fibrosis) and functional changes (i.e., reduction in systolic function and ejection hemodynamics) in the RVs, from which RVF was evident. This pilot study had 0% of mortality in the PAC animals, which was rare in the similarly reported studies since the model is known for its drawbacks in surgical mortality, especially when the goal is to induce RVF[44]. Furthermore, while prior pre-clinical studies examined the development of RVF by either structural or functional changes of the RV, our study examined both aspects comprehensively to fully validate the establishment of RVF in adult sheep.

There are some advantages of the animal-specific, graded PAC methodology. First, this method allows for a PA constriction that results in identical hemodynamic insult between animals. As shown in **Table 5.1**, many preclinical studies used a fixed degree of constriction (i.e., increase to certain pressure value, reduce to certain PA diameter, etc.) to induce pressure overload. However, each animal responds uniquely to PAC and thus a fixed constriction may lead to varied degrees of RV dysfunction (from adaptation to failure), which may complicate the assessment and diagnoses of RVF among animals. In addition, various degrees of constriction were reported (see **Table 5.1**) and there is a lack of guidance on the induction of PAC. Since RV pressure equivalent to systemic pressure has been reported in clinical and preclinical studies of RVF[60, 61], we decided to use this hemodynamic condition as the criterion of PAC in our model. Indeed, from our own data it can be seen that each animal had its own amount of saline injection to elevate the RV pressure to systemic pressure, suggesting that different thresholds are required to induce RVF in individual animals. The animal-specific and graded approach also avoids potential unexpected animal death due to a single, severe constriction as we can progressively increase or halt the insult depending on the animal's individual response.

Second, the use of an adjustable PAC method provides more flexibility in the degree of PA constriction in large animals that is impossible in rodent PAC models. In a rabbit study with a similar PAC method, reversible constriction was induced to investigate the progression and recovery of RVF. This proof of concept study has shown the regression of RV chamber size, hypertrophy and fibrosis by the removal of pressure elevation, which may support the postulate that RVF is reversible[62]. Similarly, the graded or reversible PAC could be induced in large animals such as in this ovine model to further investigate the pathogenesis of RVF, including the development from adaptive to maladaptive RV remodeling. Therefore, the model is very flexible and can be adapted to investigate different questions regarding RVF.

#### *5.1.4.2 New insights of RV failure from the study*

In addition to the clearly adverse functional changes, we have observed morphological and structural changes of the RVs in the PAC group that are characteristic of RVF[10, 11, 13]. Firstly, RV dilatation and hypertrophy were evident and the RVID/LVID was gradually increased during the progression of RVF (**Fig. 5.3C**). In a recent study, the ratio of end-diastolic volumes (EDVs) of the RV to LV (RVEDV/LVEDV) was found to increase with increased RV free wall stiffness in PH patients, and this new index was strongly and inversely correlated with RV peak contractility[63]. Thus, we speculate that the increased RVID/LVID may indicate a gradual reduction in RV contractility and explain the impaired systolic function (SV) observed in the PAC sheep.

Moreover, RV fibrosis was revealed in the PAC sheep (**Table 5.3**). This is not surprising because collagen deposition is universally reported in clinical and preclinical studies, large and small animals, as well as from early to late stage of RVF[13, 23, 44, 64]. However, it was the collagen type III, not type I, that was more markedly increased in the PAC RVs. This is unexpected because type I collagen is the major isoform of collagen fibers in the RV[65, 66], and provides more mechanical strength than type III collagen[67]. We do not know why RVF led to a more significant increase in type III collagen, which will be examined in future investigations. Even in LVs, there is no consensus on whether type I or type III collagen plays a more significant role in its pathogenesis[55, 68]. Future studies should also delineate the role of different subtypes of collagen in RVF.

Finally, we found some interesting correlations among the healthy and failing RVs. RV hypertrophy and fibrosis were strongly correlated with RV function (**Figs. 5.4F&H**). This indicated that the severity of RV hypertrophy or fibrosis were linearly linked to the adaptation of the RV and could be used as diagnostic parameters indicative of RVF. Indeed, both ventricular mass and collagen deposition have been used in preclinical and clinical settings and were found to correlate with the severity of ventricular dysfunction[69, 70]. These data also confirm that our ovine model recapitulates the behavior and pathogenesis of human RVF. Furthermore, the amount of type III collagen was strongly correlated to the Fulton index (**Fig. 5.4D**), indicating that certain molecular mechanisms in type III collagen metabolism are linked with RV hypertrophy. To date, the proof of a mechanistic link between fibrosis and RV dysfunction is insufficient[64, 71]. Despite the evidence that increased collagen accumulation is found in severe RVF, the treatment that reversed the collagen deposition in the RV failed to improve the RV function[71, 72]. Here, we observed that type III collagen content was strongly correlated with ejection time and SV (**Figs. 5.4G&H**). We suspect that the different roles of type I and type III collagen in RV dysfunction may explain the discrepancy in the literature.

#### *5.1.4.3 Agreements and other correlations of non-invasive and invasive measurements of RV function assessment*

The correlations between invasive and non-invasive may offer alternative load-independent and load-dependent ventricular measurement methods over traditional invasive measurements. AT/ET significantly correlated with RVSP suggests that reduction in AT/ET may be predictive of pressure overload to the RV (**Fig. 5.5A**). AT/ET then could serve as a noninvasive way to estimate RVSP, which is obtained invasively in order to be accurate. This would be due to a higher pressure in the RV in response to the afterload which would cause flow to accelerate faster than normal, resulting in the leftward shift of the maximum velocity and shorter AT, as well as sometimes longer ET (but not always). Cardiac output with PV velocity indicates that a larger flow is correlated with larger velocity, which is intuitive (**Figs. 5.5B-D**). Similar findings were observed in the PV flow pressure gradient (**Figs. 5.5E&F**). The correlations with cardiac output from catheterization could be useful as flow velocities and pressure gradients could potentially be surrogates of ventricular function, basically the ability of the ventricle to produce adequate blood flow. And while it is known that cardiac output can be obtained from echo, that cardiac output is estimated from velocity via the velocity time integral. With significant correlations as observed, then these findings suggest that PV velocities obtained non-invasively could be used to validate cardiac output measurements from echo and predict trends in cardiac output from traditional invasive catheterization methods. The non-invasive measures can also be used to predict pressure elevation to the RV, which requires invasive techniques and cannot be measured directly (typically estimated using a simplified Bernoulli's equation from flow velocity). Overall, our pressure and velocity measurements correlated with cardiac output and AT/ET suggest an increase in afterload on the RV, but it is unclear if these are indicative of ventricular function, and the echo measures should be validated against standard measures of function obtained via pressure-volume catheterization (not Swan-Ganz).

Other studies have attempted to correlate non-invasive imaging with invasive measurements but have performed correlations with parameters obtained from pressure-volume catheterization. A study in mice by Boehm et al. showed TAPSE, an indicator of systolic RV function, has been shown to have trends in interrelations with Ees and significantly strong correlations with Ees/Ea, end systolic elastance to arterial elastance. Isovolumic relaxation time to ECG derived R-R interval and E/E', transtricuspidal E peak velocity measured by pulsed wave Doppler to tissue doppler derived E' peak velocity, were shown to be well correlated with RV diastolic pressure[73]. Together, these data suggest that indices of systolic RV function are better correlated with RV-arterial coupling and that diastolic indices correlated with end diastolic pressure.

In pulmonary hypertension pigs, it was shown that non-invasive RV functional measurements strongly correlated with ventricular-arterial coupling when compared to that of ventricular contractility[74]. These findings suggest that non-invasive indices for RV function will correlate better with ventricular-arterial coupling than contractility.

Tello et al. showed that cardiac magnetic resonance imaging (cMRI) of RV strain was associated with RV-arterial uncoupling and RV end diastolic stiffness in patients[75]. This study was able to use pressure volume catheterization and correlate the data with measurements from cMRI, the gold standard for imaging RV function. Ideally, with pressure-volume catheterization in our studies, such non-invasive measurements from echo could be used to correlate with key functional parameters such as RV diastolic stiffness (Eed), end-systolic elastance (Ees), arterial elastance (Ea), and Ees/Ea to determine RV-arterial coupling. Substitutes of these variables obtained invasively from expensive and demanding procedures would be clinically beneficial.

Ideally, such non-invasive indices using pressure-volume catheterization (instead of only Swan-Ganz catheterization) could be used to help determine ventricular contractility (determined invasively), an important parameter reflecting the intrinsic ability of the ventricle. In the same vein, our correlations can be used with pressure-volume catheterization to further identify if such parameters are correlated with ventricular function. Additional data from pressure-volume catheterization can be found in the Appendix, for which the parameters could potentially be used for validation of non-invasive clinical diagnoses of RV function (**Figs. A1-A3**, **Tables A3-A5**).

#### *5.1.4.4 Limitations*

There are a few limitations to this study. Firstly, we did not have 3D measurements of the RV volume or strain, which are useful indices of RVF[11, 13, 76]. Cardiac magnetic resonance imaging or pressure-volume relations are the gold standard and should be used to investigate adult ovine RVF in the future[61, 77]. Secondly, even though we observed significant functional impairment, other clinical signs such as peripheral edema or body weight loss were absent[3, 13]. These signs are typically seen in the late stage of RVF and the RVF observed in this study may be in an early rather than a late stage.

#### *5.1.4.5 Conclusions*

In this study, we reported a revised animal-specific, graded pulmonary artery constriction model in adult ovine. The model led to successful right ventricle failure development with significant structural and functional changes as well as some correlations between right ventricle hypertrophy or fibrosis and functional decline. The model is robust and safe to induce various degrees of pressure overload and at multiple time points, which enables the flexibility to adapt to different protocols to answer various research questions related to the progression or treatment of right ventricle failure.

## 5.2. Failing RV Free Wall Biomechanics

### 5.2.1 Introduction

The biomechanical changes of the failing RV in response to pressure overload has been seldom investigated. To our knowledge, only four prior studies have examined such changes, and all were performed in rats. Hill et al. showed that the myo- and collagen fibers became more aligned with pressure overload and that the overall tissue stiffness increased, with a much larger increase in the longitudinal direction (outflow tract) compared to the circumferential (perpendicular to outflow tract) direction[43]. Later, Jang et al. showed a significant increase in stiffness in the longitudinal direction at low strain compared to control animals[45]. No significant differences were found at high strain. Velez-Rendon et al. showed that pressure overload led to significantly larger longitudinal and circumferential stresses, but after decellularization (with ECM remaining) only the circumferential stress was significantly larger[78]. Recently, Kia et al. showed that myofiber, longitudinal, and circumferential stiffness were all significantly increased with pressure overload[79]. Together, these studies reported the biomechanical changes likely resulting from RV remodeling, especially with significant stiffening in the longitudinal direction. These unique findings in small animals compel us to determine if such results appear in a large animal model that is more closely related to humans, with which there is no report of to date. Thus, there currently exists a knowledge gap of large animal RV biomechanics, and especially in the context of RV adaptation and failure to pressure overload.

The goal of the present study is to adopt an animal-specific, graded pressure overload method to establish chronic RVF in adult ovine and to investigate the biomechanical changes with RVF development. We hypothesize that the adult pressure overloaded RV will stiffen in the longitudinal direction. Ovine were chosen due to the widely reported similarities between human and ovine cardiovascular anatomy, function, and physiology[14, 16, 25]. Our data suggest that the RVF development in sheep led to biomechanical changes in the RV with significantly increased stiffness in the longitudinal direction and larger degree of anisotropy compared to control animals.

### 5.2.2 Methods

#### *5.2.2.1 Ovine model of pulmonary hypertension and RV failure development*

All animal works were approved by the Colorado State University Institutional Animal Care and Use Committee (IACUC#17-7590A). Six pulmonary hypertension (PH) sheep and three age-matched health sheep were recruited in this study. Sheep was chosen for this study because its anatomy and physiology are closer to human than those of small animals and thus the findings are more translatable to human physiology and cardiac biomechanics[25]. PH was induced in eight-month old male and female ovine using our recently established animal-specific, pulmonary artery constriction model[80]. Briefly, an adjustable hydraulic occluder (AUS-PORT 12x14 mm, Norfolk Vet Products, IL) was placed around the main pulmonary artery trunk to elevate the pulmonary pressure. The degree of constriction for each animal was determined by the amount of saline injected to elevate the RV systolic pressure comparable to that of the left ventricle (LV) in the same animal. The chronic pressure overload was maintained for 11-20 weeks and thus different phases of RV failure were included in these PH ovine.

#### *5.2.2.2 Ex vivo mechanical test and data analysis*

Within four hours of sacrifice, the RVs were dissected and immersed in a physiological saline solution (PBS) on ice. Because the RV free wall is relatively thin, almost the entire wall was used for mechanical tests, after the removal of epicardium layer and the trabeculae from the endocardium. To obtain the biaxial mechanical properties, the outflow tract (OT) direction of the RV was defined as the longitudinal direction in the test axis. A minimal sample aspect ratio of 3:1 (length: thickness) was used to approximate a plane-stress condition, and a cruciform section was cut to generate more homogenous strain distribution and minimize shear strains in the biaxial tests[81, 82]. A ruler and caliper were used to measure the tissue size and thickness, respectively.

The tissues then underwent equibiaxial tensile mechanical tests, either with a regular spray of PBS solution to keep the tissue moist in room air or with the bath of cardioplegic solution (CPS) and 30 mM of 2,3-butanedione monoxime (BDM) at 26 – 37°C. Our supplement experimental data confirmed that there were not significant changes of the stress-strain curves between these testing conditions (**Fig. 5.7**). Graphite powder (AGS, MI) was used for strain characterization via digital image correlation. During the test, images were taken with a digital camera (Nikon) at 1 fps. A MATLAB-based digital imagine correlation program was used to analyze the tissue deformation. Two 250 lb capacity load cells (Honeywell Sensotec, Columbus, OH) were used to obtain the forces. A custom LabVIEW code was used to control the actuators and record the data[82].

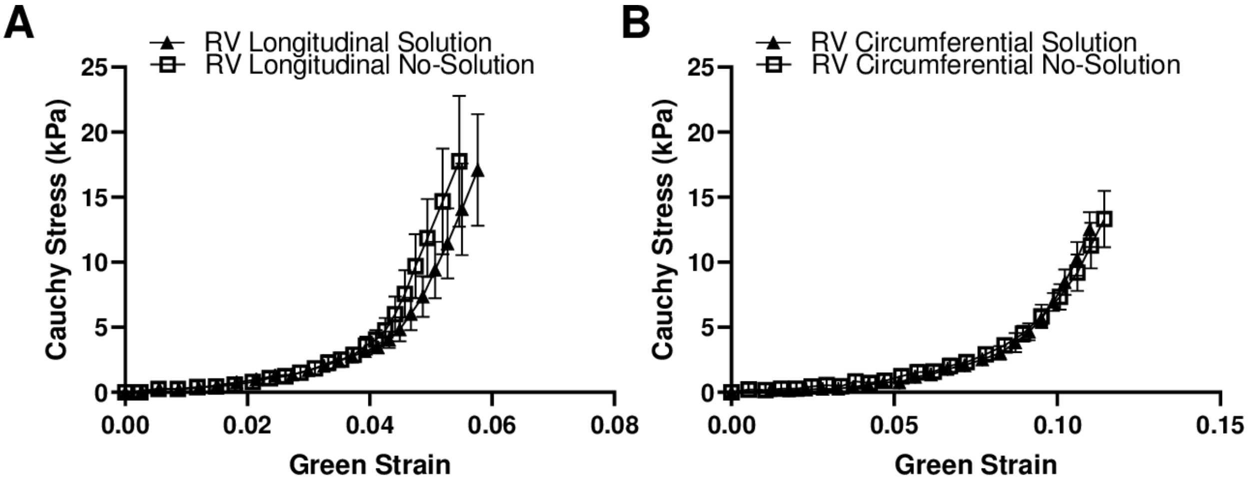

**Figure 5.7.** Comparison of the average stress-stain curves obtained from different testing conditions. (A-B) stress-strain curves in the longitudinal and circumferential directions, respectively. N=3.

After mounting, a small preload (~0.1 N) was applied to define the zero-strain configuration, and then the tissue underwent 15 cycles equibiaxial tests including preconditioning cycles (at the stretch rate of 15 mm/min, with ~25% maximal stretch). Then the last cycle of the loading curve was used to generate the Cauchy stress – Green strain curve to analyze the RV mechanical properties as previously described[83]. We were unable to obtain complete mechanical data in one control and one PH sheep. From the stress-strain curves, the RV passive stiffness (or elasticity) was quantified by the elastic moduli (EM) at the low and high strain ranges, respectively[45].

#### *4.2.2.3 Statistical and correlation analyses*

All data were analyzed by the non-parametric statistical analysis, except for the EM which were confirmed with the normal distribution by the QQ plot (GraphPad (v8.0.2)). Pearson correlation analysis was used to investigate the correlations between the tissue mechanical properties and RV function indices (Microsoft Excel). All the data were presented as mean ± SEM. $P < 0.05$ was considered statistically significant.

### 5.2.3 Results

#### *5.2.3.1 Changes in RV geometry and hemodynamic function with PH development*

The results of the individual RV geometry and hemodynamic function were summarized in Table 5.4. There was a significant increase in RVSP and significant decreases in SV and CO in the PH group compared to the CTL group ($p<0.05$). PH also led to a trend of decrease in the AT ($p = 0.07$) and significant increases in the DT, ET, as well as the AT/ET ratio compared to the CTL group ($p<0.05$). Lastly, the RV became significantly hypertrophic with the PH development ($p<0.05$). These results indicate the successful induction of pressure overload of the RV and the establishment of RV failure in the PH animals.

#### *5.2.3.2 Changes in RV passive elasticity with PH development*

Figure 5.8 presented the RV passive, biaxial elasticity obtained from the control and PH ovine. Despite a relative small number of the control animals, we observed significant stiffening of the RV in the PH group: compared to the control RVs, the PH RVs had a larger EM at low strain range ($EM_{Low}$) in the longitudinal direction (**Fig. 5.8A**, $p<0.05$). A similar trend was observed for the EM at high strain range ($EM_{High}$) in the same direction, but the difference did not reach statistical significance (**Fig. 5.8B**). In contrast, the changes in these EM in the circumferential direction were absent with PH development.

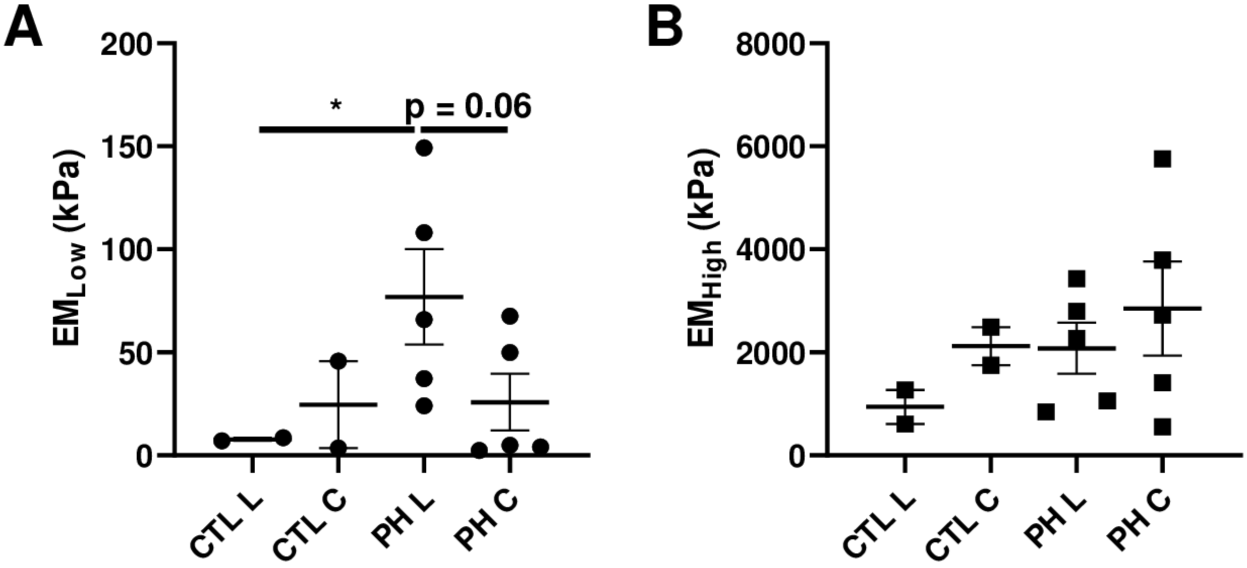

**Figure 5.8.** Different RV elasticities derived from the stress-strain curves. (A) the EM at low strain range ($EM_{Low}$) and (B) the EM at high strain range ($EM_{High}$) in both longitudinal (L) and circumferential (C) directions. CTL: control group, PH: pulmonary hypertension group. *: $p < 0.05$.

Furthermore, PH led to a strong trend of increased $EM_{Low}$ in the longitudinal direction compared to the circumferential direction (**Fig. 5.8A**, p=0.06). However, this was not observed in the control RVs. These results indicate an alteration of the anisotropic behavior at the low strain range with the progression of PH. We did not observe any anisotropic behavior from the high-strain EM in both PH and control groups.

### 5.2.4 Discussion

We observed a change in the anisotropic behavior of the RV during PH development (**Fig. 5.8**). The stiffening of the RV in the longitudinal direction and the absence of stiffening in the circumferential direction led to a more anisotropic behavior of the RV with the progression of PH. We speculate that the biaxial mechanical changes may partially explain the development of RV failure. Under persistent pressure overload, the RV typically remodels into a spherical shape and requires a higher wall strength in the circumferential direction to maintain the blood flow in the pulmonary circulation. Alternatively, a failure to enhance the circumferential wall strength will impair the ventricular function and result in RV failure.

In addition, the $EM_{Low}$ is a measurement in the diastolic stress range and thus it has been adopted as the diastolic stiffness of the RV[45, 84]. It is speculated that the $EM_{Low}$ is mainly contributed by the myofiber stiffness, which is different than the $EM_{High}$ that is measured in the high-strain range and contributed mostly by the collagen fiber stiffness[45, 85, 86].

It is unclear whether the same degree of RV failure was achieved in the present ovine study as in the previous rodent studies[43, 45, 78, 79]. While these studies had the banding or constriction for three weeks, only Kia et al. claimed to have achieved RV failure through the uncoupling of RV-PA function from Ees/Ea. While there is a lack of consensus on what RV failure is[4], we defined it as significantly reduced stroke volume and TAPSE. However, we have various durations of PAC in the PH sheep, which may include different stages of RV failure in the animals. Between our study and others, the stage of RV failure likely makes a difference in the *ex vivo* biomechanical behavior we would observe. Compensated hypertrophy, where the heart muscle wall thickens to normalize wall stress, precedes decompensated heart failure, where the heart muscle wall cannot match the increased afterload and leads to ischemia. These different stages would likely differ where decompensated heart failure would have the stiffest tissue with increasing collagen deposition[80, 87].

# References

1. Haddad F, Hunt SA, Rosenthal DN, Murphy DJ. Right ventricular function in cardiovascular disease, part i: Anatomy, physiology, aging, and functional assessment of the right ventricle. *Circulation*. 2008;117:1436-1448
2. Kohler D, Arnold R, Loukanov T, Gorenflo M. Right ventricular failure and pathobiology in patients with congenital heart disease - implications for long-term follow-up. *Front Pediatr*. 2013;1:37
3. Konstam MA, Kiernan MS, Bernstein D, Bozkurt B, Jacob M, Kapur NK, et al. Evaluation and management of right-sided heart failure a scientific statement from the american heart association. *Circulation*. 2018;137:E578-E622
4. Lahm T, Douglas IS, Archer SL, Bogaard HJ, Chesler NC, Haddad F, et al. Assessment of right ventricular function in the research setting: Knowledge gaps and pathways forward. An official american thoracic society research statement. *Am J Respir Crit Care Med*. 2018;198:e15-e43
5. Gorter TM, van Veldhuisen DJ, Bauersachs J, Borlaug BA, Celutkiene J, Coats AJS, et al. Right heart dysfunction and failure in heart failure with preserved ejection fraction: Mechanisms and management. Position statement on behalf of the heart failure association of the european society of cardiology. *Eur J Heart Fail*. 2018;20:16-37
6. Raina A, Meeran T. Right ventricular dysfunction and its contribution to morbidity and mortality in left ventricular heart failure. *Curr Heart Fail Rep*. 2018;15:94-105
7. Borgdorff MAJ, Dickinson MG, Berger RMF, Bartelds B. Right ventricular failure due to chronic pressure load: What have we learned in animal models since the nih working group statement? *Heart Failure Reviews*. 2015;20:475-491
8. Voelkel NF, Bogaard HJ, Gomez-Arroyo J. The need to recognize the pulmonary circulation and the right ventricle as an integrated functional unit: Facts and hypotheses (2013 grover conference series). *Pulm Circ*. 2015;5:81-89
9. Vonk Noordegraaf A, Galie N. The role of the right ventricle in pulmonary arterial hypertension. *Eur Respir Rev*. 2011;20:243-253
10. Malinowski M, Proudfoot AG, Eberhart L, Schubert H, Wodarek J, Langholz D, et al. Large animal model of acute right ventricular failure with functional tricuspid regurgitation. *International Journal of Cardiology*. 2018;264:124-129
11. Mulchrone A, Kellihan HB, Forouzan O, Hacker TA, Bates ML, Francois CJ, et al. A large animal model of right ventricular failure due to chronic thromboembolic pulmonary hypertension: A focus on function. *Frontiers in Cardiovascular Medicine*. 2019;5
12. Knai K, Skjaervold NK. A pig model of acute right ventricular afterload increase by hypoxic pulmonary vasoconstriction. *BMC Research Notes*. 2017;10:2
13. Aguero J, Ishikawa K, Hadri L, Santos-Gallego C, Fish K, Hammoudi N, et al. Characterization of right ventricular remodeling and failure in a chronic pulmonary hypertension model. *American Journal of Physiology-Heart and Circulatory Physiology*. 2014;307:H1204-H1215
14. Dixon JA, Spinale FG. Large animal models of heart failure: A critical link in the translation of basic science to clinical practice. *Circulation. Heart failure*. 2009;2:262-271

15. Aguero J, Ishikawa K, Hadri L, Santos-Gallego CG, Fish KM, Kohlbrenner E, et al. Intratracheal gene delivery of serca2a ameliorates chronic post-capillary pulmonary hypertension: A large animal model. *J Am Coll Cardiol*. 2016;67:2032-2046
16. Sato H, Hall CM, Griffith GW, Johnson KF, McGillicuddy JW, Bartlett RH, et al. Large animal model of chronic pulmonary hypertension. *ASAIO J*. 2008;54:396-400
17. Boulate D, Arthur Ataam J, Connolly AJ, Giraldeau G, Amsallem M, Decante B, et al. Early development of right ventricular ischemic lesions in a novel large animal model of acute right heart failure in chronic thromboembolic pulmonary hypertension. *J Card Fail*. 2017;23:876-886
18. Wang Z, Schreier DA, Abid H, Hacker TA, Chesler NC. Pulmonary vascular collagen content, not cross-linking, contributes to right ventricular pulsatile afterload and overload in early pulmonary hypertension. *Journal of Applied Physiology*. 2016;122:253-263
19. Gomez-Arroyo JG, Farkas L, Alhussaini AA, Farkas D, Kraskauskas D, Voelkel NF, et al. The monocrotaline model of pulmonary hypertension in perspective. *American Journal of Physiology-Lung Cellular and Molecular Physiology*. 2012;302:L363-L369
20. Zeng GQ, Liu R, Liao HX, Zhang XF, Qian YX, Liu BH, et al. Single intraperitoneal injection of monocrotaline as a novel large animal model of chronic pulmonary hypertension in tibet minipigs. *PLoS One*. 2013;8:e78965
21. Wang ZJ, Lakes RS, Golob M, Eickhoff JC, Chesler NC. Changes in large pulmonary arterial viscoelasticity in chronic pulmonary hypertension. *Plos One*. 2013;8
22. Wang ZJ, Patel JR, Schreier DA, Hacker TA, Moss RL, Chesler NC. Organ-level right ventricular dysfunction with preserved frank-starling mechanism in a mouse model of pulmonary arterial hypertension. *Journal of Applied Physiology*. 2018;124:1244-1253
23. Wang Z, Schreier DA, Hacker TA, Chesler NC. Progressive right ventricular functional and structural changes in a mouse model of pulmonary arterial hypertension. *Physiological Reports*. 2013;1:e00184
24. Colvin KL, Yeager ME. Animal models of pulmonary hypertension: Matching disease mechanisms to etiology of the human disease. *J Pulm Respir Med*. 2014;4
25. Camacho P, Fan H, Liu Z, He J-Q. Large mammalian animal models of heart disease. *Journal of cardiovascular development and disease*. 2016;3:30
26. Stenmark KR, Meyrick B, Galie N, Mooi WJ, McMurtry IF. Animal models of pulmonary arterial hypertension: The hope for etiological discovery and pharmacological cure. *American Journal of Physiology-Lung Cellular and Molecular Physiology*. 2009;297:L1013-L1032
27. Maarman G, Lecour S, Butrous G, Thienemann F, Sliwa K. A comprehensive review: The evolution of animal models in pulmonary hypertension research; are we there yet? *Pulm Circ*. 2013;3:739-756
28. Rabinovitch M, Guignabert C, Humbert M, Nicolls MR. Inflammation and immunity in the pathogenesis of pulmonary arterial hypertension. *Circ Res*. 2014;115:165-175
29. Hsieh C-M, Mishkel GJ, Cardoso PFG, Rakowski H, Dunn SC, Butany J, et al. Production and reversibility of right ventricular hypertrophy and right heart failure in dogs. *The Annals of Thoracic Surgery*. 1992;54:104-110
30. Leeuwenburgh BP, Schoof PH, Steendijk P, Baan J, Mooi WJ, Helbing WA. Chronic and adjustable pulmonary artery banding. *J Thorac Cardiovasc Surg*. 2003;125:231-237

31. Leeuwenburgh BPJ, Steendijk P, Helbing WA, Baan J. Indexes of diastolic rv function: Load dependence and changes after chronic rv pressure overload in lambs. *American Journal of Physiology-Heart and Circulatory Physiology*. 2002;282:H1350-H1358
32. Leeuwenburgh BPJ, Helbing WA, Steendijk P, Schoof PH, Baan J. Biventricular systolic function in young lambs subject to chronic systemic right ventricular pressure overload. *American Journal of Physiology-Heart and Circulatory Physiology*. 2001;281:H2697-H2704
33. Barbera A, Giraud GD, Reller MD, Maylie J, Morton MJ, Thornburg KL. Right ventricular systolic pressure load alters myocyte maturation in fetal sheep. *American Journal of Physiology-Regulatory, Integrative and Comparative Physiology*. 2000;279:R1157-R1164
34. Leeuwenburgh BPJ, Helbing WA, Wenink ACG, Steendijk P, de Jong R, Dreef EJ, et al. Chronic right ventricular pressure overload results in a hyperplastic rather than a hypertrophic myocardial response. *J Anat*. 2008;212:286-294
35. Verbelen T, Verhoeven J, Goda M, Burkhoff D, Delcroix M, Rega F, et al. Mechanical support of the pressure overloaded right ventricle: An acute feasibility study comparing low and high flow support. *American Journal of Physiology-Heart and Circulatory Physiology*. 2015;309:H615-H624
36. Ramos SR, Pieles G, Sun M, Slorach C, Hui W, Friedberg MK. Early versus late cardiac remodeling during right ventricular pressure load and impact of preventive versus rescue therapy with endothelin-1 receptor blockers. *J Appl Physiol (1985)*. 2018;124:1349-1362
37. Gold J, Akazawa Y, Sun M, Hunter KS, Friedberg MK. Relation between right ventricular wall stress, fibrosis and function in right ventricular pressure loading. *American Journal of Physiology-Heart and Circulatory Physiology*. 2019
38. Gaynor Sydney L, Maniar Hersh S, Bloch Jeffrey B, Steendijk P, Moon Marc R. Right atrial and ventricular adaptation to chronic right ventricular pressure overload. *Circulation*. 2005;112:I-212-I-218
39. Heitmeier T, Sydykov A, Lukas C, Vroom C, Korfei M, Petrovic A, et al. Altered proteasome function in right ventricular hypertrophy. *Cardiovasc Res*. 2019
40. Kuroha M, Isoyama S, Ito N, Takishima T. Effects of age on right ventricular hypertrophic response to pressure-overload in rats. *J Mol Cell Cardiol*. 1991;23:1177-1190
41. Schou UK, Peters CD, Wan Kim S, Frøkiær J, Nielsen S. Characterization of a rat model of right-sided heart failure induced by pulmonary trunk banding. *Journal of Experimental Animal Science*. 2007;43:237-254
42. Bogaard Harm J, Natarajan R, Henderson Scott C, Long Carlin S, Kraskauskas D, Smithson L, et al. Chronic pulmonary artery pressure elevation is insufficient to explain right heart failure. *Circulation*. 2009;120:1951-1960
43. Hill MR, Simon MA, Valdez-Jasso D, Zhang W, Champion HC, Sacks MS. Structural and mechanical adaptations of right ventricular free wall myocardium to pulmonary-hypertension induced pressure overload. *Annals of biomedical engineering*. 2014;42:2451-2465
44. Hirata M, Ousaka D, Arai S, Okuyama M, Tarui S, Kobayashi J, et al. Novel model of pulmonary artery banding leading to right heart failure in rats. *Biomed Res Int*. 2015;2015:753210
45. Jang S, Vanderpool RR, Avazmohammadi R, Lapshin E, Bachman TN, Sacks M, et al. Biomechanical and hemodynamic measures of right ventricular diastolic function:

Translating tissue biomechanics to clinical relevance. *Journal of the American Heart Association*. 2017;6

46. Wang S, Ye L, Hong H, Tang C, Li M, Zhang Z, et al. A neonatal rat model of increased right ventricular afterload by pulmonary artery banding. *The Journal of Thoracic and Cardiovascular Surgery*. 2017;154:1734-1739
47. Chery J, Huang S, Gong L, Wang S, Yuan Z, Wong J, et al. Human neonatal thymus mesenchymal stem/stromal cells and chronic right ventricle pressure overload. *Bioengineering (Basel)*. 2019;6
48. Axelsen JB, Andersen S, Sun XQ, Ringgaard S, Hyldebrandt JA, Kurakula K, et al. Effects of 6-mercaptopurine in pressure overload induced right heart failure. *PLoS One*. 2019;14:e0225122
49. McKellar SH, Javan H, Bowen ME, Liu XQ, Schaaf CL, Briggs CM, et al. Animal model of reversible, right ventricular failure. *Journal of Surgical Research*. 2015;194:327-333
50. Hon JKF, Steendijk P, Khan H, Wong K, Yacoub M. Acute effects of pulmonary artery banding in sheep on right ventricle pressure–volume relations: Relevance to the arterial switch operation. *Acta Physiologica Scandinavica*. 2001;172:97-106
51. Yerebakan C, Klopsch C, Niefeldt S, Zeisig V, Vollmar B, Liebold A, et al. Acute and chronic response of the right ventricle to surgically induced pressure and volume overload – an analysis of pressure–volume relations☆. *Interactive CardioVascular and Thoracic Surgery*. 2010;10:519-525
52. Gufler H, Niefeldt S, Boltze J, Prietz S, Klopsch C, Wagner S, et al. Right ventricular function after pulmonary artery banding: Adaptive processes assessed by cmr and conductance catheter measurements in sheep. *J Cardiovasc Transl*. 2019;12:459-466
53. Corno AF, Sekarski N, Bernath MA, Payot M, Tozzi P, von Segesser LK. Pulmonary artery banding: Long-term telemetric adjustment. *Eur J Cardiothorac Surg*. 2003;23:317-322
54. Mitchell C, Rahko PS, Blauwet LA, Canaday B, Finstuen JA, Foster MC, et al. Guidelines for performing a comprehensive transthoracic echocardiographic examination in adults: Recommendations from the american society of echocardiography. *Journal of the American Society of Echocardiography*. 2019;32:1-64
55. Namba T, Tsutsui H, Tagawa H, Takahashi M, Saito K, Kozai T, et al. Regulation of fibrillar collagen gene expression and protein accumulation in volume-overloaded cardiac hypertrophy. *Circulation*. 1997;95:2448-2454
56. Curran-Everett D, Benos DJ. Guidelines for reporting statistics in journals published by the american physiological society. *Am J Physiol Regul Integr Comp Physiol*. 2004;287:R247-249
57. Woulfe KC, Wilson CE, Nau S, Chau S, Phillips EK, Zang S, et al. Acute isoproterenol leads to age-dependent arrhythmogenesis in guinea pigs. *Am J Physiol Heart Circ Physiol*. 2018;315:H1051-H1062
58. Väisänen D, Ekblom Ö, Ekblom-Bak E, Andersson E, Nilsson J, Ekblom M. Criterion validity of the ekblom-bak and the åstrand submaximal test in an elderly population. *European Journal of Applied Physiology*. 2020;120:307-316
59. Price EO, Dally MR, Borgwardt R. Early sexual experience improves ram breeding. *California Agriculture*. 1996;50:37-40
60. Chua J, Zhou W, Ho JK, Patel NA, Mackensen GB, Mahajan A. Acute right ventricular pressure overload compromises left ventricular function by altering septal strain and rotation. *Journal of Applied Physiology*. 2013;115:186-193

61. Naeije R, Manes A. The right ventricle in pulmonary arterial hypertension. *Eur Respir Rev*. 2014;23:476-487
62. Voelkel NF, Gomez-Arroyo J, Abbate A, Bogaard HJ. Mechanisms of right heart failure-a work in progress and a plea for failure prevention. *Pulm Circ*. 2013;3:137-143
63. Finsberg H, Xi C, Zhao X, Tan JL, Genet M, Sundnes J, et al. Computational quantification of patient-specific changes in ventricular dynamics associated with pulmonary hypertension. *Am J Physiol Heart Circ Physiol*. 2019;317:H1363-H1375
64. Liu W, Wang Z. Current understanding of the biomechanics of ventricular tissues in heart failure. *Bioengineering (Basel)*. 2019;7
65. Nguyen-Truong M, Wang Z. Biomechanical properties and mechanobiology of cardiac ecm. In: al ESe, ed. *Cardiac extracellular matrix*. Springer Nature 2018.
66. Pauschinger M, Doerner A, Remppis A, Tannhauser R, Kuhl U, Schultheiss HP. Differential myocardial abundance of collagen type i and type iii mrna in dilated cardiomyopathy: Effects of myocardial inflammation. *Cardiovasc Res*. 1998;37:123-129
67. Fratzl P. *Collagen : Structure and mechanics*. New York: Springer; 2008.
68. Ishizu T, Seo Y, Kameda Y, Kawamura R, Kimura T, Shimojo N, et al. Left ventricular strain and transmural distribution of structural remodeling in hypertensive heart disease. *Hypertension*. 2014;63:500-506
69. Tandri H, Saranathan M, Rodriguez ER, Martinez C, Bomma C, Nasir K, et al. Noninvasive detection of myocardial fibrosis in arrhythmogenic right ventricular cardiomyopathy using delayed-enhancement magnetic resonance imaging. *Journal of the American College of Cardiology*. 2005;45:98-103
70. Moreo A, Ambrosio G, De Chiara B, Pu M, Tran T, Mauri F, et al. Influence of myocardial fibrosis on left ventricular diastolic function noninvasive assessment by cardiac magnetic resonance and echo. *Circ-Cardiovasc Imag*. 2009;2:437-443
71. Bogaard HJ, Voelkel NF. Is myocardial fibrosis impairing right heart function? *Am J Resp Crit Care*. 2019;199:1458-1459
72. Poble PB, Phan C, Quatremare T, Bordenave J, Thuillet R, Cumont A, et al. Therapeutic effect of pirfenidone in the sugen/hypoxia rat model of severe pulmonary hypertension. *FASEB J*. 2019;33:3670-3679
73. Boehm M, Lawrie A, Wilhelm J, Ghofrani HA, Grimminger F, Weissmann N, et al. Maintained right ventricular pressure overload induces ventricular–arterial decoupling in mice. *Experimental Physiology*. 2017;102:180-189
74. Guihaire J, Haddad F, Boulate D, Decante B, Denault AY, Wu J, et al. Non-invasive indices of right ventricular function are markers of ventricular–arterial coupling rather than ventricular contractility: Insights from a porcine model of chronic pressure overload. *European Heart Journal - Cardiovascular Imaging*. 2013;14:1140-1149
75. Tello K, Dalmer A, Vanderpool R, Ghofrani HA, Naeije R, Roller F, et al. Cardiac magnetic resonance imaging-based right ventricular strain analysis for assessment of coupling and diastolic function in pulmonary hypertension. *JACC Cardiovasc Imaging*. 2019;12:2155-2164
76. Visser LC, Scansen BA, Schober KE, Bonagura JD. Echocardiographic assessment of right ventricular systolic function in conscious healthy dogs: Repeatability and reference intervals. *J Vet Cardiol*. 2015;17:83-96

77. Vonk-Noordegraaf A, Souza R. Cardiac magnetic resonance imaging: What can it add to our knowledge of the right ventricle in pulmonary arterial hypertension? *Am J Cardiol*. 2012;110:25S-31S
78. Velez-Rendon D, Pursell E, Shieh J, Valdez-Jasso D. Contribution of matrix remodeling to biaxial mechanics of right-ventricular myocardium in pulmonary arterial hypertension. *J Biomech Eng*. 2019
79. Sharifi Kia D, Benza E, Bachman TN, Tushak C, Kim K, Simon MA. Angiotensin receptor-neprilysin inhibition attenuates right ventricular remodeling in pulmonary hypertension. *J Am Heart Assoc*. 2020;9:e015708
80. Nguyen-Truong M, Liu W, Boon J, Nelson B, Easley J, Monnet E, et al. Establishment of adult right ventricle failure in ovine using a graded, animal-specific pulmonary artery constriction model. *Animal Model Exp Med*. 2020;3:182-192
81. Witzenburg C, Raghupathy R, Kren SM, Taylor DA, Barocas VH. Mechanical changes in the rat right ventricle with decellularization. *J Biomech*. 2012;45:842-849
82. Labus KM, Puttlitz CM. An anisotropic hyperelastic constitutive model of brain white matter in biaxial tension and structural–mechanical relationships. *Journal of the Mechanical Behavior of Biomedical Materials*. 2016;62:195-208
83. Javani S, Gordon M, Azadani AN. Biomechanical properties and microstructure of heart chambers: A paired comparison study in an ovine model. *Annals of Biomedical Engineering*. 2016;44:3266-3283
84. Fatemifar F, Feldman M, Oglesby M, Han HC. Comparison of biomechanical properties and microstructure of trabeculae carneae, papillary muscles, and myocardium in human heart. *J Biomech Eng*. 2018
85. Avazmohammadi R, Hill MR, Simon MA, Zhang W, Sacks MS. A novel constitutive model for passive right ventricular myocardium: Evidence for myofiber-collagen fiber mechanical coupling. *Biomech Model Mechanobiol*. 2017;16:561-581
86. Voorhees AP, Han HC. Biomechanics of cardiac function. *Compr Physiol*. 2015;5:1623-1644
87. Liu W, Nguyen-Truong M, Labus K, Boon J, Easley J, Monnet E, et al. Correlations between the right ventricular passive elasticity and organ function in adult ovine. *Journal of Integrative Cardiology*. 2020;6:1-6

# 6. Mechanical Regulation of Pro-angiogenic Paracrine Effect of Mesenchymal Stromal Cells[4]

## 6.1 Mechanical Considerations of Electrospun Scaffolds for Myocardial Tissue and Regenerative Engineering

### 6.1.1 Clinical Significance

Heart failure is the leading cause of death worldwide and affects about 38 million people[1, 2]. There are mainly two types of heart failure, heart failure with reduced ejection fraction (HFrEF) and heart failure with preserved ejection fraction (HFpEF), which involve left ventricular (LV) or right ventricular (RV) or biventricular failures[1]. The pathological remodeling of the myocardium often results in structural and functional changes of the cardiac tissue locally (e.g., in myocardial infarction) or globally (e.g., in idiopathic cardiomyopathy). Currently, pharmaceutical or surgical therapies are not completely satisfactory and fail to halt the continuous deterioration of the myocardium. Consequently, heart transplantation or implantation of a ventricular assist device is the last resort for severe heart failure patients. A preferred treatment is to restore the diseased tissue instead.

Cardiac tissue and regenerative engineering, via the use of biomaterials with or without cells/molecules to repair heart tissue, is an emerging, interdisciplinary field that aims to improve outcomes and quality of life for these patients[3]. This new field has presented the opportunity to

---

[4] Adapted from Nguyen-Truong M, Li YV, Wang Z. Mechanical Considerations of Electrospun Scaffolds for Myocardial Tissue and Regenerative Engineering. *Bioengineering (Basel)*. 2020 Oct 3;7(4):122. doi: 10.3390/bioengineering7040122.
Adapted by permission from Nguyen-Truong M, Hematti P, Wang Z. Current status of myocardial restoration via the paracrine function of mesenchymal stromal cells. *Am J Physiol Heart Circ Physiol*. 2021 Jul 1;321(1):H112-H127. doi: 10.1152/ajpheart.00217.2021.

renew and restore the diseased heart[4-6]. In order to achieve optimal therapies, the right cell source and the right microenvironment for the cells or their secretome to function are the most important questions to answer. While other reviews have focused on the issues related to the stem/progenitor cells to employ[4, 6-8], in this review, our main interests lie in the 'right microenvironment' for cardiac restoration that is identified or provided by the use of scaffolds.

The extracellular microenvironment is composed of two aspects: biochemical cues and biophysical cues. The biochemical cues mainly refer to the neighboring cells, soluble factors, extracellular matrix (ECM) proteins, oxygen levels, etc.[9]. The impact of biochemical cues in cardiac restoration has been extensively investigated and reviewed[10-12]. The other aspect, the biophysical cues—often referred to as the mechanical environment of the native tissue or a biomaterial (e.g., the elasticity, roughness, surface topology, etc.)—are much less reviewed. It is generally accepted that the mechanical regulation of ECM plays key roles in maintaining tissue homeostasis such as cell proliferation, differentiation, gene/protein expression, and function[11, 13-22]. In this review, we bring attention to the biomechanics of the native myocardium and the microfibrous scaffolds in the consideration of myocardial restoration. We will summarize the development of microfibrous scaffolds in cardiac tissue engineering and their mechanical properties, the current understanding of the cellular responses to mechanical factors (i.e., mechanobiology) using microfibrous scaffolds, and the clinical relevance of the scaffold mechanical properties in myocardial restoration. Finally, we further identify some knowledge gaps to inspire future research and clinical applications of electrospun scaffolds for heart failure patients.

### 6.1.2 Types of Scaffolds in Cardiac Tissue Engineering and Regenerative Medicine

To date, the use of biomaterials in cardiac regenerative research is mainly to 1) serve as an in vitro model system that allows for the mechanistic studies of cardiac and/or progenitor cells to cultivate new treatment strategies; and 2) to be implanted into the myocardium in in vivo models to assist tissue healing. In the latter application, the cardiac scaffolds have been demonstrated to provide mechanical support of the ventricle wall, elicit healing responses, and/or enhance the homing and retention of stem/progenitor cells or molecules in the injured tissue[23-25]. Despite different etiologies of heart failure, the majority of regenerative research is limited to myocardial infarction (MI) in the LV as a result of acute or chronic occlusion of coronary arteries[25-27]. Recently, there are emerging areas in the restoration of the failing RV associated with pulmonary hypertension (PH)[24]. These preclinical and clinical studies have indicated the potential of scaffolds to restore the damaged myocardium (please see recent reviews[3, 4, 6, 10, 28-30]). In the past decades, we have gained significant knowledge on the manufacture and use of biomaterials in cardiac regenerative medicine. For instance, it is accepted now that no single biological substance (e.g., fibrin) or synthetic biomaterial (e.g., polyurethane) would likely lead to an optimal therapeutic effect in the MI tissues. Similarly, the delivery of stem/progenitor cells via intravenous or intramyocardial injections alone often results in poor cell retention and cell survival. Therefore, the current trends involve the combined use of a cardiac scaffold ('cardiac patch') and regenerative cells or molecules to maximize the repair and healing of ventricles[6, 29-34].

Currently, there are three main resources of cardiac scaffolds: 1) the native polymers found in biological tissues (e.g., collagen, fibrin); 2) the decellularized tissues; 3) the synthetic polymers. Native polymers inspired by the ECM proteins in native tissues are advantageous due to the absence of an immune response, but the lack of biomimetic mechanical behavior has limited the findings and interpretation of data with cells cultured in such non-physiological mechanical conditions. In addition, the synthesis of 3D scaffolds is challenging and research on 3D-printed matrix production remains at the bench stage[3, 35]. The second approach, tissue decellularization, offers a quick approach to derive scaffolds with attractive biocompatibility and desired structural and mechanical properties. However, this method is limited by the massive scaffold production with inconsistent qualities from batch to batch, thus preventing a broad use across labs or clinical trials. In contrast to the above two approaches, synthetic polymers offer appropriate mechanical behaviors similar to native tissues and enable 'off-the-shelf' production for potential clinical applications. Modifications in the fabrication protocol further enable us to adjust the degradation rates, biocompatibility, porosity, mechanical and conductive properties of the scaffolds. Therefore, in this review, we focus on the microfibrous scaffolds that are fabricated by electrospinning of synthetic materials.

### 6.1.3 Electrospinning of Microfibrous Scaffolds

Electrospinning is a well-established fiber production method wherein a polymer solution is fed through a high voltage electric field, resulting in coagulation and formation of micro- or nanofibers. The set-up protocols serve bioengineers with the control over the individual fiber size, porosity, alignment, and mechanical properties which are critical in guiding cellular attachment and orientation and eliciting optimal cellular responses[36, 37]. For detailed discussions on the methodology of electrospinning in general biomedical applications, please refer to these reviews[29, 34, 38-52]. For reviews specific to cardiac applications, the following reviews are recommended[29, 34, 39-41]. Below, we will only provide a summary of fundamental principles and recent adaptations of electrospinning to cardiac bioengineering applications.

In brief, a polymer solution is ejected through a syringe at a specific flow rate onto a metal collector at a desired distance from the needle tip (**Fig. 6.1**). A voltage difference is provided between the needle tip and the collector to supply an electric field to "draw out" the polymer fibers. In the production of fibrous sheets, electrospinning is controlled via a variety of parameters in the polymer solution (e.g., molecular weight, concentration) and in the operation of the apparatus (voltage, distance from needle tip to collector plane, injection flow rate, and duration)[6, 25, 29, 38, 39, 53, 54]. These parameters allow for the fine tuning of the chemical (e.g. molecular structure), geometrical or structural (e.g., porosity, fiber diameter, distribution, orientation, morphology), and mechanical properties of the scaffold[38].

Some modifications in electrospinning can confer improved properties of the scaffolds. First, the electrospinning process can employ either natural (collagen, silk, cellulose, etc.) or synthetic (polyurethanes, poly(ε-caprolactone), etc.) or a combination of both materials to achieve a variety of structures and utility[29, 38, 39, 55]. These polymers can be combined using either blended or core/shell electrospinning to achieve desired biocompatibility, conductivity, and mechanical strength[56-58]. For example, core/shell electrospinning has been used to fabricate a core polymer (poly(lactic acid)/polyaniline) with electroactive property and another shell polymer (poly(lactic acid)/poly(ethylene glycol)) with biocompatible interface[58]. Supporting electrical conductivity is important for synchronous cardiomyocyte contraction in cardiac scaffolds, and similar as well as different fabrication methods have also been explored[59, 60]. Second, structural and mechanical properties of scaffolds can be improved by the fabrication process. Typically, a stationary collecting plate allows fibers to be collected in a random manner, whereas a moving plate or rotating mandrel collector is used to create different degrees of aligned fibers[29, 36, 37, 61-66] (**Fig. 6.1**). The fabrication protocol can be adjusted to control scaffold fiber diameter/size, distribution/alignment, porosity, and other physical characteristics. For example, different rotating mandrel speeds could lead to different fiber orientations and anisotropic mechanical properties[63]. Third, modification or treatment of the scaffolds with functional agents (e.g., biomolecules) within or on the fiber surface can improve biological properties. These properties may support cell homing, proliferation, function, differentiation, or survival[27, 67-69]. For example, matrigel and laminin coatings have been used on electrospun scaffolds to promote cardiomyocyte attachment, morphology, and sarcomere organization[69].

Moreover, the combination of electrospinning with other techniques is able to confer more specific and realistic mechanical properties similar to the native cardiac tissues. For instance, there is a transmural change (100-degree shift) in the myo/collagen fiber orientation from the endocardium to epicardium of the LV[36, 70], and such complex 3D anisotropic architecture was achieved in the scaffolds fabricated by electrospinning and laser patterning[71]. In other studies, scaffolds with electrically conductive materials have been explored. Kai et al. presented a blended polypyrrole/poly (ε-caprolactone)/gelatin electrospun scaffolds with the polypyrrole being the driving component for conduction[59]. Moreover, electrospraying of native biomaterial (e.g., decellularized ECM) when combined with electrospinning is an attractive option to better support host cell recruitment while maintaining mechanical support, such as in a cardiac patch[72, 73]. Therefore, electrospinning offers the unique capability to fabricate scaffolds mimicking the 3D geometries, mechanical and electrical properties of native myocardial tissues.

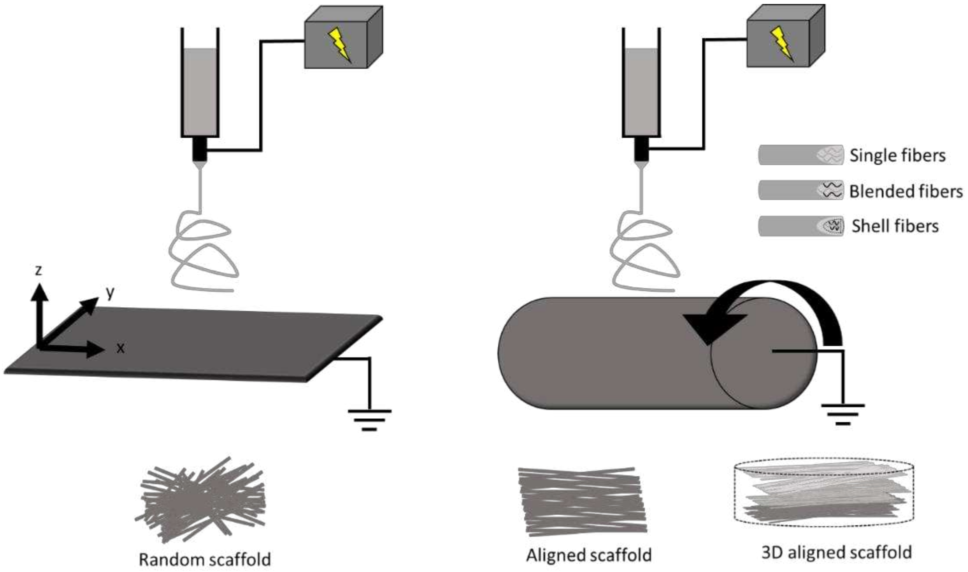

**Figure 6.1.** Schematic of electrospinning with a plane (left) and a cylinder (right) fiber collector, respectively. The movement of collectors (shown by arrows) enables the adjustment of structural properties such as fiber diameter and alignment. Other modifications in the fabrication include blended and core/shell electrospinning to include a hybrid of materials to control the scaffold properties. Scaffolds can also be functionalized, stimulated, or constructed into 3D platforms.

### 6.1.4 *In Vivo* Studies: Electrospun Scaffolds in Cardiac Therapies

#### *6.1.4.1 Cardiac Scaffold as a Mechanical Support*

The use of a cardiac scaffold to treat heart failure patients arose before the emergence of stem cell therapy. It has been found initially that the wrapping of a dilated heart with a biomaterial scaffold could effectively prevent further dilatation, maintain ventricular cavity area, reduce wall stress, and even enhance myocardial function[28, 74]. Thus, the early generations of scaffolds were mostly considered to provide mechanical support with acceptable biocompatibility[75]. Currently, the acellular scaffolds are typically in the stiffness range of tens of kPa to tens of MPa and are made of natural or synthetic materials[25, 76-80].

For instance, the supportive role of cardiac scaffolds is evident in a study using the polyester ether urethane urea (PEEUU) electrospun scaffold with the Young's modulus of ~1–2 MPa[25]. The PEEUU scaffolds were loaded with adeno-associated viral (AAV) genes and then implanted to the ischemic rat LV. The treatment improved LV function (e.g., increases in ejection fraction and fractional area change). Interestingly, despite this 'hybrid' therapeutic approach, the therapeutic effects were found most likely due to the scaffold and not the AAV genes[25]. However, most similar studies did not elaborate how much of the therapeutic effects were from the mechanical support of the scaffold and how much were from the biochemical signals elicited by the scaffolds or delivered cells/genes. In other words, none of the prior studies are designed to investigate the effect of mechanical properties of scaffolds on cardiac restoration. Therefore, the optimal mechanical properties of scaffolds remain unknown. Since the passive mechanical properties of the ventricles are important contributors to the ventricular function[81, 82], future investigations should delineate the effects of the scaffold's mechanical properties to improve the design of cardiac scaffolds.

#### *6.1.4.2 Cardiac Scaffold as a Regenerative Support*

The current perspective holds that the main mechanisms of scaffold-induced tissue restoration lie in the altered biological functions achieved by the scaffold and/or its delivered biological components, which can more proactively promote the healing of cardiac tissues. Particularly, when loaded with cells or other molecules (e.g., exosomes), the 'cardiac patch' enables a more effective induction of remodeling events for tissue renewal. Therefore, the scaffolds should provide a suitable extracellular environment for seeded cellular adhesion, infiltration, and differentiation/growth[24, 25, 74, 83]. Moreover, in order to minimize the invasive delivery of stem/progenitor cells and reduce tumorigenic risks, therapies facilitated with injectable, cell-free 'cardiac patches' have recently gained increasing awareness[6, 40]. Nevertheless, the 'match' of the mechanical property between native myocardium and the 'cardiac patch' has not been a consideration in the therapeutic mechanisms. That is, the biological responses to the altered mechanical environment are often ignored in preclinical or clinical studies.

The lack of the mechanical consideration of cardiac scaffolds is reflected by the variety of Young's moduli of the scaffolds reported in the literature. Table 6.1 summarizes the current electrospun scaffolds used in cardiac tissue and regenerative engineering research. It can be seen that the Young's modulus varies from 20 kPa to 92 MPa, covering either myofiber level tensile stiffness or supra-physiological ranges of cardiac tissue elasticity. For instance, Kai et al. showed that a poly(ε-caprolactone)/gelatin patch (with a Young's modulus of 1.45 MPa), seeded with mesenchymal stem cells (MSCs), improved the angiogenesis and cardiac function in myocardial infarction (MI) rats[74]. In another study, Guex et al. showed that a functionalized MSC-seeded poly(ε-caprolactone) scaffolds (with elastic moduli of 16–18 MPa) stabilized cardiac function and reduced dilatation in rat MI LVs[26]. While these findings are exciting, the therapeutic outcomes are not completely satisfactory and it is difficult to compare these treatments. One of the challenges to interpret and compare the results is due to the 'random' selection of scaffold stiffness. As we have noted in the previous Section 6.2.4.1, there are a lack of studies on the effects of mechanical properties of scaffolds on therapeutic outcomes. This lack of knowledge further leads to the continuous neglect of this factor in the regenerative treatment, which forms a vicious cycle. Moreover, the scaffold stiffnesses used in the above studies are in orders of magnitude higher than the healthy myocardium, which calls into a question if the cellular performance is impaired by the use of supra-physiologically stiff substrates. Thus, the overall therapeutic outcomes should not only weigh in the multiple aspects of the healing response (angiogenesis, anti-inflammation, anti-oxidant, etc.), but also in the effect of mechanical properties on these healing responses. Additionally, the microstructure and mechanical properties of the substrate are known to form a critical cue to a variety of cells including cardiomyocytes, cardiac myoblasts, and stem/progenitor cells[10, 16, 84, 85]. Overlooking or failing to consider the scaffold's mechanical impact on tissue remodeling can potentially hamper the development of optimal therapies for heart failure patients. Therefore, it is necessary to explore whether the altered mechanical environment is suitable for the new stem cells or existing cardiac cells to accelerate healing and maximize therapeutic outcomes.

**Table 6.1.** Various ranges of the Young's modulus of electrospun scaffolds used in the cardiac tissue and regenerative engineering studies.

| Measurement Method | Material(s) | Young's Modulus (E) | Summary | Ref. |
|---|---|---|---|---|
| AFM (individual fiber) and tensile test (sheet) | Polyester urethane urea | 7.5 MPa (initial E) | Validation of structural finite element model to examine mechanics of elastomeric fibrous biomaterials with or without smooth muscle cells culture. | 86 |
| Tensile test | Polyester urethane urea | 2.5–2.8 MPa (without smooth muscle cells)<br>0.3–1.7 MPa (with smooth muscle cells) | Integration of smooth muscle cells into biodegradable elastomer fiber matrix. | 87 |
| Tensile test | Polypyrrole and poly(ε-caprolactone)/gelatin | 8–50 MPa | 15 wt% polypyrrole (in 0–30%) exhibited most balanced cardiomyocyte conductivity, mechanical properties, and biodegradability. | 59 |
| Tensile test | Poly(ε-caprolactone)/gelatin (PG) | 1.5 MPa | MSC-seeded PG patch restricted expansion of LV wall, reduced scar size, and promoted angiogenesis. | 74 |
| Tensile test | Poly(ε-caprolactone) (PCL) and poly(ε-caprolactone)/gelatin (PG) | PCL:<br>Dry: 2–28 MPa<br>Wet: 2–25 MPa<br>PG:<br>Dry: 10–49 MPa<br>Wet: 1–5 MPa | Aligned PG scaffold promoted cardiomyocyte attachment and alignment. | 88 |
| Tensile test | Gelatin | 20 kPa | Construct used to study cardiomyocyte behavior (beating observed) and cardiac proteins expressed for studying cardiac function in drug testing and tissue replacement. | 89 |
| Tensile test | Polyester urethane urea; polyester ether urethane urea | 1–2 MPa | Cardiac patch to deliver viral genes to ischemic rat heart. | 25 |
| Tensile test | Poly(ε-caprolactone) | 16–18 MPa | MSC seeded matrix showed stabilized cardiac function and attenuated dilatation of chronic myocardial infarction in rat. | 26 |
| Tensile test | Poly(L-lactic acid)-co-poly(ε-caprolactone) (PLACL); poly(L-lactic acid)-co-poly(ε-caprolactone)/collagen (PLACL/collagen) | 10–18 MPa | PLACL/collagen scaffold is more suitable compared to PLACL for cardiomyocyte growth and attachment, as well functional activity and protein expression. | 90 |
| Tensile test | Poly(L-lactide-co-caprolactone) and | 1–5 MPa | Platform for cardiomyocyte culture and coculture with fibroblasts. | 66 |

| | | | | |
|---|---|---|---|---|
| | fibroblast-derived ECM | | | |
| Tensile test | Polyaniline and poly(lactic-co-glycolic acid) | 92 MPa | Development of electrically active scaffold for synchronous cardiomyocyte beating | 91 |
| Tensile test | Carbon nanotubes embedded aligned poly(glycerol sebacate):gelatin (PG) | 93–373 kPa | Contractile properties of cardiomyocytes improved with carbon nanotubes and aligned fibers. | 92 |
| Tensile test | Polyethylene glycol; polyethylene glycol and poly(ε-caprolactone) (PCL); PCL and carboxylated PCL; polyethylene glycol and PCL and carboxylated PCL | Dry: 18 MPa<br>Wet: 0.7 MPa | Embryonic stem cell derived cardiomyocyte differentiation (α-myosin heavy chain expression, intracellular Ca signaling) is promoted on softer substrates. | 21 |
| Tensile test | Carbon nanotubes embedded poly(ethylene glycol)-poly(d,l-lactide) | 10–60 MPa | Cardiomyocyte protein production and physiological pulse frequency was promoted on core-sheath fibers loaded with 5% carbon nanotubes. | 93 |
| Tensile test | Digested porcine cardiac ECM and polyethylene oxide | 203 kPa | Different rates of cell attachment, survival, and proliferation between ECM patch, electrospun scaffold, and hydrogel. | 94, 95 |
| Tensile test | Reduced graphene oxide modified silk | 12–13 MPa | Develop silk biomaterials using controllable surface deposition on nanoscale to recapitulate electrical microenvironments for cardiac tissue engineering. | 60 |
| Tensile test | Nanofiber yarns | 20–110 MPa | 3D hybrid scaffold using aligned conductive nanofiber yarns within hydrogel to mimic native cardiac tissue structure induced cardiomyocyte orientation, maturation, and anisotropy, as well as formation of endothelialized myocardium after coculture with endothelial cells. | 36 |

### 6.1.5 Mechanical Measurement of Scaffolds

Regardless of the consideration of scaffold mechanical behavior in the study design or not, this physical property is typically reported with one of the following mechanical tests discussed in this section. The most frequently reported mechanical property is the elasticity or stiffness. Furthermore, for implantation purposes, some scaffolds are fabricated to be mechanically similar to the native cardiac tissues. Thus, a proper measurement and comparison of the mechanical properties of scaffolds to those of cardiac tissues is of importance. We summarize the common mechanical testing methods used to characterize the mechanical properties of scaffolds as well as cardiac tissues below.

Typically, a thin fibrous sheet of scaffold is measured using tensile testing or atomic force microscopy, but these are 2D or 1D mechanical measurements. For cardiac tissues or 3D scaffolds, it is critical to incorporate the planar and transmural mechanical measurements to better characterize the 3D mechanical behavior[96-98]. We thus briefly introduce the proper mechanical tests for 3D mechanical measurements. Finally, as the cardiac tissues are viscoelastic, we also include a discussion on the measurement of the material's dynamic mechanical property—viscoelasticity.

#### *6.1.5.1. Elasticity (Young's Modulus) Measurement*

For a linear elastic material, the most important mechanical property is its elasticity, which is often referred to as Young's modulus (E). Experimentally, the Young's modulus is a measurement of material's ability to return to its original shape after a tensile force is applied. Based on this definition, the direct measurement of Young's modulus is via tensile mechanical tests. It is a fundamental testing method that applies a tensile force (i.e., stress) to a material and then measures the change in deformation (i.e., strain). The Young's modulus (E) is then defined as the slope of a stress–strain curve. However, native cardiac tissue often presents a nonlinear hyperelastic behavior (see the 'J-shaped' stress–strain curve in **Table 6.2**), which means that the slope of the stress–strain curve alters at different strains. Such nonlinear, elastic behavior of biological tissues is absent in electrospun scaffolds. Thus, it is important to choose the Young's modulus (E) at physiological strain ranges to fabricate biomimetic scaffolds.

Moreover, depending on whether the material is isotropic or anisotropic, uniaxial or biaxial tensile mechanical tests (**Table 6.2**) can be performed on the sample to determine E in one or two directions[25, 31, 54, 63, 89]. Since an electrospun scaffold is often a thin sheet with identical transmural mechanical behavior, the three-dimensional mechanical measurement is generally not needed. For a randomly aligned electrospun scaffold, the material can be assumed to be isotropic due to the even distribution of the fibers in x and y (planar) directions, and thus a uniaxial tensile test is adequate. But for the aligned scaffold, biaxial tensile testing is more appropriate to simultaneously characterize its anisotropic mechanical behavior[54, 63]. The cardiac tissue (myocardium) is well known for its anisotropic mechanical behavior, and thus a better fabrication and mechanical characterization of scaffolds should incorporate multi-axial measurements.

Finally, atomic force microscopy (AFM) is a useful tool for the structural and mechanical measurements of a material (**Table 6.2**). A cantilever tip "scans" the surface to obtain high resolution images with topographical characteristics (e.g., roughness) of the material (e.g., scaffold). For mechanical measurement, the cantilever contacts and indents a fiber, and then the force and indentation (deformation/displacement) are measured[99, 100]. Because this method is essentially an indentation mechanical test, it is the transverse mechanical property that is directly obtained[99]. To convert the transverse mechanical behavior to the Young's modulus (assuming isotropic behavior), an axial or planar mechanical property of the "sheet", different mathematical models are developed and the material is assumed to be isotropic (e.g., the Hertz model is used for isotropic and linear elastic materials)[99]. However, cardiac tissues are orthotropic and nonlinear materials, and electrospun scaffolds are not necessarily isotropic, either. Therefore, the Young's modulus derived from the AFM measurement may be inaccurate and in fact, it is typically smaller than the modulus directly measured from the tensile mechanical tests[101] (see a further discussion below). Furthermore, the AFM measurement is local and significantly affected by regional variability, and thus multiple measurements in different regions are required to derive a global stiffness.

### *6.1.5.2. Shear Measurement*

Sometimes a shear test can be performed to obtain the mechanical property such as shear strength, and the Young's modulus can be derived indirectly as well (assuming the material is isotropic). While shear testing is not commonly performed on thin scaffolds, its combined use with the biaxial tensile tests is becoming increasingly common to obtain the 3D mechanical property of cardiac tissues, which is orthotropic and exhibits anisotropic shear properties[96, 98]. In the development of 3D electrospun scaffolds to better replicate native cardiac tissues, this method should be included to more accurately characterize multi-layered scaffolds. This methodology should also be included in the investigation of the cellular response to a 3D mechanical environment. As shown in Table 6.2, shear testing is the measurement of an angular deformation of the object when a parallel force is applied to the object's plane. For cubic specimens, shear testing can provide triaxial shear moduli, which would be useful in the design of orthotropic biomaterials.

### *6.1.5.3. Viscoelasticity Measurement*

All the mechanical measurements discussed above are obtained from static mechanical tests (i.e., the response to applied force or deformation is time-independent) and assume the material to be perfectly elastic (i.e., there is no friction energy loss during deformation). However, cardiovascular tissues are viscoelastic materials that experience pulsatile (time-dependent) hemodynamic forces. Therefore, it is imperative to assess the tissue or matrix viscoelastic property that exhibits both viscous and elastic behaviors.

Viscoelasticity can be measured by applying dynamic mechanical loading in the same mechanical testing system (e.g., tensile tests). The dynamic loading includes cyclic linear (triangle shape) or non-linear (sinusoidal shape) forces applied on the material. Then, the hysteresis area (the area between the loading and unloading stress–strain curves) can be obtained in order to derive the viscoelastic properties. Stress relaxation and creep tests are other traditional methods to measure viscoelasticity[102]. Using a cylindrical geometry of the sample and a sinusoidal compression force applied via a dynamic mechanical analysis (DMA) tester (**Table 6.2**), storage modulus, loss modulus, and phase angle can be derived to characterize viscoelastic properties. The storage modulus (E') measures the energy storage, representing the material's elasticity, and the loss modulus (E'') measures the energy dissipation, representing the material's viscosity. Viscosity can also be measured by the material's damping ratio, the tangent of the E''/ E', or the phase angle, the arctangent of E''/E'[103, 104]. The viscoelastic measurement is not commonly used for mechanical analysis of myocardium or cardiac scaffolds, probably due to the neglect of viscoelastic behavior or the thin sheet geometry (typically about tens or hundreds of μm thickness) that is insufficient for DMA testing (with the thickness of ones of mm). To date, there is only one study that incorporated viscoelasticity into the design of the scaffold. However, this scaffold is made of an ionically crosslinked transparent hydrogel, not by electrospinning[78]. Since the implanted cardiac scaffolds are subjected to pulsatile blood flow, future patches should consider and accommodate for dynamic in vivo loading, and the dynamic mechanical properties should be taken into consideration.

**Table 6.2.** Mechanical testing methods to derive elastic modulus of a material. Young's modulus = E.

<table>
<tr><th>Type</th><th>Schematic</th><th>Modulus</th><th>Methodology</th></tr>
<tr><td>Tensile (upper row: uniaxial test; lower row: biaxial test)</td><td>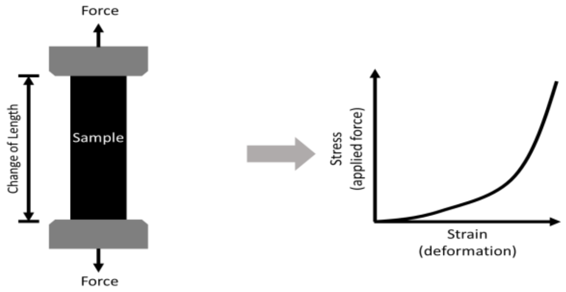

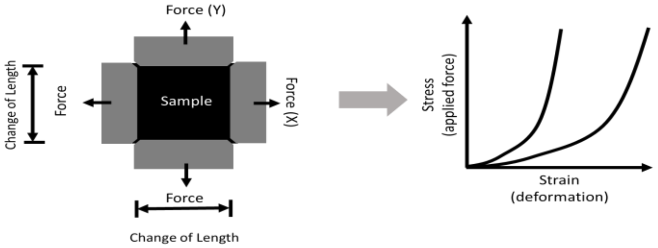
</td><td>Tensile test:<br>$Young's\ Modulus = \frac{\sigma}{\varepsilon}$<br><br>$\sigma$: stress,<br>$\varepsilon$: strain.</td><td>1D or 2D tensile (pulling) force applied to a material and the deformation is recorded.</td></tr>
<tr><td>Indentation (in AFM)</td><td>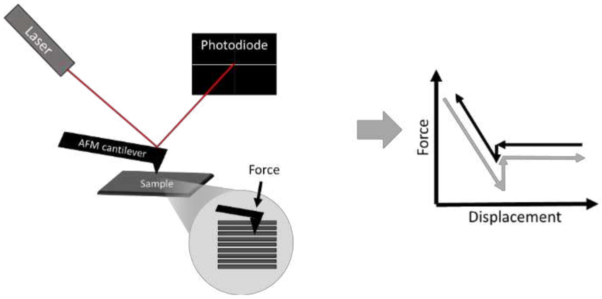
</td><td>Young's Modulus derived from a mathematical model.<br>For example, using the Hertz model:<br>$F = \frac{4}{3}\frac{E}{(1-v^2)}\sqrt{r\delta^3}$<br><br>$\delta$: sample indentation,<br>$F$: applied force,<br>$E$: elastic modulus,<br>$v$: Poisson's ratio<br>$r$: probe tip radius.</td><td>The force and indentation (deformation/displacement) are measured from cantilever deflection.</td></tr>
<tr><td>Shear</td><td>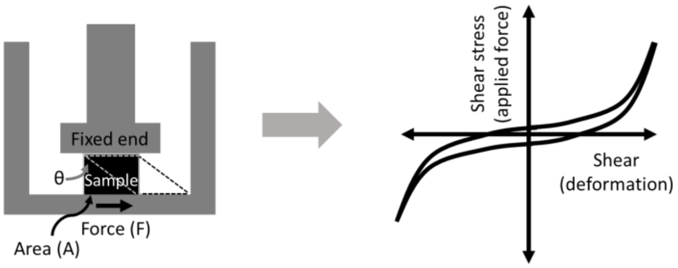
</td><td>Shear Modulus<br>$(G) = \frac{\frac{F}{A}}{\tan(\theta)}$<br>For isotropic material, $G = \frac{E}{2(1+v)} = \frac{E}{3}$<br><br>$F$: force,<br>$A$: area,<br>$v$: Poisson's ratio.</td><td>Shear, or parallel frictional force, applied to a material and the change in angle ($\theta$) is recorded.</td></tr>
</table>

| | | | |
|---|---|---|---|
| Dynamic Mechanical Analyzer (DMA) | 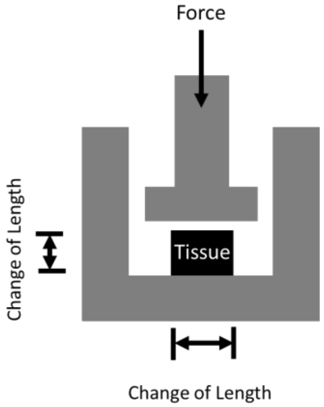 | $Storage\ Modulus = \frac{\sigma}{\varepsilon} cos\delta$<br>$Loss\ Modulus\ (E'' = \frac{\sigma}{\varepsilon} sin\delta$<br>$\sigma$: stress, $\varepsilon$: strain, $\delta$: phase lag between stress and strain. | Oscillatory force applied to a material and resulting displacement is measured. |

### 6.1.6 Discrepant Elastic Moduli Reported from Native Myocardial Tissues in the Literature

In this review, we would like to point out the important status of discrepant cardiac mechanical data in the current literature. There are a wide variety of reports on the mechanical properties of healthy and diseased myocardium as summarized in Table 6.3. Indeed, it is true that the elastic modulus of heart tissue varies in different anatomic regions and the stage of injury[78]. However, even under the same condition, the reported values are quite different; for example, the elastic modulus of healthy myocardium ranges from ones of kPa to hundreds of kPa[105-111]. These inconsistent literature data complicate the selection of appropriate mechanical stiffness for the myocardial scaffold design[111].

We noticed that the two most common methods for scaffold mechanical measurements are the AFM (essentially an indentation test) and the tensile tests. It has been well noted that the indentation and tensile mechanical tests generate very different Young's moduli for the same type of biological tissues (from ones of kPa to hundreds of MPa), with the indentation method consistently yielding lower Young's moduli[101, 111]. This has been supported and thoroughly discussed by McKee et al.[101]. Other factors that may contribute to the inconsistency include the way the tissue is prepared (e.g., solutions used prior and during testing) or mechanically tested (e.g., equibiaxial versus non-equibiaxial testing, maximal strain used)[106-108]. While the other factors can be controlled for, the inconsistency due to the intrinsic difference in methodology between the indentation and tensile tests is unavoidable. In any case, the design of cardiac scaffolds requires careful consideration of the myocardium's mechanical properties (e.g., anatomic region, health status, testing preparation, and methods) for which it replicates.

**Table 6.3.** Different Young's moduli reported for the left or right ventricular (LV/RV) tissues. * are data estimated from the original papers. Tissue mechanical property is measured either in main fiber and cross-fiber (X-fiber) directions or in anatomical directions (L: longitudinal (long-axis of ventricle), C: circumferential (short-axis of ventricle)).

| Measurement Method | Species / Tissue | Anatomic Region | Young's Modulus | Ref. |
|---|---|---|---|---|
| AFM | Mouse / LV | N/A | Embryonic: 12 kPa<br>Neonatal: 39 kPa | 105 |
| AFM | Rat / LV | Basal surface of tissue section parallel to long axis | Healthy: 18 kPa<br>Infarcted: 55 kPa | 112 |
| AFM | Mouse / LV | N/A | Healthy: 60 kPa<br>Diseased: 144–295 kPa | 113 |
| AFM | Quail / Embryonic heart tissue | Apical surface | Healthy: 1–14 kPa | 114 |
| Custom Indenter | Rat / LV&RV | N/A | Healthy LV: 15 kPa<br>Healthy RV: 13 kPa<br>Hypertensive LV: 12 kPa<br>Hypertensive RV: 22 kPa | 111 |
| Micropipette aspiration | Rat / Whole heart | N/A | Healthy:<br>Neonatal: 4–11 kPa<br>Adult: 12–46 kPa | 115 |
| Tensile test | Rat / RV | N/A | Healthy:<br>Low strain (L): 7–18 kPa<br>High strain (L): 464–1054 kPa<br>Low strain (C): 7–17 kPa<br>High strain (C): 421–965 kPa<br>Pressure overloaded:<br>Low strain (L): 18–45 kPa<br>High strain (L): 702–1157 kPa<br>Low strain (C): 5–9 kPa<br>High strain (C): 497–808 kPa | 108 |
| Tensile test | Rat / RV | Middle of the RV free wall between apex and outflow tract | Healthy:<br>Low strain: 46 kPa<br>High strain: 716 kPa<br>Hypertensive:<br>Low strain: 143 kPa<br>High Strain: 535 kPa | 109 |
| Tensile test | Rat / LV&RV | N/A | Healthy LV:<br>L: 157 kPa<br>C: 84 kPa<br>Healthy RV: | 116 |

| | | | | |
|---|---|---|---|---|
| | | | L: 20 kPa<br>C: 54 kPa | |
| Tensile test | Canine / LV&RV | RV: middle of the free wall; LV: between left anterior descending artery and major marginals of circumflex artery | Healthy LV:<br>Apex-to-base: 125–875 g/cm<br>Circumferential: 250–1375 g/cm<br>Healthy RV:<br>Apex-to-base: 63–1000 g/cm<br>Circumferential: 125–2400 g/cm | 107* |
| Tensile test | Canine / LV&RV | RV free wall sinus and conus regions; LV midwall | Healthy RV Sinus:<br>Fiber: 800 g/cm$^2$<br>X-fiber: 500 g/cm$^2$<br>Healthy RV Conus:<br>Fiber: 800 g/cm$^2$<br>X-fiber: 300 g/cm$^2$<br>Healthy LV:<br>Fiber: 600 g/cm$^2$<br>X-fiber: 500 g/cm$^2$ | 110 |
| Tensile test | Ovine / LV&RV | Anterior and posterior regions of LV and RV | Healthy LV:<br>Fiber: 113 kPa<br>X-fiber: 23 kPa<br>Healthy RV:<br>Fiber: 100 kPa<br>X-fiber: 40 kPa | 117* |
| Tensile test | Ovine / RV | RV free wall | Healthy RV:<br>L: 10–1000 kPa<br>C: 30–2000 kPa<br>Hypertensive RV:<br>L: 80–2000 kPa<br>C: 30–3000 kPa | 118 |
| Tensile test | Neonatal porcine / LV&RV | Anterior aspect of LV and RV free walls | Healthy LV:<br>Fiber: 10–200 kPa<br>X-fiber: 100–200 kPa<br>Healthy RV:<br>Fiber: 100–200 kPa<br>X-fiber: 50–150 kPa | 119 * |
| Tensile test | Human / LV&RV | Mid ventricular region of myocardial free wall where muscle structure is uniform | Diseased LV: 70–120 kPa<br>Diseased RV: 80–160 kPa | 106 * |
| Tensile test | Human / LV, RV, and Septum | N/A | Diseased LV:<br>Fiber: 80–280 kPa<br>X-fiber: 80–160 kPa<br>Diseased Septum:<br>Fiber: 80–320 kPa<br>X-fiber: 40–200 kPa<br>Diseased RV:<br>Fiber: 160–280 kPa<br>X-fiber: 120–240 kPa | 96 * |

As seen in Table 6.3, depending on the selected ‘modulus’ range, the *in vitro* experiments may lead to a different conclusion on the mechanobiology of cardiac or stem cells. A few studies have used AFM to derive the mechanical properties of myocardium tissues in small animals (rats, mice, quail)[105, 112-114]. From these studies, healthy ventricular tissue was reported to have Young's moduli in the range of ones to tens of kPa. Such mechanical data have been frequently used in the in vitro experimental design as the 'native myocardium stiffness'[16, 105, 114, 120]. On the other hand, elastic moduli obtained from tensile mechanical tests are in the range of tens to hundreds of kPa range in the same species[106, 108, 109]. These values are consistent with measurements in large animal species and humans[96, 106, 110, 117, 119]. While most of the prior cardiac tissue engineering studies have adopted the elastic modulus of the matrix as < 60 kPa[16, 114, 121-124], the findings on the cellular response should be confirmed in a more physiologically relevant stiffness range.

### 6.1.7 *In Vitro* Studies: Matrix Mechanics Dependent Cellular Functions in Regenerative Research

The extracellular matrix or scaffold provides a "house" for cells and can regulate the cellular function and behavior via cell–matrix interactions. The mechanical cues with which cells experience are intimately related with the microstructure of the scaffold. A well-known example is that stem cells differentiate into specific lineages (from neurogenic to osteogenic) depending on the relevant mechanical properties of the matrix (from brain to collagenous bone) [16]. Indeed, the influence of matrix mechanics on stem cell behavior or its secreted exosomes has been reported in numerous types of biological tissues. To date, the current cardiac mechanobiology research is performed in a variety of matrix mechanical stiffnesses (macro-scale mechanical measurements). In this section, we will mainly discuss the few mechanobiology studies using electrospun scaffolds (**Table 6.1**). In this section, the purpose of our discussion is to highlight the importance of matrix mechanical properties in cellular functions (not limited to progenitor cells), and to raise awareness of the scaffold mechanical properties in future study designs.

To find the optimized chemical and mechanical properties of an electrospun sheet for infarcted myocardial regeneration, Gupta et al. examined the differentiation of embryonic stem cells (ESCs) into cardiomyocytes in different combination of polymers (polyethylene glycol (PEG), poly(ε-caprolactone (PCL), and negatively-charged, carboxylated PCL). Interestingly, they found that it was not the hydrophilic but the elastic property of the scaffold that mostly affected the cardiac differentiation of ESCs. On the softest substrate (4% PEG - 86% PCL - 10% carboxylated PCL), the ESCs had the highest α-myosin heavy chain expression and intracellular calcium signaling dynamics as well as optimal functional cardiomyocytes [21]. Their data indicated that ESC-derived cardiomyocyte differentiation and maturation can be promoted by tuning the mechanical properties of the polymer scaffold. More importantly, the optimal electrospun scaffolds had a Young's modulus of 0.71 MPa (compared to others scaffolds of stiffness up to 0.98 MPa). The stiffness range adopted in this study is similar that of the infarcted myocardium and thus the findings are translational in the prediction of regenerative outcomes.

Another nice experimental study that demonstrated the importance of matrix mechanical properties was the investigation of cellular responses to different 3D scaffolds composed of the same ECM components (decellularized porcine myocardium)[94]. Using different fabrication methods, a decellularized patch, electrospun ECM scaffold, and hydrogel ECM were produced and hMSCs and iPSC-derived cardiomyocytes (iPSC-CMs) were separately cultured on these scaffolds. The 'stiff' electrospun scaffold (E = 203 kPa vs. E = 137 kPa from decellularized patch or 0.026 kPa from hydrogel) led to maximal cell viability after 28 days of hMSC culture. Furthermore, the iPSC-CMs presented the maximal expression of connexin-43 when cultured on the 'stiff' electrospun scaffolds after 14 days, indicating an enhanced myocyte function. However, the cardiac troponin I expression was minimal in the cells cultured in these scaffolds, indicating a reduced contractile function. While this study strongly advocates for the investigation of the effects of scaffold mechanical properties in cardiac regeneration, similar in vitro research is rarely found. Overall, the cellular response to matrix mechanical properties in the context of cardiac tissue engineering is a largely unexplored area of research, and further investigations using electrospun scaffolds are still warranted.

Other relevant matrix mechanical properties include fiber alignment and 3D structure. The alignment of microfibers has been shown to affect cardiomyocyte behavior[37]. Kai et al. demonstrated that rabbit cardiomyocytes cultured on aligned scaffolds better promoted cell attachment and alignment than those on the randomly aligned scaffolds[88]. Moreover, the design of a 3D scaffold confers the advantage of closely mimicking the orthotropic structure of native myocardium. From such electrospun scaffolds, Wu et al. showed that the 3D structure conferred greater cardiomyocyte alignment, elongation, and functional maturation over a 2D scaffold structure[36]. Therefore, these findings suggest it is critical to include the 3D mechanical property into the scaffold design, with the goal of eliciting a constructive healing response (e.g., anti-inflammatory, angiogenesis, anti-oxidant, etc.) and leading to appropriate cardiac tissue restoration.

The matrix mechanics, which are measured on a macro-scale, are linked to the microstructure of the matrix with which the cells interact. While biomaterials are commonly designed to mimic the tissue of interest on a macroscale level, the micro- or mesoscales are less considered. Ultimately, the cells interact with the matrix at the micro- or mesoscale, and therefore these smaller scales should also be considered in the design of biomimetic matrices as well[86, 125]. D'Amore et al. showed that scaffolds with similar macroscopic biaxial mechanical properties—but different mesoscale topology (i.e., lower fiber intersection density)—resulted in a higher amount of ECM synthesis from smooth muscle cells[125]. This finding was attributed to a change in the cell nuclear aspect ratio. Other studies have developed models that can help to determine the effects of fabrication variables, topology, and geometries on macroscopic mechanical test data using image analysis algorithms alone or in combination with finite element modeling[86, 126-128]. These efforts are a push to understand materials across multiple scales in order to more closely and comprehensively mimic the native tissues from micro- to macroscale. This consideration in scaffold design will then provide a more precise and accurate control of the mechanobiology in cardiac tissue engineering.

### 6.1.8 Are Current Scaffolds Mechanically Biomimetic Enough?

Besides the lack of consensus of the appropriate physiological mechanical property (i.e., elastic modulus), the neglect of other mechanical factors also hampers the complete understanding of mechanobiology in cardiac tissue engineering. The first limitation is the neglect of the non-linear elastic mechanical behavior of cardiac tissue, and thus only a narrow range of elasticity has been chosen to represent the mechanical environment of the tissue. It is known that the myocardium is a non-linear elastic, anisotropic material[110, 116, 117]. The full capture of the native tissue's non-linear elasticity should incorporate a spectrum of mechanical properties (e.g., from systole to diastole) in the design of biomimetic scaffolds. Next, the cellular response has been mostly investigated in a 'static' mechanical condition, whereas in physiological conditions the tissue is under cyclic stretch due to the rhythmic heartbeat. To date, only one pioneering study was performed to reveal how cardiomyocytes respond to the dynamic mechanical environment using electrospun silk fibroin scaffolds: it is found that the cyclic stretching (at 10% strain; 1 Hz) along the cell orientation resulted in cardiomyocyte alignment and formation of sarcomeres and gap junctions [64]. Such cellular responses were not observed in cardiomyocytes with the mechanical stimulation perpendicular to the cell orientation. Thus, the consideration of viscoelastic behavior in electrospun scaffolds would advance the understanding of mechanobiology in myocardial tissues. Overall, future studies should consider constructing scaffolds with more realistic mechanical behavior similar to that of native tissue and investigate the mechanobiology of cells under more physiologically relevant mechanical environments.

### 6.1.9 Conclusion and Other Future Perspectives

In this paper, we reviewed the applications of electrospun scaffolds in the myocardial healing process which partially achieve restored functional cardiac tissue. While most prior reviews on electrospun scaffolds focus on the biochemical aspects or fabrication methodologies, we would like to bring attention to <u>the mechanical aspects and effects</u> of the scaffolds in cardiac tissue and regenerative engineering. We briefly go over the electrospinning method, the characterization of mechanical properties with the commonly used methods, and the in vitro and in vivo studies of the application of electrospun scaffolds in cardiac research. We point out the discrepant reports of mechanical properties due to different methodologies (especially between the AFM and tensile mechanical tests), as well as the lack of consensus of the appropriate mechanical properties of the scaffolds to represent the physiological and pathological conditions of the myocardium. Future research should take into consideration the effect of substrate/scaffold mechanical properties on cardiac tissue regeneration.

In addition to the consideration of mechanical and translational aspects as discussed above, other directions are proposed here as well. Firstly, the fabrication of 3D scaffolds with similar anatomic structure of the cardiac tissue (e.g., helically aligned scaffolds) is suggested, which would allow researchers to create a more realistic in vitro model of the ventricle as both transmural and anatomical regional variations of the fiber orientation can be controlled[35, 129-132]. Second, the design of a more sophisticated and similar physiological mechanical environment is needed. Non-linear elasticity or viscoelasticity of the microfibrous scaffolds have been considered recently but the research is still at the infancy stage. The use of a static mechanical condition in cell culture experiments is not representative of the rhythmic nature of the heart; the dynamic stretch of the scaffold should be included for a more comprehensive study of mechanobiology. Together, the suggested mechanical considerations and other future perspectives will help to strengthen our understanding of cardiac mechanobiology and develop better therapeutics in regenerative medicine. Pertinent to this Aim, the content in this review was used to guide the biomaterial design for an *in vitro* platform to assess MSC mechanobiology to improve heart failure therapies.

## 6.2 Current Status of Myocardial Restoration via the Paracrine Function of Mesenchymal Stromal Cells (MSCs)

### 6.2.1 Emerging Non-differentiating Roles of MSCs in Tissue Regeneration

Mesenchymal stromal cells (MSCs; also known as mesenchymal stem cells) are one of the oldest progenitor cells that have been introduced in medical therapy and tissue restoration[133]. Over the past decades, more than 1000 phase I-III clinical trials worldwide (www.clinicaltrials.gov) have been performed to explore the therapeutic potential of MSCs in a variety of diseases and for different organ systems of the body[134]. MSCs were initially recognized as osteogenic stem/progenitor cells, and attempts were made to differentiate these cells into bone or cartilage in pre-clinical studies to promote tissue restoration[135-137]. One of the first clinical applications of these cells was to promote recovery of hematopoietic stem cells post-transplantation given the major role of these cells in the hematopoietic stem cell niche of bone marrow[133, 138]. Later, regenerative properties of MSCs for non-mesodermal tissues were recognized as a very appealing characteristic of the cells. This led to the expansion of the use of MSCs in other tissue injuries such as in brain and spinal cord diseases[139, 140], impaired kidney[141] and myocardial infarction[142-146].

Although various levels of improvements in organ function have been reported across these studies, it is also found that the ‘progenitor’ function (proliferation and differentiation) of MSCs was of limited scope in these tissues. In cardiac regeneration specifically, although the first *in vitro* differentiation of MSCs to cardiomyocytes was reported in 1999, the *in vivo* evidence has been rare in the literature (see historical review by Yan et al.[147]). Instead, the beneficial effects are mainly attributed to other mechanisms referred to as ‘paracrine’ function[148, 149]. The first evidence in cardiac restoration that the therapeutic improvement was related to the trophic factors released by MSCs rather than cell differentiation and replacement was reported in a rat myocardial infarction study in 2006[150]. To date, in all MSC cell therapy studies, including the recent reports with intact or treated MSCs[24, 151, 152], the beneficial effects of MSCs have pointed to reduced adverse remodeling events (e.g., apoptosis, inflammation, loss of blood vessels), suggesting a paracrine signaling of MSCs in the myocardium. The paracrine theory is also supported by the fact that the beneficial effects of MSCs are observed *in vivo* despite different routes of delivery (local or systemic injections). That is, even with the poor homing or rapid loss of MSCs in the myocardium (lack of MSC differentiation), cardiac improvement is still noted[147]. Since then, various mechanisms by which the MSC secretome promotes cardiac tissue healing and restoration have been explored. Moreover, the use of conditioned medium, which includes extracellular vesicles, is shown to promote healing without transfer of cells and avoids tumorigenic risk and other concerns/limitations of cell therapies. Thus, the concept of cell-free therapy (i.e., using the MSC-derived conditioned medium or extracellular vesicles) became an alternative option in the current trends of regenerative medicine (see previous reviews[148, 153-161]).

The aim of this review is to provide a brief overview on the use of MSC conditioned media (MSC-CM) and MSC-derived extracellular vesicles (MSC-EVs) in myocardial restoration, the potential mechanisms of action of MSC acellular therapy, and the strategies to optimize the paracrine functions of MSC. Prior MSC based studies on both left and ventricles (LV, RV) and ischemic and non-ischemic heart failure are included. While some aspects are shared across different types of tissues or diseases, the individual paracrine effect on myocardial restoration is likely tissue-specific or disease-specific, thereby motivating a customizable MSC derived cell-free therapy in future research.

### 6.2.2 Unique Characteristics of MSCs

MSCs are multipotent cells in various adult tissues that possess diverse properties (pro-angiogenic, immunomodulatory, anti-fibrotic, etc.)[162]. Recently, these cells were renamed as 'mesenchymal stromal cells' because 'mesenchymal stem cell' did not meet the criteria for a stem cell (i.e., a self-renewing cell capable of differentiation into multiple and specialized cell types *in vivo*)[163]. MSCs exist in almost all tissues and can be isolated from bone marrow (BM), adipose tissue, umbilical cord blood, skeletal and heart muscle, pancreas, and many other tissues[162, 164-168]. However, the two most common sources for clinical applications are the bone marrow and adipose tissue[162]. MSCs from adipose tissue are also referred to as adipose-derived stromal cells (ASCs). Bone marrow is easily renewed and adipose is typically abundant or unused, which makes the MSC sourcing from these two tissues readily available and 'off-the-shelf'[157, 162]. Thus, the BM-MSCs and ASCs are ideal candidates for regenerative medicine.

MSCs are the most studied progenitor cells for their paracrine effects. Both MSC conditioned medium (CM) and extracellular vesicles (EV) have been investigated, and the main mechanisms of action identified include promoting re-epithelialization and angiogenesis[169, 170], lowering cell apoptosis and oxidative stress (e.g., heart or kidney)[170-173], reducing tissue (e.g., heart or liver) fibrosis[172, 174-177] or inducing collagen synthesis[178-180], as well as eliciting immunomodulatory and anti-inflammatory regulations[174, 176, 181, 182]. Particularly, the modulation of immune response has raised more attention recently as this feature has shown promise in a wide range of immune-mediated disease clinical trials[183, 184]. Overall, while the paracrine effects have been investigated in a wide variety of diseases including cardiovascular diseases, kidney injuries, liver fibrosis, neurodegenerative diseases and ocular diseases[155], most of the research is still at the preclinical stage. The application of MSC-CM or MSC-EVs in myocardial restoration is very new such that there has been no clinical trial to date. Therefore, in this review, we summarized both *in vivo* preclinical studies and *in vitro* bench work related to myocardial renewal, which are important to pave the way to future clinical applications. Our focus is restricted to the use of MSC-CM or MSC-EVs to repair myocardial abnormalities including left and right-sided heart failures.

### 6.2.3 Acellular Components Derived from MSCs Emerging as a New Therapy

#### *6.2.3.1 Conditioned medium (CM)*

CM is a collection of the supernatant after centrifugation of the harvested medium from cells cultured for a certain period of time. CM contains different cell-secreted products such as soluble molecules and vesicle bound products (i.e., EVs) that include cytokines, growth factors, metabolites, etc[149, 185, 186]. Since the preparation and generation of CM is quite simple, its use has been more widespread than EVs as a cell-free therapy for cardiovascular restoration[171, 183, 187-190]. It is through the injection of MSC-CM into infarcted hearts that Gnecchi et al. first described the paracrine effects back in 2006[150]. The CM offers a quick probing of MSC-EVs potential mechanisms of action. Once a potential paracrine effect is identified with CM, the next logical step is the isolation and characterization of EVs in the CM to further elucidate the functional molecules.

### *6.2.3.2 Extracellular vesicles (EVs)*

EVs are a collection of different size lipid membrane bound vesicles released by a cell. EVs are released by many cell types and known to play important roles in cell-cell communications or pathogenesis[191-193]. Various EVs released by resident cells in cardiac tissues in physiology and pathology can be found here[161]. These microvesicles are lipid membrane bound and serve as vehicles to carry different types of cargos (lipids, proteins, cytokines, growth factors, miRNA, etc.)[194-198]. Based on the size of vesicles, EVs are classified into exosomes (with a size of 50-100/200 nm), microvesicles (MVs, with a size of 100/200-1000 nm) and apoptotic bodies (with a size of 50-5000 nm)[191, 192, 199]. The apoptotic bodies are involved in apoptosis by presenting the contents to macrophages for cell engulfation[192] and will not be a matter of further discussion in this review. In contrast, the other two types of EVs (i.e., exosomes and MVs) are involved in intercellular communications and emerged as a new, cell-free regenerative therapy for different diseases.

EVs are classically isolated using ultracentrifugation methods (centrifuging at $10^3 – 10^5$ rpm) from CM supernatants, but there are also methods which employ ultrafiltration (by porous membranes or concentration gradients), fractionation, size-exclusion chromatography, coprecipitation, immunoaffinity, or microfluidics[194, 200, 201]. However, any isolation method needs to be evaluated based on the yield, purity, and efficiency[200]. It has been reported that PEG-based precipitation has the highest yield[202], density gradient ultracentrifugation is the current gold standard for purification[203], and that any of the aforementioned methods can take hours to days to complete[200].

After isolation, the EVs will be characterized by assessing morphology or their physical or chemical properties[200, 201]. The gold standard is the use of transmission electron microscopy (TEM) to study exosome morphology[200]. Alternative methods include scanning electron microscopy (SEM), cryogenic electron microscopy, and atomic force microscopy (AFM). EV detection methods include nanoparticle tracking analysis (NTA) to quantify the concentration and size distribution, western blot to delineate protein molecular weight profile and biological properties, asymmetric-flow field-flow fractionation technology to quantify their hydrodynamic and density properties, resistive pulse sensing to quantify electrical resistance, and flow cytometry for detection of their membrane markers. Most EVs, including those from MSCs, have a set of binding proteins that have an affinity to other ligands or cell membranes, or the extracellular matrix. For MSCs, these proteins include members of the tetraspanin family (e.g., CD9, CD63 and CD81)[155, 170, 172, 192]. Therefore, the antibodies for these proteins are used to identify or separate the EVs. We refer the readers to other reviews for more detailed information on EV isolation and characterization, including the advantages and disadvantages of the above methods[158, 159, 193].

#### *6.2.3.3 Advantages of cell-free therapy*

The cell-free therapy using CM or EVs has several advantages. First, it is a copycat of ‘nature’s delivery system’ that allows for the delivery of biological molecules without endosomal pathway or lysosomal degradation. The cargo can enter into the cytoplasm (a.k.a. internalization of EVs into the cells) more efficiently and effectively to induce the desired therapeutic effects. There is also less of a concern about potential immune responses[191]. It is important to note that every effort should be made for the use of CM or exosomes to be xeno-free, to alleviate safety issues and variability associated with serum[204]. Second, through appropriate ‘pre-conditioning’ of MSCs, it is possible to regulate and derive desired EVs to elicit specific responses in the host environment. For instance, anti-inflammatory profiles of EVs can be enhanced from MSCs cultured in specified conditions and then delivered to an inflamed tissue region[205]. Third, the delivery of EVs instead of MSCs can avoid unwanted differentiation or tumorigenic (pathological proliferation) responses, which makes regenerative therapy more controllable and safer to the patients. Finally, the use of MSC-EVs may overcome the shortcomings that are due to loss of viability during freeze-thawing of cells[206], inconsistent doses of MSCs[134], inhomogeneous distribution with injection issues[201], and inefficient cell homing[184] with current administration methods.

#### *6.2.3.4 Challenges of cell-free therapy*

However, it should be noted that there are a number of challenges for the application of MSC CM or EVs. These include the inadequate understanding of the following aspects: 1) characterization of the components of the CM or EVs, 2) the optimal/standard of preparation, isolation and storage of EVs, 3) the optimal doses and delivery routes of CM or EVs, 4) the bio-distribution, toxicity and clearance of EVs, and 5) the unclear long-term safety and therapeutic effects. These challenges are relatively universal for all types of EVs therapeutics, and the readers are recommended to these reviews for more detailed discussions related to clinical applications[157, 207-209]. Due to limited information on the clinical trials of acellular therapy in cardiac regeneration, our review here mainly focuses on the challenges on the mechanisms of action and the mechanical regulation of MSC-EVs.

The specific challenges for myocardial restoration are discussed more in-depth in Sections 6.2.4&6.2.5. Since the cell-free therapy for cardiac restoration is at an infancy stage, we summarize all preclinical and clinical studies using CM or EVs of MSCs in the following Tables as an overview of the field. Table 6.4 summarizes the *preclinical* studies on the regenerative therapy of myocardium infarction (MI), using CM or EVs from intact or genetically altered MSCs. Compared to the direct use of MSCs, the administration of cell-free products from MSCs in clinical trials of any etiology of heart disease patients does not exist (from *ClinicalTrials.gov*). The most recent clinical trials of heart failure patients with MSCs are still cell-based therapies[210, 211]. Therefore, we only list the *clinical trials* using EVs and CM of MSCs in other non-cardiac diseases in Table 6.5 and Table 6.6, respectively.

**Table 6.4.** Preclinical regenerative therapy studies for infarcted myocardium (in left ventricle) using MSC conditioned medium (CM) or isolated MSC extracellular vesicles (EVs). hMSC: human mesenchymal stromal/stem cells; ESC: embryonic stem cells; BM: bone marrow; UC: umbilical cord; CM: MSC-derived condition medium; IV: intravenous injection; IC: intracoronary injection; IM: intramyocardial injection; MI: myocardial ischemia/infarction; MI/R: myocardial ischemia/reperfusion.

| **Tissue Target** | **Species** | **MSC Source** | **EVs or CM Preparation** | **Method & Dose** | **Findings** | **Reference** |
|---|---|---|---|---|---|---|
| LV/Acute MI | Rat | Mouse BM | Akt transduction; Concentrated CM (50x) | 250 μL (IM) | Acute effect of reduced infarct size; via regulation of Wnt signaling | Mirotsou et al.[189] |
| LV/Acute MI/R | Porcine | Human ESC | Concentrated CM (25x) | 1mL (IV) + 4mL (IC) pre- and post-reperfusion | Acute effects of reduced infarct size and improved function; via decreased oxidative stress and apoptosis | Timmers et al.[171] |
| LV/1-week MI | Rat | Rat BM | CM post 4-day culture | 70 μL (IM) | Chronic effect (4-week) of improved EF in all LVs treated with fresh media, CM and MSCs | Dai et al.[187] |
| LV/Acute MI/R | Mouse | Human ESC | Concentrated CM (25x) or additional HPLC fraction | 3/0.4 μg of proteins in CM/HPLC fraction (IV) | 24hr post MI/R, reduced infarct size in both treated groups | Lai et al.[188] |
| LV/Acute MI/R | Mouse | Human ESC | HPLC fraction of CM (50x) | 0.1-0.4 μg of proteins (IV) | Chronic effect (4-week) of reducing dilation and improving function, reduced inflammation | Arslan et al.[212] |

| | | | | | | |
|---|---|---|---|---|---|---|
| LV/Acute MI | Rat | Human BM | Ultracentrifugation | 80 µg of proteins (IM) | 2-day or 4-week post injection, improved cardiac function and angiogenesis | Bian et al.[169] |
| LV/Acute MI | Rat | Rat BM | Isolated by ExoQuick-TC (50-100 nm) | 80 µg of exosome (IM) | 4-week post injection, reduced fibrosis and inflammation and improved function | Teng et al.[174] |
| LV/Acute MI | Rat | Rat BM | GATA-4 transduction; isolated by ExoQuick-TC | Exosomes from 4x$10^6$ MSCs (IM) | 4-week post injection, reduced apoptosis and fibrosis and improved function | Yu et al.[172] |
| LV/48-hour MI | Mouse | Mouse BM | GATA-4 transduction; serum-free, isolated by ExoQuick TC | 20 µg of exosome (IV) | Up to 4 days post injection, reduced apoptosis and improved function and angiogenesis | He et al.[213] |
| LV/7-day MI | Rat | Rat BM | CXCR4 transduction; isolated by ExoQuick-TC | Exosome-treated MSCs delivered by CellSheet | 4-week post treatment, reduced apoptosis and improved function and angiogenesis | Kang et al.[170] |
| LV/Acute MI | Mouse | Mouse BM | Ultracentrifugation/ ExoQuick Exosome | 1 µg of exosomes (IM) | Ischemic preconditioning for MSC exosome production led to reduction of cardiac fibrosis | Feng et al.[214] |
| LV/Acute MI | Rat | Human UC | Ultracentrifugation | 400 µg of exosomes (IV) | 4 weeks after administration, improvement of cardiac systolic function, reduction of cardiac fibrosis, promotion of tube formation, | Zhao et al.[215] |

| | | | | | | |
|---|---|---|---|---|---|---|
| | | | | | and migration of endothelial cells | |
| LV/Acute MI/R | Rat | Rat BM | Ultracentrifugation | 400 μg of exosomes (IV) | Ischemic myocardium protected through Wnt/β-catenin signaling pathway to effect antiapoptotic and prosurvival effects | Cui et al.[216] |
| LV/Chronic MI | Porcine | Human BM | Ultracentrifugation | 50 μg of exosomes (IM) | Enhanced capillary and arteriolar growth; activated by protein kinase B/eNOS and mitogen-activated protein kinase signaling; increased cardiac output and stroke volume | Potz et al.[217] |
| LV/Chronic MI | Porcine | Human BM | Ultracentrifugation | 50 μg of exosomes (IM) | Promoted angiogenesis and improved cardiac function (cardiac output and stroke volume) | Scrimgeour et al.[218] |
| LV/Chronic MI | Mouse | Mouse BM | Ultracentrifugation | IV | Increased angiogenesis, reduced LV dilation and fibrosis | Wang et al.[219] |
| LV/Acute MI | Rat | Rat BM | Total Exosome Isolation Kit | 20 μg of exosomes (IM) | Inhibited cardiac fibrosis and inflammation and improved LV function | Shao et al.[220] |
| LV/Acute MI | Rat | Human UC | hMSCs transfected with activated Akt; Ultracentrifugation | 20 μg of exosomes (IV) | Increased angiogenesis and improved LV function | Ma et al.[221] |
| LV/Acute MI/R | Mouse | Mouse BM | Ultracentrifugation | 20 μg of exosomes before MI/R (pericardial sac injection) | Cardioprotection against MI through repression of genes involved cell death | Luther et al.[222] |

| | | | | | | |
|---|---|---|---|---|---|---|
| LV/Chronic MI | Rat | Rat Adipose | ExoQuick-TC | 400 µg of exosomes (IV) | Cardioprotection through reduced apoptosis, inflammation, fibrosis and increased angiogenesis | Luo et al.[223] |
| LV/Acute MI/R | Rat | Rat BM | Total Exosome Isolation Reagent | 5 µg of exosomes (IM) | Reduced apoptosis and myocardial infarct size and improved heart function | Liu et al.[224] |

**Table 6.5.** Clinical trials using MSC-Extracellular Vesicles (EV) for safety or efficacy as a treatment of various non-cardiac diseases.

| ClinicalTrials.gov Identifier | Official Title | Sponsor | Exosome/EV Preparation | Dose/route | Enrollment |
|---|---|---|---|---|---|
| NCT03857841 | A Safety Study of IV Stem Cell-derived Extracellular Vesicles (UNEX-42) in Preterm Neonates at High Risk for Bronchopulmonary Dysplasia | United Therapeutics | EVs secreted from human bone marrow-derived MSCs suspended in phosphate-buffered saline | 20, 60, and 200 pmol/phospholipid /kg body weight of UNEX-42 | 18 |
| NCT04173650 | A Safety Study of the Administration of MSC Extracellular Vesicles in the Treatment of Dystrophic Epidermolysis Bullosa Wounds | Aegle Therapeutics | AGLE 102: Allogenic derived EV from normal donor MSCs | Applied topically to body for period of 60 days | 10 |
| NCT03608631 | Phase I Study of Mesenchymal Stromal Cells-Derived Exosomes With KrasG12D siRNA for Metastatic | M.D. Anderson Cancer Center | MSC-derived Exosomes with KRAS G12D siRNA | IV of MSC-derived Exosomes with KRAS G12D siRNA over 15-20 minutes on days 1, 4, and 10. Treatment repeats every 14 days for | 28 |

| | | | | | |
|---|---|---|---|---|---|
| | Pancreas Cancer Patients Harboring KrasG12D Mutation | | | up to 3 courses in absence of disease progression or unacceptable toxicity | |
| NCT03384433 | Safety and Efficacy of Allogenic Mesenchymal Stem Cells Derived Exosome on Disability of Patients With Acute Ischemic Stroke: a Randomized, Single-blind, Placebo-controlled, Phase 1, 2 Trial | Isfahan University of Medical Sciences | Allogenic MSC-derived exosome enriched by miR-124 | CVA patients who have disability will receive 200 microgram total protein of allogenic MSC-generated exosome transfected by miR-124, one month after attack, via stereotaxis | 5 |
| NCT04276987 | A Pilot Clinical Study on Aerosol Inhalation of the Exosomes Derived From Allogenic Adipose Mesenchymal Stem Cells in the Treatment of Severe Patients With Novel Coronavirus Pneumonia | Ruijin Hospital | Exosomes derived from allogenic adipose MSC (MSCs-Exo) | Conventional treatment and aerosol inhalation of MSCs-derived exosomes treatment participants will receive conventional treatment and 5 times aerosol inhalation of MSCs-derived exosomes (2.0*10E8 nano vesicles/3 ml at Day 1, Day 2, Day 3, Day 4, Day 5). | 30 |
| NCT04313647 | A Tolerance Clinical Study On Aerosol Inhalation of Mesenchymal Stem Cells Exosomes In Healthy Volunteers | Ruijin Hospital | Exosomes derived from allogenic adipose MSC (MSCs-Exo) | 1X level of MSCs-Exo (2.0*10E8 nano vesicles/3 ml)<br>2X level of MSCs-Exo<br>4X level of MSCs-Exo<br>6X level of MSCs-Exo<br>8X level of MSCs-Exo | 27 |

| | | | | | |
|---|---|---|---|---|---|
| | | | | 10X level of MSCs-Exo | |
| NCT04356300 | Exosome of Mesenchymal Stem Cells for Multiple Organ Dysfuntion Syndrome After Surgical Repaire of Acute Type A Aortic Dissection: a Pilot Study | Fujian Medical University | Umbilical cord-derived MSC exosome | Exosome of MSC at a dose of 150mg will be given intravenously to Patients in the exosome of MSC arm once a day for 14 times. | 60 |
| NCT03437759 | Mesenchymal Stem Cells Derived Exosomes Promote Healing of Large and Refractory Macular Holes | Tianjin Medical University | MSCs were isolated from human umbilical cord, and MSC-Exosomes were isolated from supernatants of MSCs via sequential ultracentrifugation | After air-liquid exchange, 50μg or 20μg MSC-Exo in 10μl PBS was dripped into vitreous cavity around MH, leaving 20% SF6 or air as tamponade. | 44 |
| NCT04213248 | Effect of Umbilical Mesenchymal Stem Cells Derived Exosomes on Dry Eye in Patients With Chronic Graft Versus Host Diseases | Zhongshan Ophthalmic Center, Sun Yat-sen University | uMSC exosomes | Participants will receive artificial tears for 2 weeks to get the normalized baseline, followed by UMSC-exo 10ug/drop, four times a day for 14 days. The follow-up visit will be 12 weeks. | 27 |
| NCT04388982 | Open-Label, Single-Center, Phase I/II Clinical Trial to Evaluate the Safety and the Efficacy of Exosomes Derived From Allogenic Adipose Mesenchymal Stem Cells in Patients With | Ruijin Hospital | Exosomes derived from allogenic adipose MSC | 1. low dosage MSCs-Exos administrated for nasal drip Dosage (5 μg MSCs-Exos/1 mL twice a week for 12 weeks)<br>2. mild dosage MSCs-Exos administrated for nasal drip Dosage (10 μg MSCs-Exos/1 mL twice a week for 12 weeks) | 9 |

| | | | | | |
|---|---|---|---|---|---|
| | Mild to Moderate Dementia Due to Alzheimer's Disease | | | 3. high dosage MSCs-Exos administrated for nasal drip Dosage (20 µg MSCs-Exos/1 mL twice a week for 12 weeks) | |
| NCT02138331 | Phase 1 Study of The Effect of Cell-Free Cord Blood Derived Microvesicles On β-cell Mass in Type 1 Diabetes Mellitus (T1DM) Patients | General Committee of Teaching Hospitals and Institutes, Egypt | Cell-free cord-blood-derived MSC [CB-MSC] microvesicles | Exosomes: (Size) 40-100 nm, (markers) CD63, CD9, Alix, TSG 101, HSP 70<br>Microvesicles: (Size) 100-1000 nm, (markers) Annexin V, Flotillin-2, selectin, integrin, CD40 metalloproteinase | 20 |
| NCT04491240 | The Protocol of Evaluation of Safety and Efficiency of Method of Exosome Inhalation in SARS-CoV-2 Associated Two-Sided Pneumonia | State-Financed Health Facility "Samara Regional Medical Center Dinasty" | MSC-derived exosomes | 1. EXO 1 inhalation<br>Twice a day during 10 days inhalation of 3 ml special solution contained 0.5-2x$10^{10}$ of nanoparticles (exosomes) of the first type.<br>2. EXO 2 inhalation<br>Twice a day during 10 days inhalation of 3 ml special solution contained 0.5-2x$10^{10}$ of nanoparticles (exosomes) of the second type. | 90 |

**Table 6.6.** Clinical trials using MSC conditioned medium (CM) for safety or efficacy as a treatment of various non-cardiac diseases.

| ClinicalTrials.gov Identifier | Official Title | Sponsor | CM Preparation | Dose/route | Enrollment |
|---|---|---|---|---|---|
| NCT04134676 | Therapeutic Potential of Stem Cell Conditioned Medium on Chronic Ulcer Wounds : Pilot Study in Human | Sukma Skin Treatment | The soluble components of the secretome are separated from the microvesicle fraction by centrifugation, filtration, polymer precipitation-based methodologies, ion exchange chromatography and size-exclusion chromatography. | In this group, the subjects will use Conditioned Medium topical therapy for 2 weeks The Conditioned Medium gel will be applied to the wound and closed by transparent dressing. | 38 |
| NCT04314687 | Allogeneic Umbilical Cord Mesenchymal Stem Cells and Conditioned Medium for Cerebral Palsy in Children | PT. Prodia Stem Cell Indonesia | The umbilical cord was removed from the donor and brought to cell culture facility immediately. Upon arrival, pre-sterility sample testing was performed to ensure the sample was free from contaminant. Every batch of the cells was monitored by a series of quality control testing to assure the quality of the product. | MSC + CM administered via injection | 78 |

|  |  |  |  |  |  |
|---|---|---|---|---|---|
|  |  |  | Conditioned medium collected from umbilical cord MSC (UC-MSC) cultured. |  |  |
| NCT04326959 | Implantation of Mesenchymal Stem Cell, Conditioned Medium, or Triamcinolone Acetonide for Keloid Regression: Immunohistochemistry, Histopathology and Imaging Study | PT. Prodia Stem Cell Indonesia | Injection of Allogeneic Umbilical Cord Mesenchymal Stem Cells. 2 million cell/$cm^3$ in NaCl 1 cc/million cell and booster with Conditioned Medium 1 cc/$cm^3$ in 3 weeks later.<br>Conditioned Medium Injection of Conditioned Medium 1 cc/cm3 and booster with Conditioned Medium 1 cc/$cm^3$ in 3 weeks later. All treatment via intralesional injection. The maximum size of the keloid is 15 cm. | A patient will be given UC-MSCs 2 million cells / $cm^3$. After 3 weeks, the patient will be given CM 1 cc / $cm^3$. The maximum size of Keloid is 15 cm per patient.<br>All treatment via intralesional injection. The maximum size of the keloid is 15 cm. | 24 |
| NCT04235296 | Evaluation of the Safety and Effectiveness of Mesenchymal Stem Cell Conditioned Medium-derived Pleiotropic Factor in Treating Residual Burn Wound | Chinese PLA General Hospital | MSC CM-derived pleiotropic factor | Residual wounds from the same person were divided into control group and experimental group. The pleiotropic factor is | 30 |

| | | | | | |
|---|---|---|---|---|---|
| | | | | used to control group. Then the foam wound dressing was selected to cover the residual wound, and the dressing was changed every 2 days. | |
| NCT04314661 | Comparative Effectiveness of Arthroscopy and Non-Arthroscopy Using Mesenchymal Stem Cell Therapy (MSCs) and Conditioned Medium From Mesenchymal Stem Cell Culture (MSCs) for Osteoartrithis With Controlled Randomization in Phase I/II | PT. Prodia Stem Cell Indonesia | Umbilical cord MSC CM | Injection with Allogeneic Umbilical Cord MSC 5 million cells in NaCL 5 cc, two weeks later injection with Conditioned Medium Derived Umbilical Cord MSC 2 cc/knee, four weeks later injection with Conditioned Medium 2 cc/knee. All injection via Intraarticular injection. | 15 |
| NCT04234750 | The Evaluation of the Safety and Effectiveness of Mesenchymal Stem Cell-derived Pleiotropic Factor in the Treatment of Donor Sites | Chinese PLA General Hospital | MSC CM-derived pleiotropic factor | The two donor areas of the same patient were divided into a pleiotropic factor group and a blank group randomly. After | 20 |

|  |  |  |  |  |  |
|---|---|---|---|---|---|
|  |  |  |  | placing a coarse mesh vaseline oil gauze, then cover a certain thickness of sterile gauze and pressure bandage. |  |
| NCT04315025 | Safety Issues of Peribulbar Injection of Umbilical Cord Mesenchymal Stem Cell (UC-MSC) in Patients With Retinitis Pigmentosa | PT. Prodia Stem Cell Indonesia | Umbilical cord MSC conditioned medium | A total 2 ml volume of Conditioned Medium derived Umbilical Cord MSC will be injected by peribulbar | 18 |
| NCT03676400 | Clinical Study for the Assessment of the Hair Growth Efficacy and Safety of a Cosmetic Investigational Product, After Repeated Applications for 24 Weeks, Under Normal Conditions of Use, in the Asian Adult Subjects With Androgenic Alopecia | Medipost Co Ltd. | Conditioned media of umbilical cord blood-derived stem cells | NGF-574H is hair serum with 5% conditioned media of umbilical cord blood-derived stem cells containing various trophic factors that help alleviate hair loss.<br>NGF-574H will be directed to use on hair and scalp by subject her/himself at home twice a day (in the morning and evening) for 24 weeks. | 84 |

| | | | | | |
|---|---|---|---|---|---|
| NCT04398303 | A Phase 1/2 Randomized, Placebo-Controlled Trial of ACT-20 in Patients With Severe COVID-19 Pneumonia | Aspire Health Science | 100 ml of conditioned media | Conventional treatment plus ACT-20-CM administered intravenously | 70 |
| NCT04235868 | Clinical Trial of Mesenchymal Stem Cell-derived Pleiotropic Factor in Treating Non-healing Wounds | Chinese PLA General Hospital | All the bioactive factors and cytokines in MSCs secretions constitute can be collected in the conditioned medium. In here, stem cell-derived conditioned medium was further made into a lyophilized powder. | After debridement, the wounds in experimental group apply stem cell-derived lyophilized powder, and use foam dressing to wrap the wound; apply once every 2-3 days. | 30 |

### 6.2.4 MSC Paracrine Effect: Mechanisms of Action and Potential Enhancement Strategies

In this section, we will discuss the known mechanisms of action of MSC paracrine effect in cardiac restoration (for both LV and RV) and the various approaches that have been explored to enhance the individual paracrine effect (**Fig. 6.2**). Particularly, we bring in a less considered perspective of the mechanical regulation of the MSC paracrine effect. The homing or proliferation/migration of MSCs can be affected by different molecules or drug and thus paracrine effect is indirectly strengthened/impaired[151, 225, 226]. But this is beyond the scope of our below discussion. The therapeutic outcomes have been demonstrated by preclinical studies, *in vitro* bench work, or both. The miRNAs involved in these mechanisms of action for MSCs as well as other progenitor cells are summarized in recent reviews.[159-161, 193, 197]

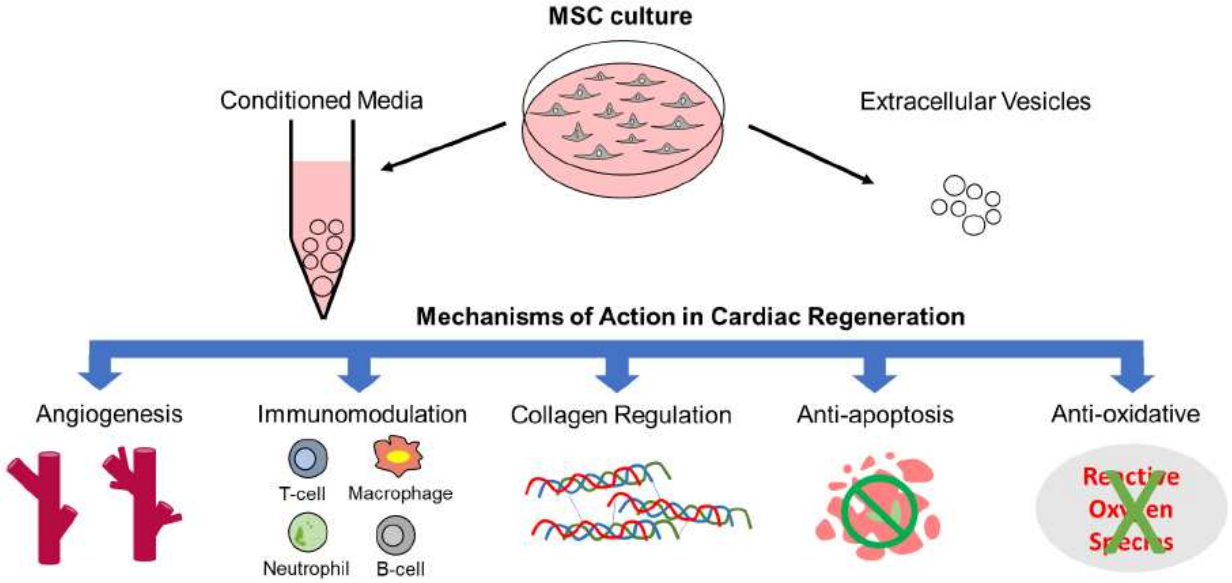

**Figure 6.2**. Various mechanisms of action for MSC paracrine effects from conditioned medium or extracellular vesicles.

### *6.2.4.1 Pro-angiogenic effect*

The products of MSCs contain a variety of pro-angiogenic factors[185, 186] such as vascular endothelial growth factor (VEGF)[123, 227-229], platelet derived growth factor (PDGF)[221], angiopoietin[227], metalloproteases[230] and micro-RNAs (miR-125a[231], miR-377[232]) that potentially promote neovessel formation. The pro-angiogenic effect can be confirmed by downstream events such as the proliferation of human umbilical vascular endothelial cells (HUVECs) or capillary tube formation[169, 170, 174]. This effect is particularly useful for cardiac restoration as cardiomyocytes are very sensitive to reduced blood perfusion because of the reliance on oxygen supply. In a sudden blockage of the coronary artery (acute infarction), the cardiomyocytes may die within minutes[233, 234]. In chronically infarcted myocardium, the central zone of infarction becomes decellularized and fibrotic. The re-distribution of blood supply to this region is key to cardiomyocyte re-population and function recovery. Indeed, an increase in pro-angiogenic factors has been found to promote

LV healing[169, 213]. In non-ischemic heart failure such as pulmonary hypertension-induced RV failure, chronic pressure overload causes a reduction in capillary density known as ‘capillary rarefaction’. Capillary rarefaction is a hallmark of ventricular dysfunction[205, 235]. It is postulated that chronic hypoxia triggers a ‘metabolic shift’ of cardiomyocytes and leads to contractile impairment. Preclinical studies with MSC delivery have shown improved RV function associated with restored capillary density[205, 236], suggesting a pro-angiogenic effect of cell therapy.

To date, a number of approaches have been reported to promote the secretion of growth factors via different cell culture conditions or genetic manipulation (i.e., chemical and/or biological priming). For instance, hypoxia stimulation (i.e., 1-5% $O_2$ vs. 21% $O_2$ in normoxia) can enhance the pro-angiogenic effect via the elevated expression of growth factors[237-239]. The stimulatory effect of hypoxia is not limited to BM-MSCs but observed with MSCs from other sources too[239]. This mechanism explains why the delivery of MSCs to the damaged, hypoxic tissue (e.g., infarcted myocardium) elicits pro-angiogenic and healing effects *in vivo*[145, 169, 174]. In addition, MSCs stimulated by nerve growth factor (NGF) are reported to improve cardiac angiogenesis from a mouse MI study. The improvement was due to MSC paracrine effect rather than NGF itself[152]. Another way to enhance the pro-angiogenic effect is via the inflammatory stimulation. The injection of CM from tumor necrosis factor-α (TNF-α)-activated MSCs was observed to promote blood perfusion in the ischemic limb compared with the treatment with CM from control MSCs[240]. In addition, the toll-like receptors (TLR) 2/6 on MSCs can be stimulated by the macrophage-activating lipopeptide of 2kDa (MALP-2), which is a bacterial lipopeptide recognized by the innate immune system. It has been found that CM derived from the MALP-2 stimulated BM-MSCs increased endothelial cell proliferation and vessel angiogenesis *in vitro* and *in vivo*[241]. Lastly, the genetic alteration to induce over-expression of certain proteins (e.g., CXCR-4, GATA-4, Akt, SDF-1α) in MSCs[144, 150, 170, 172] or pharmacological regulation of MSCs (e.g., angiotensin II, diazoxide)[143, 242] was used to enhance the angiogenesis effect as well.

The above strategies mainly aim to 'precondition' MSCs via chemical or biological modifications. In contrast, strategies that involve mechanical stimulation to 'prime' MSCs have received much less attention. To date, the following studies adopted different ranges of substrate stiffness and investigated the response in MSC pro-angiogenic function. In varied stiffnesses of hydrogel scaffolds made of poly(ethylene) glycol diacrylate (PEGDA) and gelatin methacrylate (GelMA), BM-MSCs cultured on the matrix with a compressive modulus of 5 kPa had the maximal VEGF expression, which then led to the most HUVEC proliferation and capillary sprouting formation; whereas the BM-MSCs on either higher or lower compressive modulus (at 1 or 23 kPa) matrices did not have the optimal pro-angiogenic effect[123]. Such behavior is similar to the bi-phasic dependence of cell motility on the 2D gel stiffness (i.e., with the highest motility on 3 kPa PDMS and PA gels)[18]. However, this finding is not consistent with other observations. The secretion of VEGF by MSCs is higher in stiffer (15-20 kPa) than compliant (1-2 kPa) matrices made of 2D hyaluronic acid and gelatin mixed gels[229]. Similarly, the maximal expression of trophic factors is reported on stiff 3D polyacrylamide matrix (40 kPa) compared to the softer matrices (0.5 and 10 kPa)[121], and this effect was only observed in the matrigel functionalized with fibronectin, not with collagen I or laminin. But in the Ji et al. study, human MSCs (hMSCs) on soft hydrogel substrates (elastic moduli: 0.5 kPa versus 200 kPa) produced significantly more trophic factors (PDGFA, KGF, Ang-1, IGF-1, VEGF, and bFGF)[243]. Therefore, the maximal pro-angiogenic function of MSCs has been reported in various substrate stiffness and it remains unclear about the response of MSCs in a cardiac specific mechanical environment.

Besides the substrate stiffness range and biochemical composition, another important factor that interferes with the interpretation of these discrepant findings is the quantification of the pro-angiogenic effect. The GelMA-PEDGA study measured the pro-angiogenic capability as the amount of VEGF (in pg) per $10^3$ cells, whereas the other two studies used the concentration of VEGF (in pg/ml) per $10^4$ cells, normalized tube area (formed from HUVECs), or fold increases of RNA expression over the glass culture. Therefore, for a better understanding of the mechanical regulation of pro-angiogenic effects of MSCs, at least one identical measurement as used in previous studies should be adopted for cross-study comparisons.

#### *6.2.4.2 Immunomodulatory effect*

Inflammation or recruitment of inflammatory cells in myocardium has been reported in various etiologies of heart failure and contribute to the pathological remodeling in both left ventricle (LV) and RV[244-246]. Therefore, the immuno-modulatory effect of MSCs is another major mechanistic effect considered to be beneficial in myocardial restoration. In a rat MI model, MSC exosomes decreased inflammatory cell infiltration in the infarct zone[174]. The anti-inflammatory mechanism was partly explained by the *in vitro* observation that MSC exosomes suppress lymphocyte proliferation[174]. In another preclinical study, within the first 3 days of acute MI/reperfusion induction, MSC-derived exosomes reduced the numbers of neutrophils, macrophages and peripheral white blood cells in infarcted mouse ventricles[212]. For more complete summary of MSC's immuno-modulatory paracrine effect, the readers are referred to a recent review by Yan et al. (see **Fig. 6.5** and **Table 6.4**[147]). Below, we will mainly focus on the beneficial effect on macrophages because this paracrine effect is more critical to cardiac repair remodeling, as well as the known biological and mechanical factors that regulate MSC immuno-modulatory paracrine effect.

Because monocyte recruitment is one of the first steps of inflammatory response to tissue injuries, the anti-inflammatory effect of MSCs has been investigated via their effects on activation of circulatory monocytes into tissue macrophages. One consistently observed behavior of MSCs, particularly in the MSC-EVs and MSC-CM, is the promotion of the M2 macrophage phenotype in the activation (polarization) of monocytes[247, 248]. With the treatment of MSC-EVs, the upregulation of M2 (anti-inflammatory) macrophages or downregulation of M1 (pro-inflammatory) macrophages has been observed in numerous disease models, including acute respiratory distress syndrome mouse models[249], the mouse Achilles tendon rupture model[181], the hyperoxia-induced bronchopulmonary dysplasia (BPD)[250], mouse pulmonary fibrosis model[177], mouse colitis model[251], mouse abdominal aortic aneurysm model[252], rat pulmonary arterial hypertension model[253], as well as cardiotoxin-induced skeletal muscle injury model[254]. The altered activation of macrophages can be achieved through soluble factors or miRNA secreted by live MSCs (active mechanism) and via dead MSCs (passive mechanism).

Not surprisingly, the immunomodulatory effect of MSCs is dependent on the external environments. For instance, MSCs activated by lipopolysaccharide (LPS) or tumor-resistant MSCs have altered secretory profiles (e.g., increased IL-10 when activated by LPS) or enhance the migration of monocytes to tumor sites[183]. Higher concentrations of inflammatory cytokines in infarcted myocardium (e.g., IL-1β, TNF-α) can activate the MSCs and polarize them to the immunosuppressive phenotypes[147]. The effect of MSCs on T-cells also depends on the presence of macrophages, which have been observed to prime MSCs towards the production of immunomodulatory factors. This evidence implies that there is a ‘cross-talk’ between the MSCs and macrophages (see review[255]), either from a result of ‘paracrine signaling’ of the exosomes or from the direct ‘cell-cell contact.’

Furthermore, the immunomodulatory effects are regulated by matrix elasticity as well. It is reported that the secretion of IL-8, which is classically associated with the innate immune response, was initially higher in hMSCs seeded on stiff (~20 kPa) matrices compared to the soft (~2 kPa) matrices. However, the difference disappeared after 8 days of culture[229]. In another study, IL-6 and IL-8 were significantly upregulated on soft substrates (10 kPa) compared to that of glass; nevertheless, no significant differences were found between 10 kPa and the 0.5 and 40 kPa hydrogel matrices[121]. Ji et al. showed that hMSCs on soft (~0.5 kPa) substrates produced significantly more immunomodulatory factors (COX2, TSG6, IDO, HGF, HLA-G5, and PGE2) and higher M2 macrophage polarization than those on stiff (~200 kPa) substrates[243]. While the regulation by biophysical cues is a relatively new area of research, these pilot studies provide evidence that the anti-inflammatory paracrine effect is inherently linked with matrix mechanics.

#### *6.2.4.3 Effect on collagen metabolism*

Reduced tissue fibrosis has been reported as a therapeutic effect of MSC-EVs in cardiac[170, 172, 174], lung[177], liver[175], kidney[256] and cornea[176] tissues. Interestingly, in other tissues such as cartilage or tendon, collagen synthesis is considered a beneficial outcome of MSC-EVs as well[180]. Similarly, in the restoration of ischemic myocardium, both reduction[170, 172, 174] and deposition[187] of interstitial collagen in the infarct zone have been reported as a beneficial outcome; in hypertensive ventricular failure, the decrease in collagen is considered a therapeutic outcome[205, 257]. It seems that researchers tend to report all ‘healing events’ that are anticipated for the specific tissue/organ as the effects of MSC-EVs, whereas why both increase and decrease of collagen is seen as a result of treatment remains unclear. Therefore, the exact mechanism of collagen modulation by MSCs awaits further investigation.

#### *6.2.4.4 Anti-apoptotic effect*

Cardiomyocyte apoptosis is a significant problem in advanced stages of heart failure. Therefore, anti-apoptotic strategies are potential therapeutic targets for MI patients. Several studies have shown that the EVs from MSCs with over-expression of GATA-4 or Akt elicited a significant anti-apoptosis effect, which is evidenced by increased cardiomyocyte survival and/or proliferation as well as reduced apoptotic activity (e.g., caspase-3)[150, 172, 189]. But the anti-apoptotic effect of intact MSCs is not commonly reported. To our knowledge, there is only one vascular study addressing the anti-apoptotic effect of untreated MSC-EVs: in a rat model of hypoxic pulmonary hypertension, the human umbilical cord MSC-EVs significantly inhibited endothelial cell apoptosis in pulmonary arteries. The effect was confirmed by *in vivo* and *in vitro* observations[257]. The exact molecular pathways of MSC-EVs anti-apoptotic effect in cardiac or vascular cells awaits further investigation.

#### *6.2.4.5 Anti-oxidative effect*

Oxidative stress is detrimental to cardiomyocytes through many mechanisms including the loss of mitochondria[258]. Therefore, the decrease of oxidative stress by MSC-EVs and MSC-CM was speculated to explain the improved survival of cardiomyocytes in infarcted myocardium[171, 212]. The anti-oxidative effect may be related to the increased expression of superoxide dismutase (SOD). MSCs were shown to secrete SOD3 and reduce levels of reactive oxygen species (ROS) in an *in vitro* model of ischemia-reperfusion injury of ventricular cardiomyocytes[259]. Moreover, SOD-adenovirus-infected MSCs sustained higher SOD3 expression, and the delivery of these MSCs to mouse infarcted myocardium led to a reduction of oxidative stress and improvement of cardiac function[146].

#### *6.2.4.6 Mechanosensing pathways involved in MSC paracrine effect*

A couple of pioneering studies have attempted to identify the mechanosensing pathway associated with the pro-angiogenic effect of MSCs (**Fig. 6.3**). Bandaru et al. demonstrated that the mechanical modulation of hMSCs was through the yes-associated protein (YAP), a transcription factor that localizes to the nucleus from the cytoplasm when MSCs were cultured on stiff substrates[228, 260]. When YAP signaling was inhibited, hMSC pro-angiogenic potential was abolished. Another possible mediator pathway is through the cytoskeleton. Ji et al. showed that the immunosuppressive and trophic function of hMSCs was modulated by the actin polymerization and tension[243]. While these studies help to identify the mechanotransduction pathways, the investigated mechanical range was much lower than the mechanical properties of myocardium. Therefore, the translational implications of these findings need to be confirmed. Further studies should identify and delineate the important genes and pathways involved in the mechanical regulation of other paracrine effects. These findings could serve as the groundwork for the design of *in vitro* substrates with appropriate mechanical properties to optimize the production of paracrine-mediated cell products for cardiac restoration.

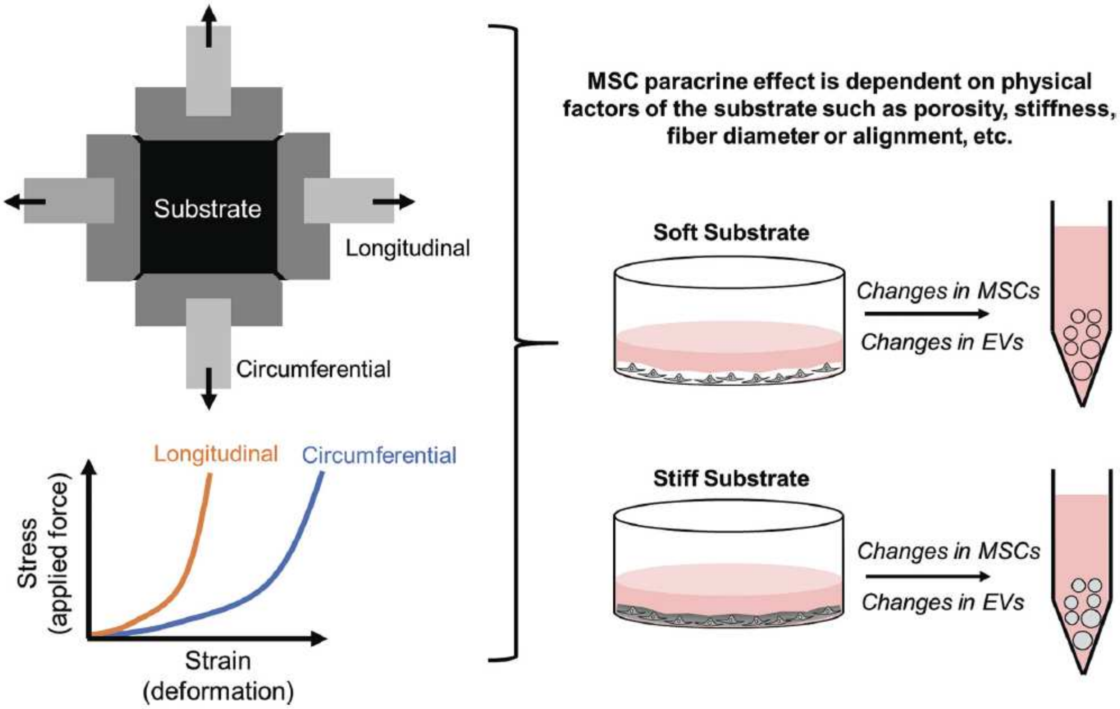

**Figure 6.3**. Mechanical regulation of MSC paracrine effect can be probed by *in vitro* experiments. Left: substrates with varying mechanical properties are fabricated and measured by biaxial tensile/compression tests; Right: substrates are seeded with MSCs to investigate the mechanosensing pathways in MSCs and downstream paracrine effects in EVs.

### 6.2.5 Remaining Challenges of MSC Mediated Paracrine Effects for Cardiac Restoration

Although the application of CM or EVs of MSCs in cardiac restoration is promising, many obstacles remain, including the characterization of the components in these cell products, the further elucidation of mechanisms of action, and the regulatory mechanism of cell products including the mechanical controls. Similar challenges are also discussed in reviews[159-161, 193] or position statements of the International Society for Extracellular Vesicle (MISEV2014 and MISEV2018) and may or may not be specific to cardiac regeneration. In general, the specific molecules responsible for the paracrine effect (e.g., miRNAs and growth factors) and whether they are secreted as free molecules or packed into EVs need to be further investigated. Since more than one paracrine effect are involved, the therapy is likely a ‘cocktail’ treatment and thus the net effect of the mechanisms of action should be evaluated.

Furthermore, as we have pointed out above, some ‘conflicting beneficial effects’ are noted (e.g., the pro-fibrosis versus anti-fibrosis effects). Similarly, both pro- and anti-proliferative roles of MSCs have been identified ‘simply’ from the therapeutic outcomes. In cardiac diseases where capillary rarefaction is a problem, MSCs or their cell products are shown to promote angiogenesis to improve oxygen supply, and thus the pro-angiogenesis role is more discussed[205, 237, 238]; however, in pulmonary arterial hypertension (vascular disease), hyperproliferation of endothelial cells contributes to the narrowing of small pulmonary arteries and disease progression, and thus the anti-proliferative role of MSC-EVs has been reported in hypoxia induced pulmonary hypertension mice or monocrotaline induced pulmonary hypertension mice[257]. A better characterization of the cell products and the mechanism of action should delineate the discrepant function of MSCs in different disease settings.

### 6.2.6 Conclusions

The MSC secretome is an emerging and important exploratory area of research for myocardial repair. This cell-free therapy, when appropriately harnessed, can lead to pro-angiogenic, immunomodulatory, collagen regulatory, anti-apoptotic, and anti-oxidative paracrine effects. Through some or all of the aforementioned pathways, the products released from the MSCs have the potential to promote the healing and renewal of diseased myocardium. However, many unanswered questions still exist: the characterization and preparation of MSC products are far from standardized; the control over the conditioned medium or EVs, particularly in regard to their mechanical regulation, is still relatively unexplored. Further research that aids in comprehensively understanding its paracrine function will ultimately bring about more precise control of therapeutics and make significant inroads towards clinical use. Relevant to this Aim, key knowledge gaps and strategies to improve MSC therapies were summarized in the above review, which were then used to guide the study design of evaluating MSC mechanobiology to enhance heart failure therapies.

## 6.3 Pro-angiogenic Potential of Mesenchymal Stromal Cells Regulated by Matrix Stiffness and Anisotropy Mimicking Right Ventricles

### 6.3.1 Introduction

Right ventricle (RV) failure is common in the advanced stages of pulmonary hypertension and is a useful predictor of mortality in these patients[261]. In the process of chronic pressure overload, the failing RV becomes stiffer, more anisotropic[262, 263], and undergoes global capillary rarefaction leading to myocardial inefficiency[24, 264-266]. Unlike hypertensive remodeling in the left ventricle (LV), capillary rarefaction plays a critical role in hypertensive RV maladaptation[267, 268], and thus pro-angiogenic strategies could potentially offer a RV-specific therapy.

Mesenchymal stromal cells (MSCs) are highly active cells with immunomodulatory and pro-angiogenic paracrine properties[24, 269]. MSCs have been proposed as novel regenerative therapies for various diseases including heart failure[269, 270]. Previous *in vitro* studies have further shown that cell behavior and function, including its pro-angiogenic paracrine effect, are dependent on (tissue) substrate stiffness[121-123, 243, 271, 272]. The mechanical regulation from cues such as substrate stiffness is shown to play a dominant role in guiding MSC proliferation and secretory function compared to biochemical components (e.g., adhesive ligands and/or GAGs)[272]. However, those prior investigations are limited to a stiffness range (0.5-200 kPa)[121-123, 243, 271, 272] that do not encompass the complete range of RV tissue stiffness obtained from rat and ovine *ex vivo* mechanical tests (with the average tensile modulus of healthy and pressure overloaded RVs ranging from ones to thousands of kPa)[263, 273, 274]. Because of the nonlinear elastic behavior (i.e., nonlinear stress-strain curves) of cardiovascular tissues[263, 275, 276], it is imperative to include the MSC response to substrate stiffness at higher physiological strains occurred during diastole to fully evaluate the MSC function related to specific tissue mechanical environments.

Moreover, the myocardium tissue is anisotropic[275, 276]. This means that the tissue elasticity is different in different directions. It has been noted that the RV anisotropy (stronger fiber alignment) increases with pressure overload in the remodeling process[262]. However, most of the MSC culture systems, including hydrogel and tissue culture plastic (TCP) methodologies, use an isotropic substrate. The physiological signature of anisotropy has thus been *ignored* in *in vitro* work. To our knowledge, the only study that examined the effect of substrate anisotropy on MSC pro-angiogenic function compared the effects of random, aligned, and mesh patterns of electrospun fibrous scaffolds on MSCs[277], although the mechanical property (i.e., stiffness) of these scaffolds was not reported. Overall, the regulation of matrix anisotropy property and the potential synergistic effects of stiffness and anisotropy on MSC function are largely unexplored.

Therefore, it remains largely unknown how MSCs respond to substrate stiffness and anisotropy that simulate healthy and diseased RV tissues. Motivated by the knowledge gap and clinical needs, the aim of this study was to investigate the effects of RV-like stiffness and anisotropy on MSC pro-angiogenic function. Tissue engineered constructs offer an opportunity to independently regulate these substrate mechanical factors and investigate the cellular responses. We hypothesize that the pro-angiogenic potential of individual MSCs is highest on the substrate with isotropic, diseased RV-like stiffness. In the present study, a class of nanofiber scaffolds was innovatively fabricated to mimic the stiffness of healthy and diseased RVs and subsequently used to decouple the effects of matrix stiffness and anisotropy. The responses of MSCs to the mechanical factors were examined by vascular endothelial growth factor (VEGF) production, cell numbers, and pro-angiogenic secretome analysis from conditioned media, as well as *in vitro* vessel tube formation assay. Our findings help to elucidate the effects of stiffening and tissue anisotropy on individual MSC pro-angiogenic potential, which will inspire improved preparation and manufacturing of MSCs or the cellular products for cardiac regenerative medicine.

### 6.3.2 Methods

#### *6.3.2.1. Polyester urethane urea (PEUU) synthesis*

Polyester urethane urea (PEUU) was synthesized and purified according to a protocol reported previously[278]. Briefly, 10 g of polycaprolactone diol (Mn 2,000), 1.27 mL of 4-diisocyanatobutane (distilled before use), and catalytic amount of stannous octoate were dissolved in anhydrous dimethyl sulfoxide and reacted at 75°C for 3 h. This prepolymer was further reacted with 0.5 mL putrescine (distilled before use) at 50°C for overnight. The final fine product (PEUU) was obtained after being precipitated in excess cold distilled water, washed with isopropyl alcohol, and dried under vacuum. The inherent viscosity of PEUU was 1.04 dL/g, which was calculated from the equation $\ln\left(\frac{tp}{ts}\right)/Cp$, where ts (s) is the traverse time of 1,1,1,3,3,3-hexafluoro-2-propanol (HFIP), tp (s) is the traverse time of PEUU solution in HFIP at a concentration of 0.1 g/dL, and Cp (g/dL) is the PEUU concentration. The traverse time was measured using an Ubbelohde viscometer at 22 ºC and five repetitions were applied for the calculation.

#### *6.3.2.2. PEUU scaffold fabrication*

The synthesized PEUU was used for fabrication of electrospun scaffolds mimicking RV tissue mechanics. Polyester urethane urea (PEUU)[25] was completely dissolved (w/v%) in HFIP. The solution was then loaded into a 5 mL syringe with a 20-gauge blunt end stainless steel needle

(KT868280-2001; VWR, Radnor, PA). Fibrous scaffolds were then fabricated using a custom electrospinning apparatus with a rotating mandrel (diameter: 7.46 cm). Four different scaffolds mimicking normal (Norm) and failing (Fail) RVs at different degrees of anisotropy (isotropic: Iso; anisotropic: Ani) were successfully fabricated. For the Fail&Iso scaffolds, we mixed soluble 0.5% polyethylene oxide (PEO; 200,000 Mw) with 6% PEUU in HFIP to improve the isotropic behavior and help with the clean removal of the electrospun mat off the foil when soaked in 1X phosphate buffered saline (PBS). The fiber direction of anisotropic scaffolds was aligned with the mandrel direction of rotation and the cross-fiber direction was perpendicular to the mandrel direction of rotation. The fixed parameters used for electrospinning all scaffold groups are: voltage: 16 kV, injection flow rate: 1.5 mL/h, and distance between needle to collector: 9-10 cm. Using the high-strain elastic modulus of rat RVs reported previously, the key parameters leading to the different scaffold groups are listed in Table 6.7.

**Table 6.7.** Key altered parameters for electrospinning of different scaffold groups.

| | **Isotropic (Iso)** | **Anisotropic (Ani)** |
|---|---|---|
| **Normal RV (Norm) (~500 kPa)** | <br>Solution: 12% PEUU<br>Mandrel speed: 100 rpm | 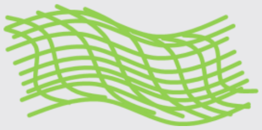<br>Solution: 12% PEUU<br>Mandrel speed: 890 rpm |
| **Failing RV (Fail) (~1000 kPa)** | <br>Solution: 6% PEUU:0.5% PEO<br>Mandrel speed: 1250 rpm | 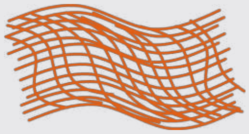<br>Solution: 12% PEUU<br>Mandrel speed: 1250 rpm |

#### *6.3.2.3. PEUU scaffold microstructural measurements*

The average diameter of the electrospun fibers and surface porosity of the scaffolds were quantified from scanning electron microscopy (SEM) (JEOL, Tokyo, Japan) images (n=6-10 per group). Briefly, samples were sputtered with 10 nm of gold prior to SEM imaging. ImageJ (NIH, Betheseda, MD) color thresholding and measurement tools were used for evaluation of porosity and diameter, respectively.

#### *6.3.2.4. PEUU scaffold mechanical measurements*

To obtain the global mechanical behavior, scaffolds (30 mm x 30 mm) were then measured using an in-house biaxial tensile tester after 24 h of 1X PBS soak at room temperature. The fiber and cross-fiber directions were aligned with the biaxial axes. After mounting, samples were stretched to a maximum deformation of strain of 20% at a speed of 3 mm/min. Deformations of graphite powder-speckled samples were tracked with a CCD camera (Nikon, Tokyo, Japan) at 1 frame per second. Biaxial stretch forces were obtained by 50-lb load cells (FUTEK Advanced Sensor Technology, Irvine, CA, USA). The Young's moduli ($E$) along the fiber direction and cross-fiber direction of the scaffolds (n=6-12 per group) were then calculated using linear regression of the stress-strain curve. The anisotropy degree of the scaffold was represented by an anisotropy index calculated as the ratio of the Young's moduli in the fiber direction to the Young's moduli in the cross-fiber direction.

#### *6.3.2.5. MSC culture and cell counting*

Scaffolds were sterilized with 15 minutes of 70% ethanol soak and three subsequent 1X PBS washes. Scaffolds were then soaked in 1X PBS for 24 h prior to cell culture. Human bone marrow MSCs (hMSCs) (Lonza, Basel, Switzerland; or donated from Dr. Steven Dow at Colorado State University) through passage 6 were cultured in Minimum Essential Medium (Cytiva, Marlborough, MA) supplemented with 10% (v/v) fetal bovine serum and 1% (v/v) penicillin-streptomycin. hMSCs were seeded on the sterilized scaffolds and tissue culture plastic (TCP; as control) in 24-well plates at ~$1x10^4$ cells/cm2 and incubated at 37°C and 5% CO2. Due to the potential presence of pro-angiogenic biomolecules in the MSC culture media, we used the MSC culture media alone as another control. The conditioned media (CM) derived from MSCs and the culture media control were collected at 48 h and stored in -80°C.

After collecting CM, hMSCs were washed once with 1X PBS and trypsinized (TrypLE, Thermo Fisher Scientific, Waltham, MA) from the scaffolds or TCP and then mixed in a 1:1 dilution of Trypan Blue (MP Biomedicals, Santa Ana, CA) and cell solution. Cells were visualized using a brightfield microscope and counted via hemocytometer at 10X.

#### *6.3.2.6. VEGF production measurement by ELISA*

The CM was centrifuged at 1400 rpm for 1 minute to remove cell debris and the supernatant was then collected for quantification of human VEGF using an ELISA kit (VEGF Human ELISA Kit KHG0111; Thermo Fisher Scientific, Waltham, MA) per manufacturer's protocol. The VEGF concentrations of the samples (n=8-9 per group) were read for absorbance at 450 nm on a microplate reader (FLUOstar Omega, Ortenberg, Germany). All results were normalized by the VEGF expression obtained from the MSCs cultured on the TCP group.

#### *6.3.2.7. Angiogenesis profiling multiplex array*

Pooled conditioned media of three independent experiments (n=3 per group) were stored at -80°C. Upon thawing, supernatants were centrifuged at 2000 rpm for 10 min to remove debris. The CM were subsequently analyzed by magnetic bead-based multiplex Luminex$^{TM}$ assays for 18-plex angiogenic proteins which included: angiopoietin-1, bone morphogenetic protein-9 (BMP-9), cluster of differentiation-31/platelet endothelial cell adhesion molecule-1 (CD31 (PECAM-1)), epidermal growth factor (EGF), extracellular matrix metalloproteinase inducer (EMMPRIN), follistatin, fibroblast growth factor-2 (FGF-2), granulocyte colony-stimulating factor (G-CSF (CSF-3)), heparin-binding EGF-like growth factor (HB-EGF), hepatocyte growth factor (HGF), interleukin-8 (IL-8 (CXCL8)), leptin, lymphatic vessel endothelial hyaluronan receptor (LYVE-1), platelet-derived growth factor-BB (PDGF-BB), Syndecan, TEK tyrosine kinase/angiopoietin-1 receptor (TIE-2), vascular endothelial growth factor-A (VEGF-A), and vascular endothelial growth factor-D (VEGF-D). The assay was performed according to the manufacturer's instructions (Angiogenesis 18-Plex Human ProcartaPlex Panel EPX180-15806-901; Thermo Fisher Scientific, Waltham, MA) using Luminex xMAP$^{TM}$ (multi-analyte profiling) technology. Results were plotted as picograms per milliliter.

#### *6.3.2.8. Tube formation assay*

Human umbilical vein endothelial cells (HUVECs) (ATCC, Manassas, VA) through passage 5 were cultured in endothelial growth medium supplemented with growth factors (R&D Systems, Minneapolis, MN) and 1% (v/v) penicillin-streptomycin. 32 μL of Geltrex (Gibco Geltrex LDEV-Free, hESC-Qualified, Reduced Growth Factor Basement Membrane Matrix A1413301; Thermo Fisher Scientific, Waltham, MA) was added into 96 well plates and allowed to solidify for 30 minutes in an incubator. Then, ~2x10$^4$ HUVECs were plated onto the Geltrex and incubated with CM collected from hMSCs in various scaffold groups. Brightfield images of neovessel tube formation were taken at 22 h with an AmScope microscope at 4X. Total branching length and number of branches (n=8-9 per group) were quantified using the Angiogenesis Analyzer plugin in ImageJ (NIH, Betheseda, MD). All results were normalized by the total tube length obtained from the MSCs cultured on the TCP group.

#### *6.3.2.9. Statistical evaluation*

Data are presented as mean ± SEM. A one-way ANOVA and Tukey post-hoc test were performed for VEGF concentration because the data were normally distributed and standard deviations did not vary between the groups. PEUU scaffold mechanics, MSC count, VEGF production per MSC, and tube formation data were compared using a Welch ANOVA and Dunnett's T3 multiple comparisons test because the data were normally distributed and standard deviations were variable. A Kruskal-Wallis's test and Dunn's multiple comparisons test were performed on the non-normally distributed data in the multiplex assay evaluation. $p<0.05$ was considered statistically significant.

### 6.3.3 Results

#### *6.3.3.1. PEUU scaffolds with varied stiffness and anisotropy*

To represent the diastolic stiffness of the rat RV at high strains, we chose to fabricate the scaffolds with the Young's modulus in the fiber direction at ~550 kPa to mimic healthy RVs and at ~1100 kPa to mimic diseased RVs[263, 274]. Moreover, the scaffolds at the same stiffness range were fabricated with and without anisotropy to decouple the effects of stiffness and anisotropy on MSC behavior. Mechanical test data confirmed the design of these scaffold groups: the Norm scaffold groups had significantly lower Young's moduli ($E$, $p<0.05$) than the Fail scaffold groups (**Fig. 6.4A**). Next, we quantified the anisotropy index of the scaffold as the ratio of the $E$ in the fiber direction to the $E$ in the cross-fiber direction. The anisotropic index showed a ratio of ~1.0 in the isotropic groups and a ratio of ~1.7 in the anisotropic groups, with the two anisotropic groups showing a significantly ($p<0.05$) larger ratio versus isotropic groups (**Fig. 6.4B**).

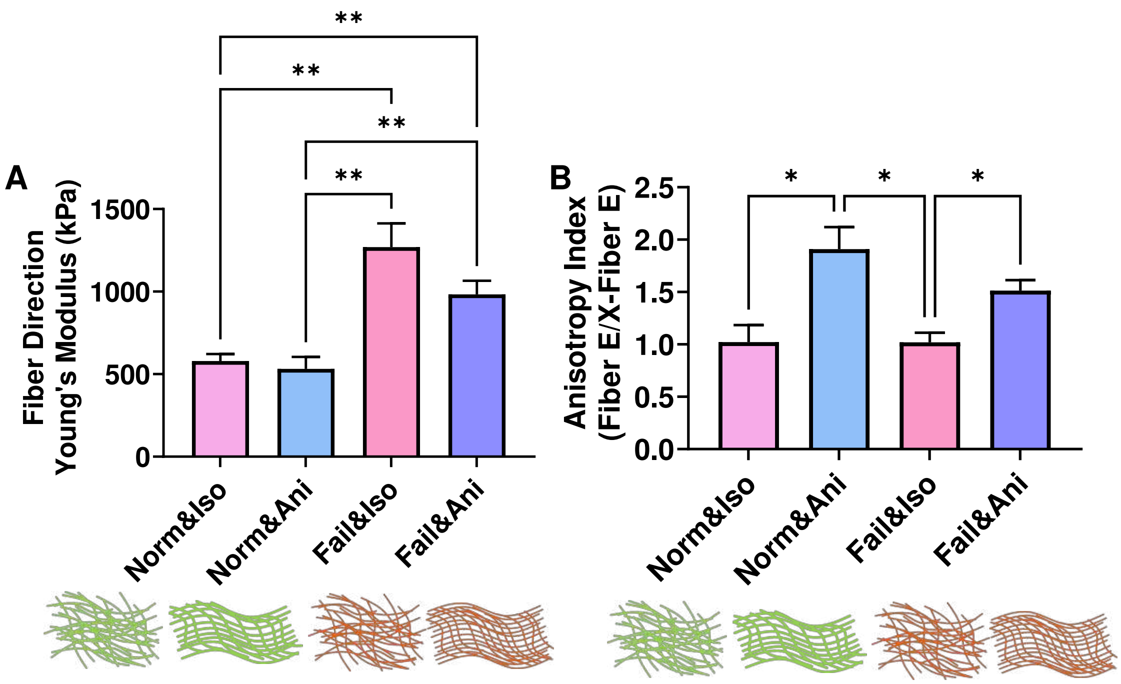

**Figure 6.4.** PEUU scaffolds with varied stiffness mimicking healthy and diseased RV, in the absence and presence of mechanical anisotropy. (**A**) Fail PEUU groups show significantly stiffer Young's moduli compared to Norm PEUU groups. (**B**) Ani PEUU groups show significantly larger anisotropy compared to Iso PEUU groups. n = 6-12 per group. $^*p < 0.05$. $^{**}p < 0.01$. $E$ = Young's modulus. X-Fiber: cross-fiber.

Besides these mechanical properties, we also examined other physical properties of the scaffolds such as the porosity and fiber diameter (**Table 6.8**). We observed no significant differences in porosity between any groups, but the fiber diameter differed between the groups. First, the anisotropic groups presented larger fiber diameters compared to their isotropic counterparts at the same stiffness range; second, the stiffer, failing scaffold groups presented smaller fiber diameters compared to their normal counterparts at the same anisotropy level.

**Table 6.8**. Representative SEM images and other structural factors in the electrospun PEUU scaffolds. The horizontal direction is the main fiber direction in the anisotropic groups. n = 6-10 per group. $^*p < 0.05$ versus Norm&Iso. $^{\&}p < 0.05$ versus Norm&Ani. $^{\#}p < 0.05$ versus Fail&Iso.

| | **Norm&Iso** | **Norm&Ani** | **Fail&Iso** | **Fail&Ani** |
|---|---|---|---|---|
| **Representative SEM Images** | 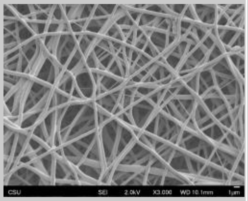 | 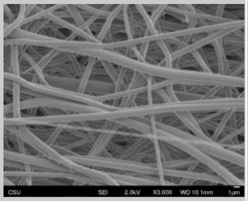 | 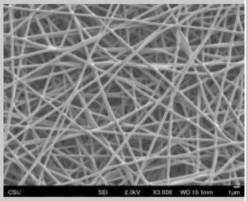 | 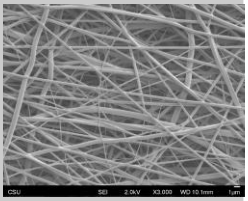 |
| **Porosity (%)** | 53±1.5 | 51±0.74 | 49±2.3 | 51±1.8 |
| **Fiber Diameter (μm)** | 0.64±0.03 | 0.87±0.02* | 0.43±0.01$^{*, \&}$ | 0.49±0.01$^{*, \&, \#}$ |

### *6.3.3.2. VEGF production and MSC numbers regulated by scaffold mechanics*

After 48 h of culture on the four scaffold groups, we measured the total VEGF concentration, MSC count, and VEGF concentration per cell (**Fig. 6.5**). There was a trend (p=0.09) of higher total VEGF production in the Norm&Ani group compared to the Norm&Iso group (**Fig. 6.5A**), but there were no significant differences or trends between the Norm and Fail groups or between the Fail&Iso and Fail&Ani groups.. But when we examined the VEGF production per cell, the Fail&Iso group had the largest value among all scaffold groups, and it had significantly higher VEGF production per MSC compared to that of the Norm&Iso group ($p<0.05$, **Fig. 6.5C**). The different trends between the total VEGF production and VEGF production per cell were due to different cell populations after 48 h of culture. Lower MSC counts in the Fail&Iso scaffold group were noted, and all other three scaffold groups had similar number of cells (**Fig. 6.5B**). Finally, the stiffer scaffolds (Fail&Iso, Fail&Ani) led to higher values of VEGF production per cell compared to the soft scaffolds (Norm&Iso, Norm&Ani) in general (**Fig. 6.5C**).

Moreover, we incorporated the measurements of MSCs cultured on TCP as the internal control for all experiments. The total VEGF production was >1 in all groups except for the Norm&Iso

group (**Figs. 6.5A&C**), thus most scaffold groups seemed to result in an enhanced (although insignificant) pro-angiogenic function. The cell count data clearly showed improved MSC proliferation in all groups (~1.5x of the cell number seen on TCP culture) except for the Fail&Iso group, suggesting that the MSC proliferation was suppressed by this scaffold's mechanical environment (**Fig. 6.5B**). Finally, the VEGF concentration per cell seemed to be enhanced (>1.5x of VEGF concentration seen on TCP culture) in the stiff scaffolds, whereas in the soft scaffolds, the concentration was comparable (~1x) to or even lower (~0.6x) than the TCP group (**Fig. 6.5C**).

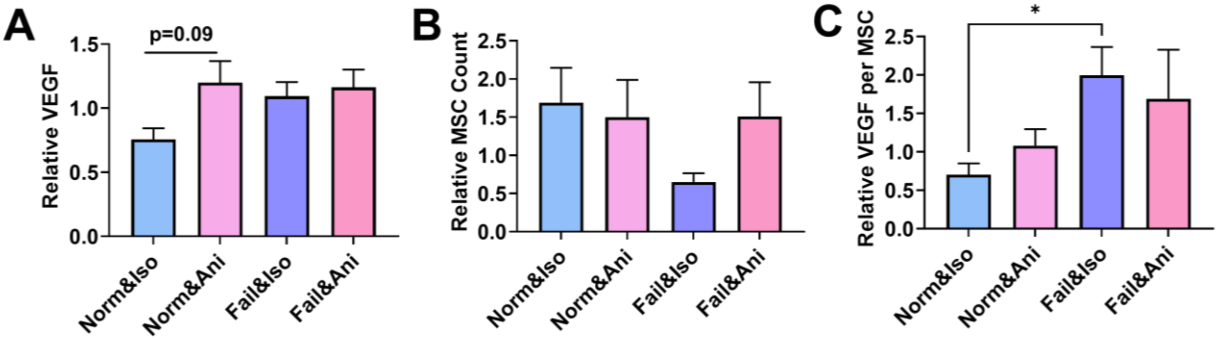

**Figure 6.5.** Effect of stiffness and anisotropy on total VEGF production, MSC count, and VEGF/MSC normalized with TCP after 48 h. (**A**) VEGF expression data from ELISA. Trends of highest total VEGF expression on Norm&Ani group versus Norm&Iso group. (**B**) MSC count. (**C**) VEGF per MSC is significantly higher on Fail&Iso group compared to Norm&Iso group. n = 8-9 per group. *$p < 0.05$.

### *6.3.3.3. Expression of various angiogenic factors regulated by scaffold mechanics*

From the multiplex angiogenesis assay, we further determined six proteins (interleukin-8 (IL-8), extracellular matrix metalloproteinase inducer (EMMPRIN), follistatin, leptin, VEGF-A, hepatocyte growth factor (HGF)) that were markedly detected above the background values ('control') obtained from the culture media alone. These data are shown in Fig. 6.6 and the complete list of all proteins and their concentrations can be found in Table 6.9.

In the total expressions of these proteins, we found that the Norm&Ani group had significantly higher EMMPRIN expression ($p<0.05$) and tended to have a higher IL-8 expression ($p=0.09$)

compared to the TCP group (**Figs. 6.6A&B**). The TCP group showed significantly higher concentration of HGF than the Norm&Iso group ($p<0.05$, **Fig. 6.6F**). We also examined the protein expressions per MSC to measure individual MSC's pro-angiogenic potential. We found that the Fail&Iso group had significantly higher EMMPRIN expression per MSC than the TCP group ($p<0.05$, data not shown), whereas all other scaffold groups showed comparable expressions as the TCP group. There were no significant differences among these groups for other proteins in either total expression (**Fig. 6.6**) or expression per MSC (data not shown).

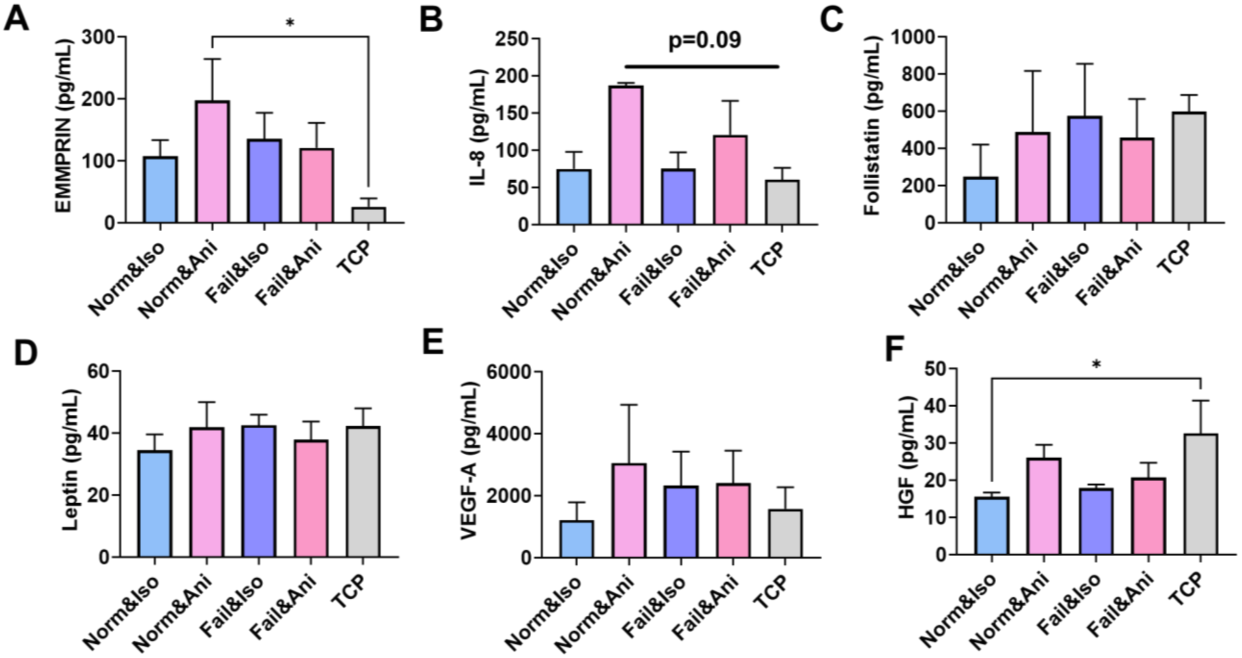

**Figure 6.6.** Pro-angiogenic factors detected in the CM collected at 48 h from the multiplex assay. IL-8: interleukin 8; EMMPRIN: extracellular matrix metalloproteinase inducer; VEGF-A: vascular endothelial growth factor-A; HGF: hepatocyte growth factor. n = 3 per group. *$p < 0.05$.

**Table 6.9**. Mean ± SEM of 18 cytokines from CM assessed via multiplex angiogenesis assay. n = 3 per group. n.d. = not detected. IL-8: interleukin-8; EMMPRIN: extracellular matrix metalloproteinase inducer; VEGF-A: vascular endothelial growth factor-A; HGF: hepatocyte growth factor; LYVE-1: lymphatic vessel endothelial hyaluronan receptor; G-CSF: granulocyte colony-stimulating factor; VEGF-D: vascular endothelial growth factor-D; EGF: epidermal growth factor; HB-EGF: heparin-binding EGF-like growth factor; BMP-9: bone morphogenetic protein-9; TIE-2: TEK tyrosine kinase/angiopoietin-1 receptor; FGF-2: fibroblast growth factor-2; CD-31: cluster of differentiation-31/platelet endothelial cell adhesion molecule-1; PDGF-BB: platelet-derived growth factor-BB.

| | **Norm&Iso (pg/mL)** | **Norm&Ani (pg/mL)** | **Fail&Iso (pg/mL)** | **Fail&Ani (pg/mL)** | **TCP (pg/mL)** | **Background (pg/mL)** |
|---|---|---|---|---|---|---|
| **IL-8** | 75.0±22.9 | 186.8±6.6 | 75.3±21.8 | 120.7±15.8 | 60.5±15.8 | <2.5 |
| **EMMPRIN** | 107.1±26.5 | 197.6±66.8 | 135.4±42.3 | 121.2±40.1 | 25.8±13.7 | <4.7 |
| **Follistatin** | 247.0±173.4 | 487.7±328.3 | 574.3±280.0 | 458.2±207.3 | 597.3±90.0 | <19.8 |
| **Leptin** | 34.5±5.1 | 41.9±8.1 | 42.5±3.4 | 37.8±5.9 | 42.2±5.7 | <15.9 |
| **VEGF-A** | 1214±573.2 | 3054±1880 | 2324±1097 | 2402±1048 | 1580±691.0 | <6.3 |
| **HGF** | 15.5±1.2 | 26.1±3.5 | 17.9±1.0 | 20.8±4.0 | 32.6±8.8 | <6.5 |
| **Angiopoietin-1** | n.d. | n.d. | n.d. | n.d. | n.d. | <32.4 |
| **LYVE-1** | n.d. | n.d. | n.d. | n.d. | n.d. | <10.6 |
| **G-CSF** | n.d. | n.d. | n.d. | n.d. | n.d. | <10 |
| **VEGF-D** | n.d. | n.d. | n.d. | n.d. | n.d. | <0.3 |
| **EGF** | n.d. | n.d. | n.d. | n.d. | n.d. | <2.8 |
| **HB-EGF** | n.d. | n.d. | n.d. | n.d. | n.d. | <1.3 |
| **BMP-9** | n.d. | n.d. | n.d. | n.d. | n.d. | <6.5 |
| **TIE-2** | n.d. | n.d. | n.d. | n.d. | n.d. | <31.2 |
| **Syndecan** | n.d. | n.d. | n.d. | n.d. | n.d. | <16.9 |
| **FGF-2** | n.d. | n.d. | n.d. | n.d. | n.d. | <4.5 |
| **CD-31** | n.d. | n.d. | n.d. | n.d. | n.d. | <515.3 |
| **PDGF-BB** | n.d. | n.d. | n.d. | n.d. | n.d. | <5.8 |

*6.3.3.4. Neovessel tube formation regulated by scaffold mechanics*

The overall pro-angiogenic potential of the MSC-derived CM was assessed using a HUVEC tube formation assay. There were no significant differences between the groups in terms of total tube length (**Figs. 6.7A&B**) and this trend is similar to what we observed in the total VEGF production (**Fig. 6.5A**). However, the total tube length formed per MSC was most pronounced in the Fail&Iso group and it was significantly higher compared to the Norm&Iso group ($p<0.05$, **Fig. 6.7C**). Similar results were observed for the total number of branches formed per MSC ($p<0.05$, data not shown). There was also a strong trend ($p=0.07$) of higher total tube length per MSC in the Fail&Iso group compared to the Fail&Ani group (**Fig. 6.7C**). Therefore, as we observed in the VEGF production (**Fig. 6.5C**), the Fail&Iso scaffold's mechanical environment led to the strongest pro-angiogenic potential for individual MSCs.

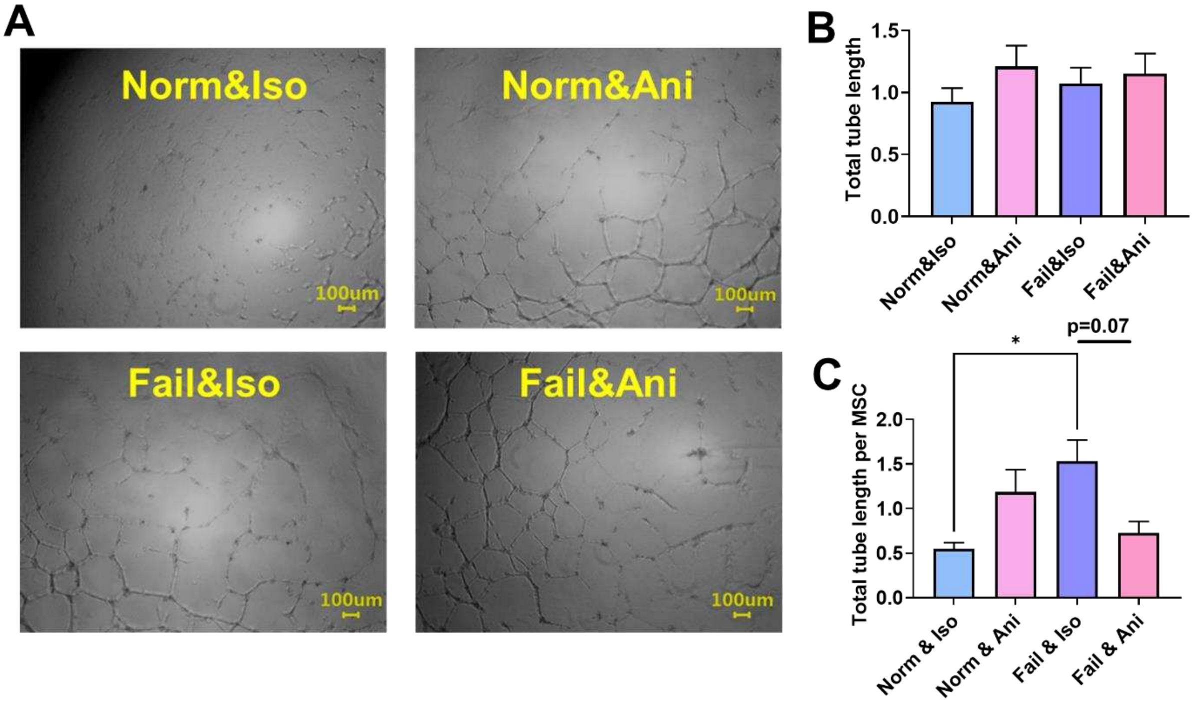

**Figure 6.7.** (**A**) Representative brightfield images of HUVECs in conditioned media from different groups. (**B&C**) Total tube length and total tube length/MSC normalized with TCP determined from the tube formation assay. n = 8-9 per group. $*p < 0.05$.

### 6.3.4 Discussion

In this study, we assessed how two mechanical factors - RV-like diastolic stiffness and tissue anisotropy - affect MSC pro-angiogenic potential. By fabricating PEUU matrices that had decoupled matrix stiffness and anisotropy, we were able to investigate the MSC behavior in response to the varied mechanical conditions. In terms of the individual MSC's pro-angiogenic potential, we found the highest values of VEGF production and total tube length from MSCs cultured on the Fail&Iso scaffold group, and these values were significantly higher than the Norm&Iso scaffold group. Multiplex assays showed a similar peak EMMPRIN expression per MSC in the same group (Fail&Iso). But in terms of the overall pro-angiogenic function of the entire MSC population, the Norm&Ani group had the highest values in VEGF production, total tube length, IL-8 and EMMPRIN expression, although the differences were not always significant. Such differences were attributed to different cell numbers and these data suggested that the MSC proliferation and pro-angiogenic potential are differently regulated. Finally, the presence of anisotropy led to consistent trends of increased pro-angiogenic potential in the soft (Norm) scaffold groups, but this 'positive' effect was absent on the stiff (Fail) scaffold groups. These results indicate that the MSC pro-angiogenic potential is regulated by RV-like end-diastolic stiffness and tissue anisotropy. Thus, these mechanical factors should be taken into consideration for the *in vitro* or *in vivo* research involved with MSC pro-angiogenic functionality.

#### *6.3.4.1. Biomimetic PEUU scaffold with RV-specific mechanical properties*

The production of the four PEUU scaffold groups incorporating RV-specific mechanical properties will aid in teasing out the effects of tissue stiffness and anisotropy on cell behavior. The average stiffness range of our scaffolds from ~500 to ~1000 kPa represents the higher end of stiffness in the non-linear elastic range of the healthy and diseased RV tissues in diastole[263, 274], which to our knowledge has not been investigated in the current literature. In fact, a limited stiffness range has been used in the cardiac tissue engineering field[105, 273]. Moreover, the inclusion of isotropic versus anisotropic characteristics in RV-specific stiffness ranges will help elucidate how anisotropy (the real nature of RV tissue) affects cell behavior as well. This innovative design also enables us to investigate the individual and combined effects of tissue stiffness and anisotropy on MSC behaviors. Understanding how MSCs will respond to RV mechanical changes with disease progression is valuable to improving our understanding of the mechanisms of action regulated by the mechanical environment and determining ways to optimize the overall production of therapeutic cytokines. Such approach and knowledge are not only relevant to MSC treatments for RV failure, but may also be extended to cell or cell-free therapies in the broader population of heart failure patients who exhibit altered myocardial biomechanical properties.

The scaffold's global mechanics are affected by microstructural properties of the matrix[62, 279, 280]. While it is critical to understand how micro-to-macroscale coupling replicates native tissue's biaxial mechanics, such knowledge is unavailable; and we firstly examined the regulation of MSC behavior by the tissue-level mechanical properties. Thus, the scope of the present study was to examine the role of the matrix global (macroscopic), not microscopic, mechanical properties on the MSC response. Nevertheless, we examined the porosity and fiber diameter of the scaffolds from the SEM images. Porosity did not vary between the groups, so the changes of stiffness and anisotropy in the PEUU groups are not attributable to porosity. We did however observe significant differences between the fiber diameters of the groups. When comparing different degrees of anisotropies at a fixed stiffness, it was noted that the diameters were larger in the anisotropic compared to isotropic groups. When comparing different stiffnesses at the same type (isotropy or anisotropy), the fiber diameters were smaller in stiffer scaffolds (**Table 6.8**). While larger fiber diameters have been noted to correspond with larger stiffnesses in fibrous PEUU or PCL scaffolds[279, 281], other factors such as polymer concentration, cross-link/fusion formation between fibers, and fiber alignment also have significant impact on the overall scaffold mechanical properties. Since the global mechanical behavior of the scaffold is the main goal of fabrication in this study, we found the current electrospinning protocol best satisfied our needs to decouple the changes of stiffness and anisotropy in the matrices. However, it is difficult to keep all other physical properties constant and we observed a difference in fiber diameter. But we have not observed any consistent 'effect' of fiber diameter on the MSC behavior from the *in vitro* data and thus ignored the related discussion in the below content.

#### *6.3.4.2. MSC pro-angiogenic function and count are affected by matrix stiffness*

Matrix stiffness is an important regulator of angiogenic cytokine production[121-123, 243, 271, 272]. In this study, we originally examined the impact of RV-specific diastolic stiffness on the MSCs. Both stiff scaffold groups (Fail&Iso, Fail&Ani) showed higher values of VEGF production per cell than the soft scaffold groups (Norm&Iso, Norm&Ani) (**Fig. 6.5C**). We further found that the Fail&Iso scaffold led to significantly higher ($p<0.05$) VEGF production per MSC compared to the Norm&Iso scaffold, indicating an enhanced angiogenic function of MSCs with increased matrix stiffness. This finding was supported by significantly greater total tube length formed per MSC (**Fig. 6.7C**). It was then logical to deduce that VEGF secreted from individual MSCs is a key player in driving tube formation. But the multiplex assay showed that instead of VEGF-A or VEGF-D protein, the EMMPRIN expression per MSC was the highest in the same (Fail&Iso) scaffold group. It is known that EMMPRIN directly promotes angiogenesis through the paracrine regulation of VEGF production in endothelial cells[282]. Therefore, the overall pro-angiogenic function of MSCs may be contributed from both factors and the interplay between VEGF-A and EMMPRIN awaits further investigations.

However, despite the enhanced pro-angiogenic function *per MSC*, the overall angiogenesis outcome was limited by the low cell counts in this scaffold group. Actually, this group had the lowest cell numbers after 48 h of culture, which indicates minimal cell proliferation in this mechanical environment compared to other scaffold groups. The 'opposite' potentials of cell proliferation and pro-angiogenic function of MSCs remind us of the mechanical regulation on MSC differentiation and proliferation. In order to promote the off-shelf regenerative therapy with MSCs, it is important to establish the protocols to maintain cell population (i.e., proliferation) and cell stemness (i.e., un-differentiation) at the same time. However, it has been shown from prior studies that TCP (a stiff substrate with ~ 1 GPa stiffness) has improved cell proliferation over the hydrogel matrix (a soft substrate with < 20 kPa stiffness)[17, 283], but the MSC stemness is impaired in the TCP culture and better preserved in the hydrogel culture[284]. Therefore, the challenge to improve both aspects – MSC proliferation (or cell population) and its regenerative potential such as pro-angiogenic function – needs to be further investigated prior to large scale clinical studies.

It is obvious that the overall pro-angiogenic potential of MSC-derived CM is a combined outcome of the individual cell's pro-angiogenic function and the total number of cells after the mechanical 'treatment' of scaffolds. Therefore, the measurement of the total pro-angiogenic outcome such as total VEGF production (**Fig. 6.5A**) or total tube length formation (**Fig. 6.7B**) showed different trends than the individual MSC's function. The Norm&Ani scaffold group, not the Fail&Iso scaffold group, presented the highest values among all groups, although statistical significance was not reached. Similarly, the multiplex assay also revealed that this group (Norm&Ani) had significantly higher EMMPRIN expression and a strong trend of elevated IL-8 expression than the TCP group (**Figs. 6.6A&B**), whereas other scaffold groups had comparable expressions as the TCP group. The IL-8 production data is in agreement with Abdeen et al.[121], which showed that IL-8 was significantly higher on 10 kPa hydrogel substrates compared to the glass substrate, and with Ogle et al.[272], which showed higher IL-8 production on 30 kPa hydrogels compared to TCP.

From our multiplex panel, we observed six significant factors (IL-8, EMMPRIN, follistatin, leptin, VEGF-A, HGF). These data suggest that in an RV-like microenvironment, these cytokines are more relevant angiogenesis promoters and should be closely examined when developing RV-specific therapies.

#### *6.3.4.3. MSC pro-angiogenic function and count are affected by matrix anisotropy*

Matrix anisotropy is rarely investigated as a mechanical regulator of MSC angiogenic cytokine production, except in a recent study by Su et al.[277]. But in cardiac tissues, the mechanical anisotropy is an intrinsic property, and with disease progression, the degree of anisotropy is altered (e.g., RV anisotropy increased in RV failure subjects). On the other hand, the common cell culture systems (e.g., TCP, hydrogels) use isotropic substrates, and the impact of anisotropy or its coupling with matrix stiffness on cell behavior is mostly ignored. Thus, it is critical to explore the effect of substrate anisotropy on MSC behavior in the stiffness replicating healthy and diseased RVs to fully reveal the *in vivo* responses after cell therapy.

In this study, the induction of anisotropy in RV-like mechanical scaffolds and the investigation of its effect on MSC pro-angiogenic function are unique and highly innovative. The degree of scaffold anisotropy was quantified by the anisotropic index, with the values ~1 to be isotropic and >1 to be anisotropic. In all experimental data (VEGF production, tube formation, multiplex assay for angiogenic factors), the addition of anisotropy consistently led to a trend of higher value compared to the isotropic scaffold when the stiffness was that of healthy RVs. We then speculate that tissue anisotropy improves the MSC pro-angiogenic potential (no matter in overall function or at individual cell levels). In other words, the substrate mechanics that best mimic the healthy RV tissue (soft and anisotropic) seem to elicit improved pro-angiogenic function of MSCs than the non-physiological counterpart (soft and isotropic). However, when the scaffold stiffness was similar to failing RVs, the addition of tissue anisotropy showed different effects - it seemed to suppress the total tube formation (**Fig. 6.7C**) or did not change the VEGF expression (**Fig. 6.5C**) in individual cells. Because the increased stiffness and greater alignment represent a failing RV in vivo, these results imply that the pathological environment may limit the MSC pro-angiogenic potential to improve blood perfusion for the diseased RV. Lastly, these observations also suggest that there may be some synergistic effect of matrix stiffness and anisotropy on individual MSC behavior, which awaits further investigation.

To our knowledge, only one study has examined the effect of anisotropy on MSC pro-angiogenic function. Su et al. compared different anisotropy patterns of electrospun scaffolds and found that the highest pro-angiogenic factor secretion (e.g., VEGF, HGF, etc.) was on aligned and mesh structures compared to that of random pattern and microplate patterns[277]. They also found that tube length was significantly higher on the aligned and mesh pattern than the microplate and random pattern. This suggests that anisotropy (versus isotropy) plays an important role in promoting MSC VEGF production. Our results from Norm scaffold groups agree with their finding, but the results from Fail scaffold groups do not. These data suggest that there is a synergistic effect of matrix stiffness and anisotropy on MSC paracrine function, and the exact molecular mechanisms (through the mechanosensing from integrins to actin fibers and the nucleus) awaits further investigation. Overall, the matrix anisotropy—which is often overlooked in prior studies of MSC pro-angiogenic function—should be considered in future studies to optimize the cell-based therapies.

#### *6.3.4.4 Conclusions*

In this study, we assessed how the MSC pro-angiogenic property is affected by RV-like stiffness and tissue anisotropy conditions. We fabricated matrices that allowed us to decouple the effects of stiffness (mimicking healthy and failing RVs) and anisotropy on MSC behavior. In individual MSCs, we found significantly higher VEGF production and total tube length formation when cultured on the scaffold with stiff and isotropic mechanics than those cultured on the soft and isotropic group. But the cell number was compromised in this group. Moreover, in the soft scaffold groups, the anisotropic group consistently had a trend of increased pro-angiogenic function than the isotropic group, indicating a beneficial effect of anisotropy on MSC paracrine function. However, this effect was absent in the stiff scaffold groups that mimic the diseased RV. Taken together, these results originally reveal the evidence of mechanical regulation of the MSC pro-angiogenic function in the context of RV-like mechanics and tissue anisotropy, which will help to inspire the development of tissue-specific, MSC-based therapies for heart failure patients.

# References

1. Inamdar AA, Inamdar AC. Heart failure: Diagnosis, management and utilization. *Journal of Clinical Medicine*. 2016;5:62
2. Pagidipati NJ, Gaziano TA. Estimating deaths from cardiovascular disease: A review of global methodologies of mortality measurement. *Circulation*. 2013;127:749-756
3. Rodrigues ICP, Kaasi A, Maciel Filho R, Jardini AL, Gabriel LP. Cardiac tissue engineering: Current state-of-the-art materials, cells and tissue formation. *Einstein (Sao Paulo)*. 2018;16:eRB4538
4. Si M-S, Ohye RG. Stem cell therapy for the systemic right ventricle. *Expert Review of Cardiovascular Therapy*. 2017;15:813-823
5. Müller P, Lemcke H, David R. Stem cell therapy in heart diseases – cell types, mechanisms and improvement strategies. *Cellular Physiology and Biochemistry*. 2018;48:2607-2655
6. Zhang J, Zhu W, Radisic M, Vunjak-Novakovic G. Can we engineer a human cardiac patch for therapy? *Circulation Research*. 2018;123:244-265
7. Bernstein HS, Srivastava D. Stem cell therapy for cardiac disease. *Pediatr Res*. 2012;71:491-499
8. Karantalis V, Hare JM. Use of mesenchymal stem cells for therapy of cardiac disease. *Circulation research*. 2015;116:1413-1430
9. Huang G, Li F, Zhao X, Ma Y, Li Y, Lin M, et al. Functional and biomimetic materials for engineering of the three-dimensional cell microenvironment. *Chem Rev*. 2017;117:12764-12850
10. Wissing TB, Bonito V, Bouten CVC, Smits AIPM. Biomaterial-driven in situ cardiovascular tissue engineering—a multi-disciplinary perspective. *npj Regenerative Medicine*. 2017;2:18
11. Ding S, Kingshott P, Thissen H, Pera M, Wang P-Y. Modulation of human mesenchymal and pluripotent stem cell behavior using biophysical and biochemical cues: A review. *Biotechnology and Bioengineering*. 2017;114:260-280
12. Budniatzky I, Gepstein L. Concise review: Reprogramming strategies for cardiovascular regenerative medicine: From induced pluripotent stem cells to direct reprogramming. *Stem Cells Transl Med*. 2014;3:448-457
13. Wang JH, Thampatty BP. An introductory review of cell mechanobiology. *Biomech Model Mechanobiol*. 2006;5:1-16
14. Jansen KA, Donato DM, Balcioglu HE, Schmidt T, Danen EH, Koenderink GH. A guide to mechanobiology: Where biology and physics meet. *Biochim Biophys Acta*. 2015;1853:3043-3052
15. Liu H, Paul C, Xu M. Optimal environmental stiffness for stem cell mediated ischemic myocardium repair. *Methods Mol Biol*. 2017;1553:293-304
16. Engler AJ, Sen S, Sweeney HL, Discher DE. Matrix elasticity directs stem cell lineage specification. *Cell*. 2006;126:677-689
17. Skardal A, Mack D, Atala A, Soker S. Substrate elasticity controls cell proliferation, surface marker expression and motile phenotype in amniotic fluid-derived stem cells. *J Mech Behav Biomed Mater*. 2013;17:307-316

18. Saxena N, Mogha P, Dash S, Majumder A, Jadhav S, Sen S. Matrix elasticity regulates mesenchymal stem cell chemotaxis. *J Cell Sci*. 2018;131
19. Wang M, Cheng B, Yang Y, Liu H, Huang G, Han L, et al. Microchannel stiffness and confinement jointly induce the mesenchymal-amoeboid transition of cancer cell migration. *Nano Letters*. 2019;19:5949-5958
20. Forte G, Pagliari S, Ebara M, Uto K, Tam JK, Romanazzo S, et al. Substrate stiffness modulates gene expression and phenotype in neonatal cardiomyocytes in vitro. *Tissue Eng Part A*. 2012;18:1837-1848
21. Gupta MK, Walthall JM, Venkataraman R, Crowder SW, Jung DK, Yu SS, et al. Combinatorial polymer electrospun matrices promote physiologically-relevant cardiomyogenic stem cell differentiation. *PLoS One*. 2011;6:e28935
22. Mason BN, Califano JP, Reinhart-King CA. Matrix stiffness: A regulator of cellular behavior and tissue formation. In: Bhatia SK, ed. *Engineering biomaterials for regenerative medicine: Novel technologies for clinical applications*. New York, NY: Springer New York; 2012:19-37.
23. Tao ZW, Wu S, Cosgriff-Hernandez EM, Jacot JG. Evaluation of a polyurethane-reinforced hydrogel patch in a rat right ventricle wall replacement model. *Acta Biomater*. 2020;101:206-218
24. Schmuck EG, Hacker TA, Schreier DA, Chesler NC, Wang Z. Beneficial effects of mesenchymal stem cell delivery via a novel cardiac bioscaffold on right ventricles of pulmonary arterial hypertensive rats. *Am J Physiol Heart Circ Physiol*. 2019;316:H1005-H1013
25. Gu X, Matsumura Y, Tang Y, Roy S, Hoff R, Wang B, et al. Sustained viral gene delivery from a micro-fibrous, elastomeric cardiac patch to the ischemic rat heart. *Biomaterials*. 2017;133:132-143
26. Guex AG, Frobert A, Valentin J, Fortunato G, Hegemann D, Cook S, et al. Plasma-functionalized electrospun matrix for biograft development and cardiac function stabilization. *Acta Biomaterialia*. 2014;10:2996-3006
27. Spadaccio C, Rainer A, Trombetta M, Centola M, Lusini M, Chello M, et al. A g-csf functionalized scaffold for stem cells seeding: A differentiating device for cardiac purposes. *J Cell Mol Med*. 2011;15:1096-1108
28. Nelson DM, Ma Z, Fujimoto KL, Hashizume R, Wagner WR. Intra-myocardial biomaterial injection therapy in the treatment of heart failure: Materials, outcomes and challenges. *Acta Biomater*. 2011;7:1-15
29. Zhao GX, Zhang XH, Lu TJ, Xu F. Recent advances in electrospun nanofibrous scaffolds for cardiac tissue engineering. *Advanced Functional Materials*. 2015;25:5726-5738
30. Zhu Y, Matsumura Y, Wagner WR. Ventricular wall biomaterial injection therapy after myocardial infarction: Advances in material design, mechanistic insight and early clinical experiences. *Biomaterials*. 2017;129:37-53
31. Jamadi ES, Ghasemi-Mobarakeh L, Morshed M, Sadeghi M, Prabhakaran MP, Ramakrishna S. Synthesis of polyester urethane urea and fabrication of elastomeric nanofibrous scaffolds for myocardial regeneration. *Materials Science & Engineering C-Materials for Biological Applications*. 2016;63:106-116
32. Huang S, Yang Y, Yang Q, Zhao Q, Ye X. Engineered circulatory scaffolds for building cardiac tissue. *J Thorac Dis*. 2018;10:S2312-S2328

33. Domenech M, Polo-Corrales L, Ramirez-Vick JE, Freytes DO. Tissue engineering strategies for myocardial regeneration: Acellular versus cellular scaffolds? *Tissue Eng Part B Rev*. 2016;22:438-458
34. Kim P-H, Cho J-Y. Myocardial tissue engineering using electrospun nanofiber composites. *BMB Rep*. 2016;49:26-36
35. Qasim M, Haq F, Kang M-H, Kim J-H. 3d printing approaches for cardiac tissue engineering and role of immune modulation in tissue regeneration. *Int J Nanomedicine*. 2019;14:1311-1333
36. Wu Y, Wang L, Guo B, Ma PX. Interwoven aligned conductive nanofiber yarn/hydrogel composite scaffolds for engineered 3d cardiac anisotropy. *ACS Nano*. 2017;11:5646-5659
37. Jin G, He R, Sha B, Li W, Qing H, Teng R, et al. Electrospun three-dimensional aligned nanofibrous scaffolds for tissue engineering. *Mater Sci Eng C Mater Biol Appl*. 2018;92:995-1005
38. Bhardwaj N, Kundu SC. Electrospinning: A fascinating fiber fabrication technique. *Biotechnology Advances*. 2010;28:325-347
39. Liang D, Hsiao BS, Chu B. Functional electrospun nanofibrous scaffolds for biomedical applications. *Advanced Drug Delivery Reviews*. 2007;59:1392-1412
40. Pok S, Jacot JG. Biomaterials advances in patches for congenital heart defect repair. *J Cardiovasc Transl*. 2011;4:646-654
41. Kitsara M, Agbulut O, Kontziampasis D, Chen Y, Menasché P. Fibers for hearts: A critical review on electrospinning for cardiac tissue engineering. *Acta Biomaterialia*. 2017;48:20-40
42. Chen S, John JV, McCarthy A, Xie J. New forms of electrospun nanofiber materials for biomedical applications. *J Mater Chem B*. 2020;8:3733-3746
43. Senthamizhan A, Balusamy B, Uyar T. Recent progress on designing electrospun nanofibers for colorimetric biosensing applications. *Current Opinion in Biomedical Engineering*. 2020;13:1-8
44. Asghari S, Rezaei Z, Mahmoudifard M. Electrospun nanofibers: A promising horizon toward the detection and treatment of cancer. *Analyst*. 2020;145:2854-2872
45. Senthamizhan A, Balusamy B, Uyar T. Glucose sensors based on electrospun nanofibers: A review. *Anal Bioanal Chem*. 2016;408:1285-1306
46. Feng X, Li J, Zhang X, Liu T, Ding J, Chen X. Electrospun polymer micro/nanofibers as pharmaceutical repositories for healthcare. *Journal of Controlled Release*. 2019;302:19-41
47. Zhang Y, Ding J, Qi B, Tao W, Wang J, Zhao C, et al. Multifunctional fibers to shape future biomedical devices. *Advanced Functional Materials*. 2019;29:1902834
48. Balusamy B, Celebioglu A, Senthamizhan A, Uyar T. Progress in the design and development of “fast-dissolving” electrospun nanofibers based drug delivery systems - a systematic review. *Journal of Controlled Release*. 2020;326:482-509
49. Senthamizhan A, Balusamy B, Uyar T. 1 - electrospinning: A versatile processing technology for producing nanofibrous materials for biomedical and tissue-engineering applications. In: Uyar T, Kny E, eds. *Electrospun materials for tissue engineering and biomedical applications*. Woodhead Publishing; 2017:3-41.
50. Balusamy B, Senthamizhan A, Uyar T. Design and development of electrospun nanofibers in regenerative medicine. 2019:47-79.

51. Balusamy B, Senthamizhan A, Uyar T. 8 - electrospun nanofibrous materials for wound healing applications. In: Uyar T, Kny E, eds. *Electrospun materials for tissue engineering and biomedical applications*. Woodhead Publishing; 2017:147-177.
52. Uyar T, Kny E. *Electrospun materials for tissue engineering and biomedical applications: Research, design and commercialization*. 2017.
53. Loh QL, Choong C. Three-dimensional scaffolds for tissue engineering applications: Role of porosity and pore size. *Tissue Eng Part B Rev*. 2013;19:485-502
54. Amoroso NJ, D'Amore A, Hong Y, Wagner WR, Sacks MS. Elastomeric electrospun polyurethane scaffolds: The interrelationship between fabrication conditions, fiber topology, and mechanical properties. *Advanced Materials*. 2011;23:106-111
55. Willerth SM, Sakiyama-Elbert SE. Combining stem cells and biomaterial scaffolds for constructing tissues and cell delivery. *Stembook*. Cambridge (MA); 2019.
56. Prabhakaran MP, Nair AS, Kai D, Ramakrishna S. Electrospun composite scaffolds containing poly(octanediol-co-citrate) for cardiac tissue engineering. *Biopolymers*. 2012;97:529-538
57. Prabhakaran MP, Mobarakeh LG, Kai D, Karbalaie K, Nasr-Esfahani MH, Ramakrishna S. Differentiation of embryonic stem cells to cardiomyocytes on electrospun nanofibrous substrates. *Journal of Biomedical Materials Research Part B: Applied Biomaterials*. 2014;102:447-454
58. Bertuoli PT, Ordoño J, Armelin E, Pérez-Amodio S, Baldissera AF, Ferreira CA, et al. Electrospun conducting and biocompatible uniaxial and core-shell fibers having poly(lactic acid), poly(ethylene glycol), and polyaniline for cardiac tissue engineering. *ACS Omega*. 2019;4:3660-3672
59. Kai D, Prabhakaran MP, Jin G, Ramakrishna S. Polypyrrole-contained electrospun conductive nanofibrous membranes for cardiac tissue engineering. *Journal of Biomedical Materials Research Part A*. 2011;99A:376-385
60. Zhao G, Qing H, Huang G, Genin GM, Lu TJ, Luo Z, et al. Reduced graphene oxide functionalized nanofibrous silk fibroin matrices for engineering excitable tissues. *NPG Asia Materials*. 2018;10:982-994
61. Kai D, Jin GR, Prabhakaran MP, Ramakrishna S. Electrospun synthetic and natural nanofibers for regenerative medicine and stem cells. *Biotechnology Journal*. 2013;8:59-+
62. Stella JA, Wagner WR, Sacks MS. Scale-dependent fiber kinematics of elastomeric electrospun scaffolds for soft tissue engineering. *J Biomed Mater Res A*. 2010;93:1032-1042
63. Courtney T, Sacks MS, Stankus J, Guan J, Wagner WR. Design and analysis of tissue engineering scaffolds that mimic soft tissue mechanical anisotropy. *Biomaterials*. 2006;27:3631-3638
64. Zhao G, Bao X, Huang G, Xu F, Zhang X. Differential effects of directional cyclic stretching on the functionalities of engineered cardiac tissues. *ACS Applied Bio Materials*. 2019
65. Parrag IC, Zandstra PW, Woodhouse KA. Fiber alignment and coculture with fibroblasts improves the differentiated phenotype of murine embryonic stem cell-derived cardiomyocytes for cardiac tissue engineering. *Biotechnol Bioeng*. 2012;109:813-822
66. Suhaeri M, Subbiah R, Kim S-H, Kim C-H, Oh SJ, Kim S-H, et al. Novel platform of cardiomyocyte culture and coculture via fibroblast-derived matrix-coupled aligned electrospun nanofiber. *ACS Applied Materials & Interfaces*. 2017;9:224-235

67. Hussain A, Collins G, Yip D, Cho CH. Functional 3-d cardiac co-culture model using bioactive chitosan nanofiber scaffolds. *Biotechnol Bioeng*. 2013;110:637-647
68. Yu J, Lee A-R, Lin W-H, Lin C-W, Wu Y-K, Tsai W-B. Electrospun plga fibers incorporated with functionalized biomolecules for cardiac tissue engineering. *Tissue engineering. Part A*. 2014;20:1896-1907
69. Flaig F, Ragot H, Simon A, Revet G, Kitsara M, Kitasato L, et al. Design of functional electrospun scaffolds based on poly(glycerol sebacate) elastomer and poly(lactic acid) for cardiac tissue engineering. *ACS Biomaterials Science & Engineering*. 2020;6:2388-2400
70. LeGrice IJ, Smaill BH, Chai LZ, Edgar SG, Gavin JB, Hunter PJ. Laminar structure of the heart: Ventricular myocyte arrangement and connective tissue architecture in the dog. *Am J Physiol*. 1995;269:H571-582
71. Fleischer S, Shapira A, Feiner R, Dvir T. Modular assembly of thick multifunctional cardiac patches. *Proceedings of the National Academy of Sciences*. 2017;114:1898
72. D'Amore A, Yoshizumi T, Luketich SK, Wolf MT, Gu X, Cammarata M, et al. Bi-layered polyurethane - extracellular matrix cardiac patch improves ischemic ventricular wall remodeling in a rat model. *Biomaterials*. 2016;107:1-14
73. Kashiyama N, Kormos RL, Matsumura Y, D'Amore A, Miyagawa S, Sawa Y, et al. Adipose-derived stem cell sheet under an elastic patch improves cardiac function in rats after myocardial infarction. *The Journal of Thoracic and Cardiovascular Surgery*. 2020
74. Kai D, Wang QL, Wang HJ, Prabhakaran MP, Zhang YZ, Tan YZ, et al. Stem cell-loaded nanofibrous patch promotes the regeneration of infarcted myocardium with functional improvement in rat model. *Acta Biomaterialia*. 2014;10:2727-2738
75. Zhu Y, Wagner WR. Chapter 30 - design principles in biomaterials and scaffolds. In: Atala A, Lanza R, Mikos AG, Nerem R, eds. *Principles of regenerative medicine (third edition)*. Boston: Academic Press; 2019:505-522.
76. Stuckey DJ, Ishii H, Chen Q-Z, Boccaccini AR, Hansen U, Carr CA, et al. Magnetic resonance imaging evaluation of remodeling by cardiac elastomeric tissue scaffold biomaterials in a rat model of myocardial infarction. *Tissue Engineering Part A*. 2010;16:3395-3402
77. Fujimoto KL, Tobita K, Merryman WD, Guan J, Momoi N, Stolz DB, et al. An elastic, biodegradable cardiac patch induces contractile smooth muscle and improves cardiac remodeling and function in subacute myocardial infarction. *J Am Coll Cardiol*. 2007;49:2292-2300
78. Lin X, Liu Y, Bai A, Cai H, Bai Y, Jiang W, et al. A viscoelastic adhesive epicardial patch for treating myocardial infarction. *Nat Biomed Eng*. 2019;3:632-643
79. Serpooshan V, Zhao M, Metzler SA, Wei K, Shah PB, Wang A, et al. The effect of bioengineered acellular collagen patch on cardiac remodeling and ventricular function post myocardial infarction. *Biomaterials*. 2013;34:9048-9055
80. Vilaeti AD, Dimos K, Lampri ES, Mantzouratou P, Tsitou N, Mourouzis I, et al. Short-term ventricular restraint attenuates post-infarction remodeling in rats. *Int J Cardiol*. 2013;165:278-284
81. Trip P, Rain S, Handoko ML, van der Bruggen C, Bogaard HJ, Marcus JT, et al. Clinical relevance of right ventricular diastolic stiffness in pulmonary hypertension. *Eur Respir J*. 2015;45:1603-1612
82. Murayama M, Okada K, Kaga S, Iwano H, Tsujinaga S, Sarashina M, et al. Simple and noninvasive method to estimate right ventricular operating stiffness based on

echocardiographic pulmonary regurgitant velocity and tricuspid annular plane movement measurements during atrial contraction. *Int J Cardiovasc Imaging*. 2019;35:1871-1880

83. Chen QZ, Bismarck A, Hansen U, Junaid S, Tran MQ, Harding SE, et al. Characterisation of a soft elastomer poly(glycerol sebacate) designed to match the mechanical properties of myocardial tissue. *Biomaterials*. 2008;29:47-57
84. Wanjare M, Hou L, Nakayama KH, Kim JJ, Mezak NP, Abilez OJ, et al. Anisotropic microfibrous scaffolds enhance the organization and function of cardiomyocytes derived from induced pluripotent stem cells. *Biomater Sci*. 2017;5:1567-1578
85. Chen PH, Liao HC, Hsu SH, Chen RS, Wu MC, Yang YF, et al. A novel polyurethane/cellulose fibrous scaffold for cardiac tissue engineering. *Rsc Advances*. 2015;5:6932-6939
86. D'Amore A, Amoroso N, Gottardi R, Hobson C, Carruthers C, Watkins S, et al. From single fiber to macro-level mechanics: A structural finite-element model for elastomeric fibrous biomaterials. *J Mech Behav Biomed Mater*. 2014;39:146-161
87. Stankus JJ, Guan J, Fujimoto K, Wagner WR. Microintegrating smooth muscle cells into a biodegradable, elastomeric fiber matrix. *Biomaterials*. 2006;27:735-744
88. Kai D, Prabhakaran MP, Jin G, Ramakrishna S. Guided orientation of cardiomyocytes on electrospun aligned nanofibers for cardiac tissue engineering. *J Biomed Mater Res B Appl Biomater*. 2011;98:379-386
89. Elamparithi A, Punnoose AM, Paul SFD, Kuruvilla S. Gelatin electrospun nanofibrous matrices for cardiac tissue engineering applications. *International Journal of Polymeric Materials and Polymeric Biomaterials*. 2017;66:20-27
90. Mukherjee S, Reddy Venugopal J, Ravichandran R, Ramakrishna S, Raghunath M. Evaluation of the biocompatibility of placl/collagen nanostructured matrices with cardiomyocytes as a model for the regeneration of infarcted myocardium. *Advanced Functional Materials*. 2011;21:2291-2300
91. Hsiao C-W, Bai M-Y, Chang Y, Chung M-F, Lee T-Y, Wu C-T, et al. Electrical coupling of isolated cardiomyocyte clusters grown on aligned conductive nanofibrous meshes for their synchronized beating. *Biomaterials*. 2013;34:1063-1072
92. Kharaziha M, Shin SR, Nikkhah M, Topkaya SN, Masoumi N, Annabi N, et al. Tough and flexible cnt–polymeric hybrid scaffolds for engineering cardiac constructs. *Biomaterials*. 2014;35:7346-7354
93. Liu Y, Lu J, Xu G, Wei J, Zhang Z, Li X. Tuning the conductivity and inner structure of electrospun fibers to promote cardiomyocyte elongation and synchronous beating. *Mater Sci Eng C Mater Biol Appl*. 2016;69:865-874
94. Efraim Y, Schoen B, Zahran S, Davidov T, Vasilyev G, Baruch L, et al. 3d structure and processing methods direct the biological attributes of ecm-based cardiac scaffolds. *Sci Rep*. 2019;9:5578
95. Schoen B, Avrahami R, Baruch L, Efraim Y, Goldfracht I, Elul O, et al. Electrospun extracellular matrix: Paving the way to tailor-made natural scaffolds for cardiac tissue regeneration. *Advanced Functional Materials*. 2017;27:1700427
96. Sommer G, Schriefl AJ, Andrä M, Sacherer M, Viertler C, Wolinski H, et al. Biomechanical properties and microstructure of human ventricular myocardium. *Acta Biomaterialia*. 2015;24:172-192

97. Holzapfel GA, Ogden RW. Constitutive modelling of passive myocardium: A structurally based framework for material characterization. *Philosophical Transactions of the Royal Society A*. 2009;367:3445-3475
98. Dokos S, Smaill BH, Young AA, LeGrice IJ. Shear properties of passive ventricular myocardium. *Am J Physiol Heart Circ Physiol*. 2002;283:H2650-2659
99. Neugirg BR, Koebley SR, Schniepp HC, Fery A. Afm-based mechanical characterization of single nanofibres. *Nanoscale*. 2016;8:8414-8426
100. Lee D, Zhang H, Ryu S. Elastic modulus measurement of hydrogels. In: Mondal MIH, ed. *Cellulose-based superabsorbent hydrogels*. Cham: Springer International Publishing; 2018:1-21.
101. McKee CT, Last JA, Russell P, Murphy CJ. Indentation versus tensile measurements of young's modulus for soft biological tissues. *Tissue Eng Part B Rev*. 2011;17:155-164
102. Liu W, Wang Z. Current understanding of the biomechanics of ventricular tissues in heart failure. *Bioengineering (Basel)*. 2019;7
103. Sherif R, Narinder P, Hani EN. Standardized static and dynamic evaluation of myocardial tissue properties. *Biomedical Materials*. 2017;12:025013
104. Lakes R. *Viscoelastic materials*. Cambridge: Cambridge University Press; 2009.
105. Jacot JG, Martin JC, Hunt DL. Mechanobiology of cardiomyocyte development. *J Biomech*. 2010;43:93-98
106. Fatemifar F, Feldman M, Oglesby M, Han HC. Comparison of biomechanical properties and microstructure of trabeculae carneae, papillary muscles, and myocardium in human heart. *J Biomech Eng*. 2018
107. Humphrey JD, Strumpf RK, Yin FCP. Biaxial mechanical-behavior of excised ventricular epicardium. *American Journal of Physiology*. 1990;259:H101-H108
108. Jang S, Vanderpool RR, Avazmohammadi R, Lapshin E, Bachman TN, Sacks M, et al. Biomechanical and hemodynamic measures of right ventricular diastolic function: Translating tissue biomechanics to clinical relevance. *Journal of the American Heart Association*. 2017;6
109. Hill MR, Simon MA, Valdez-Jasso D, Zhang W, Champion HC, Sacks MS. Structural and mechanical adaptations of right ventricular free wall myocardium to pulmonary-hypertension induced pressure overload. *Annals of biomedical engineering*. 2014;42:2451-2465
110. Sacks MS, Chuong CJ. Biaxial mechanical properties of passive right ventricular free wall myocardium. *Journal of Biomechanical Engineering*. 1993;115:202-205
111. Rubiano A, Qi Y, Guzzo D, Rowe K, Pepine C, Simmons C. Stem cell therapy restores viscoelastic properties of myocardium in rat model of hypertension. *Journal of the mechanical behavior of biomedical materials*. 2016;59:71-77
112. Berry MF, Engler AJ, Woo YJ, Pirolli TJ, Bish LT, Jayasankar V, et al. Mesenchymal stem cell injection after myocardial infarction improves myocardial compliance. *American Journal of Physiology - Heart and Circulatory Physiology*. 2006;290:H2196-H2203
113. Hiesinger W, Brukman MJ, McCormick RC, Fitzpatrick JR, III, Frederick JR, Yang EC, et al. Myocardial tissue elastic properties determined by atomic force microscopy after stromal cell derived factor 1α angiogenic therapy for acute myocardial infarction in a murine model. *The Journal of Thoracic and Cardiovascular Surgery*. 2012;143:962-966

114. Engler AJ, Carag-Krieger C, Johnson CP, Raab M, Tang H-Y, Speicher DW, et al. Embryonic cardiomyocytes beat best on a matrix with heart-like elasticity: Scar-like rigidity inhibits beating. *Journal of Cell Science*. 2008;121:3794-3802

115. Bhana B, Iyer RK, Chen WLK, Zhao R, Sider KL, Likhitpanichkul M, et al. Influence of substrate stiffness on the phenotype of heart cells. *Biotechnology and Bioengineering*. 2010;105:1148-1160

116. Engelmayr GC, Jr., Cheng M, Bettinger CJ, Borenstein JT, Langer R, Freed LE. Accordion-like honeycombs for tissue engineering of cardiac anisotropy. *Nat Mater*. 2008;7:1003-1010

117. Javani S, Gordon M, Azadani AN. Biomechanical properties and microstructure of heart chambers: A paired comparison study in an ovine model. *Annals of Biomedical Engineering*. 2016;44:3266-3283

118. Liu W, Nguyen-Truong M, Labus K, Boon J, Easley J, Monnet E, et al. Correlations between the right ventricular passive elasticity and organ function in adult ovine. *Journal of Integrative Cardiology*. 2020;6:1-6

119. Ahmad F, Prabhu Rj, Liao J, Soe S, Jones MD, Miller J, et al. Biomechanical properties and microstructure of neonatal porcine ventricles. *Journal of the Mechanical Behavior of Biomedical Materials*. 2018;88:18-28

120. Stoppel WL, Hu D, Domian IJ, Kaplan DL, Black LD, 3rd. Anisotropic silk biomaterials containing cardiac extracellular matrix for cardiac tissue engineering. *Biomed Mater*. 2015;10:034105

121. Abdeen AA, Weiss JB, Lee J, Kilian KA. Matrix composition and mechanics direct proangiogenic signaling from mesenchymal stem cells. *Tissue Engineering. Part A*. 2014;20:2737-2745

122. Seib FP, Prewitz M, Werner C, Bornhäuser M. Matrix elasticity regulates the secretory profile of human bone marrow-derived multipotent mesenchymal stromal cells (mscs). *Biochemical and Biophysical Research Communications*. 2009;389:663-667

123. Nasser M, Wu Y, Danaoui Y, Ghosh G. Engineering microenvironments towards harnessing pro-angiogenic potential of mesenchymal stem cells. *Mater Sci Eng C Mater Biol Appl*. 2019;102:75-84

124. McCain ML, Agarwal A, Nesmith HW, Nesmith AP, Parker KK. Micromolded gelatin hydrogels for extended culture of engineered cardiac tissues. *Biomaterials*. 2014;35:5462-5471

125. D'Amore A, Nasello G, Luketich SK, Denisenko D, Jacobs DL, Hoff R, et al. Meso-scale topological cues influence extracellular matrix production in a large deformation, elastomeric scaffold model. *Soft Matter*. 2018;14:8483-8495

126. Stella JA, D'Amore A, Wagner WR, Sacks MS. On the biomechanical function of scaffolds for engineering load-bearing soft tissues. *Acta Biomater*. 2010;6:2365-2381

127. D'Amore A, Stella JA, Wagner WR, Sacks MS. Characterization of the complete fiber network topology of planar fibrous tissues and scaffolds. *Biomaterials*. 2010;31:5345-5354

128. Stella JA, Liao J, Hong Y, David Merryman W, Wagner WR, Sacks MS. Tissue-to-cellular level deformation coupling in cell micro-integrated elastomeric scaffolds. *Biomaterials*. 2008;29:3228-3236

129. Lee A, Hudson AR, Shiwarski DJ, Tashman JW, Hinton TJ, Yerneni S, et al. 3d bioprinting of collagen to rebuild components of the human heart. *Science*. 2019;365:482-487

130. Gao L, Kupfer ME, Jung JP, Yang L, Zhang P, Da Sie Y, et al. Myocardial tissue engineering with cells derived from human-induced pluripotent stem cells and a native-like, high-resolution, 3-dimensionally printed scaffold. *Circ Res*. 2017;120:1318-1325

131. Jia W, Gungor-Ozkerim PS, Zhang YS, Yue K, Zhu K, Liu W, et al. Direct 3d bioprinting of perfusable vascular constructs using a blend bioink. *Biomaterials*. 2016;106:58-68

132. Jang J, Park H-J, Kim S-W, Kim H, Park JY, Na SJ, et al. 3d printed complex tissue construct using stem cell-laden decellularized extracellular matrix bioinks for cardiac repair. *Biomaterials*. 2017;112:264-274

133. Lazarus HM, Haynesworth SE, Gerson SL, Rosenthal NS, Caplan AI. Ex vivo expansion and subsequent infusion of human bone marrow-derived stromal progenitor cells (mesenchymal progenitor cells): Implications for therapeutic use. *Bone Marrow Transplant*. 1995;16:557-564

134. Kabat M, Bobkov I, Kumar S, Grumet M. Trends in mesenchymal stem cell clinical trials 2004-2018: Is efficacy optimal in a narrow dose range? *Stem Cells Transl Med*. 2020;9:17-27

135. Pittenger MF, Mackay AM, Beck SC, Jaiswal RK, Douglas R, Mosca JD, et al. Multilineage potential of adult human mesenchymal stem cells. *Science*. 1999;284:143-147

136. Caplan AI. Mesenchymal stem cells. *Journal of Orthopaedic Research*. 1991;9:641-650

137. Friedenstein AJ, Piatetzky S, II, Petrakova KV. Osteogenesis in transplants of bone marrow cells. *J Embryol Exp Morphol*. 1966;16:381-390

138. Battiwalla M, Hematti P. Mesenchymal stem cells in hematopoietic stem cell transplantation. *Cytotherapy*. 2009;11:503-515

139. Petrou P, Gothelf Y, Argov Z, Gotkine M, Levy YS, Kassis I, et al. Safety and clinical effects of mesenchymal stem cells secreting neurotrophic factor transplantation in patients with amyotrophic lateral sclerosis: Results of phase 1/2 and 2a clinical trials. *JAMA Neurol*. 2016;73:337-344

140. Sykova E, Rychmach P, Drahoradova I, Konradova S, Ruzickova K, Vorisek I, et al. Transplantation of mesenchymal stromal cells in patients with amyotrophic lateral sclerosis: Results of phase i/iia clinical trial. *Cell Transplant*. 2017;26:647-658

141. Reinders ME, Dreyer GJ, Bank JR, Roelofs H, Heidt S, Roelen DL, et al. Safety of allogeneic bone marrow derived mesenchymal stromal cell therapy in renal transplant recipients: The neptune study. *J Transl Med*. 2015;13:344

142. Mathiasen AB, Qayyum AA, Jorgensen E, Helqvist S, Fischer-Nielsen A, Kofoed KF, et al. Bone marrow-derived mesenchymal stromal cell treatment in patients with severe ischaemic heart failure: A randomized placebo-controlled trial (msc-hf trial). *Eur Heart J*. 2015;36:1744-1753

143. Afzal MR, Haider H, Idris NM, Jiang S, Ahmed RP, Ashraf M. Preconditioning promotes survival and angiomyogenic potential of mesenchymal stem cells in the infarcted heart via nf-kappab signaling. *Antioxid Redox Signal*. 2010;12:693-702

144. Tang J, Wang J, Guo L, Kong X, Yang J, Zheng F, et al. Mesenchymal stem cells modified with stromal cell-derived factor 1 alpha improve cardiac remodeling via paracrine activation of hepatocyte growth factor in a rat model of myocardial infarction. *Mol Cells*. 2010;29:9-19

145. Zhang D, Fan GC, Zhou X, Zhao T, Pasha Z, Xu M, et al. Over-expression of cxcr4 on mesenchymal stem cells augments myoangiogenesis in the infarcted myocardium. *J Mol Cell Cardiol*. 2008;44:281-292
146. Pan Q, Qin X, Ma S, Wang H, Cheng K, Song X, et al. Myocardial protective effect of extracellular superoxide dismutase gene modified bone marrow mesenchymal stromal cells on infarcted mice hearts. *Theranostics*. 2014;4:475-486
147. Yan W, Abu-El-Rub E, Saravanan S, Kirshenbaum LA, Arora RC, Dhingra S. Inflammation in myocardial injury: Mesenchymal stem cells as potential immunomodulators. *American Journal of Physiology-Heart and Circulatory Physiology*. 2019;317:H213-H225
148. Caplan AI, Correa D. The msc: An injury drugstore. *Cell Stem Cell*. 2011;9:11-15
149. Hodgkinson CP, Bareja A, Gomez JA, Dzau VJ. Emerging concepts in paracrine mechanisms in regenerative cardiovascular medicine and biology. *Circ Res*. 2016;118:95-107
150. Gnecchi M, He H, Noiseux N, Liang OD, Zhang L, Morello F, et al. Evidence supporting paracrine hypothesis for akt-modified mesenchymal stem cell-mediated cardiac protection and functional improvement. *FASEB J*. 2006;20:661-669
151. He Y, Guo Y, Xia Y, Guo Y, Wang R, Zhang F, et al. Resistin promotes cardiac homing of mesenchymal stem cells and functional recovery after myocardial ischemia-reperfusion via the erk1/2-mmp-9 pathway. *Am J Physiol Heart Circ Physiol*. 2019;316:H233-H244
152. Luo W, Gong Y, Qiu F, Yuan Y, Jia W, Liu Z, et al. Ngf nanoparticles enhance the potency of transplanted human umbilical cord mesenchymal stem cells for myocardial repair. *Am J Physiol Heart Circ Physiol*. 2021;320:H1959-H1974
153. Baraniak PR, McDevitt TC. Stem cell paracrine actions and tissue regeneration. *Regen Med*. 2010;5:121-143
154. van Berlo JH, Molkentin JD. An emerging consensus on cardiac regeneration. *Nat Med*. 2014;20:1386-1393
155. Phinney DG, Pittenger MF. Concise review: Msc-derived exosomes for cell-free therapy. *Stem Cells*. 2017;35:851-858
156. Park SR, Kim JW, Jun HS, Roh JY, Lee HY, Hong IS. Stem cell secretome and its effect on cellular mechanisms relevant to wound healing. *Mol Ther*. 2018;26:606-617
157. Forsberg MH, Kink JA, Hematti P, Capitini CM. Mesenchymal stromal cells and exosomes: Progress and challenges. *Front Cell Dev Biol*. 2020;8:665
158. Chatterjee V, Yang X, Ma Y, Wu MH, Yuan SY. Extracellular vesicles: New players in regulating vascular barrier function. *American Journal of Physiology-Heart and Circulatory Physiology*. 2020;319:H1181-H1196
159. Nguyen BY, Azam T, Wang X. Cellular signaling cross-talk between different cardiac cell populations: An insight into the role of exosomes in the heart diseases and therapy. *American Journal of Physiology-Heart and Circulatory Physiology*. 2021;320:H1213-H1234
160. Karbasiafshar C, Sellke FW, Abid MR. Mesenchymal stem cell-derived extracellular vesicles in the failing heart: Past, present, and future. *Am J Physiol Heart Circ Physiol*. 2021;320:H1999-H2010
161. Saheera S, Jani VP, Witwer KW, Kutty S. Extracellular vesicle interplay in cardiovascular pathophysiology. *Am J Physiol Heart Circ Physiol*. 2021;320:H1749-H1761

162. Pittenger MF, Discher DE, Peault BM, Phinney DG, Hare JM, Caplan AI. Mesenchymal stem cell perspective: Cell biology to clinical progress. *NPJ Regen Med*. 2019;4:22
163. Horwitz EM, Le Blanc K, Dominici M, Mueller I, Slaper-Cortenbach I, Marini FC, et al. Clarification of the nomenclature for msc: The international society for cellular therapy position statement. *Cytotherapy*. 2005;7:393-395
164. Lushaj EB, Anstadt E, Haworth R, Roenneburg D, Kim J, Hematti P, et al. Mesenchymal stromal cells are present in the heart and promote growth of adult stem cells in vitro. *Cytotherapy*. 2011;13:400-406
165. Hanson SE, Kim J, Hematti P. Comparative analysis of adipose-derived mesenchymal stem cells isolated from abdominal and breast tissue. *Aesthet Surg J*. 2013;33:888-898
166. Kim J, Breunig MJ, Escalante LE, Bhatia N, Denu RA, Dollar BA, et al. Biologic and immunomodulatory properties of mesenchymal stromal cells derived from human pancreatic islets. *Cytotherapy*. 2012;14:925-935
167. Jabbehdari S, Yazdanpanah G, Kanu LN, Anwar KN, Shen X, Rabiee B, et al. Reproducible derivation and expansion of corneal mesenchymal stromal cells for therapeutic applications. *Transl Vis Sci Technol*. 2020;9:26
168. Jackson WM, Nesti LJ, Tuan RS. Potential therapeutic applications of muscle-derived mesenchymal stem and progenitor cells. *Expert Opin Biol Ther*. 2010;10:505-517
169. Bian S, Zhang L, Duan L, Wang X, Min Y, Yu H. Extracellular vesicles derived from human bone marrow mesenchymal stem cells promote angiogenesis in a rat myocardial infarction model. *Journal of molecular medicine (Berlin, Germany)*. 2014;92:387-397
170. Kang K, Ma R, Cai W, Huang W, Paul C, Liang J, et al. Exosomes secreted from cxcr4 overexpressing mesenchymal stem cells promote cardioprotection via akt signaling pathway following myocardial infarction. *Stem Cells Int*. 2015;2015:659890
171. Timmers L, Lim SK, Arslan F, Armstrong JS, Hoefer IE, Doevendans PA, et al. Reduction of myocardial infarct size by human mesenchymal stem cell conditioned medium. *Stem Cell Res*. 2007;1:129-137
172. Yu B, Kim HW, Gong M, Wang J, Millard RW, Wang Y, et al. Exosomes secreted from gata-4 overexpressing mesenchymal stem cells serve as a reservoir of anti-apoptotic micrornas for cardioprotection. *Int J Cardiol*. 2015;182:349-360
173. Bruno S, Grange C, Collino F, Deregibus MC, Cantaluppi V, Biancone L, et al. Microvesicles derived from mesenchymal stem cells enhance survival in a lethal model of acute kidney injury. *PLoS One*. 2012;7:e33115
174. Teng X, Chen L, Chen W, Yang J, Yang Z, Shen Z. Mesenchymal stem cell-derived exosomes improve the microenvironment of infarcted myocardium contributing to angiogenesis and anti-inflammation. *Cell Physiol Biochem*. 2015;37:2415-2424
175. Li T, Yan Y, Wang B, Qian H, Zhang X, Shen L, et al. Exosomes derived from human umbilical cord mesenchymal stem cells alleviate liver fibrosis. *Stem Cells Dev*. 2013;22:845-854
176. Shojaati G, Khandaker I, Funderburgh ML, Mann MM, Basu R, Stolz DB, et al. Mesenchymal stem cells reduce corneal fibrosis and inflammation via extracellular vesicle-mediated delivery of mirna. *Stem Cells Transl Med*. 2019;8:1192-1201
177. Mansouri N, Willis GR, Fernandez-Gonzalez A, Reis M, Nassiri S, Mitsialis SA, et al. Mesenchymal stromal cell exosomes prevent and revert experimental pulmonary fibrosis through modulation of monocyte phenotypes. *JCI Insight*. 2019;4

178. Amable PR, Teixeira MV, Carias RB, Granjeiro JM, Borojevic R. Protein synthesis and secretion in human mesenchymal cells derived from bone marrow, adipose tissue and wharton's jelly. *Stem Cell Res Ther*. 2014;5:53

179. Wang L, Tran I, Seshareddy K, Weiss ML, Detamore MS. A comparison of human bone marrow-derived mesenchymal stem cells and human umbilical cord-derived mesenchymal stromal cells for cartilage tissue engineering. *Tissue Eng Part A*. 2009;15:2259-2266

180. Gissi C, Radeghieri A, Antonetti Lamorgese Passeri C, Gallorini M, Calciano L, Oliva F, et al. Extracellular vesicles from rat-bone-marrow mesenchymal stromal/stem cells improve tendon repair in rat achilles tendon injury model in dose-dependent manner: A pilot study. *PLoS One*. 2020;15:e0229914

181. Chamberlain CS, Clements AEB, Kink JA, Choi U, Baer GS, Halanski MA, et al. Extracellular vesicle-educated macrophages promote early achilles tendon healing. *Stem Cells*. 2019;37:652-662

182. Jabbehdari S, Yazdanpanah G, Kanu LN, Chen E, Kang K, Anwar KN, et al. Therapeutic effects of lyophilized conditioned-medium derived from corneal mesenchymal stromal cells on corneal epithelial wound healing. *Curr Eye Res*. 2020;45:1490-1496

183. Zhou Y, Yamamoto Y, Xiao Z, Ochiya T. The immunomodulatory functions of mesenchymal stromal/stem cells mediated via paracrine activity. *J Clin Med*. 2019;8

184. Ullah M, Liu DD, Thakor AS. Mesenchymal stromal cell homing: Mechanisms and strategies for improvement. *iScience*. 2019;15:421-438

185. Maacha S, Sidahmed H, Jacob S, Gentilcore G, Calzone R, Grivel JC, et al. Paracrine mechanisms of mesenchymal stromal cells in angiogenesis. *Stem Cells Int*. 2020;2020:4356359

186. Todorova D, Simoncini S, Lacroix R, Sabatier F, Dignat-George F. Extracellular vesicles in angiogenesis. *Circ Res*. 2017;120:1658-1673

187. Dai W, Hale SL, Kloner RA. Role of a paracrine action of mesenchymal stem cells in the improvement of left ventricular function after coronary artery occlusion in rats. *Regen Med*. 2007;2:63-68

188. Lai RC, Arslan F, Lee MM, Sze NS, Choo A, Chen TS, et al. Exosome secreted by msc reduces myocardial ischemia/reperfusion injury. *Stem Cell Res*. 2010;4:214-222

189. Mirotsou M, Zhang Z, Deb A, Zhang L, Gnecchi M, Noiseux N, et al. Secreted frizzled related protein 2 (sfrp2) is the key akt-mesenchymal stem cell-released paracrine factor mediating myocardial survival and repair. *Proc Natl Acad Sci U S A*. 2007;104:1643-1648

190. Danieli P, Malpasso G, Ciuffreda MC, Cervio E, Calvillo L, Copes F, et al. Conditioned medium from human amniotic mesenchymal stromal cells limits infarct size and enhances angiogenesis. *Stem Cells Transl Med*. 2015;4:448-458

191. Stahl PD, Raposo G. Extracellular vesicles: Exosomes and microvesicles, integrators of homeostasis. *Physiology (Bethesda)*. 2019;34:169-177

192. Ha D, Yang NN, Nadithe V. Exosomes as therapeutic drug carriers and delivery vehicles across biological membranes: Current perspectives and future challenges. *Acta Pharm Sin B*. 2016;6:287-296

193. Lin Y, Anderson JD, Rahnama LMA, Gu SV, Knowlton AA. Exosomes in disease and regeneration: Biological functions, diagnostics, and beneficial effects. *American Journal of Physiology-Heart and Circulatory Physiology*. 2020;319:H1162-H1180

194. Konoshenko MY, Lekchnov EA, Vlassov AV, Laktionov PP. Isolation of extracellular vesicles: General methodologies and latest trends. *Biomed Res Int*. 2018;2018:8545347

195. Kwon J-S, Schumacher SM, Gao E, Chuprun JK, Ibetti J, Roy R, et al. Characterization of βarkct engineered cellular extracellular vesicles and model specific cardioprotection. *American Journal of Physiology-Heart and Circulatory Physiology*. 2021;320:H1276-H1289
196. Turner A, Aggarwal P, Matter A, Olson B, Gu CC, Hunt SC, et al. Donor-specific phenotypic variation in hipsc cardiomyocyte-derived exosomes impacts endothelial cell function. *American Journal of Physiology-Heart and Circulatory Physiology*. 2021;320:H954-H968
197. Tan PPS, Hall D, Chilian WM, Chia YC, Mohd Zain S, Lim HM, et al. Exosomal micrornas in the development of essential hypertension and its potential as biomarkers. *American Journal of Physiology-Heart and Circulatory Physiology*. 2021;320:H1486-H1497
198. Wen Z, Mai Z, Zhu X, Wu T, Chen Y, Geng D, et al. Mesenchymal stem cell-derived exosomes ameliorate cardiomyocyte apoptosis in hypoxic conditions through microrna144 by targeting the pten/akt pathway. *Stem Cell Research & Therapy*. 2020;11:36
199. Mentkowski KI, Mursleen A, Snitzer JD, Euscher LM, Lang JK. Cdc-derived extracellular vesicles reprogram inflammatory macrophages to an arginase 1-dependent proangiogenic phenotype. *American Journal of Physiology-Heart and Circulatory Physiology*. 2020;318:H1447-H1460
200. Zhou M, Weber SR, Zhao Y, Chen H, Sundstrom JM. Chapter 2 - methods for exosome isolation and characterization. In: Edelstein L, Smythies J, Quesenberry P, Noble D, eds. *Exosomes*. Academic Press; 2020:23-38.
201. Reiner AT, Witwer KW, van Balkom BWM, de Beer J, Brodie C, Corteling RL, et al. Concise review: Developing best-practice models for the therapeutic use of extracellular vesicles. *STEM CELLS Translational Medicine*. 2017;6:1730-1739
202. Tang YT, Huang YY, Zheng L, Qin SH, Xu XP, An TX, et al. Comparison of isolation methods of exosomes and exosomal rna from cell culture medium and serum. *Int J Mol Med*. 2017;40:834-844
203. Van Deun J, Mestdagh P, Sormunen R, Cocquyt V, Vermaelen K, Vandesompele J, et al. The impact of disparate isolation methods for extracellular vesicles on downstream rna profiling. *J Extracell Vesicles*. 2014;3
204. Karnieli O, Friedner OM, Allickson JG, Zhang N, Jung S, Fiorentini D, et al. A consensus introduction to serum replacements and serum-free media for cellular therapies. *Cytotherapy*. 2017;19:155-169
205. Kink JA, Forsberg MH, Reshetylo S, Besharat S, Childs CJ, Pederson JD, et al. Macrophages educated with exosomes from primed mesenchymal stem cells treat acute radiation syndrome by promoting hematopoietic recovery. *Biol Blood Marrow Transplant*. 2019;25:2124-2133
206. Cui LL, Kinnunen T, Boltze J, Nystedt J, Jolkkonen J. Clumping and viability of bone marrow derived mesenchymal stromal cells under different preparation procedures: A flow cytometry-based in vitro study. *Stem Cells Int*. 2016;2016:1764938
207. Thery C, Witwer KW, Aikawa E, Alcaraz MJ, Anderson JD, Andriantsitohaina R, et al. Minimal information for studies of extracellular vesicles 2018 (misev2018): A position statement of the international society for extracellular vesicles and update of the misev2014 guidelines. *J Extracell Vesicles*. 2018;7:1535750

208. Fuster-Matanzo A, Gessler F, Leonardi T, Iraci N, Pluchino S. Acellular approaches for regenerative medicine: On the verge of clinical trials with extracellular membrane vesicles? *Stem Cell Res Ther*. 2015;6:227

209. Lener T, Gimona M, Aigner L, Börger V, Buzas E, Camussi G, et al. Applying extracellular vesicles based therapeutics in clinical trials - an isev position paper. *J Extracell Vesicles*. 2015;4:30087

210. Lalu MM, Mazzarello S, Zlepnig J, Dong YYR, Montroy J, McIntyre L, et al. Safety and efficacy of adult stem cell therapy for acute myocardial infarction and ischemic heart failure (safecell heart): A systematic review and meta-analysis. *Stem Cells Transl Med*. 2018;7:857-866

211. Jeong H, Yim HW, Park HJ, Cho Y, Hong H, Kim NJ, et al. Mesenchymal stem cell therapy for ischemic heart disease: Systematic review and meta-analysis. *Int J Stem Cells*. 2018;11:1-12

212. Arslan F, Lai RC, Smeets MB, Akeroyd L, Choo A, Aguor EN, et al. Mesenchymal stem cell-derived exosomes increase atp levels, decrease oxidative stress and activate pi3k/akt pathway to enhance myocardial viability and prevent adverse remodeling after myocardial ischemia/reperfusion injury. *Stem Cell Res*. 2013;10:301-312

213. He JG, Li HR, Han JX, Li BB, Yan D, Li HY, et al. Gata-4-expressing mouse bone marrow mesenchymal stem cells improve cardiac function after myocardial infarction via secreted exosomes. *Sci Rep*. 2018;8:9047

214. Feng Y, Huang W, Wani M, Yu X, Ashraf M. Ischemic preconditioning potentiates the protective effect of stem cells through secretion of exosomes by targeting mecp2 via mir-22. *PloS one*. 2014;9:e88685-e88685

215. Zhao Y, Sun X, Cao W, Ma J, Sun L, Qian H, et al. Exosomes derived from human umbilical cord mesenchymal stem cells relieve acute myocardial ischemic injury. *Stem Cells Int*. 2015;2015:761643

216. Cui X, He Z, Liang Z, Chen Z, Wang H, Zhang J. Exosomes from adipose-derived mesenchymal stem cells protect the myocardium against ischemia/reperfusion injury through wnt/β-catenin signaling pathway. *Journal of Cardiovascular Pharmacology*. 2017;70

217. Potz BA, Scrimgeour LA, Pavlov VI, Sodha NR, Abid MR, Sellke FW. Extracellular vesicle injection improves myocardial function and increases angiogenesis in a swine model of chronic ischemia. *J Am Heart Assoc*. 2018;7

218. Scrimgeour LA, Potz BA, Aboul Gheit A, Shi G, Stanley M, Zhang Z, et al. Extracellular vesicles promote arteriogenesis in chronically ischemic myocardium in the setting of metabolic syndrome. *J Am Heart Assoc*. 2019;8:e012617

219. Wang N, Chen C, Yang D, Liao Q, Luo H, Wang X, et al. Mesenchymal stem cells-derived extracellular vesicles, via mir-210, improve infarcted cardiac function by promotion of angiogenesis. *Biochimica et Biophysica Acta (BBA) - Molecular Basis of Disease*. 2017;1863:2085-2092

220. Shao L, Zhang Y, Lan B, Wang J, Zhang Z, Zhang L, et al. Mirna-sequence indicates that mesenchymal stem cells and exosomes have similar mechanism to enhance cardiac repair. *BioMed research international*. 2017;2017:4150705-4150705

221. Ma J, Zhao Y, Sun L, Sun X, Zhao X, Sun X, et al. Exosomes derived from akt-modified human umbilical cord mesenchymal stem cells improve cardiac regeneration and promote

angiogenesis via activating platelet-derived growth factor d. *Stem Cells Transl Med*. 2017;6:51-59

222. Luther KM, Haar L, McGuinness M, Wang Y, Lynch Iv TL, Phan A, et al. Exosomal mir-21a-5p mediates cardioprotection by mesenchymal stem cells. *J Mol Cell Cardiol*. 2018;119:125-137
223. Luo Q, Guo D, Liu G, Chen G, Hang M, Jin M. Exosomes from mir-126-overexpressing adscs are therapeutic in relieving acute myocardial ischaemic injury. *Cell Physiol Biochem*. 2017;44:2105-2116
224. Liu L, Jin X, Hu CF, Li R, Zhou Z, Shen CX. Exosomes derived from mesenchymal stem cells rescue myocardial ischaemia/reperfusion injury by inducing cardiomyocyte autophagy via ampk and akt pathways. *Cell Physiol Biochem*. 2017;43:52-68
225. Anderson JD, Johansson HJ, Graham CS, Vesterlund M, Pham MT, Bramlett CS, et al. Comprehensive proteomic analysis of mesenchymal stem cell exosomes reveals modulation of angiogenesis via nuclear factor-kappab signaling. *Stem Cells*. 2016;34:601-613
226. Ammar HI, Shamseldeen AM, Shoukry HS, Ashour H, Kamar SS, Rashed LA, et al. Metformin impairs homing ability and efficacy of mesenchymal stem cells for cardiac repair in streptozotocin-induced diabetic cardiomyopathy in rats. *Am J Physiol Heart Circ Physiol*. 2021;320:H1290-H1302
227. Takeuchi R, Katagiri W, Endo S, Kobayashi T. Exosomes from conditioned media of bone marrow-derived mesenchymal stem cells promote bone regeneration by enhancing angiogenesis. *PLoS One*. 2019;14:e0225472
228. Bandaru P, Cefaloni G, Vajhadin F, Lee K, Kim HJ, Cho HJ, et al. Mechanical cues regulating proangiogenic potential of human mesenchymal stem cells through yap-mediated mechanosensing. *Small*. 2020;16:e2001837
229. Seib FP, Prewitz M, Werner C, Bornhauser M. Matrix elasticity regulates the secretory profile of human bone marrow-derived multipotent mesenchymal stromal cells (mscs). *Biochem Biophys Res Commun*. 2009;389:663-667
230. Lopatina T, Bruno S, Tetta C, Kalinina N, Porta M, Camussi G. Platelet-derived growth factor regulates the secretion of extracellular vesicles by adipose mesenchymal stem cells and enhances their angiogenic potential. *Cell Commun Signal*. 2014;12:26-26
231. Liang X, Zhang L, Wang S, Han Q, Zhao RC. Exosomes secreted by mesenchymal stem cells promote endothelial cell angiogenesis by transferring mir-125a. *J Cell Sci*. 2016;129:2182-2189
232. Wen Z, Huang W, Feng Y, Cai W, Wang Y, Wang X, et al. Microrna-377 regulates mesenchymal stem cell-induced angiogenesis in ischemic hearts by targeting vegf. *PLoS One*. 2014;9:e104666
233. Hofstra L, Liem IH, Dumont EA, Boersma HH, van Heerde WL, Doevendans PA, et al. Visualisation of cell death in vivo in patients with acute myocardial infarction. *Lancet*. 2000;356:209-212
234. Olivetti G, Quaini F, Sala R, Lagrasta C, Corradi D, Bonacina E, et al. Acute myocardial infarction in humans is associated with activation of programmed myocyte cell death in the surviving portion of the heart. *J Mol Cell Cardiol*. 1996;28:2005-2016
235. Rakusan K, Flanagan MF, Geva T, Southern J, Van Praagh R. Morphometry of human coronary capillaries during normal growth and the effect of age in left ventricular pressure-overload hypertrophy. *Circulation*. 1992;86:38-46

236. Wehman B, Sharma S, Pietris N, Mishra R, Siddiqui OT, Bigham G, et al. Mesenchymal stem cells preserve neonatal right ventricular function in a porcine model of pressure overload. *Am J Physiol Heart Circ Physiol*. 2016;310:H1816-1826
237. Xue C, Shen Y, Li X, Li B, Zhao S, Gu J, et al. Exosomes derived from hypoxia-treated human adipose mesenchymal stem cells enhance angiogenesis through the pka signaling pathway. *Stem Cells Dev*. 2018;27:456-465
238. Han Y, Ren J, Bai Y, Pei X, Han Y. Exosomes from hypoxia-treated human adipose-derived mesenchymal stem cells enhance angiogenesis through vegf/vegf-r. *Int J Biochem Cell Biol*. 2019;109:59-68
239. Madrigal M, Rao KS, Riordan NH. A review of therapeutic effects of mesenchymal stem cell secretions and induction of secretory modification by different culture methods. *J Transl Med*. 2014;12:260
240. Kwon YW, Heo SC, Jeong GO, Yoon JW, Mo WM, Lee MJ, et al. Tumor necrosis factor-alpha-activated mesenchymal stem cells promote endothelial progenitor cell homing and angiogenesis. *Biochim Biophys Acta*. 2013;1832:2136-2144
241. Grote K, Petri M, Liu C, Jehn P, Spalthoff S, Kokemuller H, et al. Toll-like receptor 2/6-dependent stimulation of mesenchymal stem cells promotes angiogenesis by paracrine factors. *Eur Cell Mater*. 2013;26:66-79; discussion 79
242. Shi RZ, Wang JC, Huang SH, Wang XJ, Li QP. Angiotensin ii induces vascular endothelial growth factor synthesis in mesenchymal stem cells. *Exp Cell Res*. 2009;315:10-15
243. Ji Y, Li J, Wei Y, Gao W, Fu X, Wang Y. Substrate stiffness affects the immunosuppressive and trophic function of hmscs via modulating cytoskeletal polymerization and tension. *Biomater Sci*. 2019;7:5292-5300
244. Bauters A, Ennezat PV, Tricot O, Lallemant R, Aumegeat V, Segrestin B, et al. Relation of admission white blood cell count to left ventricular remodeling after anterior wall acute myocardial infarction. *Am J Cardiol*. 2007;100:182-184
245. Chia S, Nagurney JT, Brown DF, Raffel OC, Bamberg F, Senatore F, et al. Association of leukocyte and neutrophil counts with infarct size, left ventricular function and outcomes after percutaneous coronary intervention for st-elevation myocardial infarction. *Am J Cardiol*. 2009;103:333-337
246. Campian ME, Hardziyenka M, de Bruin K, van Eck-Smit BL, de Bakker JM, Verberne HJ, et al. Early inflammatory response during the development of right ventricular heart failure in a rat model. *Eur J Heart Fail*. 2010;12:653-658
247. Kim J, Hematti P. Mesenchymal stem cell-educated macrophages: A novel type of alternatively activated macrophages. *Exp Hematol*. 2009;37:1445-1453
248. Zhang B, Zhao N, Zhang J, Liu Y, Zhu D, Kong Y. Mesenchymal stem cells rejuvenate cardiac muscle through regulating macrophage polarization. *Aging (Albany NY)*. 2019;11:3900-3908
249. Morrison TJ, Jackson MV, Cunningham EK, Kissenpfennig A, McAuley DF, O'Kane CM, et al. Mesenchymal stromal cells modulate macrophages in clinically relevant lung injury models by extracellular vesicle mitochondrial transfer. *Am J Respir Crit Care Med*. 2017;196:1275-1286
250. Willis GR, Fernandez-Gonzalez A, Anastas J, Vitali SH, Liu X, Ericsson M, et al. Mesenchymal stromal cell exosomes ameliorate experimental bronchopulmonary dysplasia and restore lung function through macrophage immunomodulation. *Am J Respir Crit Care Med*. 2018;197:104-116

251. Liu H, Liang Z, Wang F, Zhou C, Zheng X, Hu T, et al. Exosomes from mesenchymal stromal cells reduce murine colonic inflammation via a macrophage-dependent mechanism. *JCI Insight*. 2019;4

252. Zhou YZ, Cheng Z, Wu Y, Wu QY, Liao XB, Zhao Y, et al. Mesenchymal stem cell-derived conditioned medium attenuate angiotensin ii-induced aortic aneurysm growth by modulating macrophage polarization. *J Cell Mol Med*. 2019;23:8233-8245

253. Klinger JR, Pereira M, Del Tatto M, Brodsky AS, Wu KQ, Dooner MS, et al. Mesenchymal stem cell extracellular vesicles reverse sugen/hypoxia pulmonary hypertension in rats. *Am J Respir Cell Mol Biol*. 2020;62:577-587

254. Lo Sicco C, Reverberi D, Balbi C, Ulivi V, Principi E, Pascucci L, et al. Mesenchymal stem cell-derived extracellular vesicles as mediators of anti-inflammatory effects: Endorsement of macrophage polarization. *Stem Cells Transl Med*. 2017;6:1018-1028

255. Carty F, Mahon BP, English K. The influence of macrophages on mesenchymal stromal cell therapy: Passive or aggressive agents? *Clin Exp Immunol*. 2017;188:1-11

256. Eirin A, Lerman LO. Stem cell-derived extracellular vesicles for renal repair: Do cardiovascular comorbidities matter? *Am J Physiol Renal Physiol*. 2019;317:F1414-F1419

257. Zhang S, Liu X, Ge LL, Li K, Sun Y, Wang F, et al. Mesenchymal stromal cell-derived exosomes improve pulmonary hypertension through inhibition of pulmonary vascular remodeling. *Respir Res*. 2020;21:71

258. Pisano A, Cerbelli B, Perli E, Pelullo M, Bargelli V, Preziuso C, et al. Impaired mitochondrial biogenesis is a common feature to myocardial hypertrophy and end-stage ischemic heart failure. *Cardiovascular pathology : the official journal of the Society for Cardiovascular Pathology*. 2016;25:103-112

259. DeSantiago J, Bare DJ, Banach K. Ischemia/reperfusion injury protection by mesenchymal stem cell derived antioxidant capacity. *Stem Cells and Development*. 2013;22:2497-2507

260. Dupont S, Morsut L, Aragona M, Enzo E, Giulitti S, Cordenonsi M, et al. Role of yap/taz in mechanotransduction. *Nature*. 2011;474:179-183

261. Lahm T, Douglas IS, Archer SL, Bogaard HJ, Chesler NC, Haddad F, et al. Assessment of right ventricular function in the research setting: Knowledge gaps and pathways forward. An official american thoracic society research statement. *Am J Respir Crit Care Med*. 2018;198:e15-e43

262. Hill MR, Simon MA, Valdez-Jasso D, Zhang W, Champion HC, Sacks MS. Structural and mechanical adaptations of right ventricle free wall myocardium to pressure overload. *Ann Biomed Eng*. 2014;42:2451-2465

263. Jang S, Vanderpool RR, Avazmohammadi R, Lapshin E, Bachman TN, Sacks M, et al. Biomechanical and hemodynamic measures of right ventricular diastolic function: Translating tissue biomechanics to clinical relevance. *J Am Heart Assoc*. 2017;6

264. Ryan JJ, Archer SL. The right ventricle in pulmonary arterial hypertension: Disorders of metabolism, angiogenesis and adrenergic signaling in right ventricular failure. *Circ Res*. 2014;115:176-188

265. Sutendra G, Dromparis P, Paulin R, Zervopoulos S, Haromy A, Nagendran J, et al. A metabolic remodeling in right ventricular hypertrophy is associated with decreased angiogenesis and a transition from a compensated to a decompensated state in pulmonary hypertension. *Journal of molecular medicine (Berlin, Germany)*. 2013;91:1315-1327

266. Bogaard HJ, Natarajan R, Henderson SC, Long CS, Kraskauskas D, Smithson L, et al. Chronic pulmonary artery pressure elevation is insufficient to explain right heart failure. *Circulation*. 2009;120:1951-1960

267. LeBar K, Wang Z. Extracellular matrix in cardiac tissue mechanics and physiology: Role of collagen accumulation. 2021.

268. Frump AL, Bonnet S, de Jesus Perez VA, Lahm T. Emerging role of angiogenesis in adaptive and maladaptive right ventricular remodeling in pulmonary hypertension. *Am J Physiol Lung Cell Mol Physiol*. 2018;314:L443-L460

269. Nguyen-Truong M, Hematti P, Wang Z. Current status of myocardial restoration via the paracrine function of mesenchymal stromal cells. *Am J Physiol Heart Circ Physiol*. 2021;321:H112-H127

270. VeDepo MC, Flores K, Jacot JG. Chemokine-induced pbmc and subsequent msc migration toward decellularized heart valve tissue. *Cardiovasc Eng Technol*. 2021;12:325-338

271. Bandaru P, Cefaloni G, Vajhadin F, Lee K, Kim H-J, Cho H-J, et al. Mechanical cues regulating proangiogenic potential of human mesenchymal stem cells through yap-mediated mechanosensing. *Small*. 2020;16:2001837

272. Ogle ME, Doron G, Levy MJ, Temenoff JS. Hydrogel culture surface stiffness modulates mesenchymal stromal cell secretome and alters senescence. *Tissue Eng Part A*. 2020;26:1259-1271

273. Nguyen-Truong M, Li YV, Wang Z. Mechanical considerations of electrospun scaffolds for myocardial tissue and regenerative engineering. *Bioengineering (Basel)*. 2020;7

274. Liu W, Nguyen-Truong M, Labus K, Boon J, Easley J, Monnet E, et al. Correlations between the right ventricular passive elasticity and organ function in adult ovine. *Journal of Integrative Cardiology*. 2020;6

275. Liu W, Nguyen-Truong M, Ahern M, Labus KM, Puttlitz CM, Wang Z. Different passive viscoelastic properties between the left and right ventricles in healthy adult ovine. *J Biomech Eng*. 2021;143

276. Nguyen-Truong M, Liu W, Doherty C, LeBar K, Labus KM, Puttlitz CM, et al. The interventricular septum is biomechanically distinct from the ventricular free walls. *Bioengineering (Basel)*. 2021;8

277. Su N, Gao PL, Wang K, Wang JY, Zhong Y, Luo Y. Fibrous scaffolds potentiate the paracrine function of mesenchymal stem cells: A new dimension in cell-material interaction. *Biomaterials*. 2017;141:74-85

278. Hong Y, Guan J, Fujimoto KL, Hashizume R, Pelinescu AL, Wagner WR. Tailoring the degradation kinetics of poly(ester carbonate urethane)urea thermoplastic elastomers for tissue engineering scaffolds. *Biomaterials*. 2010;31:4249-4258

279. Stankus JJ, Guan J, Wagner WR. Fabrication of biodegradable elastomeric scaffolds with sub-micron morphologies. *J Biomed Mater Res A*. 2004;70:603-614

280. Bhardwaj N, Kundu SC. Electrospinning: A fascinating fiber fabrication technique. *Biotechnol Adv*. 2010;28:325-347

281. Jana S, Bhagia A, Lerman A. Optimization of polycaprolactone fibrous scaffold for heart valve tissue engineering. *Biomed Mater*. 2019;14:065014

282. Bougatef F, Quemener C, Kellouche S, Naïmi B, Podgorniak MP, Millot G, et al. Emmprin promotes angiogenesis through hypoxia-inducible factor-2alpha-mediated regulation of soluble vegf isoforms and their receptor vegfr-2. *Blood*. 2009;114:5547-5556

283. Sun M, Chi G, Li P, Lv S, Xu J, Xu Z, et al. Effects of matrix stiffness on the morphology, adhesion, proliferation and osteogenic differentiation of mesenchymal stem cells. *Int J Med Sci*. 2018;15:257-268

284. Rao VV, Vu MK, Ma H, Killaars AR, Anseth KS. Rescuing mesenchymal stem cell regenerative properties on hydrogel substrates post serial expansion. *Bioeng Transl Med*. 2019;4:51-60

# 7. Conclusions and Future Work

My research into the biomechanical mechanisms of right ventricle failure secondary to pressure overload and stromal cell mechanobiology in the context of pro-angiogenic paracrine effect fill critical knowledge gaps in the biomechanical mechanism of RV failure and will pave the foundation leading to RV-specific treatment for RV failure treatments. With the completion of Aims 1-4, these works establish the necessary groundwork in delineating the unique biomechanical mechanisms of RV failure and will support biophysical strategies to improve MSC-based therapies for RV failure. In summary, the ventricular free wall and septum biomechanics were investigated, an *in vivo* ovine model of adult RV failure was established, and the MSC response to mechanical cues of stiffness and anisotropy were studied on an established RV-like biomimetic platform. Together, the completion of all four aims will make significant inroads in filling critical knowledge gaps to more effectively manage and treat RV failure secondary to pressure overload.

Having observed biomechanical changes in the ventricular free walls and septum from *ex vivo* biaxial mechanical testing, it would be of great interest to investigate the multi-scale changes such as alterations in the myofiber and collagen fiber structure of the free walls and septum, as well as those in the individual cardiomyocytes. Particularly, the microstructural changes of the RV free wall and septum can help explain the macroscale tissue level biomechanics by understanding fiber-level or cell-level adaptations to pressure overload. While the RV free wall has been a main focus, more work needs to be done to elucidate the adaptations of the septum to pressure overload and the specific contribution of septum to overall RV chamber function. The RV free wall and septum have different biomechanical properties and different collagen content, and thus require specific investigation and subsequent treatment. The traditional view of the septum as a single entity also needs to be further elucidated, as there are two reports that the septum shows different strain and strain rates between two or three layers, suggesting that the septum is a layered structure that may serve each ventricle differently. A future direction would be to tease out the structure-function relationships of the septal layers. These can provide useful insights on RV therapeutic targets as well as guide the development of RV failure therapies that alleviate wall stress and restore ventricular function.

Another direction of future research would be a more in-depth study of the mechanobiology of MSCs to understand the regulation of mechanical cues on the production of therapeutic trophic factors. In contrast to the traditional route of regenerative therapy using MSC differentiation, the emerging trend is to use its paracrine function to restore diseased tissues. The collective paracrine function of MSCs (which yield therapeutic products) is dependent on their stemness and proliferation. Prior research and our current study have shown a mechanical regulation of MSC stemness and proliferation, which ultimately affect the paracrine function. However, the molecular mechanisms underlying the mechanical regulation have not been fully understood. The yes-associated protein (YAP), a key mechanotransduction protein, has been shown to regulate MSC phenotype (i.e., maintenance of "stemness" or differentiation into specific lineages like osteogenic, adipogenic, etc.) and proliferation. How MSC YAP regulation and the downstream events are altered by the mechanical factors investigated in this study (i.e., anisotropy and RV-like stiffness) is unknown. Future research could tease out the answers which will ultimately help to optimize MSC therapy using their paracrine function in the context of RV mechanics.

With an improved understanding of MSC paracrine function, this knowledge can be harnessed towards the implementation or refinement of cell-based or cell-free therapies for RV failure. For instance, the MSC conditioned medium or their secretome (e.g., extracellular vesicles) could be used to repair failing heart. The growing research on the application of cell-free products can promote healing by avoiding the limitations of cell therapies (i.e., simplifies the preparation and execution of therapy and avoids risk of tumorigenicity when applied *in vivo*) and provide patient-specific treatment plans. With the aforementioned novel biomimetic platform, we could explore the strategies to improve the MSC yield of MSC cytokines (e.g., pro-angiogenic, anti-inflammatory, anti-fibrotic, anti-oxidative, etc.) for RV failure therapy. Depending on the future yields observed, these products could be applied in an *in vivo* model of RV failure to assess the healing potential.

Taken together, there are many exciting and unexplored avenues to build off of this current work. I am thrilled to have had the opportunity to push the boundaries of science and create knowledge in my multidisciplinary research. I look forward to the future advances in improving the understanding and treatment of right heart failure, as well as deepening the knowledge of mesenchymal stromal cell mechanobiology and enhancing relevant cell-based heart failure therapies.

# Appendix

**Table A1**. Overview of the roles of cardiac ECM in mechanobiology during cardiac remodeling[5].

| **Effects on cardiac ECM** | |
|---|---|
| **Passive roles (regulated by surrounding cells)** | ECM mechanical properties |
| | ECM composition (different ECM proteins and their subtypes, cross-linking formation) |
| | ECM synthesis and degradation |
| **Functions of cardiac ECM** | |
| **Active roles** | Contribute to mechanical properties of cardiac tissues |
| | Contribute to passive tension and mechanical function |
| | Provide scaffold and mechanical environment to surrounding cells |
| | Alter cell function with chemical or mechanical cues |
| | Assist mechanotransduction via cell-ECM binding sites (e.g., integrins, focal adhesions, receptors) |

**Table A2**. Hemodynamic and mechanical differences between the LV and RV[5].

| **Properties** | **LV** | **RV** |
|---|---|---|
| Mass (g/$m^2$) | 87±12 | 26±5 |
| Wall thickness (mm) | 7-11 | 2-5 |
| Ventricular pressure (mmHg) | 0-140 | 0-40 |
| Ventricular elastance (mmHg/mL) | 5.48 ± 1.23 | 1.30 ± 0.84 |
| Vascular resistance (dyne/s/$cm^5$) | 1238 ± 407 | 97 ± 55 |
| Passive stiffness in normal strain (N/mm) | 5.2 (in porcine LV) | 1.2 (in porcine RV) |
| Myocardial compliance ($mmHg^{-1}$) | 0.006 ± 0.002 | 0.313 ± 0.084 |
| Coronary blood flow (ml/min/g) | High (0.5-2.0) | Low (0.5-1.0) |
| Pressure-flow autoregulation | Presence | Absence |
| Accommodation to imposed load | Better in response to pressure overload | Better in response to volume overload |

---

[5] Adapted by permission from Springer Nature Customer Service Centre GmbH: Springer. *Cardiac Extracellular Matrix.* “Biomechanical Properties and Mechanobiology of Cardiac ECM”. Nguyen-Truong M and Wang Z, 2018. https://doi.org/10.1007/978-3-319-97421-7_1.

## Pressure-Volume Data from *In Vivo* RV Failure Animal Model

*In vivo* pressure-volume data were obtained from invasive catheterization at baseline and after 20 weeks of RV failure to derive other hemodynamic and biomechanical parameters such as contractility by end-systolic pressure volume relations (ESPVR or Ees), stroke work (SW), dP/dtmax and preload adjusted maximal power (PAMP). Other parameters we wanted to include arterial elastance (Ea), total pulmonary vascular resistance (tPVR), total energy (pressure-volume area; PVA) and elastic potential energy (PE), diastolic stiffness (end-diastolic pressure-volume relations/EDPVR), wall compliance ($\Delta V/\Delta P$), relaxation factor $\tau$, dP/dtmin and ventricular vascular coupling (VVC; by Ees/Ea or stroke volume (SV)/end-systolic volume (ESV)).

A conductance catheter (1.9 Fr Pressure-Volume Catheter; Millar) was introduced via an introducer and 6F guide catheter to the RV. The catheter output was processed (MPVS Ultra, Millar) and analyzed (LabChart). Representative sample data from one ovine at baseline are shown in Figure A1 and Table A3 and at week 20 of RVF are shown in Figure A2 and Table A4. Table A3 has average data from n=3 ovine at baseline and week 20 of RVF. Figures A3 and A4 show representative vena cava occlusion pressure-volume loops at baseline and week 20 of RVF.

Currently, there still remain issues with the volume measurement on some datasets. The pressure measurement is realistic. The generation of some loops is reversed (clockwise instead of counter-clockwise) leading to negative stroke work, which is unrealistic (**Table A3; Table A5**). Some animals present stroke volumes that are unrealistic (SV~10 mL) despite following protocol (**Fig. A5**).

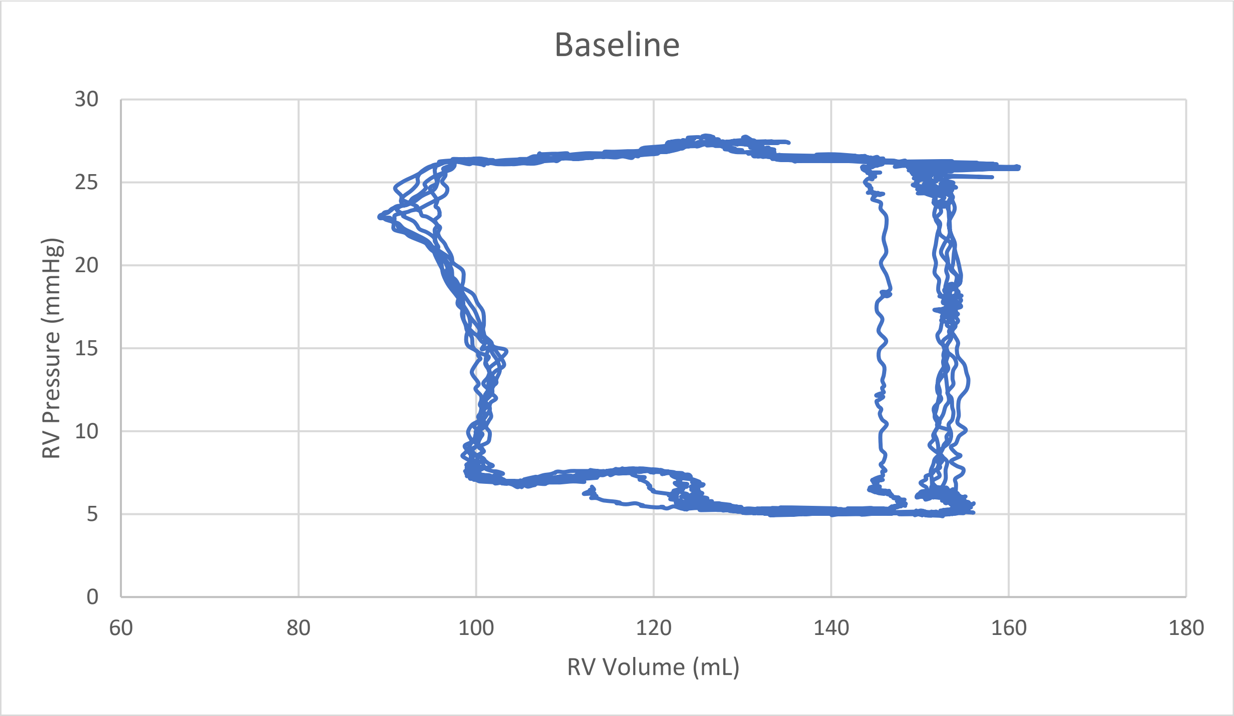

**Figure A1**. Representative pressure-volume loop of ovine at baseline.

**Table A3**. Pressure-volume data of one ovine at baseline.

| **Baseline** | | | | | | | | | | | |
|---|---|---|---|---|---|---|---|---|---|---|---|
| Loop # | 1 | 2 | 3 | 4 | 5 | | Avg | Std | Min | Max | Count |
| SW (mmHg*mL) | -1119 | -1130 | -1094 | -1146 | -1095 | | -1117 | 22.5 | -1146 | -1094 | 5 |
| CO (mL/min) | 7472 | 6578 | 6711 | 7046 | 6667 | | 6895 | 368.1 | 6578 | 7472 | 5 |
| SV (mL) | 71.61 | 63.81 | 64.53 | 70.23 | 61.89 | | 66.41 | 4.3 | 61.89 | 71.61 | 5 |
| Vmax (mL) | 161.2 | 154.9 | 155.3 | 161.1 | 156.7 | | 157.8 | 3.1 | 154.9 | 161.2 | 5 |
| Vmin (mL) | 89.56 | 91.07 | 90.73 | 90.88 | 94.8 | | 91.41 | 2.0 | 89.56 | 94.8 | 5 |
| Ves (mL) | 97.4 | 94.49 | 97.31 | 94.86 | 95.17 | | 95.85 | 1.4 | 94.49 | 97.4 | 5 |
| Ved (mL) | 105 | 104.8 | 103.9 | 103.9 | 100.4 | | 103.6 | 1.9 | 100.4 | 105 | 5 |
| Pmax (mmHg) | 27.76 | 27.54 | 27.54 | 27.48 | 27.41 | | 27.55 | 0.1 | 27.41 | 27.76 | 5 |
| Pmin (mmHg) | 4.933 | 4.933 | 4.87 | 4.964 | 5.027 | | 4.946 | 0.1 | 4.87 | 5.027 | 5 |
| Pmean (mmHg) | 15.18 | 15.19 | 15.15 | 14.89 | 15.38 | | 15.16 | 0.2 | 14.89 | 15.38 | 5 |
| Pdev (mmHg) | 22.83 | 22.61 | 22.67 | 22.51 | 22.39 | | 22.6 | 0.2 | 22.39 | 22.83 | 5 |
| Pes (mmHg) | 26.41 | 25.88 | 26.29 | 25.91 | 26.03 | | 26.1 | 0.2 | 25.88 | 26.41 | 5 |
| Ped (mmHg) | 6.689 | 6.814 | 6.846 | 6.908 | 7.347 | | 6.921 | 0.3 | 6.689 | 7.347 | 5 |
| HR (bpm) | 104.3 | 103.1 | 104 | 100.3 | 107.7 | | 103.9 | 2.7 | 100.3 | 107.7 | 5 |
| EF (%) | 72.96 | 65.14 | 64.01 | 71.42 | 61.4 | | 66.99 | 5.0 | 61.4 | 72.96 | 5 |
| Ea (mmHg/mL) | 0.3688 | 0.4056 | 0.4073 | 0.3689 | 0.4206 | | 0.3943 | 0.0 | 0.3688 | 0.4206 | 5 |
| PowMax (mmHg*mL/s) | 1.41E+05 | 1.20E+05 | 1.52E+05 | 1.76E+05 | 1.82E+05 | | 1.54E+05 | 25440.5 | 1.20E+05 | 1.82E+05 | 5 |
| dP/dt max (mmHg/s) | 721.2 | 752.5 | 721.2 | 721.2 | 721.2 | | 727.4 | 14.0 | 721.2 | 752.5 | 5 |
| dP/dt min (mmHg/s) | -627.1 | -627.1 | -627.1 | -627.1 | -595.7 | | -620.8 | 14.0 | -627.1 | -595.7 | 5 |
| dV/dt max (mL/s) | 5369 | 6947 | 5766 | 7840 | 7393 | | 6663 | 1058.1 | 5369 | 7840 | 5 |
| dV/dt min (mL/s) | -7453 | -6877 | -7869 | -7512 | -8127 | | -7568 | 473.5 | -8127 | -6877 | 5 |
| P@dV/dt max (mmHg) | 5.027 | 5.215 | 26.38 | 4.996 | 5.184 | | 9.36 | 9.5 | 4.996 | 26.38 | 5 |
| P@dP/dt max (mmHg) | 17.88 | 18.07 | 16.06 | 18.38 | 17.19 | | 17.52 | 0.9 | 16.06 | 18.38 | 5 |
| V@dP/dt max (mL) | 98.15 | 97.95 | 100.8 | 98.34 | 100.8 | | 99.21 | 1.5 | 97.95 | 100.8 | 5 |
| V@dP/dt min (mL) | 153.3 | 153.3 | 152 | 153.3 | 152.3 | | 152.8 | 0.6 | 152 | 153.3 | 5 |
| Tau (ms) | 58.11 | 57.05 | 59.81 | 67.15 | 27.2 | | 53.86 | 15.4 | 27.2 | 67.15 | 5 |
| ESPVR (mmHg/mL) | | | | | | | | | | | |
| Piso (mmHg) | | | | | | | | | | | |

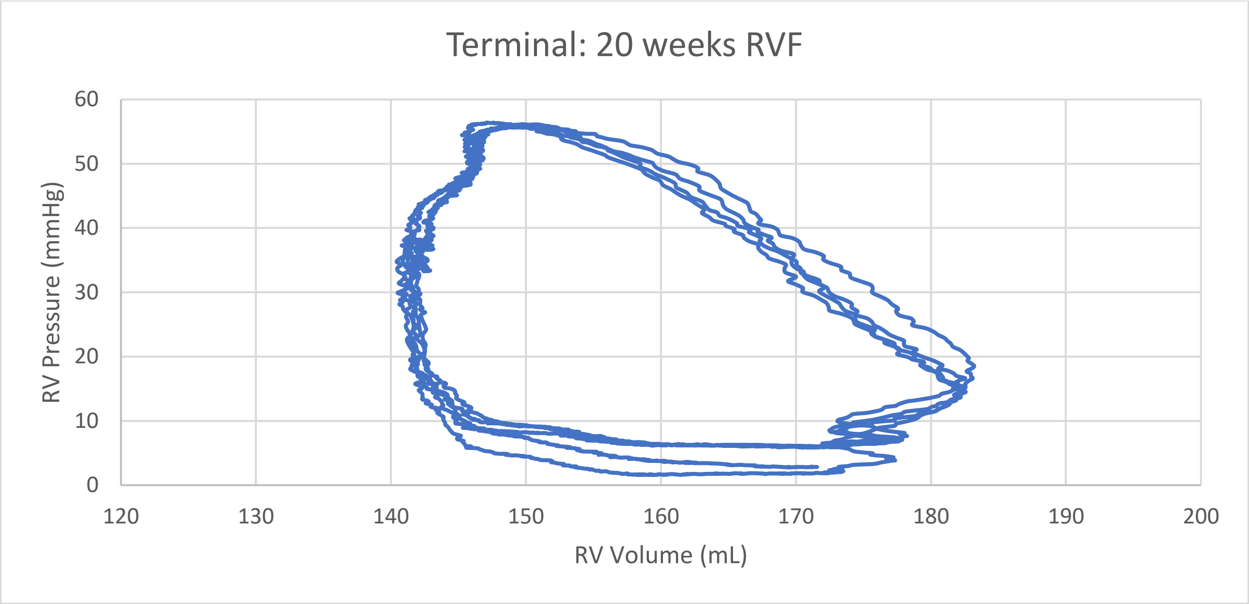

**Figure A2**. Representative pressure-volume loop of ovine at week 20 of RVF.

**Table A4**. Pressure-volume data of one ovine at week 20 of RVF.

| **Terminal - 20 weeks RVF** | | | | | | | | | | | | | | | | | | | | |
|---|---|---|---|---|---|---|---|---|---|---|---|---|---|---|---|---|---|---|---|---|
| Loop # | 1 | 2 | 3 | 4 | 5 | 6 | 7 | 8 | 9 | 10 | 11 | 12 | 13 | 14 | | Avg | Std | Min | Max | Count |
| SW (mmHg*mL) | 1297 | 1191 | 1269 | 1090 | 1215 | 1292 | 1198 | 1339 | 1106 | 1239 | 1186 | 1225 | 1383 | 1150 | | 1227 | 83.8 | 1090 | 1383 | 14 |
| CO (mL/min) | 4317 | 4213 | 4149 | 4307 | 4267 | 4281 | 4157 | 4173 | 4294 | 4262 | 4274 | 4286 | 4296 | 4259 | | 4252 | 56.3 | 4149 | 4317 | 14 |
| SV (mL) | 42.38 | 41.36 | 41.63 | 41.35 | 41.74 | 41.81 | 40.88 | 41.59 | 40.72 | 41.98 | 41.95 | 42.07 | 42.68 | 40.32 | | 41.6 | 0.6 | 40.32 | 42.68 | 14 |
| Vmax (mL) | 183.2 | 182.4 | 182.6 | 182.5 | 182.4 | 182.7 | 182 | 182.6 | 182.4 | 182.6 | 182.8 | 183.1 | 183.4 | 182 | | 182.6 | 0.4 | 182 | 183.4 | 14 |
| Vmin (mL) | 140.8 | 141.1 | 141 | 141.2 | 140.6 | 140.9 | 141.1 | 141 | 141.7 | 140.7 | 140.8 | 141 | 140.8 | 141.7 | | 141 | 0.3 | 140.6 | 141.7 | 14 |
| Ves (mL) | 141.8 | 141.9 | 141.9 | 142.4 | 141.3 | 141.6 | 141.9 | 141.7 | 142.3 | 141 | 141.2 | 142.2 | 141.8 | 142.3 | | 141.8 | 0.4 | 141 | 142.4 | 14 |
| Ved (mL) | 172 | 170.9 | 171.7 | 175.8 | 171.7 | 172.6 | 171.4 | 173.6 | 176.4 | 170.3 | 172.2 | 171.8 | 173.7 | 175.6 | | 172.8 | 1.9 | 170.3 | 176.4 | 14 |
| Pmax (mmHg) | 53.3 | 55.62 | 56.15 | 53.61 | 55.96 | 53.18 | 56.09 | 56.37 | 54.65 | 55.96 | 51.45 | 56.15 | 55.68 | 55.87 | | 55 | 1.5 | 51.45 | 56.37 | 14 |
| Pmin (mmHg) | 1.102 | 5.83 | 4.515 | 5.329 | 5.987 | 1.039 | 5.799 | 3.263 | 5.674 | 5.924 | 2.762 | 5.83 | 1.572 | 5.768 | | 4.314 | 1.9 | 1.039 | 5.987 | 14 |
| Pmean (mmHg) | 25.17 | 26.72 | 26.66 | 25.76 | 27.53 | 25.22 | 26.95 | 26.46 | 26.49 | 27.41 | 24.77 | 27.42 | 25.68 | 27.15 | | 26.39 | 0.9 | 24.77 | 27.53 | 14 |
| Pdev (mmHg) | 52.2 | 49.79 | 51.64 | 48.29 | 49.98 | 52.14 | 50.29 | 53.11 | 48.97 | 50.04 | 48.69 | 50.32 | 54.11 | 50.1 | | 50.69 | 1.7 | 48.29 | 54.11 | 14 |
| Pes (mmHg) | 53.3 | 55.62 | 56.09 | 53.61 | 55.71 | 53.11 | 56.06 | 56.12 | 54.62 | 55.81 | 51.36 | 56.12 | 55.62 | 55.81 | | 54.93 | 1.5 | 51.36 | 56.12 | 14 |
| Ped (mmHg) | 9.337 | 6.237 | 9.337 | 6.582 | 9.181 | 9.463 | 6.237 | 9.4 | 5.705 | 9.118 | 9.15 | 8.21 | 9.494 | 5.768 | | 8.087 | 1.6 | 5.705 | 9.494 | 14 |
| HR (bpm) | 101.9 | 101.9 | 99.67 | 104.2 | 102.2 | 102.4 | 101.7 | 100.3 | 105.4 | 101.5 | 101.9 | 101.9 | 100.7 | 105.6 | | 102.2 | 1.7 | 99.67 | 105.6 | 14 |
| EF (%) | 24.29 | 23.78 | 23.84 | 23.78 | 24.14 | 23.85 | 23.65 | 23.89 | 23.44 | 24.01 | 23.97 | 24.26 | 24.36 | 23.25 | | 23.89 | 0.3 | 23.25 | 24.36 | 14 |
| Ea (mmHg/mL) | 1.258 | 1.345 | 1.347 | 1.297 | 1.335 | 1.27 | 1.371 | 1.349 | 1.341 | 1.329 | 1.224 | 1.334 | 1.303 | 1.384 | | 1.321 | 0.0 | 1.224 | 1.384 | 14 |
| PowMax (mmHg*mL/s) | 2.92E+04 | 2.73E+04 | 2.56E+04 | 2.90E+04 | 2.84E+04 | 2.37E+04 | 3.04E+04 | 2.76E+04 | 2.79E+04 | 2.35E+04 | 2.94E+04 | 2.89E+04 | 2.77E+04 | 2.23E+04 | | 2.72E+04 | 2475.4 | 2.23E+04 | 3.04E+04 | 14 |
| dP/dt max (mmHg/s) | 845.5 | 814.2 | 845.5 | 876.8 | 814.2 | 845.5 | 814.2 | 814.2 | 908.1 | 845.5 | 814.2 | 751.5 | 782.8 | 908.1 | | 834.3 | 43.6 | 751.5 | 908.1 | 14 |
| dP/dt min (mmHg/s) | -845.5 | -845.5 | -782.8 | -845.5 | -845.5 | -876.8 | -814.2 | -751.5 | -876.8 | -1002 | -814.2 | -782.8 | -876.8 | -845.5 | | -843.2 | 59.5 | -1002 | -751.5 | 14 |
| dV/dt max (mL/s) | 1001 | 953.3 | 1059 | 1146 | 1223 | 1078 | 1194 | 1175 | 1030 | 982.2 | 1252 | 1117 | 1117 | 1165 | | 1107 | 92.5 | 953.3 | 1252 | 14 |
| dV/dt min (mL/s) | -1290 | -1146 | -1050 | -1011 | -991.8 | -1069 | -972.5 | -1030 | -1165 | -1454 | -1146 | -1050 | -1098 | -1117 | | -1114 | 128.4 | -1454 | -972.5 | 14 |
| P@dV/dt max (mmHg) | 10.81 | 8.868 | 24.21 | 7.49 | 9.337 | 5.705 | 9.369 | 5.392 | 20.58 | 9.525 | 23.46 | 7.49 | 4.045 | 5.768 | | 10.86 | 6.8 | 4.045 | 24.21 | 14 |
| P@dP/dt max (mmHg) | 24.05 | 21.86 | 25.71 | 19.98 | 23.49 | 24.84 | 21.39 | 24.15 | 19.8 | 24.77 | 23.46 | 21.93 | 24.27 | 20.2 | | 22.85 | 2.0 | 19.8 | 25.71 | 14 |
| V@dP/dt max (mL) | 174.5 | 173.9 | 174.6 | 173.9 | 172.9 | 175.3 | 172.8 | 174 | 173.7 | 174.9 | 175.1 | 173.4 | 175.2 | 173.4 | | 174.1 | 0.8 | 172.8 | 175.3 | 14 |
| V@dP/dt min (mL) | 141.4 | 142 | 141 | 141.2 | 141.1 | 141 | 141.5 | 141.2 | 142.1 | 140.8 | 141.1 | 141.5 | 140.9 | 141.9 | | 141.3 | 0.4 | 140.8 | 142.1 | 14 |
| PVA (mmHg*mL) | 1012 | 994.4 | 1038 | 893.4 | 1031 | 1017 | 1021 | 1075 | 936 | 1051 | 931.5 | 1055 | 1073 | 974.5 | | 1007 | 55.4 | 893.4 | 1075 | 14 |
| PE (mmHg*mL) | -284.2 | -196.9 | -231 | -196.4 | -183.7 | -275.4 | -177.1 | -264.1 | -170.4 | -188 | -254 | -170.3 | -309.4 | -175.3 | | -219.7 | 48.5 | -309.4 | -170.3 | 14 |
| CE | 1.281 | 1.198 | 1.223 | 1.22 | 1.178 | 1.271 | 1.173 | 1.246 | 1.182 | 1.179 | 1.273 | 1.161 | 1.288 | 1.18 | | 1.218 | 0.0 | 1.161 | 1.288 | 14 |
| Tau (ms) | 41.29 | 53.26 | 53.58 | 52.12 | 53.63 | 41.33 | 53.93 | 49.67 | 54.28 | 52.7 | 44.97 | 53.37 | 44.84 | 54.36 | | 50.24 | 4.9 | 41.29 | 54.36 | 14 |
| ESPVR (mmHg/mL) | | | | | | | | | | | | | | | | | | | | |
| Piso (mmHg) | | | | | | | | | | | | | | | | | | | | |

**Table A5**. Pressure-volume data averages and standard deviations (STD) of three ovine at baseline and week 20 of RVF.

| | **Baseline (n=3)** | | | **Terminal – 20-week RVF (n=3)** | |
|---|---|---|---|---|---|
| | **Average** | **STD** | | **Average** | **STD** |
| **SW (mmHg*mL)** | -778.0 | 388.4 | | 935.5 | 650.6 |
| **CO (mL/min)** | 6406.0 | 625.0 | | 2931.3 | 2187.0 |
| **SV (mL)** | 54.0 | 14.5 | | 28.3 | 20.6 |
| **Vmax (mL)** | 97.6 | 66.4 | | 66.6 | 60.3 |
| **Vmin (mL)** | 43.6 | 62.6 | | 21.8 | 25.4 |
| **Ves (mL)** | 58.4 | 51.4 | | 25.4 | 30.6 |
| **Ved (mL)** | 52.1 | 69.4 | | 56.4 | 62.6 |
| **Pmax (mmHg)** | 26.3 | 2.9 | | 50.9 | 16.3 |
| **Pmin (mmHg)** | 6.0 | 0.9 | | 3.7 | 2.9 |
| **Pmean (mmHg)** | 14.2 | 1.3 | | 26.3 | 9.6 |
| **Pdev (mmHg)** | 20.4 | 3.3 | | 47.2 | 13.4 |
| **Pes (mmHg)** | 22.1 | 4.3 | | 49.8 | 15.5 |
| **Ped (mmHg)** | 7.4 | 0.9 | | 9.0 | 6.4 |
| **HR (bpm)** | 124.7 | 26.4 | | 103.5 | 5.4 |
| **EF (%)** | -38.2 | 164.4 | | 54.1 | 13.4 |
| **Ea (mmHg/mL)** | 0.4 | 0.1 | | -286.4 | 498.1 |
| **PowMax (mmHg*mL/s)** | 78510.0 | 68252.1 | | 27450.0 | 17829.5 |
| **dP/dt max (mmHg/s)** | 804.8 | 121.7 | | 999.6 | 398.8 |
| **dP/dt min (mmHg/s)** | -639.4 | 346.0 | | -710.7 | 190.3 |
| **dV/dt max (mL/s)** | 3476.0 | 2875.3 | | 1194.2 | 810.8 |
| **dV/dt min (mL/s)** | -3762.0 | 3426.9 | | -1097.0 | 709.8 |
| **P@dV/dt max (mmHg)** | 15.4 | 6.2 | | 13.9 | 9.6 |
| **P@dP/dt max (mmHg)** | 17.6 | 1.4 | | 25.5 | 8.2 |
| **V@dP/dt max (mL)** | 54.3 | 68.5 | | 54.8 | 46.8 |
| **V@dP/dt min (mL)** | 93.6 | 64.7 | | 25.9 | 29.9 |
| **PVA (mmHg*mL)** | | | | 4159.5 | 2163.0 |
| **PE (mmHg*mL)** | | | | 2849.0 | 2093.0 |
| **CE** | | | | 0.4 | 0.2 |
| **Tau (ms)** | 45.0 | 21.9 | | 44.7 | 6.2 |
| **VVC (SV/ESV)** | 0.60 | 0.13 | | 3.31 | 3.19 |

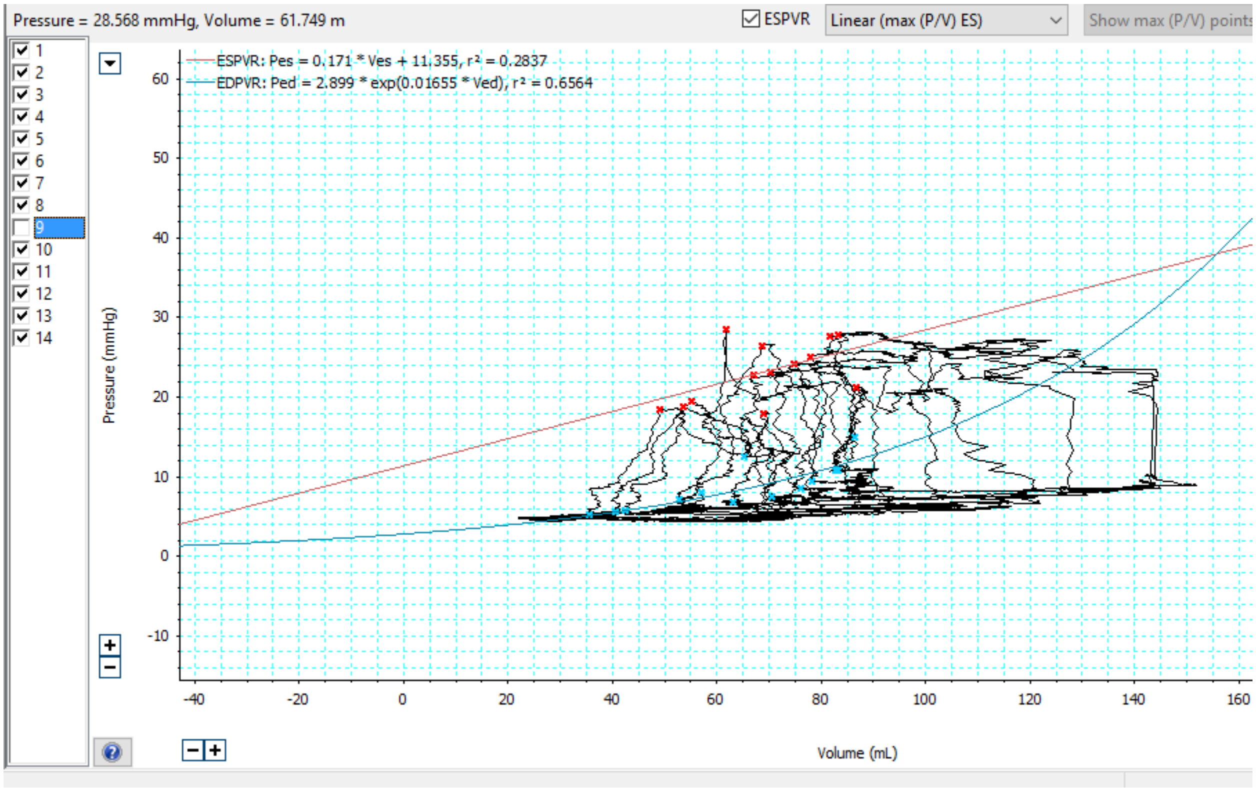
Pressure = 28.568 mmHg, Volume = 61.749 m

☑ ESPVR Linear (max (P/V) ES)

Show max (P/V) points

ESPVR: Pes = 0.171 * Ves + 11.355, r² = 0.2837

EDPVR: Ped = 2.899 * exp(0.01655 * Ved), r² = 0.6564

**Figure A3**. Representative pressure-volume loop during vena-cava occlusion of ovine at baseline.

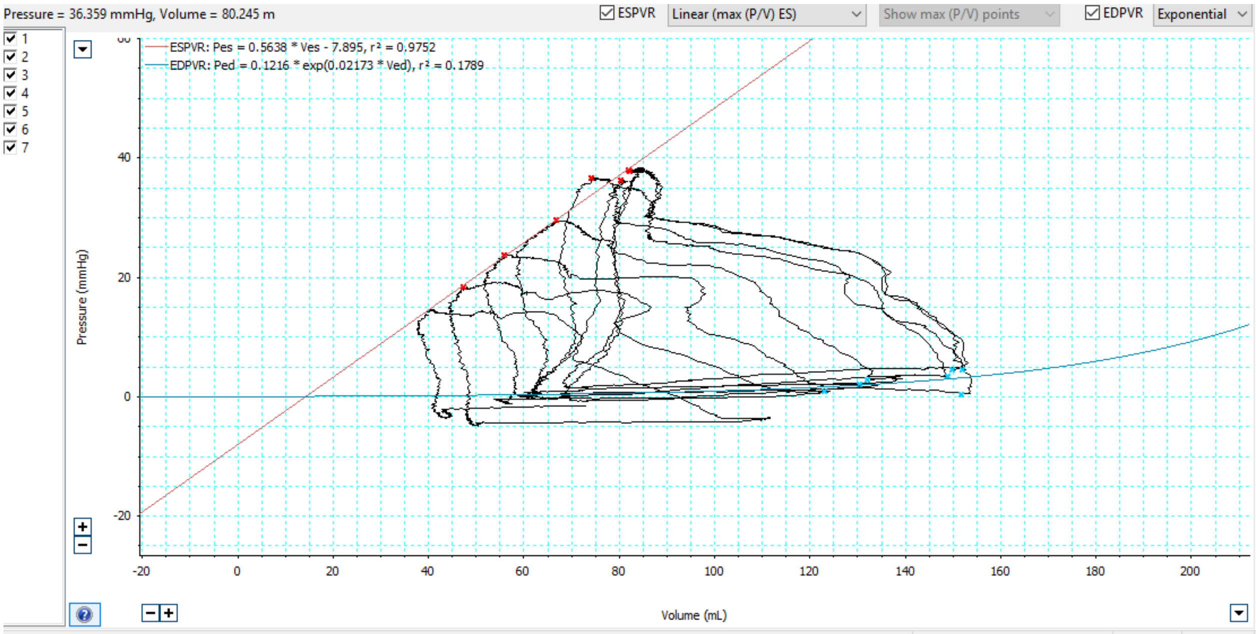
Pressure = 36.359 mmHg, Volume = 80.245 m

☑ ESPVR Linear (max (P/V) ES)

Show max (P/V) points

☑ EDPVR Exponential

ESPVR: Pes = 0.5638 * Ves - 7.895, r² = 0.9752

EDPVR: Ped = 0.1216 * exp(0.02173 * Ved), r² = 0.1789

**Figure A4**. Representative pressure-volume loop during vena-cava occlusion of ovine at week 20 of RVF.

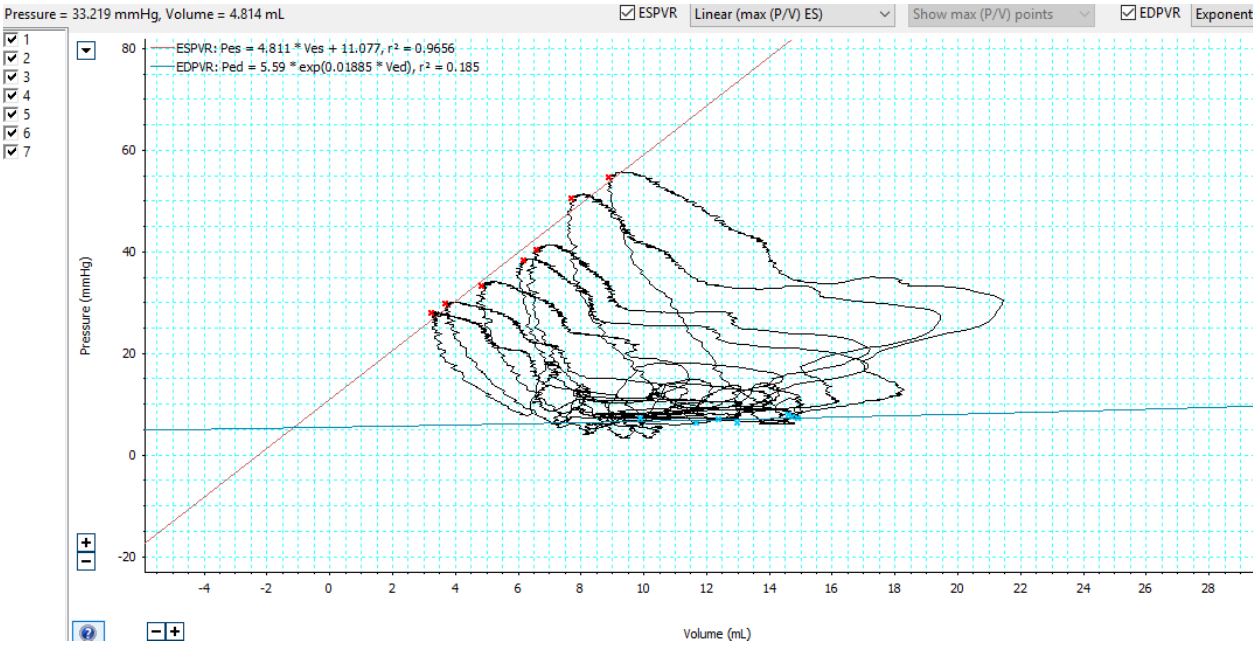

Pressure = 33.219 mmHg, Volume = 4.814 mL

☑ ESPVR Linear (max (P/V) ES)

☑ EDPVR Exponent

ESPVR: Pes = 4.811 * Ves + 11.077, r² = 0.9656

EDPVR: Ped = 5.59 * exp(0.01885 * Ved), r² = 0.185

**Figure A5**. Pressure-volume loop during vena-cava occlusion of ovine at week 20 of RVF with unrealistic stroke volume.